

Advanced Structured Materials

Holm Altenbach
Michael Brünig *Editors*

Inelastic Behavior of Materials and Structures Under Monotonic and Cyclic Loading

 Springer

Advanced Structured Materials

Volume 57

Series editors

Andreas Öchsner, Southport Queensland, Australia

Lucas F.M. da Silva, Porto, Portugal

Holm Altenbach, Magdeburg, Germany

More information about this series at <http://www.springer.com/series/8611>

Holm Altenbach · Michael Brünig
Editors

Inelastic Behavior of Materials and Structures Under Monotonic and Cyclic Loading

 Springer

Editors

Holm Altenbach
Fakultät für Maschinenbau, Institut für
Mechanik
Otto-von-Guericke University Magdeburg
Magdeburg
Germany

Michael Brüning
Fakultät für Bauingenieurwesen und
Umweltwissenschaften, Institut für
Mechanik und Statik
Universität der Bundeswehr München
Neubiberg
Germany

ISSN 1869-8433

Advanced Structured Materials

ISBN 978-3-319-14659-1

DOI 10.1007/978-3-319-14660-7

ISSN 1869-8441 (electronic)

ISBN 978-3-319-14660-7 (eBook)

Library of Congress Control Number: 2014958992

Springer Cham Heidelberg New York Dordrecht London

© Springer International Publishing Switzerland 2015

This work is subject to copyright. All rights are reserved by the Publisher, whether the whole or part of the material is concerned, specifically the rights of translation, reprinting, reuse of illustrations, recitation, broadcasting, reproduction on microfilms or in any other physical way, and transmission or information storage and retrieval, electronic adaptation, computer software, or by similar or dissimilar methodology now known or hereafter developed.

The use of general descriptive names, registered names, trademarks, service marks, etc. in this publication does not imply, even in the absence of a specific statement, that such names are exempt from the relevant protective laws and regulations and therefore free for general use.

The publisher, the authors and the editors are safe to assume that the advice and information in this book are believed to be true and accurate at the date of publication. Neither the publisher nor the authors or the editors give a warranty, express or implied, with respect to the material contained herein or for any errors or omissions that may have been made.

Printed on acid-free paper

Springer International Publishing AG Switzerland is part of Springer Science+Business Media
(www.springer.com)

Preface

This book is a collection of papers devoted to modeling of inelastic material behavior related to structures under normal and advanced conditions. At the moment there exist various approaches, among them phenomenological, mechanism-based, physically motivated, and others. In this sense this book is some kind of a state of the art.

Accurate and realistic modeling of inelastic behavior of advanced materials is essential for the solution of a numerous boundary-value problems occurring in different engineering fields. For example, various microscopic defects cause reduction in strength of materials and shorten the lifetime of engineering structures. Therefore, a main issue in engineering applications is to provide realistic information on the stress distribution within elements of such materials or assessment of safety factor against failure.

During the last years important progress has been observed in the testing practice for monotonic and cyclic behavior delivering important information on deformation patterns and damage evolution in interaction with material microstructure. Great efforts have been made in the attempt to develop more physically based constitutive models for predicting the occurrence of damage and failure in materials and structures under general loading conditions. At the same time, different research fields in solid mechanics and, especially, modeling of advanced materials have evolved due to development of multi-scale approaches. Although some progress has been made in theoretical fields, the application of multi-scale models to numerically analyze real components subjected to monotonic and cyclic loading conditions is still at an early stage. Different research groups around the world have proposed promising approaches and part of them are discussed in the present book.

The aim of the book is not only to consolidate the advances in inelastic material research but also to provide a forum to discuss new trends in damage and fracture mechanics proposing models that are either phenomenological ones or micro-mechanically motivated. Discussion of new multi-scale approaches at several length scales applied to nonlinear and heterogeneous materials have been emphasized from different related disciplines including metal physics, micro-mechanics, as well as mathematical and computational mechanics.

The editors wish to thank all authors for their contribution and the reviewers for their valuable comments and recommendations. After the peer review process, 12 papers are finally presented in this book aiming to become a helpful and valuable reference in the field of mechanics for scientists as well as for engineers.

Magdeburg, October 2014
Neubiberg

Holm Altenbach
Michael Brünig

Contents

Creep Behavior Modeling of Polyoxymethylene (POM) Applying Rheological Models	1
Holm Altenbach, Anna Girchenko, Andreas Kutschke and Konstantin Naumenko	
Experiments and Numerical Simulations on Stress-State-Dependence of Ductile Damage Criteria	17
Michael Brüinig, Steffen Gerke and Daniel Brenner	
Constitutive Modeling of Dissipative Phenomena in Austenitic Metastable Steels at Cryogenic Temperatures	35
Halina Egner, Błażej Skoczeń and Maciej Ryś	
Modeling of Continuous Damage Deactivation Accompanying Low Cycle Fatigue of Al-2024 Under Complex Loading	49
Artur Ganczarski and Maciej Oleksy	
Computational Multiscale Modeling of Nickel-Based Superalloys Containing Gamma-Gamma' Precipitates	67
Somnath Ghosh, Shahriyar Keshavarz and George Weber	
Homogenized Elastic-Viscoplastic Behavior of Thick Perforated Plates with Pore Pressure	97
Kazutaka Ikenoya, Nobutada Ohno and Naoto Kasahara	
Experimental and Numerical Investigations of the Effects Associated to Complex Loading Combinations	117
Zbigniew L. Kowalewski, Tadeusz Szymczak and Jan Maciejewski	

Fracture of Cortical Bone Tissue	143
Simin Li, Adel Abdel-Wahab, Emrah Demirci and Vadim V. Silberschmidt	
A Nonlocal Model of Plasticity and Damage with Different Internal Lengths	171
Francesco Marotti de Sciarra	
Hysteresis Loop Analysis in Cyclically Strained Materials	185
Jaroslav Polák and Roman Petráš	
Creep, Plasticity and Fatigue of Single Crystal Superalloys: Physics-Based Life Prediction for Turbine Components in Severe Operating Environments	207
Alexander Staroselsky and Thomas J. Martin	
Ratchetting of Snake Skin: Experiments and Viscoelastic-Plastic Constitutive Model	243
Yilin Zhu and Guozheng Kang	

Contributors

Adel Abdel-Wahab Wolfson School of Mechanical and Manufacturing Engineering, Loughborough University, Leicestershire, UK

Holm Altenbach Lehrstuhl für Technische Mechanik, Institut für Mechanik, Fakultät für Maschinenbau, Otto-von-Guericke-Universität Magdeburg, Magdeburg, Germany

Daniel Brenner Institut für Mechanik und Statik, Universität der Bundeswehr München, Neubiberg, Germany

Michael Brüning Institut für Mechanik und Statik, Universität der Bundeswehr München, Neubiberg, Germany

Emrah Demirci Wolfson School of Mechanical and Manufacturing Engineering, Loughborough University, Leicestershire, UK

Halina Egner Department of Mechanical Engineering, Institute of Applied Mechanics, Cracow University of Technology, Cracow, Poland

Artur Ganczarski Institute of Applied Mechanics, Cracow University of Technology, Kraków, Poland

Steffen Gerke Institut für Mechanik und Statik, Universität der Bundeswehr München, Neubiberg, Germany

Somnath Ghosh Departments of Civil and Mechanical Engineering, Johns Hopkins University, Baltimore, MD, USA

Anna Girchenko Lehrstuhl für Technische Mechanik, Institut für Mechanik, Fakultät für Maschinenbau, Otto-von-Guericke-Universität Magdeburg, Magdeburg, Germany

Kazutaka Ikenoya Department of Mechanical Science and Engineering, School of Engineering, Nagoya University, Nagoya, Japan

Guozheng Kang School of Mechanics and Engineering, Southwest Jiaotong University, Chengdu, People's Republic of China

Naoto Kasahara Department of Nuclear Engineering and Management, School of Engineering, The University of Tokyo, Tokyo, Japan

Shahriyar Keshavarz Departments of Civil and Mechanical Engineering, Johns Hopkins University, Baltimore, MD, USA

Zbigniew L. Kowalewski Institute of Fundamental Technological Research, Warsaw, Poland; Motor Transport Institute, Warsaw, Poland

Andreas Kutschke Lehrstuhl für Technische Mechanik, Institut für Mechanik, Fakultät für Maschinenbau, Otto-von-Guericke-Universität Magdeburg, Magdeburg, Germany

Simin Li Wolfson School of Mechanical and Manufacturing Engineering, Loughborough University, Leicestershire, UK

Jan Maciejewski Warsaw University of Technology, Warsaw, Poland

Francesco Marotti de Sciarra Department of Structures for Engineering and Architecture, University of Naples Federico II, Napoli, Italy

Thomas J. Martin United Technologies Research Center, East Hartford, USA

Konstantin Naumenko Lehrstuhl für Technische Mechanik, Institut für Mechanik, Fakultät für Maschinenbau, Otto-von-Guericke-Universität Magdeburg, Magdeburg, Germany

Nobutada Ohno Department of Mechanical Science and Engineering, School of Engineering, Nagoya University, Nagoya, Japan

Maciej Oleksy Dephi, Kraków, Poland

Roman Petráš Institute of Physics of Materials, Academy of Sciences of the Czech Republic, Brno, Czech Republic

Jaroslav Polák Institute of Physics of Materials, Academy of Sciences of the Czech Republic, Brno, Czech Republic; CEITEC, Institute of Physics of Materials Academy of Sciences of the Czech Republic, Brno, Czech Republic

Maciej Ryś Department of Mechanical Engineering, Institute of Applied Mechanics, Cracow University of Technology, Cracow, Poland

Vadim V. Silberschmidt Wolfson School of Mechanical and Manufacturing Engineering, Loughborough University, Leicestershire, UK

Błażej Skoczeń Department of Mechanical Engineering, Institute of Applied Mechanics, Cracow University of Technology, Cracow, Poland

Alexander Staroselsky United Technologies Research Center, East Hartford, USA

Tadeusz Szymczak Motor Transport Institute, Warsaw, Poland

George Weber Departments of Civil and Mechanical Engineering, Johns Hopkins University, Baltimore, MD, USA

Yilin Zhu School of Mechanics and Engineering, Southwest Jiaotong University, Chengdu, People's Republic of China

Creep Behavior Modeling of Polyoxymethylene (POM) Applying Rheological Models

Holm Altenbach, Anna Girchenko, Andreas Kutschke
and Konstantin Naumenko

Abstract Polyoxymethylene (POM) is a semi-crystalline thermoplastic polymer with broad technical application. Microstructure after solidifying is strongly dependent on the thermodynamical conditions. As an outcome macroscopic observable time dependent behavior is complex and significantly non-linear. To describe creep behavior of POM a rheological model with five elements is utilized. Creep behavior of POM under monotonic loading and constant temperature conditions can be described in a satisfying manner according to experimental results. A three-dimensional generalization with a comparable backstress formulation will be given. Finally, influence of data scattering will be estimated applying statistical analysis.

Keywords Creep · Polyoxymethylene · Rheological models · Backstress

1 Introduction

POM is widely used in technical application especially for high performance engineering components, because compared to other widely used thermoplastics, e.g. Polyethylene and Polypropylene, POM posses higher stiffness, ultimate strength as well as better long term properties, see Bonnet (2014) among others. A reliable material model in the design process of high performance components is of essential use

H. Altenbach (✉) · A. Girchenko · A. Kutschke · K. Naumenko
Lehrstuhl für Technische Mechanik, Institut für Mechanik,
Fakultät für Maschinenbau, Otto-von-Guericke-Universität Magdeburg,
Universitätsplatz 2, 39106 Magdeburg, Germany
e-mail: holm.altenbach@ovgu.de

A. Girchenko
e-mail: anna.girchenko@ovgu.de

A. Kutschke
e-mail: andreas.kutschke@ovgu.de

K. Naumenko
e-mail: konstantin.aumenko@ovgu.de

© Springer International Publishing Switzerland 2015
H. Altenbach and M. Brünig (eds.), *Inelastic Behavior of Materials
and Structures Under Monotonic and Cyclic Loading*, Advanced
Structured Materials 57, DOI 10.1007/978-3-319-14660-7_1

to avoid or at least reduce expensive prototype tests during shape or construction optimization.

Description of material response under mechanical loadings, temperature changes, etc., can be performed applying various approaches (Altenbach 2012). Two general main directions exist: the deductive approach (top-down modeling) and the inductive approach (bottom-up modeling). The first one is presented in monographs of Haupt (2002), Palmov (1998), among others, and as usual this approach is applied for materials with very complex behavior, see for example Altenbach et al. (2003), Vilchevskaya et al. (2014). The starting point are mathematical forms of constitutive equations, application of constitutive axioms, etc. The second approach is usual in most of engineering applications. Simple experimental observations are transferred in equations, which are generalized step by step. At each level correctness, for example, w.r.t. the second law of thermodynamics should be proved. The method of using rheological models is somehow a combination of both ways. Basic rheological elements, for which thermodynamical consistency is proved, see Krawietz (1986), Palmov (1998), are combined (series or parallel connections) in a bottom up way for description of complex behavior (Längler et al. 2014; Naumenko and Altenbach 2005; Naumenko et al. 2011; Naumenko and Gariboldi 2014).

2 POM—Microstructure and Macroscopic Behavior

After solidifying POM shows a significant microstructure, see Fig. 1, crystalline lamellae are radially arranged, separated by amorphous phase, and form so called spherulitic crystal volumes. Although some typical dimensions are indicated in the schematic sketch of Fig. 1. The resulting dimensions are strongly dependent on the

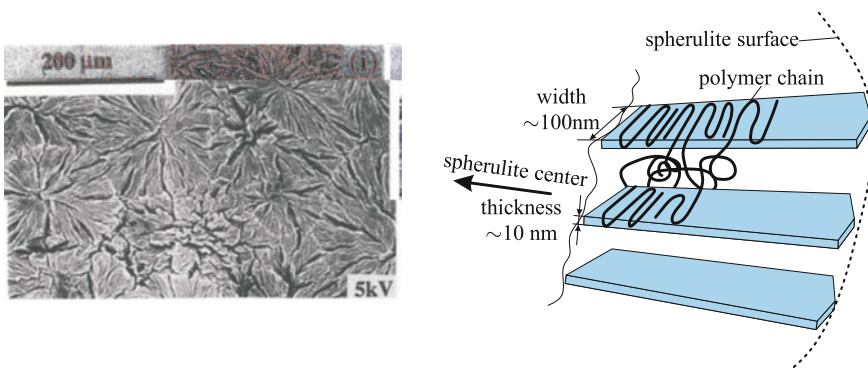


Fig. 1 Microstructure of partially crystalline polymers (SEM-pictures from Plummer and Kausch 1995, the schematic sketch after Katti and Schultz 1982)

conditions during solidification mainly cooling rate, shear rate and pressure, see Mileva et al. (2012).

This complex microstructure leads to a number of deformation mechanism under mechanical and thermal load, like formation, growth and coalescence of crazes, reorientation of broken crystalline lamellae, see Kim and Michler (1998). It is obvious that a description on the micro scale directly based on these mechanism resulting in an applicable material model is not only a challenging task but with the current state of computational methods as well as mechanical models is impossible.

Therefore, in this paper the phenomenological approach is utilized. To this end phenomena to describe have to be taken from experimental results like Fig. 2. A typical creep strain rate versus creep strain curve is shown with two main stages primary creep, reduction of creep rate to a minimum, and tertiary creep, increase of creep strain rate after minimum creep rate. During the first stage, usually addressed as hardening, several deformation mechanism may take place, e.g. polymer chain stretching and sliding in the amorphous phase and stress accumulation in bad, in the sense of deformation, orientated crystalline lamellae. Usually the tertiary creep stage is accompanied by damage and/or micro-mechanical changes and thus a consequently reduced area to withstand mechanical load. However, for this paper only the macroscopic test data was available, so a mechanism based material model can not be derived.

Nonetheless, a material model according to experimental results should reflect primary creep, a non-linear stress dependent minimum creep rate and tertiary creep.

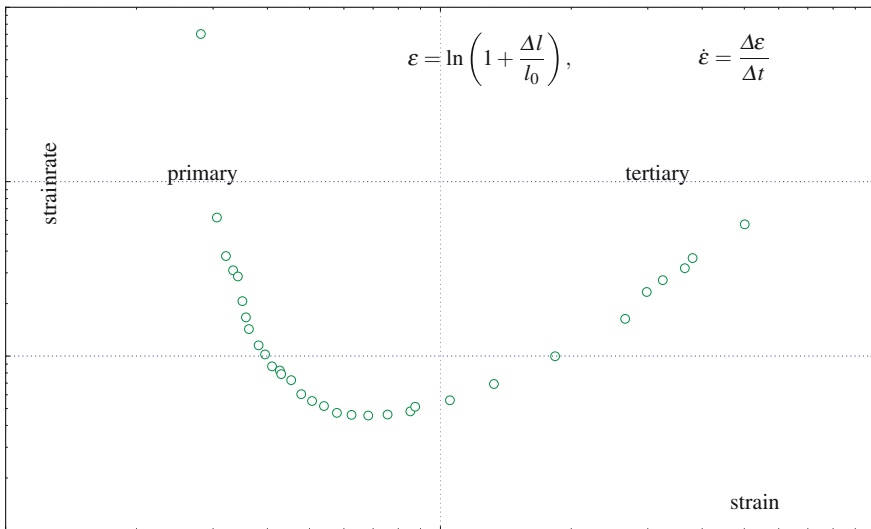


Fig. 2 Typical example of creep test data for POM, in this plot as well as the following axes of the diagram are normalized: strain rate $\dot{\epsilon}^{cr} / \dot{\epsilon}_{min}^{cr}$ and strain $\epsilon^{cr} / \epsilon_{min}^{cr}$, where $\dot{\epsilon}_{min}^{cr}$ and ϵ_{min}^{cr} are minimum creep rate and the strain at minimum creep rate, respectively. $\Delta \epsilon = \epsilon_n - \epsilon_{n-1}$, $\Delta t = t_n - t_{n-1}$ are the strain and time increment, n denotes the data point in experiment

3 One-Dimensional (1D) Material Model

The method of rheological modeling is widely used for describing viscoelastic and viscoplastic behavior of plastics. Basics are given in the pioneering monograph Reiner (1960). Later developments are given, for example, in Palmov (1998), Gisekus (1994). Starting point of any rheological models are the basic elements: elasticity, viscosity and plasticity. For creep behavior of POM it is sufficient to use springs (mechanical elastic elements) and dashpots (viscous or more general time dependent elements), Figs. 3 and 4. Both elements can be, as shown in the figures, utilized to show linear and non-linear response.

Let us develop a complex rheological model for creep behavior of POM. The Maxwell model (Fig. 5) does not fit the experimental data even in the simplest case of applied constant stress σ_0 , where σ_0 is related to the initial cross section. Because with such an arrangement creep rate will be obviously constant if the applied stress is constant. Hardening will be incorporated into the model by arranging a spring parallel to the dashpot. In this case the spring will try to pull back the dashpot with increasing creep strain. Primary creep can be modeled with such an approach presented by two elements. But with this arrangement no minimum creep rate will be reached, refer Fig. 6. To reach a minimum creep rate a second dashpot in series to the last introduced spring is necessary and thus hardening and stress dependent minimum creep rate behavior can be described, Fig. 7.

To describe the tertiary creep stage we will only take geometric non linearity into account. On one hand this is a strong limitation in the sense of mechanism based phenomenological modeling and intuitively not realistic according to the briefly mentioned damage mechanism, but on the other hand no appropriate experimental data was accessible to differentiate between damage and geometric effects. Concluding from this we decided that there is no benefit from an additional damage equation of unknown influence whereas geometric effects have to be taken into account according to the conducted creep tests with constant initial load. Influence of the geometric non-linearity can be visualized as shown in Fig. 8.

For numerical implementation it is necessary to express creep rate in terms of actual stress, the stress active in the current configuration of any time t . This can be obtained by assuming incompressible material during inelastic deformation which means that there is no change of volume during the deformation process. In the case of incompressibility geometric considerations will lead to an equation where initial

Fig. 3 Elastic rheological element



$$\sigma = E\varepsilon \text{ -linear elastic response}$$

$$\sigma = \Phi(\varepsilon)\text{-nonlinear elastic response}$$

Fig. 4 Viscose rheological element



$$\sigma = \eta\dot{\varepsilon} \text{ -linear viscose response}$$

$$\sigma = \Psi(\dot{\varepsilon})\text{-nonlinear viscose response}$$

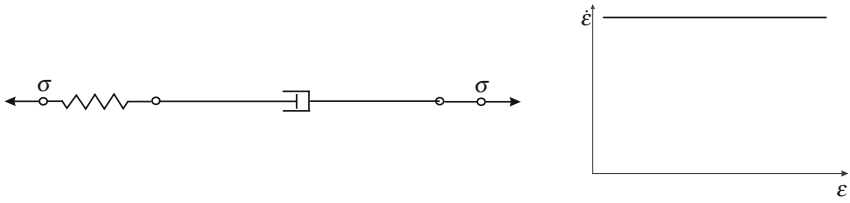


Fig. 5 Maxwell element

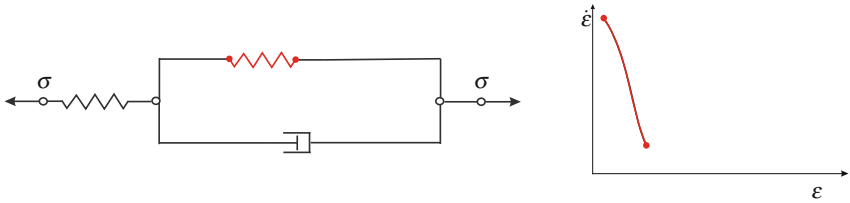


Fig. 6 Influence of the second elastic element

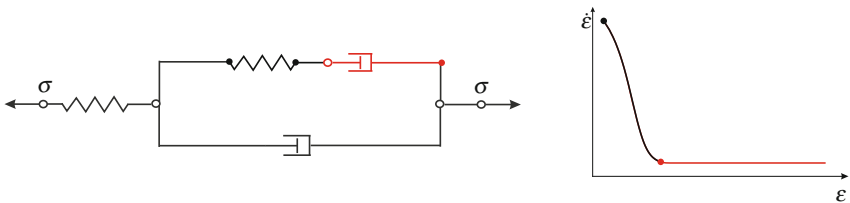


Fig. 7 Influence of the second viscose rheological element

stress and actual stress are linked by cross section shrinkage, among others derived in Besseling and Giessen (1994).

Finally one can write in the one-dimensional case

$$\sigma_{\text{Cauchy}} = \frac{f}{A} = \frac{f}{A_0}(1 + \epsilon) = P(1 + \epsilon),$$

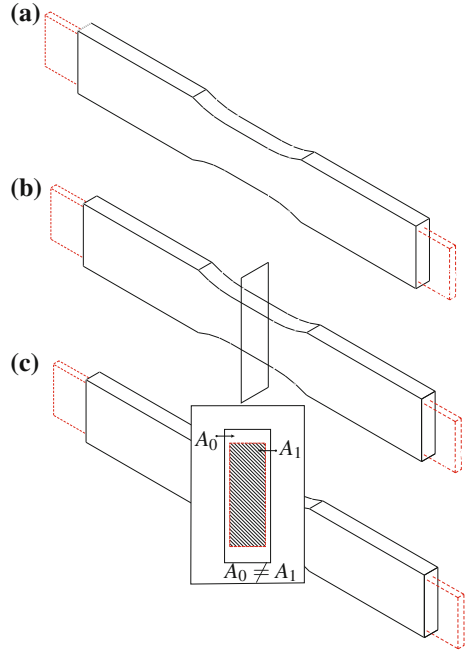
where l_0 is the initial length, $\Delta l = l - l_0$ is the current change of length, f is the normal force to A_0 , A respectively,

$$\epsilon = \ln\left(1 + \frac{\Delta l}{l_0}\right)$$

is the Hencky strain. With this formulation it is clear that a constant initial stress as argument of a viscosity function will lead to increasing strain rates with increasing creep strain.

With these basic remarks it is possible to analyze the following proposed rheological model for creep behavior of POM. The arrangement of our model is

Fig. 8 Visualization of the geometrical non-linearity. **a** Undeformed and deformed state, **b** orthogonal cross-section under consideration, **c** significant cross-section reduction: A_0 —reference cross-section, A_1 —current cross-section (indicate to distinguish between engineering and true stresses)



shown in Fig. 9 and is similar to the one in Fig. 7 but contains an additional dashpot parallel to our hardening spring. The additional introduced dashpot was found to be necessary to describe the hardening behavior accurately.

In what follows we present a straight forward derivation of our model to obtain a formulation in which the creep rate is only dependent on known quantities. Henceforth, we assume that the

- engineering stress is constant: $\sigma_0 = \text{const}$
- and creep strain can be presented as

$$\dot{\varepsilon}^{\text{cr}} = f [(\sigma_0 - \beta_0) (1 + \varepsilon^{\text{cr}})],$$

where σ_0 is the applied stress and β_0 is the backstress

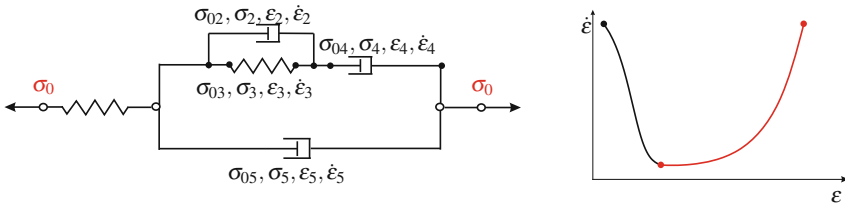


Fig. 9 Proposed four-element rheological model

Here and later the index 0 is related to quantities of initial configuration. It is now necessary to provide a proper formulation for the backstress β_0 as well as to define response functions.

- the creep strain ε^{cr} is equal to the nonlinear strain part of the rheological arrangement

$$\varepsilon^{\text{cr}} = \varepsilon_5 \quad (1)$$

that leads consequently to

$$\dot{\varepsilon}^{\text{cr}} = \dot{\varepsilon}_5 \quad (2)$$

- for the strain rate of the dashpot the following stress response function was chosen

$$\dot{\varepsilon}_5 = A \sinh(B\sigma_5), \quad (3)$$

where A and B are constants that need to be calibrated and σ_5 is the active Cauchy stress in the dashpot

- σ_5 has to be replaced in terms of the known σ_0
- considering nonlinear geometric effects we know the relation for the 1D case

$$\sigma_5 = \sigma_{05}(1 + \varepsilon_5), \quad (4)$$

where σ_{05} is the initial stress and ε_5 is the strain of the dashpot (for sake of simplicity we assume volume constant deformation for all rheological elements)

- the sum of the stresses in the two branches is equal to σ_0 , i.e.

$$\sigma_0 = \sigma_{05} + \beta_0, \quad (5)$$

where β_0 is the stress in the branch with the spring and the two dashpots and will be termed as backstress

- the expression $\sigma_{05} = \sigma_0 - \beta_0$ derived from (5) inserted in the statement (4) yields to

$$\sigma_5 = (\sigma_0 - \beta_0)(1 + \varepsilon_5) \quad (6)$$

- the remaining task is to find an expression for β_0
- similar to statement (5) β_0 can be represented as

$$\beta_0 = \sigma_{02} + \sigma_{03}, \quad (7)$$

where σ_{02} is the initial stress load of the spring and σ_{03} the initial stress load of the dashpot

- referring to the relation (4) the initial stress loads σ_{02} and σ_{03} can be expressed in terms of the active Cauchy stress

$$\sigma_{02} = \frac{\sigma_2}{1 + \varepsilon_2} \quad \text{and} \quad \sigma_{03} = \frac{\sigma_3}{1 + \varepsilon_3} \quad (8)$$

- from the isostrain condition it is plain to see that

$$\varepsilon_2 = \varepsilon_3 \quad (9)$$

- using (9) ε_3 can be replaced in the second Eq. (8)

$$\sigma_{03} = \frac{\sigma_3}{1 + \varepsilon_2} \quad (10)$$

- The first Eq. (8) and (10) are inserted in (7)

$$\beta_0 = \frac{\sigma_2 + \sigma_3}{1 + \varepsilon_2} \quad (11)$$

- for the spring one can write

$$\sigma_2 = E_2 \varepsilon_2, \quad (12)$$

where E_2 is the Young's modulus of the spring and a model parameter to be calibrated

- a hyperbolic sine law was chosen as response function for the dashpot, so we can express

$$\sigma_3 = \frac{1}{D} \sinh^{-1} \left(\frac{1}{C} \dot{\varepsilon}_3 \right), \quad (13)$$

where C and D are model parameters to calibrate

- now we insert (12) and (13) in (11),

$$\beta_0 = \frac{E_2 \varepsilon_2 + \frac{1}{D} \sinh^{-1} \left(\frac{1}{C} \dot{\varepsilon}_3 \right)}{1 + \varepsilon_2} \quad (14)$$

- the sum of the strains and the rates respectively of the elements in the back stress branch are equal to strain and the rate of the creep branch

$$\varepsilon_5 = \varepsilon_2 + \varepsilon_4 \quad (15)$$

and

$$\dot{\varepsilon}_5 = \dot{\varepsilon}_3 + \dot{\varepsilon}_4 \quad (16)$$

- with the help of (15) and (16) we can replace ε_2 and $\dot{\varepsilon}_3$ in (14)

$$\beta_0 = \frac{E_2(\varepsilon_5 - \varepsilon_4) + \frac{1}{D} \sinh^{-1} \left[\frac{1}{C} (\dot{\varepsilon}^{\text{cr}} - \dot{\varepsilon}_4) \right]}{1 + \varepsilon_5 - \varepsilon_4} \quad (17)$$

- finally we have to define the response function for the second dashpot in the back stress branch,

$$\dot{\varepsilon}_4 = F \sinh[G\beta_0(1 + \varepsilon_5)], \quad (18)$$

where F and G are model parameters to calibrate

Finally, we obtain the following set of equations

- a set of ordinary differential equations which has to be solved:

$$\dot{\varepsilon}^{\text{cr}} = A \sinh [B(\sigma_0 - \beta_0)(1 + \varepsilon_5)], \quad (19)$$

received after putting (7) in (3)

$$\dot{\varepsilon}_4 = F \sinh (G\beta_0 [1 + \varepsilon_5]) \quad (20)$$

- for each integration step the equation for β_0 needs to be computed:

$$\beta_0 = \frac{E_2(\varepsilon_5 - \varepsilon_4) + \frac{1}{D} \sinh^{-1} \left[\frac{1}{C} (\dot{\varepsilon}^{\text{cr}} - \dot{\varepsilon}_4) \right]}{1 + \varepsilon_5 - \varepsilon_4} \quad (21)$$

4 Results of the One-Dimensional Material Model

Parameters of the rheological model were identified by a minimizing procedure, where the minimizing statement is “experimental data”-“model prediction”. The minimizing method is of gradient type and available as a ready-to-use package in the programming language Python. During the minimizing procedure Eqs. (19)–(21) were solved also with a ready-to-use package from Python for integrating ordinary differential equation as well as root finding. Diagrams a–f in Fig. 10 show the comparison of experimental data with model predictions for different stress levels in the 1D case. Our investigation results from an industrial cooperation and therefore the parameter set is confidential.

One can see a good agreement of model prediction and uniaxial tension creep test. Especially the primary creep stage is for all stress levels well described as well as the stress dependency of the minimum creep rate. For the tertiary creep stage it is observable that only for higher stresses, diagram a and b, the deviation is small. At lower stress levels the tendency of the tertiary creep is correct but the characteristic shape is not well predicted. This is a strong indication that our decision to consider only geometric non linear effects is not completely justified. For higher stresses and short lifetime specimen failure due to deformation is observable, so one can argue that in this case geometric effects are more dominant than damage processes. Whereas for lower stresses and longer lifetime damage processes have time to evolve, get more and more dominant so that a description with only geometric effects fails to reproduce the characteristic shape of tertiary creep.

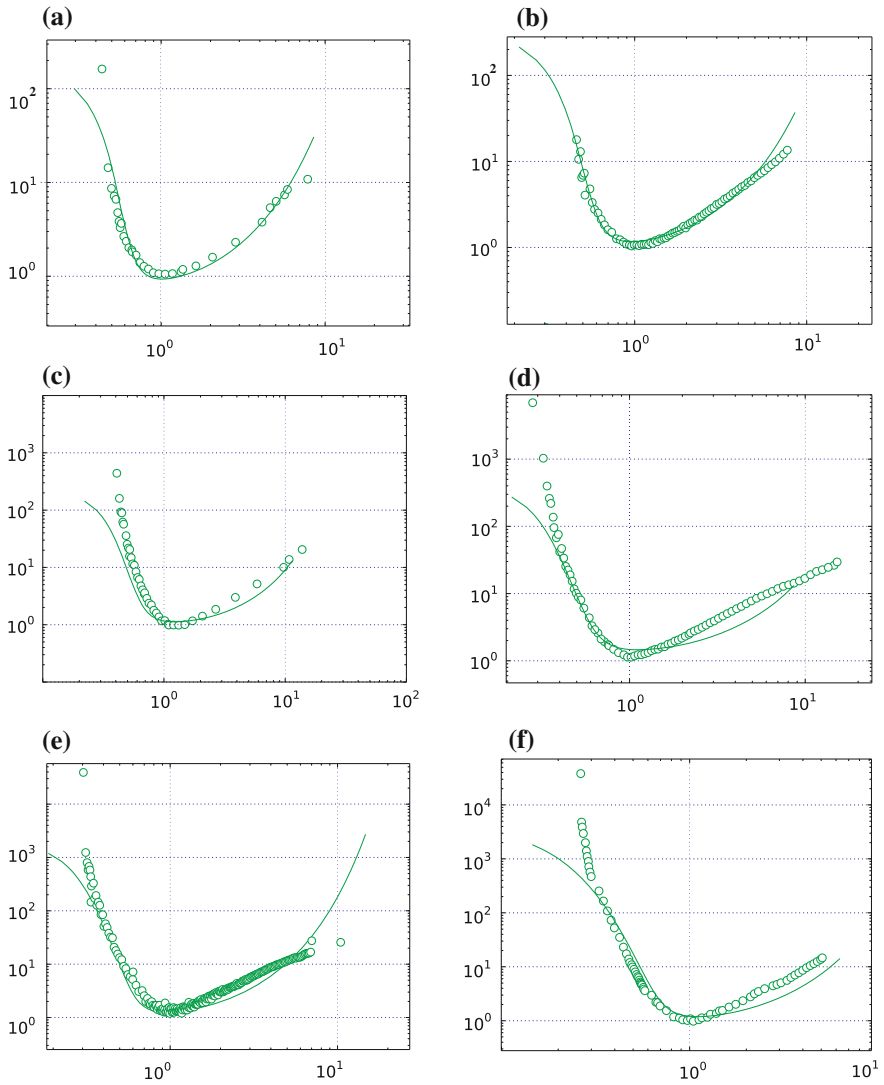


Fig. 10 Comparison of averaged uniaxial creep tension experimental data, *circle symbols*, and model prediction, *solid line*. Applied load: **a** 55 MPa, **b** 53 MPa, **c** 47 MPa, **d** 44 MPa, **e** 40 MPa, **f** 38.5 MPa

5 Statistical Analysis

Another reason to consider only geometric effects and to set a damage evolution equation aside is scatter of experimental data. For each stress level a set of three creep curves was available and geometric mean curves were computed to compare with the model prediction. Moreover with help of mean deviation and the formula displayed in Fig. 11 the confidence interval was calculated. The confidence interval is interpreted

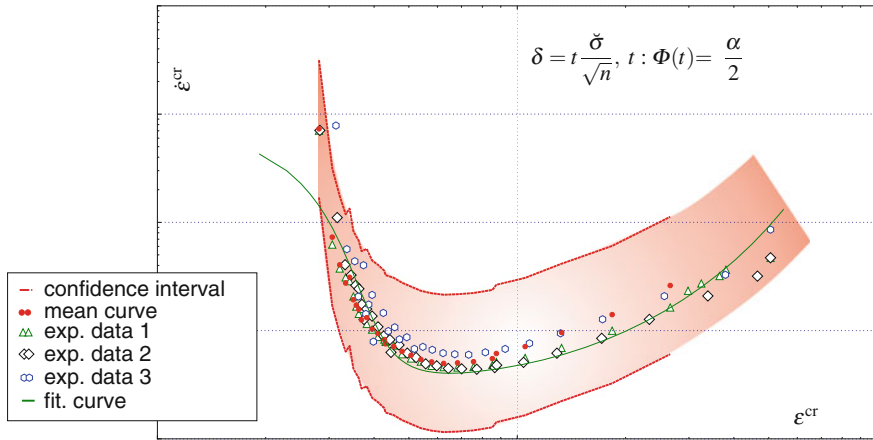


Fig. 11 Creep strain rate versus creep rate (confidence interval 75 %)

as an area around the mean curve in which our prediction should lie according to mean deviation and significance level. So the higher the confidence interval is and our model prediction still lies inside the confidence interval there is no need to change the model. This procedure should ensure that only material model behavior is fitted and no additional parameter is introduced to fit some special characteristic of a single curve. This method helps to keep the number of material model parameters minimal.

Let us assume at first the confidence interval (75 %) for the mean curve (Fig. 11). δ is width of the confidence interval, n is the sample quantity, $\bar{\sigma}$ is the standard deviation, α is the significance level and t is argument of Laplace function $\Phi(t)$.

The second example is related to the confidence interval (95 %) for the mean curve (Fig. 12). The third example is performed with the confidence interval (99 %) for the mean curve (Fig. 13).

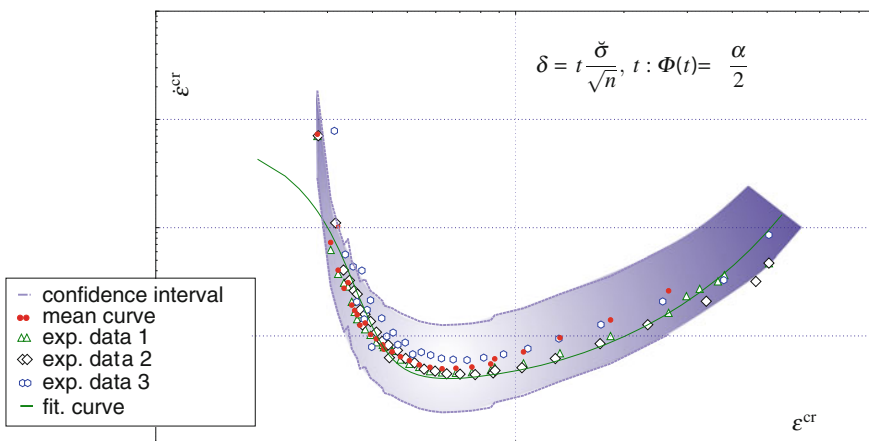


Fig. 12 Creep strain rate versus creep rate (confidence interval 95 %)

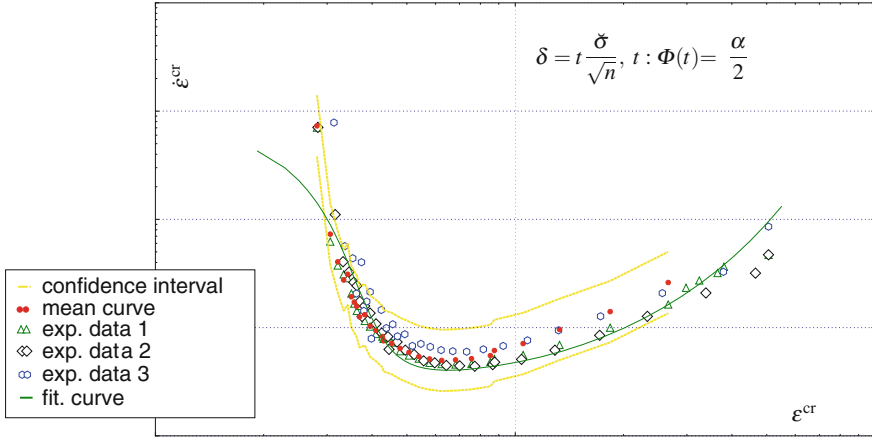


Fig. 13 Creep strain rate versus creep rate (confidence interval 99 %)

From evaluation of Figs. 11–13 one can conclude that even for the confidence interval of 99 % our model prediction lies inside the bounds of the confidence interval. This is a satisfying result and *a posteriori* justifies to take only geometric effects into account.

6 Extension to Three-Dimensional Equations

Usually, for technical components it is sufficient to simulate deformation up to 5 % of strain, because often 2 % of inelastic strain is a failure limit. The component itself may not fail in the sense of rupture but it loses functionality due to exceeded dimensional limits.

That is the reason our formulation of 3D state deformation is based on the so-called small strain assumption. Furthermore, if only the first part of the creep curve needs to be taken into account, it is fair to use a less complex model. To this end, we will use the following equations

$$\dot{\epsilon}^{cr} = f[(\sigma - \beta)], \quad \dot{\beta} = \frac{E}{c_h} \left[\dot{\epsilon}^{cr} - \dot{\epsilon}^{cr} \frac{\beta}{\beta_*(\sigma)} \right], \quad (22)$$

where f is a viscosity function of hyperbolic sine type, β is the backstress with c_h and $\beta_*(\sigma)$ as parameters.

These equations will now be generalized to 3D deformation states assuming isotropic and incompressible inelastic flow

$$\dot{\epsilon}^{cr} = \frac{3}{2} f(\bar{\sigma}_{vM}) \frac{\bar{s}}{\bar{\sigma}_{vM}}, \quad (23)$$

$$\begin{aligned} \bar{\mathbf{s}} &= \mathbf{s} - \boldsymbol{\beta}, \quad \mathbf{s} = \boldsymbol{\sigma} - \frac{1}{3}\text{tr}(\boldsymbol{\sigma})\mathbf{I}, \\ \bar{\sigma}_{\text{VM}} &= \sqrt{\frac{3}{2}\text{tr}(\bar{\mathbf{s}})^2}, \quad \dot{\epsilon}_{\text{VM}} = \sqrt{\frac{2}{3}\text{tr}(\dot{\boldsymbol{\epsilon}}^{\text{cr}})^2}, \quad \sigma_{\text{VM}} = \sqrt{\frac{3}{2}\text{tr}(\mathbf{s})^2} \end{aligned} \tag{24}$$

$$\dot{\boldsymbol{\beta}} = \frac{E}{c_h} \left[\dot{\boldsymbol{\epsilon}}^{\text{cr}} - \frac{3}{2}\dot{\epsilon}_{\text{VM}} \frac{\boldsymbol{\beta}}{\beta_*(\sigma_{\text{VM}})} \right] \tag{25}$$

where \mathbf{s} is the stress deviator, \mathbf{I} is the second rank unit tensor and E is the Young’s modulus. For further information see Naumenko et al. (2011).

If one gives a closer look to the backstress formulation it can be identified of Frederick-Armstrong type. Moreover, it is very close, refer to Eq. (17), to the backstress formulation which is found by using our rheological arrangement. Backstress tends toward a saturation value, is driven by inelastic strain and the non linearity is controlled by exponential functions. Only the backstress formulation derived by our rheological model contains a viscoelastic part which is necessary to simulate the whole creep curve.

7 Results of Three-Dimensional Simulation

The above set of Eqs. (23)–(25) will be implemented as UMAT-subroutine in the commercial FE-Code Abaqus. Two types of specimen will be analyzed. At first a smooth specimen, Fig. 14a, in which will be a one dimensional stress state if unidirectional loaded. Secondly a specimen slightly notched, Fig. 14b, which is dimensionally equal to the real specimen used in the unidirectional tension creep tests. The first specimen will be used to test if the numerical implementation was successful. In that case it is expected that the simulation of the smooth specimen unidirectional with a constant stress loaded gives the same result as the integration of Eqs. (19)–(21) with the same stress. After that formal implementation check the second specimen is simulated to verify the calibration and the 3D formulation. A successful result will be if the

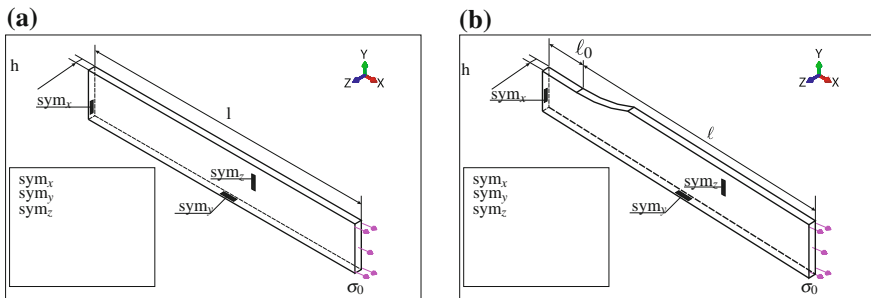


Fig. 14 Investigated specimen types to verify implementation and to compare reduced model with experimental results: **a** Smooth specimen; **b** Non-smooth specimen

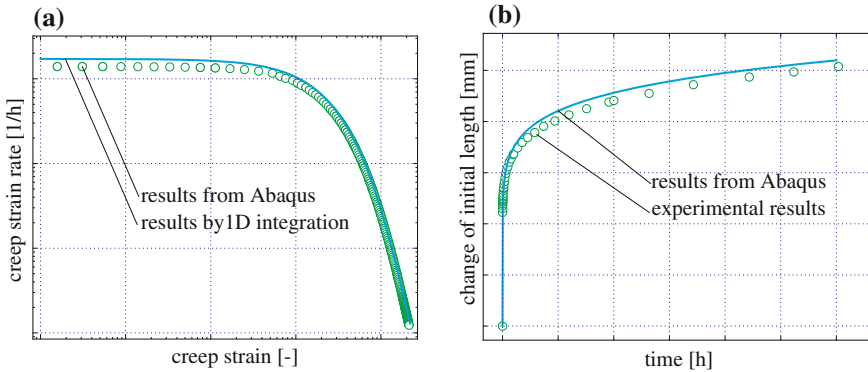


Fig. 15 Results of implementation as user subroutine in Abaqus: **a** One-dimensional solution versus three-dimensional solution for uniaxial loading; **b** Experiment versus simulation

simulation leads to the same Δl versus t curve that was recorded during the test for the according stress level. The obtained results can be taken from Fig. 15a and b.

The investigated specimens are shown in Fig. 14.

It can be attested that for both numerical simulations aimed results were achieved. The result of the numerical implementation check is as it should be. There is no significant deviation of 3D simulation from 1D directly integrated solution. For the compared Δl versus t curves it is fair to state that one can observe a satisfying agreement of simulation and experimental results.

8 Summary and Outlook

Modeling the whole creep curve with a rheological approach was successfully done. Even the strict assumption to consider only non linear geometric effects could be justified with help of a statistical analysis of experimental scatter. A comparable reduced model to simulate only hardening was suggested, implemented in the commercial FE-code Abaqus and verified against experimental data.

Our current output can be summarized as follows:

- Deformation processes on the microstructure level are briefly proposed,
- Model parameters for the whole creep curve behavior are determined with the help of macroscopic creep tests,
- Complex creep curves: primary creep stage, stress level dependent minimum creep rate and tertiary creep stage are well predicted by our model,
- If only primary creep stage is of interest a reduced model is proposed,
- Numerical implementation of the reduced model is verified,
- Experimental results were reproduced by a FE-simulation with a very good agreement.

Several open questions are:

- So far a temperature dependence is not incorporated in the material model.
- If appropriate experimental data is accessible a damage evolution equation should enter the material model.
- A proper 3D formulation for finite deformation of our model needs to be derived.

References

- Altenbach H (2012) *Kontinuumsmechanik*, 2nd edn. Springer, Berlin
- Altenbach H, Naumenko K, Zhilin P (2003) A micro-polar theory for binary media with application to phase-transitional flow of fiber suspensions. *Contin Mech Thermodyn* 15(6):539–570
- Besseling JF (1994) *Mathematical modelling of inelastic deformation*. Springer, New York
- Bonnet M (2014) Werkstoffauswahl-Kunststoffe. In: *Kunststofftechnik*. Springer, pp 219–234
- Gisokus H (1994) *Phänomenologische Rheologie: Eine Einführung*. Springer, Berlin
- Haupt P (2002) *Continuum mechanics and theory of materials*, 2nd edn. *Advanced Texts in Physics*. Springer, Berlin
- Katti S, Schultz M (1982) The microstructure of injection-molded semicrystalline polymers: a review. *Polym Eng Sci* 22(16):1001–1017
- Kim GM, Michler G (1998) Micromechanical deformation processes in toughened and particle-filled semicrystalline polymers: part 1. Characterization of deformation processes in dependence on phase morphology. *Polymer* 39(23):5689–5697
- Krawietz A (1986) *Materialtheorie: mathematische Beschreibung des phänomenologischen thermomechanischen Verhaltens*. Springer, New York
- Längler F, Naumenko K, Altenbach H, Ievdokymov M (2014) A constitutive model for inelastic behavior of casting materials under thermo-mechanical loading. *J Strain Anal Eng Des* 49(6):421–428
- Mileva D, Androsch R, Cavallo D, Alfonso G (2012) Structure formation of random isotactic copolymers of propylene and 1-hexene or 1-octene at rapid cooling. *Eur Polym J* 48:1082–1092
- Naumenko K, Altenbach H (2005) A phenomenological model for anisotropic creep in a multipass weld metal. *Arch Appl Mech* 74(11–12):808–819
- Naumenko K, Gariboldi E (2014) A phase mixture model for anisotropic creep of forged Al-Cu-Mg-Si alloy. *Mater Sci Eng: A* 618:368–376
- Naumenko K, Altenbach H, Kutschke A (2011) A combined model for hardening, softening, and damage processes in advanced heat resistant steels at elevated temperature. *Int J Damage Mech* 20(4):578–597
- Palmov V (1998) *Vibrations of elasto-plastic bodies*. *Foundation of Engineering Mechanics*. Springer, Berlin
- Plummer C, Kausch HH (1995) Real-time image analysis and numerical simulation of isothermal spherulite nucleation and growth in polyoxymethylene. *Colloid Polym Sci* 273(8):719–732
- Reiner M (1960) *Deformation, strain and flow: an elementary introduction to rheology*. H.K Lewis, London
- Vilchevskaya E, Ivanova E, Altenbach H (2014) Description of liquid–gas phase transition in the frame of continuum mechanics. *Contin Mech Thermodyn* 26(2):221–245. doi:10.1007/s00161-013-0298-5

Experiments and Numerical Simulations on Stress-State-Dependence of Ductile Damage Criteria

Michael Brüinig, Steffen Gerke and Daniel Brenner

Abstract The paper deals with a series of new experiments and corresponding numerical simulations to be able to study the effect of stress state on damage behavior of ductile metals. In this context, a thermodynamically consistent anisotropic continuum damage model is presented. It takes into account the effect of stress state on damage and failure conditions as well as on evolution equations of damage strains. Different branches of the respective criteria are considered corresponding to various damage and failure mechanisms depending on stress intensity, stress triaxiality and the Lode parameter. Since it is not possible to propose and to validate stress-state-dependent criteria only based on tests with uniaxially loaded specimens for a wide range of stress states, new experiments with two-dimensionally loaded specimens have been developed. Corresponding numerical simulations of these experiments show that they cover a wide range of stress triaxialities and Lode parameters in the tension, shear and compression domains. The new series of experiments allow validation of stress-state-dependent functions for the damage criteria and are used to identify parameters of the continuum model.

Keywords Ductile damage · Stress state dependence · Experiments · Numerical simulations

1 Introduction

Modeling of inelastic behavior and fracture of materials employed in various engineering applications is an important topic in solid mechanics, for example, in numerical analyses of complex structural components, in assessment of structural reliability,

M. Brüinig (✉) · S. Gerke · D. Brenner
Institut für Mechanik und Statik, Universität der Bundeswehr München,
85577 Neubiberg, Germany
e-mail: michael.bruenig@unibw.de

S. Gerke
e-mail: steffen.gerke@unibw.de

D. Brenner
e-mail: daniel.brenner@unibw.de

© Springer International Publishing Switzerland 2015
H. Altenbach and M. Brüinig (eds.), *Inelastic Behavior of Materials and Structures Under Monotonic and Cyclic Loading*, Advanced Structured Materials 57, DOI 10.1007/978-3-319-14660-7_2

or in optimization of structural design. Based on many experiments it is well known that finite or large inelastic deformations caused by loading of ductile metals and metal alloys are accompanied by damage and local failure mechanisms acting on different scales which lead to macro-failure of structural elements. In particular, under tension dominated loading conditions (high positive stress triaxialities) damage in ductile metals is mainly caused by nucleation, growth and coalescence of voids whereas under shear and compression dominated conditions (small positive or negative stress triaxialities) evolution of micro-shear-cracks is the predominant damage mechanism. Therefore, to be able to develop a realistic, accurate and efficient phenomenological model it is important to analyze and to understand the complex stress-state-dependent processes of damage and fracture as well as its respective mechanisms acting on different scales. In this context, in the last years various damage models have been published based on experimental observations as well as on multi-scale approaches (Brünig 2003a; Gurson 1977; Lemaitre 1996; Voyiadjis and Kattan 1999). In this context, Brünig et al. (2008, 2011b), Brünig and Gerke (2011) have proposed a generalized and thermodynamically consistent, phenomenological continuum damage model which has been implemented as user-defined material subroutines in commercial finite element programs allowing analyses of static and dynamic problems in differently loaded metal specimens. To be able to detect stress triaxiality dependence of the constitutive equations tension tests with carefully designed specimens have been developed. For example, differently pre-notched specimens and corresponding numerical simulations have been used by Bai and Wierzbicki (2008), Bao and Wierzbicki (2004), Becker et al. (1988), Bonora et al. (2005), Brünig et al. (2008, 2011b), Dunand and Mohr (2011), Gao et al. (2010). However, these experiments with unnotched and differently notched flat specimens showed stress triaxialities only in a small region of positive values. Larger triaxialities appear in tension tests with cylindrical (axi-symmetric) specimens but they cannot be manufactured when the behavior of thin sheets is investigated. Therefore, it is necessary to develop new series of experiments with flat specimens where a larger range of stress triaxialities will occur.

Thus, specimens with new geometries have been designed to be able to analyze stress states with small hydrostatic parts. Tension tests with these specimens have been performed (Bao and Wierzbicki 2004; Gao et al. 2010) leading to shear mechanisms in their centers. Similar specimens have been developed and tested (Brünig et al. 2008; Driemeier et al. 2010). Furthermore, to be able to take into account other regions of stress triaxialities butterfly specimens have been manufactured (Bai and Wierzbicki 2008; Dunand and Mohr 2011; Mohr and Henn 2007) which can be tested in different directions using special experimental equipment. Alternatively, in the present paper series of new tests with biaxially loaded new flat specimens taken from thin sheets will be developed leading to experimental results on inelastic behavior, damage and fracture of ductile metals for a wide range of stress triaxialities not obtained by the experiments discussed above.

Further information on damage and failure mechanisms can be obtained by performing numerical simulations on the micro-level (Brocks et al. 1995; Brünig et al. 2011a, 2013, 2014; Chew et al. 2006; Kuna and Sun 1996; Needleman and Kushner

1990; Zhang et al. 2001) considering individual behavior of growth and coalescence of voids and micro-shear-cracks as well as their accumulation to macro-cracks. The numerical results elucidated which parameters had remarkable effect on macroscopic stress-strain relations and on evolution equations for the damage variables and which ones only had marginal influence. With these numerical studies taking into account a large range of stress states it was possible to detect different damage mechanisms which have not been exposed by experiments. The equations for damage criteria and damage evolution equations proposed by analyzing in detail the numerical results of the micro-mechanical studies considering differently loaded micro-defect containing representative volume elements showed remarkable dependence on stress triaxiality and—especially in regions with small or negative triaxialities—additional dependence on the Lode parameter or third deviatoric stress invariant. However, the proposed functions are only based on numerical simulations on the micro-level with void-containing unit-cells and, therefore, further experiments with carefully designed specimens are necessary for their validation.

In the present paper fundamental governing equations of the phenomenological continuum damage model proposed by Brünig (2003a) are briefly discussed. Experiments on inelastic and damage behavior of an aluminum alloy are performed. Uniaxial tension tests are used to identify basic elastic-plastic material parameters. Furthermore, newly developed biaxial experiments with 2D-specimens up to final fracture will be presented. These combined shear-tension and shear-compression tests cover a wide range of stress states. Corresponding numerical simulations of these biaxial experiments will reveal various stress measures in critical regions. Experimental and numerical data are used to propose and to validate damage criteria as well as to identify corresponding constitutive parameters.

2 Continuum Damage Model

Irreversible material behavior and anisotropic damage of ductile metals are predicted by Brünig's continuum model (Brünig 2003a). It is based on series of experimental results and observations and, additionally, takes into account information of microscopic mechanisms due to individual micro-defects and their interactions. The phenomenological approach is based on the introduction of damaged and corresponding fictitious undamaged configurations and has been implemented into finite element programs. An extended version of this model takes into account a stress-state-dependent damage criterion based on experimental results of different tension and shear tests with smooth and pre-notched specimens as well as on data from corresponding numerical simulations (Brünig et al. 2008, 2011b). Furthermore, numerical analyses using unit cell models have been performed (Brünig et al. 2011a, 2013, 2014). Based on their numerical results covering a wide range of stress states they proposed damage equations as functions of the stress intensity, the stress triaxiality and the Lode parameter and estimated micro-mechanically based material parameters.

The kinematic approach of the continuum model is based on the introduction of initial, current and elastically unloaded configurations each defined as damaged and fictitious undamaged configurations, respectively. This leads to the additive decomposition of the strain rate tensor into an elastic ($\dot{\mathbf{H}}^{\text{el}}$), a plastic ($\dot{\mathbf{H}}^{\text{pl}}$) and a damage part ($\dot{\mathbf{H}}^{\text{da}}$) (see Brünig 2003a for further details).

The undamaged configurations are considered to describe the constitutive behavior of the undamaged matrix material. This leads to the effective Kirchhoff stress tensor $\bar{\mathbf{T}}$. In addition, plastic behavior of ductile metals is governed by the yield condition

$$f^{\text{pl}}(\bar{I}_1, \bar{J}_2, c) = \sqrt{\bar{J}_2} - c \left(1 - \frac{a}{c} \bar{I}_1\right) = 0, \quad (1)$$

where $\bar{I}_1 = \text{tr} \bar{\mathbf{T}}$ and $\bar{J}_2 = \frac{1}{2} \text{dev} \bar{\mathbf{T}} \cdot \text{dev} \bar{\mathbf{T}}$ are invariants of the effective stress tensor $\bar{\mathbf{T}}$, c denotes the yield stress of the matrix material and a represents the hydrostatic stress coefficient where a/c is a constant material parameter.

Since only isochoric plastic deformations have been observed in ductile metals the plastic potential function

$$g^{\text{pl}}(\bar{\mathbf{T}}) = \sqrt{\bar{J}_2} \quad (2)$$

depends only on the second invariant of the effective stress deviator which leads to the non-associated isochoric effective plastic strain rate

$$\dot{\mathbf{H}}^{\text{pl}} = \dot{\lambda} \frac{\partial g^{\text{pl}}}{\partial \bar{\mathbf{T}}} = \dot{\lambda} \frac{1}{2\sqrt{\bar{J}_2}} \text{dev} \bar{\mathbf{T}} = \dot{\gamma} \bar{\mathbf{N}}. \quad (3)$$

In Eq. (3) $\dot{\lambda}$ is a non-negative scalar-valued factor,

$$\bar{\mathbf{N}} = \frac{1}{\sqrt{2 \bar{J}_2}} \text{dev} \bar{\mathbf{T}}$$

represents the effective normalized deviatoric stress tensor and

$$\dot{\gamma} = \bar{\mathbf{N}} \cdot \dot{\mathbf{H}}^{\text{pl}} = \frac{1}{\sqrt{2}} \dot{\lambda}$$

characterizes the equivalent plastic strain rate measure used in the present continuum model.

Moreover, the damaged configurations are considered to describe the constitutive behavior of the damaged material (material sample including micro-defects). It is well known that damage remarkably affects the elastic behavior and leads to deterioration of elastic material properties. The corresponding elastic law of the damaged material leads to the Kirchhoff stress tensor \mathbf{T} (see Brünig 2003a for further details). In addition, constitutive equations for damage evolution are required and the determination of onset and continuation of damage is based on the concept of damage

surface formulated in stress space at the macroscopic damaged continuum level. The damage condition

$$f^{\text{da}} = \alpha I_1 + \beta \sqrt{J_2} - \sigma = 0 \quad (4)$$

is expressed in terms of the stress invariants of the Kirchhoff stress tensor, $I_1 = \text{tr} \mathbf{T}$ and $J_2 = \frac{1}{2} \text{dev} \mathbf{T} \cdot \text{dev} \mathbf{T}$, and the damage threshold σ . In Eq. (4) the variables α and β denote damage mode parameters depending on the stress intensity $\sigma_{\text{eq}} = \sqrt{3J_2}$, the stress triaxiality

$$\eta = \frac{\sigma_m}{\sigma_{\text{eq}}} = \frac{I_1}{3\sqrt{3}J_2} \quad (5)$$

defined as the ratio of the mean stress σ_m and the von Mises equivalent stress σ_{eq} as well as on the Lode parameter

$$\omega = \frac{2T_2 - T_1 - T_3}{T_1 - T_3} \quad \text{with } T_1 \geq T_2 \geq T_3, \quad (6)$$

expressed in terms of the principal Kirchhoff stress components T_1 , T_2 and T_3 (Brüning et al. 2013).

Furthermore, increase in macroscopic irreversible strains caused by the simultaneous nucleation, growth and coalescence of micro-defects is modeled by a stress-state-dependent damage rule. In this context, the damage potential function

$$g^{\text{da}}(\tilde{\mathbf{T}}) = g^{\text{da}}(I_1, J_2, J_3), \quad (7)$$

is introduced where $\tilde{\mathbf{T}}$ represents the stress tensor formulated in the damaged configuration which is work-conjugate to the damage strain rate tensor $\dot{\mathbf{H}}^{\text{da}}$ (see Brüning 2003a for further details) and I_1 , J_2 and J_3 are corresponding invariants which coincide with those of the Kirchhoff stress tensor. This leads to the damage strain rate tensor

$$\dot{\mathbf{H}}^{\text{da}} = \dot{\mu} \frac{\partial g^{\text{da}}}{\partial \tilde{\mathbf{T}}} = \dot{\mu} \left(\frac{\partial g^{\text{da}}}{\partial I_1} \mathbf{1} + \frac{\partial g^{\text{da}}}{\partial J_2} \text{dev} \tilde{\mathbf{T}} + \frac{\partial g^{\text{da}}}{\partial J_3} \text{dev} \tilde{\mathbf{S}} \right) \quad (8)$$

where $\dot{\mu}$ is a non-negative scalar-valued factor and

$$\tilde{\mathbf{S}} = \text{dev} \tilde{\mathbf{T}} \text{dev} \tilde{\mathbf{T}} - \frac{2}{3} J_2 \mathbf{1} \quad (9)$$

represents the second order deviatoric stress tensor. Alternatively, the damage strain rate tensor (8) can be written in the form

$$\dot{\mathbf{H}}^{\text{da}} = \dot{\mu} \left(\bar{\alpha} \frac{1}{\sqrt{3}} \mathbf{1} + \bar{\beta} \mathbf{N} + \bar{\delta} \mathbf{M} \right) \quad (10)$$

where the normalized tensors

$$\mathbf{N} = \frac{1}{2\sqrt{J_2}} \operatorname{dev} \tilde{\mathbf{T}}$$

and

$$\mathbf{M} = \frac{1}{\|\operatorname{dev} \tilde{\mathbf{S}}\|} \operatorname{dev} \tilde{\mathbf{S}}$$

have been used. In Eq. (10) the parameters $\bar{\alpha}$, $\bar{\beta}$ and $\bar{\delta}$ are kinematic variables describing the respective portion of volumetric and isochoric damage-based deformations. The damage rule (10) takes into account isotropic and anisotropic parts corresponding to isotropic growth of voids and anisotropic evolution of micro-shear-cracks, respectively. The inclusion of the isochoric terms in Eq. (10) rests on the notion that the volume of micro-defects undergoing shear dominated loadings may not significantly increase but deformation of micro-defects and their reorientation also constitute an effective increase in damage and will, therefore, contribute to softening of material behavior. Thus, the damage rule (10) is able to model the stress-state-dependent mechanisms discussed above.

Stress-state-dependence of the parameters in the damage condition (4) and in the damage rule (8) has been investigated in detail performing numerical simulations on the micro-level (Brünig et al. 2013). Based on various unit-cell calculations taking into account a wide range of stress triaxiality coefficients η and Lode parameters ω the damage mode parameter α in the damage criterion (4) has been proposed to be

$$\alpha(\eta) = \begin{cases} 0 & \text{for } \frac{-1}{3} \leq \eta \leq 0 \\ \frac{1}{3} & \text{for } \eta > 0 \end{cases} \quad (11)$$

whereas β is taken to be the non-negative function

$$\beta(\eta, \omega) = \beta_0(\eta, \omega = 0) + \beta_\omega(\omega) \geq 0, \quad (12)$$

see Fig. 1, with

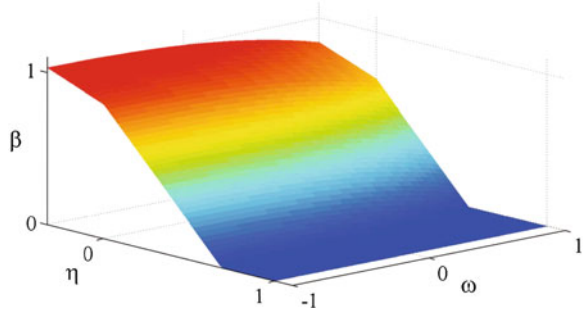
$$\beta_0(\eta) = \begin{cases} -0.45 \eta + 0.85 & \text{for } \frac{-1}{3} \leq \eta \leq 0 \\ -1.28 \eta + 0.85 & \text{for } \eta > 0 \end{cases} \quad (13)$$

and

$$\beta_\omega(\omega) = -0.017 \omega^3 - 0.065 \omega^2 - 0.078 \omega. \quad (14)$$

Figure 1 clearly shows that in the negative stress triaxiality regime $-1/3 \leq \eta \leq 0$ the damage mode parameter β is large signifying remarkable influence of the second deviatoric stress invariant J_2 on onset of damage whereas the influence of the negative hydrostatic stress is small and does not remarkably affect the damage behavior. This corresponds to dominant shear mechanisms and marginal volume changes caused by

Fig. 1 Parameter β versus stress triaxiality η and Lode parameter ω (Brünig et al. 2013)



damage. On the other hand, for high stress triaxialities the damage mode parameter is taken to be $\beta = 0$ and, thus, only the first stress invariant I_1 is taken to determine the onset of damage caused by predominant, nearly isotropic void growth mechanisms. However, this stress-state-dependent damage criterion is only based on numerical unit-cell calculations and, therefore, it will be validated in the present paper by various experiments and corresponding numerical simulations on the macro-level covering a wide range of stress triaxialities and Lode parameters.

3 Identification of Material Parameters

Elastic-plastic material parameters are identified using experimental results from uniaxial tension tests with unnotched specimens. Equivalent stress–equivalent plastic strain curves are easily obtained from load-displacement curves as long as the uniaxial stress field remains homogeneous between the clip gauges fixed on the specimens during the tests. It is worthy to note that equivalent stress–equivalent strain curves especially at large inelastic deformations have to be modeled accurately because material response for multi-axial loading conditions as well as localization phenomena are very sensitive to the identified parameters, especially to the current plastic hardening modulus.

For the aluminum alloy of the series 2017 investigated in the present paper, fitting of numerical curves and experimental data leads to Young’s modulus $E = 65,000$ MPa and Poisson’s ratio is taken to be $\nu = 0.3$. For the plastic material behavior, the power law function for the equivalent stress–equivalent plastic strain function appearing in the yield criterion (1)

$$c = c_0 \left(\frac{H \gamma}{n c_0} + 1 \right)^n \tag{15}$$

is used to model the work-hardening behavior. Good agreement of experimental data and numerical results is achieved for the initial yield strength $c_0 = 175$ MPa, the hardening modulus $H = 2,100$ MPa and the hardening exponent $n = 0.22$.

In addition, experimental results of notched uniaxial specimens are used to determine the hydrostatic stress dependence of the yield condition (1). Performing elastic-plastic numerical calculations leads to the hydrostatic stress coefficient $a/c = 0.000055$.

Furthermore, onset of damage is determined by comparison of experimental results of tension tests with corresponding elastic-plastic numerical analyses (Brünig et al. 2011b). For the aluminum alloy under investigation the damage threshold appearing in the damage criterion (4) is identified to be $\sigma = 300$ MPa.

4 Experiments with Biaxially Loaded Specimens

The main purpose of the experimental program is to develop and to propose a set of new tests revealing the effect of stress state on damage and failure in ductile metals. The experiments are performed using the biaxial test machine (Type LFM-BIAX 20 kN from Walter and Bai, Switzerland) shown in Fig. 2. It is composed of four electro-mechanically, individually driven cylinders with load maxima and minima of ± 20 kN (tension and compression loading is possible). The specimens are fixed in the four heads of the cylinders where clamped or hinged boundary conditions are possible. The geometry of the newly designed flat specimens and the loading conditions are shown in Fig. 3. The geometry is similar to that one of specimens recently

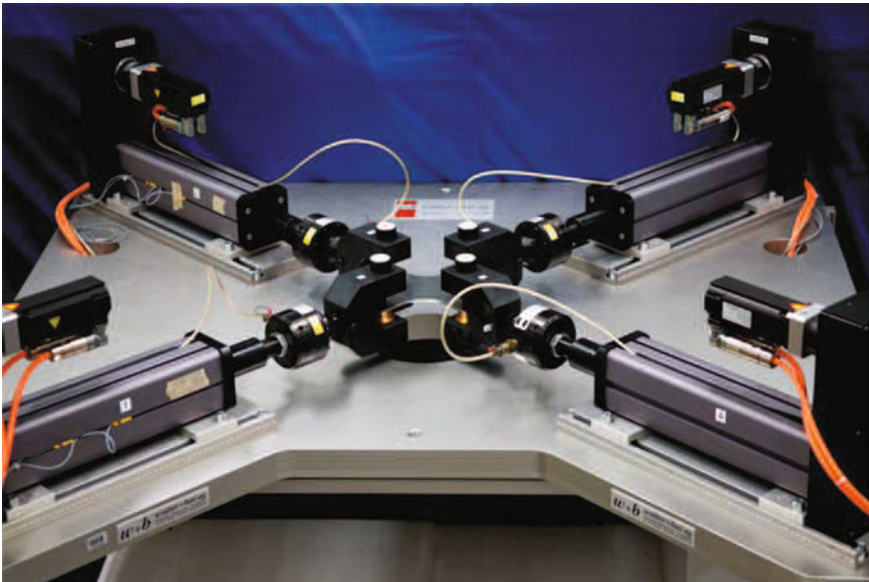
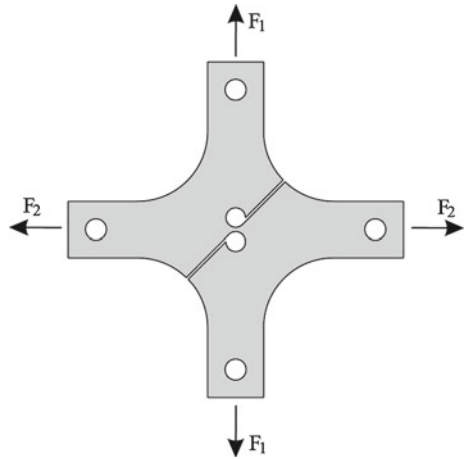


Fig. 2 Biaxial test machine

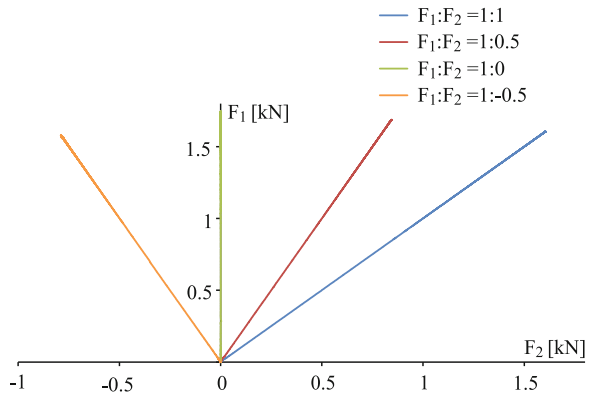
Fig. 3 Specimen and loading conditions



tested firstly in tension and subsequently in shear tests or vice versa (Driemeier et al. 2010), but here the specimens are biaxially strained. The load F_1 will lead to shear mechanisms in the center of the specimen whereas the simultaneous loading with F_2 leads to superimposed tension or compression modes leading to shear-tension or shear-compression deformation and failure modes. Therefore, this extension of experimental work covers the full range of stress states corresponding to the damage and failure mechanisms discussed above with focus on high positive as well as low positive, nearly zero and negative stress triaxialities where the Lode parameter also plays an important role.

In particular, the load ratios $F_1 : F_2$ remain constant during the entire experiments up to final fracture, see Fig. 4. This leads to load-displacement curves shown in Fig. 5 for four different load ratios. Figure 5 clearly shows that the amount of the vertical load F_1 (leading to shear modes) is only marginally affected by the different superimposed horizontal loads F_2 . However, different load ratios $F_1 : F_2$ have

Fig. 4 Vertical load F_1 versus horizontal load F_2



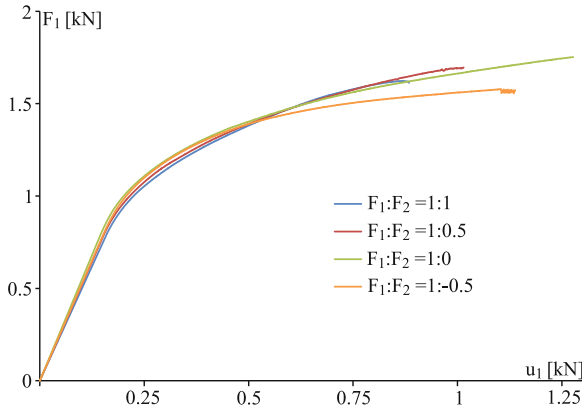


Fig. 5 Load-displacement curves

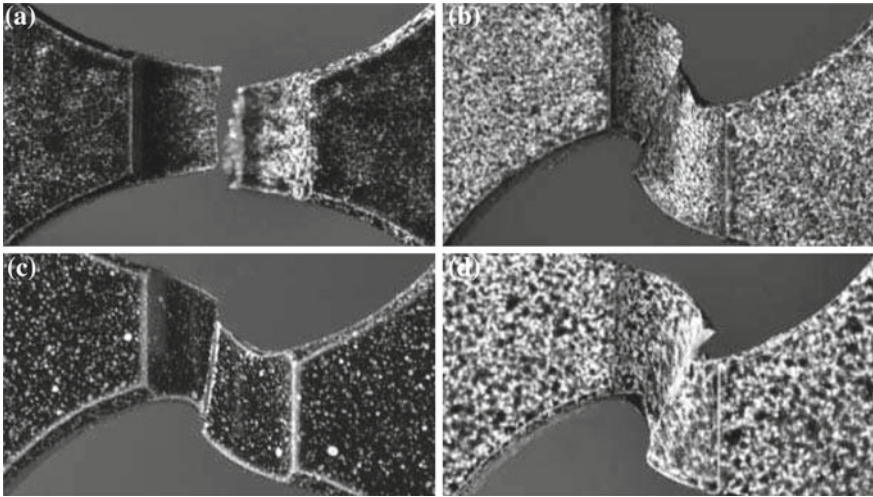


Fig. 6 Fracture modes of differently loaded specimens: **a** $F_1 : F_2 = 0 : 1$, **b** $F_1 : F_2 = 1 : 0$, **c** $F_1 : F_2 = 1 : 0.5$, **d** $F_1 : F_2 = 1 : -0.5$

remarkable influence on the damage and final fracture modes, see Fig. 6. For example, for the tension test without shear loading, $F_1 : F_2 = 0 : 1$, a nearly vertical fracture line is obtained. Under this loading condition, damage is mainly caused by growth and coalescence of voids with small influence of micro-shear-cracks leading to the macroscopic tensile fracture mode with small cup-cone fracture effect (Fig. 6a). On the other hand, for pure shear loading, $F_1 : F_2 = 1 : 0$, shear fracture is observed where the fracture line has an angle of about 25° with respect to the vertical line. Under this loading condition, damage is mainly caused by formation of micro-shear-cracks leading to the macro-shear-crack shown in Fig. 6b. For

shear-tension loading, $F_1 : F_2 = 1 : 0.5$, shear-tension fracture is obtained and the fracture line has an angle of only about 10° with respect to the vertical line. Under this loading condition, damage is caused by the simultaneous growth of voids and formation of micro-shear-cracks leading to the macroscopic fracture mode shown in Fig. 6c which is between tensile fracture (Fig. 6a) and shear fracture (Fig. 6b). And for shear-compression loading, $F_1 : F_2 = 1 : -0.5$, again shear fracture is observed and the fracture line again has an angle of about 25° with respect to the vertical line. Under this loading condition damage seems to be caused only by formation of micro-shear-cracks leading to the macro-shear-crack shown in Fig. 6d. It is worthy to note that the damage and failure mechanisms for $F_1 : F_2 = 1 : 0$ (Fig. 6b) and $F_1 : F_2 = 1 : -0.5$ (Fig. 6d) seem to be very similar and damage modes characteristic for shear loading will not be remarkably affected by superimposed small compression loads.

5 Numerical Simulations of the 2D Experiments

In the experiments with biaxially loaded specimens discussed above the stress and strain fields are not homogeneous and only quantities in an average sense can be evaluated from these tests. Therefore, corresponding numerical simulations have been performed to be able to get detailed information on amounts and distributions of different stress and strain measures as well as further parameters of interest especially in critical regions. The numerical calculations have been carried out using the finite element program ANSYS enhanced by a user-defined material subroutine. This subroutine takes into account numerical integration of the constitutive equations by an extended version of the inelastic predictor–elastic corrector technique and corresponding consistent tangent moduli (Brüning 2003b).

The finite element mesh of the discretized biaxially loaded specimen is shown in Fig. 7. The three-dimensional finite element mesh is based on 42,248 eight-node-elements of the type Solid185. Remarkable refinement of the finite element mesh can be seen in the central part of the specimen where high gradients of the stress and strain related quantities are expected.

Figure 8 shows comparison of experimental and numerically predicted load-displacement curves for the load ratio $F_1 : F_2 = 1 : 1$. The numerical results are based only on an elastic-plastic analysis to be able to identify the onset of damage (Brüning et al. 2011b). In particular, good agreement of experimental and corresponding numerical curve is shown in Fig. 8 for the first part of the biaxial test and only deviation in the last part is observed. This deviation is caused by the occurrence of damage in the experiment which was not taken into account by the elastic-plastic analysis. Thus, this loading stage characterizes onset of damage in the specimen during this test and at this point the stress and strain states in the critical specimen's center will be analyzed in detail. The numerically predicted data for this calculation and also for other loading ratios $F_1 : F_2$ will give information on the effect of stress state on the damage criterion.

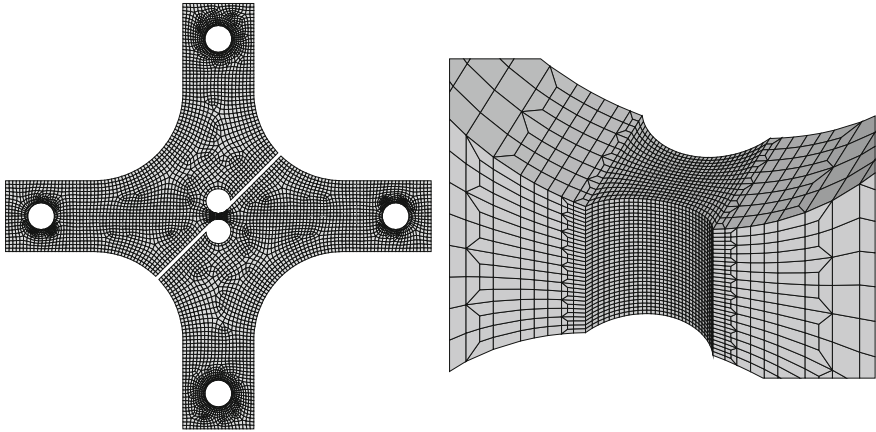


Fig. 7 Finite element mesh of the 2D specimen

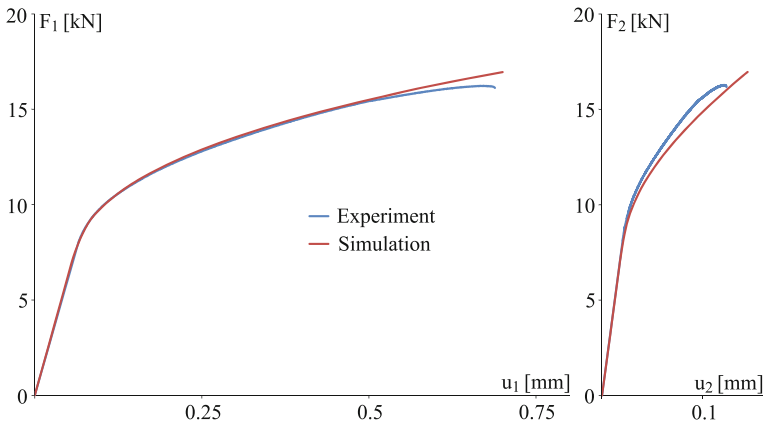


Fig. 8 Load-displacement curves for $F_1 : F_2 = 1 : 1$

For the load ratio $F_1 : F_2 = 1 : 1$, Fig.9 shows the distribution of the first and second deviatoric stress invariants I_1 and $\sqrt{J_2}$ in the center of the biaxially loaded specimen. In particular, maximum of the first stress invariant I_1 is seen on the boundaries of the notched part near the center of the specimen. In this part, also very high values of the second deviatoric stress invariant $\sqrt{J_2}$ are numerically predicted. Thus, damage will start here caused by growth of voids and micro-shear-cracks. Furthermore, maximum of $\sqrt{J_2}$ can be seen in the center of the specimen and in this region the first stress invariant I_1 is moderate. This means that after onset of damage on the boundaries further damage will also occur here mainly caused by the formation of micro-shear-cracks with small effect of isotropic growth of micro-voids.

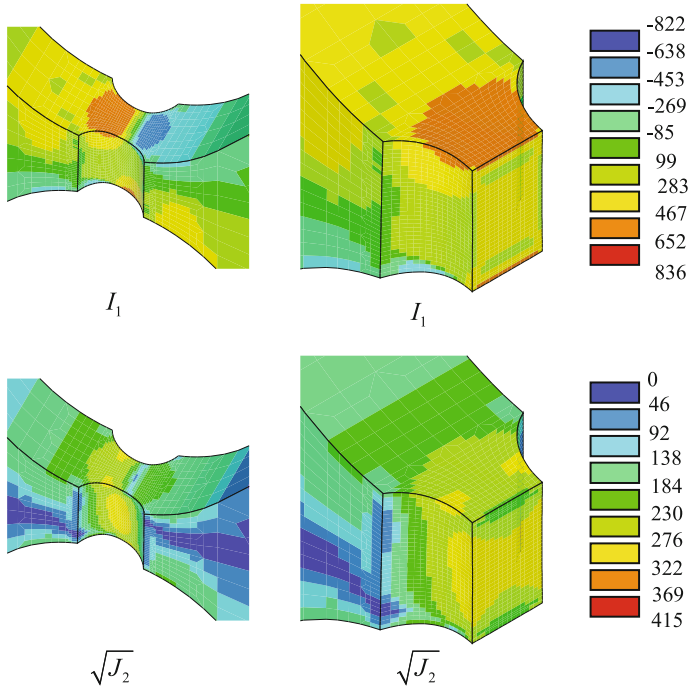


Fig. 9 Distribution of the stress invariants I_1 and $\sqrt{J_2}$ for $F_1 : F_2 = 1 : 1$

The stress state in critical regions of the specimen is remarkably influenced by loading conditions. In this context, numerically predicted distributions of the stress triaxiality η at the onset of damage are shown in Fig. 10 for different load ratios. In particular, for uniaxial tension loading $F_1 : F_2 = 0 : 1$ remarkable high stress triaxialities up to $\eta = 0.84$ are numerically predicted in the center of the specimen. These high values are caused by the notches in horizontal and thickness direction leading to high hydrostatic stress during elongation of the specimen. This will lead to damage and failure mainly due to growth of voids. In addition, when the specimen is only loaded by $F_1 : F_2 = 1 : 0$ (shear loading condition) the stress triaxiality η is numerically predicted to be nearly zero in the whole vertical section shown in Fig. 10. Thus, damage will start in the specimen's center and will be caused by formation and growth of micro-shear-cracks. Furthermore, combined loading in vertical and horizontal direction, F_1 and F_2 , will lead to combination of these basic damage modes. For example, for the load ratio $F_1 : F_2 = 1 : 1$ the stress triaxiality is again nearly constant in the vertical section with $\eta = 0.25$, and very similar distribution is numerically predicted for $F_1 : F_2 = 1 : 0.5$ with $\eta = 0.14$. On the other hand, the load ratio $F_1 : F_2 = 1 : -0.5$ represents combined shear-compression loading with the stress triaxiality $\eta = -0.14$ which is nearly constant in the vertical section shown

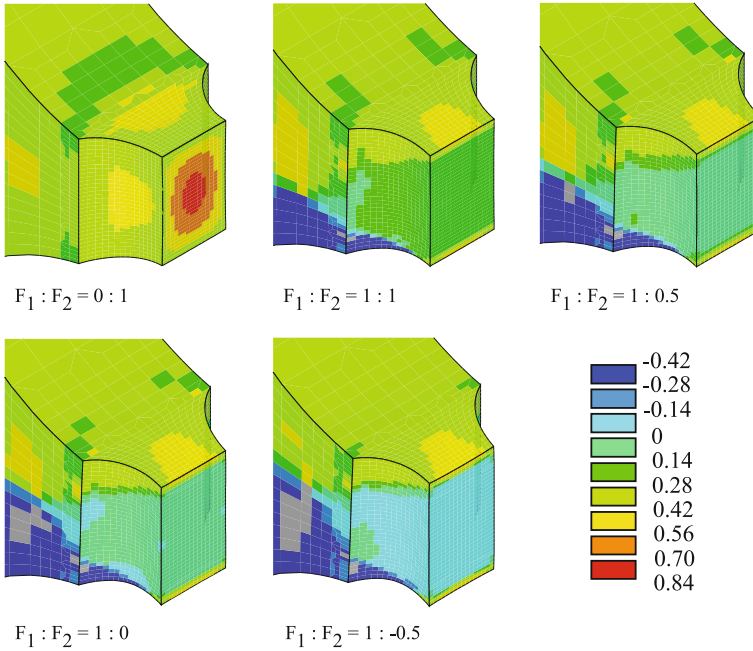


Fig. 10 Distribution of the stress triaxiality η for different load ratios

in Fig. 10. For this negative stress triaxiality damage and failure will be caused by formation and growth of micro-shear-cracks only.

Moreover, the distribution of the Lode parameter ω at onset of damage in the specimen's center depending on loading conditions is shown in Fig. 11. In particular, for tensile loading with $F_1:F_2 = 0:1$ the Lode parameter is nearly constant in the vertical section with $\omega = -1$ which is characteristic for uniaxial tension. In addition, for shear loading with $F_1:F_2 = 1:0$ also nearly constant Lode parameter in the vertical section is numerically predicted with $\omega = 0$ and small zones with negative values can be seen at the boundaries. However, combined shear-tension loading will lead to more inhomogeneous distribution of the Lode parameter in the vertical section of the specimen at the onset of damage. For example, for $F_1:F_2 = 1:1$ different Lode parameters between $\omega = 0.0$ and $\omega = -0.5$ are numerically predicted. The effect of superimposed tension force is much smaller for $F_1:F_2 = 1:0.5$ and the distribution of the Lode parameter at onset of damage becomes again more homogeneous with maximum $\omega = -0.1$ in the specimens center. In addition, also small inhomogeneity in distribution of the Lode parameter is numerically predicted for shear-compression loading ($F_1:F_2 = 1:-0.5$) with maximum $\omega = 0.2$.

The stress triaxialities η covered by experiments with different flat specimens manufactured from thin sheets are shown in Fig. 12. In particular, for unnotched dog-bone-shape specimens (green) nearly homogeneous stress states occur in the small part during uniaxial tension tests with stress triaxiality $\eta = 1/3$. Higher stress

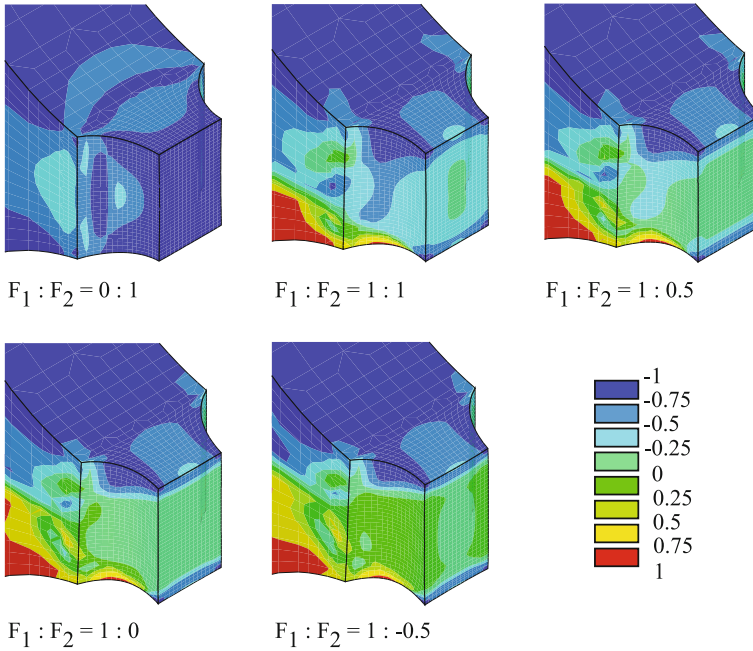
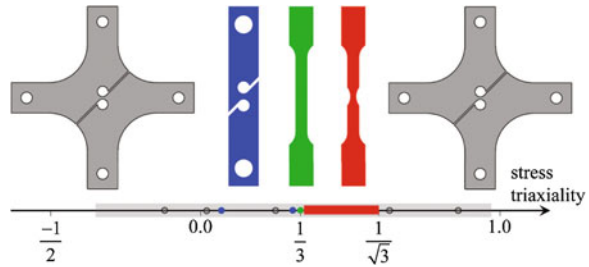


Fig. 11 Distribution of the Lode parameter ω for different load ratios

triaxialities can be obtained in uniaxial tension tests when notches with different radii are added in the middle part of the specimens (red). Decrease in notch radius will lead to an increase in stress triaxiality in the specimen's center up to $\eta = 1/\sqrt{3}$. In addition, shear specimens (blue) elongated in uniaxial tension test will lead to stress triaxialities of about $\eta = 0.1$ when notches in thickness direction are added in the central part (Brünig et al. 2008, 2011b; Driemeier et al. 2010) whereas without additional notch they will also lead to onset of damage at nearly $\eta = 1/3$. However, with these flat specimens taken from thin sheets elongated in uniaxial tension tests only the stress triaxialities shown in Fig. 12 (green, red and blue points) can be taken into account whereas no information is obtained for high positive ($\eta > 1/\sqrt{3}$), low positive (between $0.1 < \eta < 1/3$) or negative stress triaxialities. However, further experiments with new specimens (grey) tested under biaxial loading conditions discussed in the present paper will lead to stress triaxialities in the requested regimes. The grey points shown in Fig. 12 correspond to the loading conditions discussed above but variation of the load ratios $F_1 : F_2$ may lead to stress triaxialities marked by the grey zone shown in Fig. 12. Therefore, biaxial tests with 2D specimens presented in this paper cover a wide range of stress triaxialities and Lode parameters. Comparison of the experimental results and the corresponding numerical data are used to validate the stress-state-dependent damage criterion (4) and the corresponding parameters (11)–(14) for the aluminum alloy under investigation.

Fig. 12 Stress triaxialities covered by different specimens



6 Conclusions

A continuum model taking into account stress-state-dependent damage criteria and damage evolution laws has been discussed. Parameters depending on stress triaxiality and Lode parameter have been proposed based on numerical results from unit-cell calculations on the micro-level. Since the functions are only based on numerical analyses validation of the stress-state-dependent model was required. In this context, a series of new experiments with biaxially loaded specimens has been proposed. Different load ratios led to shear-tension and shear-compression mechanisms with different fracture modes. Corresponding finite element simulations of the experiments revealed a wide range of stress triaxialities and Lode parameters covered by the tests depending on biaxial loading conditions and allowed validation of the proposed stress-state-dependent functions of the continuum model.

References

- Bai Y, Wierzbicki T (2008) A new model of metal plasticity and fracture with pressure and lode dependence. *Int J Plast* 24:1071–1096
- Bao Y, Wierzbicki T (2004) On the fracture locus in the equivalent strain and stress triaxiality space. *Int J Mech Sci* 46:81–98
- Becker R, Needleman A, Richmond O, Tvergaard V (1988) Void growth and failure in notched bars. *J Mech Phys Solids* 36:317–351
- Bonora N, Gentile D, Pirondi A, Newaz G (2005) Ductile damage evolution under triaxial state of stress: theory and experiments. *Int J Plast* 21:981–1007
- Brocks W, Sun DZ, Höing A (1995) Verification of the transferability of micromechanical parameters by cell model calculations with visco-plastic material. *Int J Plast* 11:971–989
- Brünig M (2003a) An anisotropic ductile damage model based on irreversible thermodynamics. *Int J Plast* 19:1679–1713
- Brünig M (2003b) Numerical analysis of anisotropic ductile continuum damage. *Comput Methods Appl Mech Eng* 192:2949–2976
- Brünig M, Chyra O, Albrecht D, Driemeier L, Alves M (2008) A ductile damage criterion at various stress triaxialities. *Int J Plast* 24:1731–1755
- Brünig M, Albrecht D, Gerke S (2011a) Modelling of ductile damage and fracture behavior based on different micro-mechanisms. *Int J Damage Mech* 20:558–577

- Brüning M, Albrecht D, Gerke S (2011b) Numerical analyses of stress-triaxiality-dependent inelastic deformation behavior of aluminium alloys. *Int J Damage Mech* 20:299–317
- Brüning M, Gerke S (2011) Simulation of damage evolution in ductile metals undergoing dynamic loading conditions. *Int J Plast* 27:1617–1998
- Brüning M, Gerke S, Hagenbrock V (2013) Micro-mechanical studies on the effect of the stress triaxiality and the lode parameter on ductile damage. *Int J Plast* 50:49–65
- Brüning M, Gerke S, Hagenbrock V (2014) Stress-state-dependence of damage strain rate tensors caused by growth and coalescence of micro-defects. *Int J Plast* 63:49–63
- Chew H, Guo T, Cheng L (2006) Effects of pressure-sensitivity and plastic dilatancy on void growth and interaction. *Int J Solids Struct* 43:6380–6397
- Drümeier L, Brüning M, Micheli G, Alves M (2010) Experiments on stress-triaxiality dependence of material behavior of aluminum alloys. *Mech Mater* 42:207–217
- Dunand M, Mohr D (2011) On the predictive capabilities of the shear modified Gurson and the modified Mohr-Coulomb fracture models over a wide range of stress triaxialities and lode angles. *J Mech Phys Solids* 59:1374–1394
- Gao X, Zhang G, Roe C (2010) A study on the effect of the stress state on ductile fracture. *Int J Damage Mech* 19:75–94
- Gurson AL (1977) Continuum theory of ductile rupture by void nucleation and growth: part I—yield criteria and flow rules for porous ductile media. *J Eng Mater Technol* 99:2–15
- Kuna M, Sun D (1996) Three-dimensional cell model analyses of void growth in ductile materials. *Int J Fract* 81:235–258
- Lemaitre J (1996) *A course on damage mechanics*. Springer, Berlin
- Mohr D, Henn S (2007) Calibration of stress-triaxiality dependent crack formation criteria: a new hybrid experimental-numerical method. *Exp Mech* 47:805–820
- Needleman A, Kushner A (1990) An analysis of void distribution effects on plastic flow in porous solids. *Eur J Mech A Solids* 9:193–206
- Voyiadjis G, Kattan P (1999) *Advances in damage mechanics: metals and metal matrix composites*. Elsevier, Amsterdam
- Zhang K, Bai J, Francois D (2001) Numerical analysis of the influence of the lode parameter on void growth. *Int J Solids Struct* 38:5847–5856

Constitutive Modeling of Dissipative Phenomena in Austenitic Metastable Steels at Cryogenic Temperatures

Halina Egner, Błażej Skoczeń and Maciej Rys

Abstract In the present paper the constitutive model of dissipative material at cryogenic temperature is presented. Three coupled dissipative phenomena: plastic flow, plastic strain induced phase transformation and evolution of damage are considered using a thermodynamically consistent framework. The theory relies on notion of local state, and involves one state potential for the writing of the state laws, and dissipation potential for the description of the irreversible part of the model. The kinetic laws for state variables are derived from the generalized normality rule applied to the plastic potential, while the consistency multiplier is obtained from the consistency condition applied to the yield function. The model is applied for simulation of two distinct dissipative phenomena taking place in FCC metals and alloys at low temperatures: plastic strain induced transformation from the parent austenitic phase to the secondary martensitic phase, and evolution of micro-damage.

Keywords Constitutive behaviour · Dissipative material · Phase transformation · Damage · Cryogenic temperature

1 Introduction

There is a large variety of materials suitable for applications at extremely low temperatures. The choice of the material for a given application depends on a number of required features and parameters, like yield and ultimate strength, moduli of

H. Egner (✉) · B. Skoczeń · M. Rys
Department of Mechanical Engineering, Institute of Applied Mechanics,
Cracow University of Technology, Cracow, Poland
e-mail: halina.egner@pk.edu.pl

B. Skoczeń
e-mail: blazej.skoczen@pk.edu.pl

M. Rys
e-mail: Maciej_Rys@o2.pl

elasticity at room and low temperatures, thermal properties like conductivity and surface emissivity, physical properties like magnetic permeability, etc.

Among metallic materials we can often find austenitic stainless steels, since they preserve ductility practically down to 0 K. They are applied for components of superconducting magnets and cryogenic transfer lines, tubes, cylinders, braiding wires, thin walled shells (like bellows expansion joints) or massive parts like vacuum barriers.

The constitutive description presented here addresses the main phenomena driven by plastic strains at low temperatures: strain induced $\gamma \rightarrow \alpha'$ phase transformation, and evolution of micro-damage. Both $\gamma \rightarrow \alpha'$ phase transformation and damage are of dissipative nature and lead to irreversible rearrangements in the material lattice. Although the metastable stainless steels have been chosen in the present paper as a field of application of the constitutive description, the model presented in the course of the paper can easily be adopted to describe other materials used at cryogenic temperatures.

The $\gamma \rightarrow \alpha'$ phase transformation yields the initially homogeneous material strongly heterogeneous, as a result of the presence of α' -martensite platelets embedded in the γ -austenite matrix. Since the α' -martensite behaves in the flow range of austenite-martensite composite mostly in elastic way (yield point of α' -martensite is much higher than the yield point of γ -austenite (Sun et al. 2009)) its presence in the lattice affects the plastic flow and the process of hardening. The evolution of micro-damage at cryogenic temperatures represents a dissipative and irreversible process that leads to creation of micro-cracks and micro-voids (micro-damage fields) and results in material softening (decrease of effective elasticity modulus).

The evolution of damage fields has been postulated both in the matrix and in the inclusions (Stolarz et al. 2001), and separate variables representing the state of damage were introduced. Moreover, as the austenite behaves in a ductile way practically over the whole range of cryogenic temperatures, whereas the martensite shows—for the same range of stress—brittle behavior, the kinetics of micro-damage evolution is different in each case. This assumption makes the model more general.

2 Constitutive Description of Elastic-Plastic-Damage-Two Phase Material

2.1 Basic Assumptions

We consider a material that is susceptible to several coupled dissipative phenomena: plasticity, damage, and phase transformation, that are formalized on the macroscopic level by the use of a proper set of state variables. The motions within the considered thermodynamic system obey the fundamental laws of continuum mechanics (conservation of mass, conservation of linear momentum, conservation of angular momentum) and two laws of thermodynamics written here in the local form:

1. Conservation of energy

$$\rho \dot{u} - \varepsilon_{ij} \sigma_{ij} - r + q_{i,i} = 0 \quad (1)$$

2. Clausius-Duhem inequality

$$\pi = -\rho(\dot{\psi} + s\dot{\theta}) + \varepsilon_{ij} \sigma_{ij} - q_i \frac{\theta_{,i}}{\theta} \geq 0 \quad (2)$$

where π denotes the rate of dissipation per unit volume, ρ is the mass density per unit volume; σ_{ij} are the components of the stress tensor; u stands for the internal energy per unit mass; ε_{ij} denote the components of the total strain tensor; r is the distributed heat source per unit volume; q_i is the outward heat flux; s denotes the internal entropy production per unit mass, ψ stands for Helmholtz' free energy and θ is the absolute temperature.

Classical dissipation inequality (2) is replaced here with stronger condition, requiring that both mechanical and thermal dissipations, π^{mech} and π^θ , are non-negative (Clausius-Planck inequality and heat conduction inequality, respectively):

$$\pi^{\text{mech}} = -\rho(\dot{\psi} + s\dot{\theta}) + \sigma_{ij} \dot{\varepsilon}_{ij} \geq 0, \pi^\theta = -q_i \frac{\theta_{,i}}{\theta} \geq 0 \Leftrightarrow -q_i \theta_{,i} \geq 0; \quad \theta > 0 \quad (3)$$

The constitutive model presented here is based on the methods of continuum mechanics: instead of a real, discontinuous and heterogeneous material a concept of the effective quasi-continuum is applied by the use of the concept of representative volume element. We consider here a two-phase material, composed of austenitic matrix and martensitic platelets, randomly distributed and randomly oriented in the matrix (see Fig. 1). The current state of phase transformation will be therefore described by the scalar variable ξ , being the volume fraction of martensite dV_ξ in the representative volume dV :

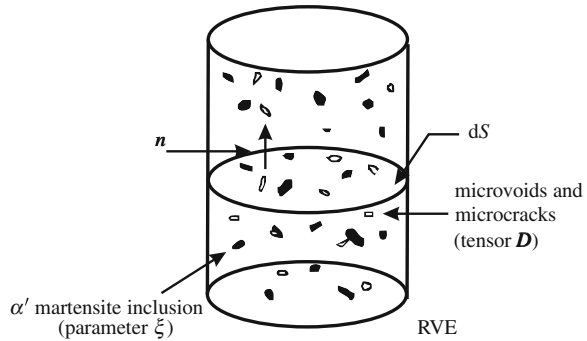
$$\xi = \frac{dV_\xi}{dV} \quad (4)$$

The austenitic matrix is subjected to plastic deformation and ductile damage development, whereas the martensitic inclusions show purely brittle response. For the description of the current state of damage we therefore introduce two second order damage tensors: for ductile damage in austenitic phase, D_{ij}^γ , and for brittle damage in martensitic inclusions, $D_{ij}^{\alpha'}$:

$$\mathbf{D}^\gamma = \sum_{i=1}^3 D_i^\gamma \mathbf{n}_i^\gamma \otimes \mathbf{n}_i^\gamma, \quad \mathbf{D}^{\alpha'} = \sum_{i=1}^3 D_i^{\alpha'} \mathbf{n}_i^{\alpha'} \otimes \mathbf{n}_i^{\alpha'} \quad (5)$$

The total material degradation in the RVE is described by the damage tensor \mathbf{D}^{avg} , being a superposition of the ductile and brittle part. For this reason one can introduce

Fig. 1 RVE with α' -martensite inclusions and micro-damage fields, after Egner and Skoczeń (2010)



a scalar function m of the argument ξ to define the general mixture rule:

$$D_{ij}^{\text{avg}} = [1 - m(\xi)]D_{ij}^{\gamma} + m(\xi)D_{ij}^{\alpha'} \quad (6)$$

The composition factor m has to fulfill two constraints: $m(0) = 0$ and $m(1) = 1$. The simplest, linear rule of mixture involves $m(\xi) = \xi$.

The current state of the material in isothermal conditions is described by the set of state variables, which contains: the total strain tensor ε_{ij} as the observable variable, the second order tensors D_{ij}^{γ} and $D_{ij}^{\alpha'}$ describing the current state of ductile damage in austenitic matrix and brittle damage in martensitic inclusions, respectively, scalar variable ξ reflecting the current state of phase transformation, and plastic hardening internal variables α_{ij}^p and r^p .

In the case of infinitesimal deformation the total strain ε_{ij} can be expressed as a sum of the elastic (reversible) strain ε_{ij}^E , inelastic (irreversible) strain ε_{ij}^I and thermal strain $\varepsilon_{ij}^{\theta}$:

$$\varepsilon_{ij} = \varepsilon_{ij}^E + \varepsilon_{ij}^I + \varepsilon_{ij}^{\theta} \quad (7)$$

Other assumptions are as follows:

1. rate independent plasticity is applied: it is assumed that the influence of the strain rate $\dot{\varepsilon}_{ij}^p$ is small for the considered range of temperatures (2–77 K),
2. we confine our modeling to isothermal conditions,
3. mixed isotropic/kinematic plastic hardening affected by the presence of martensite fraction is included,
4. the two-phase material obeys the associated flow rule (volume fraction of new phase not exceeding 0.5).

2.2 Coupled Damage/Plasticity/Phase Transformation Thermodynamic Formulation

2.2.1 State Potential and State Equations

In generalised thermodynamics one of the main hypotheses is that the constitutive behaviour is entirely defined by the specification of two potentials: an energy potential, and a dissipation potential. In our modeling we adopt Helmholtz free energy as a state potential. By the use of state variables the Helmholtz free energy of the material can be written as a sum of elastic, inelastic and chemical terms:

$$\begin{aligned} \rho\psi = & \frac{1}{2}\varepsilon_{ij}^E E_{ijkl}\varepsilon_{kl}^E + \frac{1}{3}C^P\alpha_{ij}^P\alpha_{ij}^P + R_\infty^P \left[r^P + \frac{1}{b^P} \exp(-b^P r^P) \right] \\ & + (1-n)\rho\psi_\gamma^{\text{CH}} + n\rho\psi_{\alpha'}^{\text{CH}} \end{aligned} \quad (8)$$

The terms $\rho\psi_\gamma^{\text{CH}}$ and $\rho\psi_{\alpha'}^{\text{CH}}$ are the chemical energies of the respective phases (Hallberg et al. 2010; Mahnken and Schneidt 2010; Fischer and Reisner 1998). This internally stored energy is different for the two phases and it will affect the generation of heat during phase transformation, as well as the transformation itself. Symbol n denotes a function of argument ξ , similar to $m(\xi)$ in expression (6).

Since the $\gamma \rightarrow \alpha'$ phase transformation does not affect the elastic properties of the material, in the Eq. (8) $E_{ijkl}(D_{pq}^{\text{avg}})$ stands for the current elastic stiffness tensor affected only by damage.

On the other hand, it is assumed here that damage does not affect plastic hardening properties, therefore, in the expression (8) the material parameters: $R_\infty^P(\xi)$, $C^P(\xi)$, and $b^P(\xi)$ depend on the current state of phase transformation only.

By eliminating all the reversible processes from the Clausius-Duhem inequality (2), the state equation which expresses the thermodynamic force conjugated to the observable state variable is obtained (see Table 1):

$$\sigma_{ij} = \frac{\partial(\rho\psi)}{\partial\varepsilon_{ij}^E} = E_{ijkl} \left(\varepsilon_{kl} - \varepsilon_{kl}^P - \xi\varepsilon_{kl}^{\text{bs}} \right) \quad (9)$$

where ε_{ij}^P is the plastic strain tensor, and $\varepsilon_{ij}^{\text{bs}} = \frac{1}{3}\Delta v\delta_{ij}$ denotes the free deformation called Bain strain, expressed in terms of the relative volume change Δv . In addition, the forces conjugated to other state variables are postulated in a similar form to (9), see Table 1 (Chaboche 1988; Saanouni 2012). The simplest, linear functions of ξ were assumed here for material hardening parameters $C(\xi)$, $R_\infty^P(\xi)$ and $b^P(\xi)$:

$$C(\xi) = C_0(1 + h_C\xi), \quad R_\infty^P(\xi) = R_{\infty,0}^P(1 + h_R\xi), \quad b^P(\xi) = b_0^P(1 + h_b\xi) \quad (10)$$

Table 1 State variables and corresponding thermodynamic forces

Phenomenon	Pairs of variables and forces	State equation
Mechanical variables: total strain, Cauchy stress	<i>Observable variables</i> $\varepsilon_{ij}, \sigma_{ij}$	$\sigma_{ij} = E_{ijkl}(\varepsilon_{kl} - \varepsilon_{kl}^1)$
	<i>Internal variables:</i>	
Kinematic plastic hardening	α_{ij}^p, X_{ij}^p	$X_{ij}^p = \frac{2}{3} C(\xi) \alpha_{ij}^p$
Isotropic plastic hardening	r^p, R^p	$R^p = R_\infty^p(\xi) \{1 - \exp[-b^p(\xi)r^p]\}$
Phase transformation	ξ, Z	$Z = \frac{\partial(\rho\psi^I)}{\partial\xi} + \frac{dn}{d\xi} (\rho\psi_{\alpha'}^{CH} - \rho\psi_\gamma^{CH})$
Ductile damage (austenite)	$D_{ij}^\gamma, -Y_{ij}^\gamma$	$-Y_{ij}^\gamma = \frac{\partial(\rho\psi)}{\partial D_{ij}^\gamma} = -(1-m)Y_{ij}^{\text{avg}}$
Brittle damage (martensite)	$D_{ij}^{\alpha'}, -Y_{ij}^{\alpha'}$	$-Y_{ij}^{\alpha'} = \frac{\partial(\rho\psi)}{\partial D_{ij}^{\alpha'}} = -m(\xi)Y_{ij}^{\text{avg}}$

The Clausius-Planck inequality (3) takes therefore the following form:

$$\begin{aligned} \pi^{\text{mech}} &= \sigma_{ij} \left(\dot{\varepsilon}_{ij}^p + \dot{\varepsilon}_{ij}^{id} + \dot{\xi} \varepsilon_{ij}^{bs} \right) + Y_{ij}^\gamma \dot{D}_{ij}^\gamma + Y_{ij}^{\alpha'} \dot{D}_{ij}^{\alpha'} - Z \dot{\xi} - X_{ij}^p \dot{\alpha}_{ij}^p - R^p \dot{r}^p \\ &= \underbrace{\sigma_{ij} \dot{\varepsilon}_{ij}^p - X_{ij}^p \dot{\alpha}_{ij}^p - R^p \dot{r}^p}_{\pi^p} + \underbrace{\left(\sigma_{ij} \varepsilon_{ij}^{bs} - Z \right) \dot{\xi}}_{\pi^{\text{tr}}} + \underbrace{Y_{ij}^\gamma \dot{D}_{ij}^\gamma + Y_{ij}^{\alpha'} \dot{D}_{ij}^{\alpha'}}_{\pi^d} \geq 0 \quad (11) \end{aligned}$$

It can be seen from (11) that the mechanical dissipation π^{mech} can be subdivided into plastic π^p , transformational π^{tr} , and damage π^d parts. The quantity $Q = \sigma_{ij} \varepsilon_{ij}^{bs} - Z$ is conjugated to the transformation rate $\dot{\xi}$ and can be treated as a thermodynamic force that drives the phase front through the material, cf. Hallberg et al. (2007, 2010); Fischer and Reisner (1998); Levitas (1997a, b).

3 Evolution of State Variables: Mechanisms Governed by Plasticity

It is assumed here that ductile damage and phase transformation mechanisms are governed by plasticity with a single dissipation potential F :

$$F = F^p \left(\sigma_{ij}, X_{ij}^p, R^p, D_{ij}^{\text{avg}}, \xi \right) + F^{\text{d}\gamma} \left(Y_{ij}^\gamma, D_{ij}^\gamma \right) + F^{\text{tr}} \left(Q, \xi, D_{ij}^\gamma \right) \quad (12)$$

and normality rule involving only one plastic multiplier, determined by the consistency condition. In such approach the ductile damage and the phase transformation progress only when there is plastic flow. Similarly, beyond damage threshold there is no plasticity without a corresponding increase in damage, and beyond phase transformation threshold there is no plasticity without a corresponding increase in martensite content.

Plastic potential F^P is here equal to von Mises type yield surface:

$$F^P = f^P = J_2 \left(\tilde{\sigma}_{ij} - \tilde{X}_{ij}^P \right) - \sigma_y - \tilde{R}^P = 0 \quad (13)$$

where

$$\begin{aligned} \tilde{\sigma}_{ij} &= M_{ikjl}^{\text{avg}} \sigma_{kl}, \quad \tilde{X}_{ij}^P = M_{ikjl}^{\text{avg}} X_{kl}^P, \quad \tilde{R}^P = R^P / \left(1 - D_{\text{eq}}^{\text{avg}} \right), \\ D_{\text{eq}}^{\text{avg}} &= \sqrt{D_{ij}^{\text{avg}} D_{ij}^{\text{avg}}}, \quad J_2 \left(\tilde{\sigma}_{ij} - \tilde{X}_{ij}^P \right) = \sqrt{\frac{3}{2} \left(\tilde{\sigma}_{ij} - \tilde{X}_{ij}^P \right) \left(\tilde{\sigma}_{ij} - \tilde{X}_{ij}^P \right)} \end{aligned} \quad (14)$$

In the above equations M_{ijkl}^{avg} denotes the fourth-order damage effect tensor expressed in terms of damage tensor D_{ij}^{avg} . The relevant potential of damage dissipation reads (Garion and Skoczen 2003):

$$F^{\text{d}\gamma} = \frac{1}{2} C_{ik} Y_{kl}^{\gamma} C_{lj} Y_{ij}^{\gamma} \sqrt{\frac{\left(\tilde{s}_{mn} - \tilde{X}_{mn}^P \right) L_{mnpq}^{\text{avg}} \left(\tilde{s}_{pq} - \tilde{X}_{pq}^P \right)}{\left(\tilde{s}_{rs} - \tilde{X}_{rs}^P \right) \left(\tilde{s}_{rs} - \tilde{X}_{rs}^P \right)}} - B^{\text{d}\gamma} = 0, \quad (15)$$

where

$$L_{ijkl}^{\text{avg}} = M_{imjn}^{\text{avg}} M_{mknl}^{\text{avg}} \quad (16)$$

C_{ij} is a tensor that defines the material properties related to texture, and $B^{\text{d}\gamma}$ denotes the barrier force for damage. Symbols \tilde{s}_{ij} and \tilde{X}_{ij}^P stand for effective stress and effective back stress deviators, respectively.

The phase transformation dissipation potential is assumed here in a simple form:

$$F^{\text{tr}} = A Q \sqrt{\frac{\left(\tilde{s}_{mn} - \tilde{X}_{mn}^P \right) L_{mnpq}^{\text{avg}} \left(\tilde{s}_{pq} - \tilde{X}_{pq}^P \right)}{\left(\tilde{s}_{rs} - \tilde{X}_{rs}^P \right) \left(\tilde{s}_{rs} - \tilde{X}_{rs}^P \right)}} - B^{\text{tr}} = 0 \quad (17)$$

where $A(\theta, \sigma_{ij}, \dot{\varepsilon}_{ij}^P)$, in general, is a function of temperature, stress state and strain rate, and B^{tr} is the barrier force for phase transformation (Mahnken and Schneidt 2010; Fischer et al. 2000). For rate independent plasticity, isothermal process and small stress variations function A may be treated as a constant value.

On the basis of normality rule applied to plastic dissipation potential (13), the following plastic flow rule is obtained:

$$\dot{\varepsilon}_{ij}^p = \dot{\lambda}^p \frac{\partial f^p(\tilde{\sigma}_{pq}, \tilde{X}_{pq}^p, \tilde{R})}{\partial \tilde{\sigma}_{kl}} \frac{\partial \tilde{\sigma}_{kl}}{\partial \sigma_{ij}} \quad (18)$$

Plastic hardening variables evolve according to the following expressions:

$$\dot{\alpha}_{ij}^p = \dot{\varepsilon}_{ij}^p, \quad \dot{r}^p = \frac{\dot{\lambda}^p}{1 - D_{\text{eq}}^{\text{avg}}} \quad (19)$$

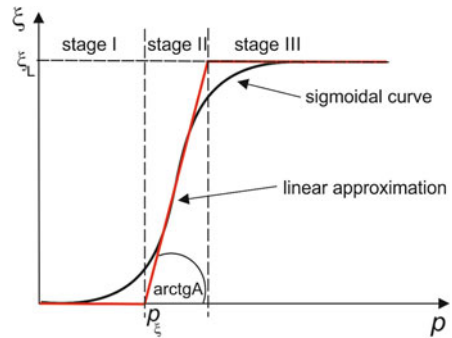
Kinetics of phase transformation, developed by Olson and Cohen (1975), is reflected by a typical sigmoidal curve defining the evolution of the martensite content as a function of plastic strain (see Fig. 2). At very low temperatures the phase transformation process can be subdivided into three stages: low rate transformation below the threshold p_ξ (stage I), fast transformation with a high and nearly constant transformation rate (stage II) and asymptotically vanishing transformation with the rate decreasing to 0 and the volume fraction of martensite reaching a maximum ξ_L (stage III). If the plastic strain induced phase transformation occurs at very low temperatures (typically liquid helium 4.2 K or liquid nitrogen 77 K) then the steep part of the transformation curve is close to linear (stage II) and remains in the domain of relatively small strains. By taking into account the normality rule and (17) the evolution of phase transformation variable takes a simple linear form:

$$\dot{\xi} = A \dot{p} H[(p - p_\xi)(\xi_L - \xi)] \quad (20)$$

Symbol H denotes the Heaviside step function. Relation (20) introduces a simplified evolution law for the martensite content, with respect to the linear part (region II) of the sigmoidal curve, Fig. 2 (Garion and Skoczen 2003).

The evolution of damage versus plastic strain can be experimentally obtained from the measured unloading modules. Therefore uniaxial tension tests with frequent

Fig. 2 Volume fraction of α' -martensite versus accumulated plastic strain p



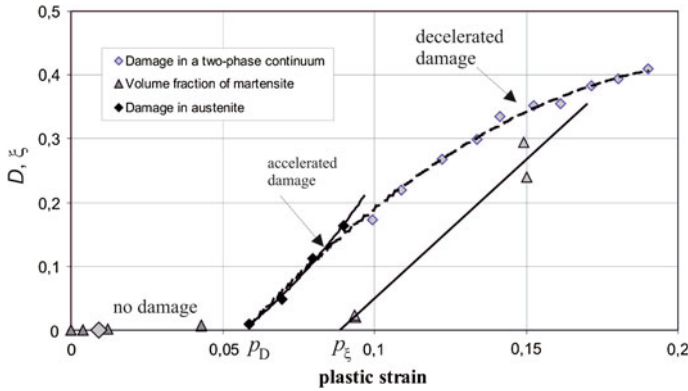


Fig. 3 Evolution of damage and martensite content versus plastic strains for 316L stainless steel subjected to uniaxial tension at 4.2 K, after Egner and Skoczefi (2010)

unloading were performed, and changes of unloading modulus were transformed into the changes of damage state. Three stages of damage development can be detected: no damage until a threshold value p_D is reached, then accelerated damage until p_ξ , and above that damage hardening is observed. It seems justified to correlate the hardening effect with the phase transformation, that starts from the equivalent plastic strain close to p_ξ (see Fig. 3).

It is therefore assumed here that as soon as the ductile damage threshold p_D is reached, damage starts developing, driven by the increase in the accumulated plastic strain p :

$$\dot{p} = \sqrt{\frac{2}{3} \dot{\varepsilon}_{ij}^p \dot{\varepsilon}_{ij}^p} = \dot{\lambda}^p \sqrt{\frac{(\tilde{s}_{mn} - \tilde{X}_{mn}^p) L_{mnpq}^{\text{avg}} (\tilde{s}_{pq} - \tilde{X}_{pq}^p)}{(\tilde{s}_{rs} - \tilde{X}_{rs}^p) (\tilde{s}_{rs} - \tilde{X}_{rs}^p)}}} \quad (21)$$

However, damage evolution is different along the principal directions. Ductile damage rate is governed by the relation resulting from normality rule applied to potential function (15):

$$\dot{D}_{ij}^p = C_{ik} Y_{kl}^p C_{lj} \dot{p} H(p - p_D) \quad (22)$$

The consistency multiplier $\dot{\lambda}^p$ is obtained from the consistency condition:

$$\dot{f}^p = \frac{\partial f^p}{\partial \sigma_{ij}} (\dot{\sigma}_{ij} - \dot{X}_{ij}^p) + \frac{\partial f^p}{\partial R^p} \dot{R}^p + \frac{\partial f^p}{\partial D_{ij}^{\text{avg}}} \dot{D}_{ij}^{\text{avg}} + \frac{\partial f^p}{\partial \xi} \dot{\xi} = 0 \quad (23)$$

4 Brittle Damage in Martensitic Inclusions

Martensite inclusions are subjected to brittle damage described by the second order damage tensor $D_{ij}^{\alpha'}$. According to Litewka and Debinski (2003) the deterioration of brittle material structure due to applied load can be described by damage evolution equation expressed in the form of tensorial function:

$$\begin{aligned} D_{ij}^{\alpha'} &= B_1 s_{kl} s_{kl} (1 + P \det \sigma_{ij})^F \delta_{ij} + B_2 \sqrt{\sigma_{kl} \sigma_{kl}} (1 + P \det \sigma_{ij})^F \sigma_{ij} \\ &= f_1 \delta_{ij} + f_2 \sigma_{ij} \end{aligned} \quad (24)$$

The first term of Eq. (24) represents the isotropic damage, while the second one accounts for the oriented damage due to different effects of the stress tensor. Symbol s_{kl} is the stress deviator and B_1 , B_2 , P and F are unknown material parameters to be determined experimentally.

It should be pointed out here, that the fact that brittle damage tensor depends directly on the stresses applied is very convenient in the cases where the composition factor $m(\xi)$ between ductile and brittle component of total damage (6) is not constant but subjected to evolution. More advanced models of damage in rock-like materials, where damage rate is derived from the generalized normality rule applied to the damage potential were derived for example by Cicekli et al. (2007); Voyiadjis et al. (2008); Kintzel et al. (2010); Murakami (2012); Skrzypek and Kuna-Ciskal (2003).

5 Numerical Implementation

In the present work the Newton-Raphson scheme is adopted to solve all nonlinear equations and the fully implicit (backward Euler) scheme is applied. The residual vector can be defined as: $R = [R_{(\sigma)ij}, R_{(X)ij}, R_R, R_f, R_\xi, R_{(D^{avg})ij}]^T$ and the vector of unknowns is $U = [\sigma_{ij}, X_{ij}^p, R^p, \Delta\lambda^p, \xi, D_{ij}^{avg}]^T$. The numerical algorithm is shown in Fig. 4. The uniaxial tension test for 316L stainless steel at temperature 4.2 K was used to determine all the unknown parameters of the model (see Table 2).

Accounting for three dissipative phenomena: plasticity, damage and phase transformation in the present constitutive model allows to obtain a satisfactory reproduction of the experimental stress-strain curve for 316L stainless steel subjected to uniaxial tension at cryogenic temperatures (see Fig. 5). Hardening effect due to phase transformation combined with softening effect due to damage evolution enables to model the initially linear plastic hardening, followed by plastic plateau and nonlinear hardening in the final stage of plastic flow.

The proposed model was also applied to numerical simulations of cyclic loading. The results are shown in Figs. 6 and 7, and they are consistent with the results of monotonic loading simulations.

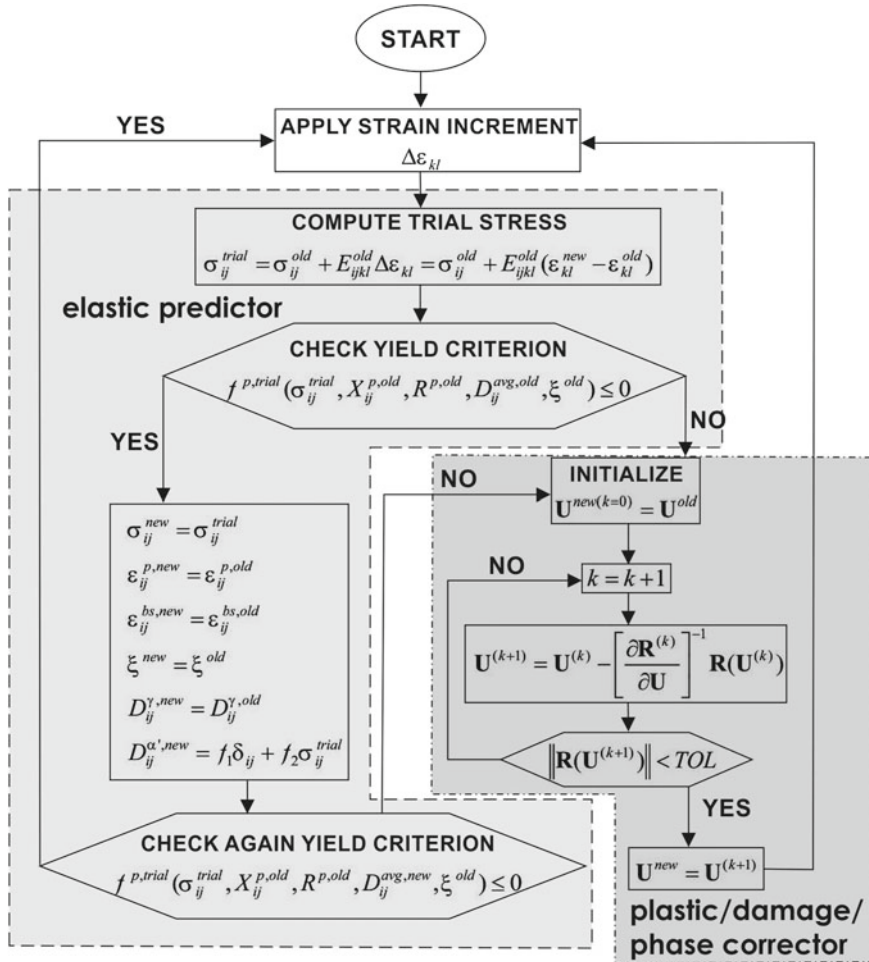


Fig. 4 Numerical algorithm

Table 2 Material data for 316L stainless steel at the temperature of 4.2 K

E (MPa)	176818	C_0 (MPa)	950
σ_y (MPa)	470	h_C	0.5
A	4.37	$R_{\infty,0}^p$ (MPa)	440
C_{11} (MPa $^{-1/2}$)	1.2	h_R	2.2
b_0^p	129	h_b	0.7
p_D	0.05	p_ξ	0.0886
ξ_L	0.9	$\Delta\nu$	0.05

Fig. 5 Numerical simulations of uniaxial tension

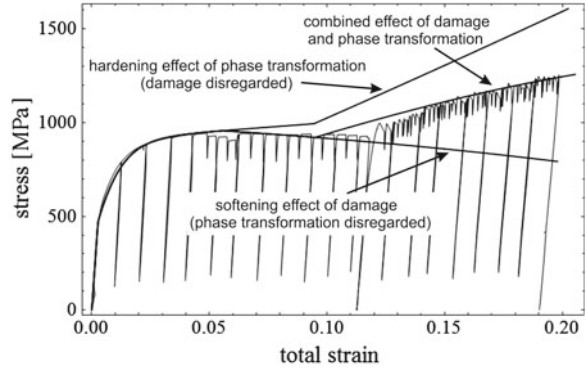


Fig. 6 Numerical simulations of cyclic loading

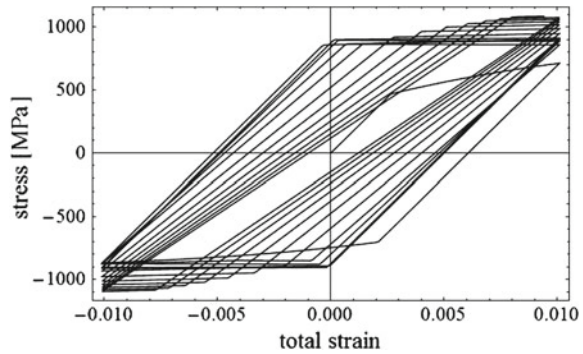
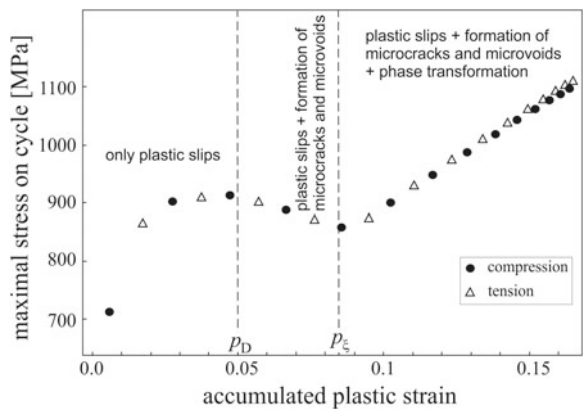


Fig. 7 Maximal stress on cycle versus accumulated plastic strain



6 Conclusions

The constitutive model presented in the paper results from identification of fundamental dissipative phenomena that occur at cryogenic temperatures in the materials characterized by low stacking fault energy:

1. Plastic strain induced transformation from the parent phase (γ) to the secondary phase (α'), characteristic of meta-stable materials.
2. Evolution of micro-damage (micro-voids and micro-cracks) reflected by decreasing unloading modulus in the course of deformation.

A consistent thermodynamic framework has been built in order to describe all dissipative phenomena (plasticity, phase transformation and damage) as well as coupling between them in a unified way.

The total material degradation was assumed to be a superposition of the ductile and the brittle parts, with the use of phase transformation variable as a composition factor (weight function). In the Clausius-Planck inequality, the mechanical dissipation has been decomposed into the plastic, the transformational and the damage components. In the same way the dissipation potential has been built. The kinetics of evolution of: plastic strain fields, volume fraction of secondary phase and micro-damage has been defined by means of the relevant dissipation potentials. In the coupled formulation, presented in the paper, both monotonic and cyclic loads are included. The results were discussed in such a way, so as to decouple and illustrate the effect of strain hardening and the effect of softening due to damage evolution. The combined result fits well to the available experimental data.

Acknowledgments This work has been supported by the National Science Centre through the Grant No. 2284/B/T02/2011/40.

References

- Chaboche JL (1988) Continuum damage mechanics: part I—general concepts. *ASME J Appl Mech* 55(1):59–64
- Cicekli U, Voyiadjis GZ, Al-Rub RKA (2007) A plasticity and anisotropic damage model for plain concrete. *Int J Plast* 23(10–11):1874–1900 (in Honor of Professor Dusan Krajcinovic)
- Egner H, Skoczni B (2010) Ductile damage development in two-phase metallic materials applied at cryogenic temperatures. *Int J Plast* 26(4):488–506
- Fischer FD, Reisner G (1998) A criterion for the martensitic transformation of a microregion in an elastic–plastic material. *Acta Materialia* 46(6):2095–2102
- Fischer FD, Reisner G, Werner E, Tanaka K, Cailletaud G, Antretter T (2000) A new view on transformation induced plasticity (TRIP). *Int J Plast* 16(7–8):723–748
- Garion C, Skoczni B (2003) Combined model of strain induced phase transformation and orthotropic damage in ductile materials at cryogenic temperatures. *Int J Damage Mech* 12(4):331–356
- Hallberg H, Hakansson P, Ristinmaa M (2007) A constitutive model for the formation of martensite in austenitic steels under large strain plasticity. *Int J Plast* 23(7):1213–1239
- Hallberg H, Hakansson P, Ristinmaa M (2010) Thermo-mechanically coupled model of diffusionless phase transformation in austenitic steel. *Int J Solids Struct* 47(11–12):1580–1591
- Kintzel O, Khan S, Mosler J (2010) A novel isotropic quasi-brittle damage model applied to LCF analyses of Al2024. *Int J Fatigue* 32(12):1948–1959
- Levitas VI (1997a) Phase transitions in elastoplastic materials: continuum thermomechanical theory and examples of control—part I. *J Mech Phys Solids* 45(6):923–947

- Levitas VI (1997b) Phase transitions in elastoplastic materials: continuum thermomechanical theory and examples of control—part II. *J Mech Phys Solids* 45(7):1203–1222
- Litewka A, Debinski J (2003) Load-induced oriented damage and anisotropy of rock-like materials. *Int J Plast* 19(12):2171–2191 (Special Issue in Honour of Professor Zenon Mroz)
- Mahnken R, Schneidt A (2010) A thermodynamics framework and numerical aspects for transformation-induced plasticity at large strains. *Arch Appl Mech* 80(3):229–253
- Murakami S (2012) *Continuum damage mechanics: a continuum mechanics approach to the analysis of damage and fracture*. Springer, Berlin
- Olson GB, Cohen M (1975) Kinetics of strain-induced martensitic nucleation. *Arch Appl Mech* 80(3):791–795
- Saanouni K (2012) *Damage mechanics in metal forming: advanced modeling and numerical simulation*. ISTE/Wiley, London
- Skrzypek JJ, Kuna-Ciskal H (2003) Anisotropic elastic-brittle-damage and fracture models based on irreversible thermodynamics. In: Skrzypek JJ, Ganczarski AW (eds) *Anisotropic behaviour of damaged materials. Lecture Notes in Applied and Computational Mechanics*, vol 9. Springer, Berlin, Heidelberg, pp 143–184
- Stolarz J, Baffie N, Magnin T (2001) Fatigue short crack behaviour in metastable austenitic stainless steels with different grain sizes. *Mater Sci Eng A* 319–321:521–526
- Sun X, Choi KS, Liu WN, Khaleel MA (2009) Predicting failure modes and ductility of dual phase steels using plastic strain localization. *Int J Plast* 25(10):1888–1909
- Voyiadjis GZ, Taqieddin ZN, Kattan PI (2008) Anisotropic damage-plasticity model for concrete. *Int J Plast* 24:1946–1965

Modeling of Continuous Damage Deactivation Accompanying Low Cycle Fatigue of Al-2024 Under Complex Loading

Artur Ganczarski and Maciej Oleksy

Abstract Present paper deals with numerical modeling of the damage deactivation accompanying low cycle fatigue under complex loading. Based on kinetic theory of damage evolution by Lemaitre and Chaboche (*Mécanique des Matériaux Solides*, 1985) the continuous function of the crack closure parameter is proposed. Results of numerical simulation are verified with experimental tests for aluminum alloy Al-2024 by Abdul-Latif and Chadli (*Int J Damage Mech* 16:133–158, 2007). Detailed quantitative and qualitative analysis of solutions obtained for uniaxial and biaxial cyclic tests confirms the necessity and correctness of an application of proposed continuous damage deactivation effect.

Keywords Continuous damage deactivation · Low cycle fatigue

Nomenclature

Superscripts \pm	Refer to tension or compression, respectively
Superscripts e, p, D	Refer to elastic, plastic or damage variable, respectively
Tilde \sim over a symbol	Denotes quantity modified by damage
$\langle \rangle$	The Mac Auley brackets given by the relations: $\langle x \rangle = x$ if $\langle x \rangle \geq 0$ and $\langle x \rangle = 0$ if $x < 0$
a, b, R_∞, X_∞	Material constants
D	Damage parameter
E, E_{ijkl}, G, ν	Young's modulus, tensor of elasticity, shear modulus and Poisson ratio

A. Ganczarski (✉)
Institute of Applied Mechanics, Cracow University of Technology,
Al. Jana Pawła II 37, 31-864 Kraków, Poland
e-mail: artur.ganczarski@pk.edu.pl

M. Oleksy
Dephi, ul. Podgórci Tynieckie 2, 30-399 Kraków, Poland
e-mail: maciej.oleksy@zax.pl

© Springer International Publishing Switzerland 2015
H. Altenbach and M. Brünig (eds.), *Inelastic Behavior of Materials and Structures Under Monotonic and Cyclic Loading*, Advanced Structured Materials 57, DOI 10.1007/978-3-319-14660-7_4

F	Dissipation potential
h, h_c	Crack closure parameter and its critical value
H	Heaviside's function
n	Number of cycles
p, p^D	Accumulated plastic strain, damage threshold
r, α_{ij}	Isotropic and kinematic strain hardening variables
R, X_{ij}, X'_{ij}	Isotropic hardening parameter, back stress tensor and back stress deviator
s_{ij}, S	Stress deviator and damage strength
Y	Strain energy density release rate
$\varepsilon, \varepsilon_{ij}, \varepsilon_{eq}, \gamma$	Axial strain, strain tensor, maximum von Mises equivalent total strain, shear strain
λ	Plastic multiplier
ρ	Mass density
$\sigma, \sigma_{ij}, \sigma_y, \tau$	Axial stress, stress tensor, yield stress and shear stress
ψ	State potential
χ	Hayhurst's function
δ_{ij}	Kronecker's symbol

1 Introduction

In the case of cycle fatigue, when the stress level is larger than the yield stress, damage develops together with the cyclic plastic strain, after the incubation period that precedes the nucleation and growth of micro-defects is met. In the most frequent approach to the cycle fatigue, in case when a loading is the periodic strain-controlled of constant amplitude, the following assumptions are made: the material becomes perfectly plastic during first cycle, the variation of damage is neglected for the integration over one cycle and the strain-damage relations are identical both for tension and compression. These allow to simplify calculations of damage cumulation per one cycle and give linear dependency of damage with n , finally leading to the Manson-Coffin law of low cycle fatigue, see Lemaitre and Chaboche (1985), Skrzypek and Ganczarski (1999).

On the other hand, the more refined approaches to cycle fatigue presented by Lemaitre (1992) and also by Brocks and Steglich (2003), based on the kinetic theory of damage evolution and the Gurson-Tvergaard-Needleman model of damage incorporating isotropic hardening, respectively, are able to predict some qualitative phenomena of damage accumulation, crack initiation and fracture only approximately, since they do not account for the unilateral damage.

The phenomenon of the unilateral damage, also called the damage deactivation or the crack closure/opening effect is typical for materials subjected to reverse tension-compression cycles. In the simplest one-dimensional case, if the loading is reversed from tension to compression, the cracks will completely close

such that the material behaves as uncracked, or in other words, its initial stiffness is recovered. The mathematical description of unilateral damage is based on the decomposition of the stress or strain into the positive and negative projections, see Ladeveze (1992), Litewka (1991), Mazars (1986), Krajcinovic (1996), Saanouni and Forster (1994) and Saanouni and Abdul-Latif (1996). In the simplest case the damage modified stress or strain are used, based on the concept of the Heaviside function, where the negative principal components are ruled out. This means that the negative principal strain or stress components become

Table 1 Loss of symmetry or lack of continuity of two first components of effective stiffness tensor in classical vector or second-order tensor formulations in comparison to consistent formulation (after Chaboche (2006); Welemane and Cormery (2002))

Formulation	Signs of strain components		
	$\epsilon_1 > 0$	$\epsilon_2 > 0$	
vector by	$\lambda + 2\mu + 2(C_1 + C_2)\omega_1^2$	$\lambda + C_1(\omega_1^2 + \omega_2^2)$	lack of continuity
Krajcinovic and Fonseka (1981a,b)	$\lambda + C_1(\omega_1^2 + \omega_2^2)$	$\lambda + 2\mu + 2(C_1 + C_2)\omega_2^2$	
(damage variables ω_1, ω_2)	$\epsilon_1 < 0$	$\epsilon_2 > 0$	
	$\lambda + 2\mu$	$\lambda + C_1\omega_2^2$	
	$\lambda + C_1\omega_2^2$	$\lambda + 2\mu + 2(C_1 + C_2)\omega_2^2$	
2nd rank tensor by	$\epsilon_1 > 0$	$\epsilon_2 > 0$	
Ramtani (1990)	$h_{11}^{+2} + \lambda(1 - \delta)$	$h_{12}^{+2} + \lambda(1 - \delta)$	loss of symmetry
(damage variable δ)	$h_{12}^{+2} + \lambda(1 - \delta)$	$h_{22}^{+2} + \lambda(1 - \delta)$	
	$\epsilon_1 < 0$	$\epsilon_2 > 0$	
	$h_{11}^{-2} + \lambda(1 - \delta)$	$h_{12}^{+2} + \lambda(1 - \delta)$	
	$h_{12}^{-2} + \lambda(1 - \delta)$	$h_{22}^{+2} + \lambda(1 - \delta)$	
	$\epsilon_1 > 0$	$\epsilon_2 > 0$	
2nd rank tensor by	$(\lambda + 2\mu)(1 - d_1)^2$	$\lambda(1 - d_1)(1 - d_2)$	lack of continuity
Cordebois and Sidoroff (1983)	$\lambda(1 - d_1)(1 - d_2)$	$(\lambda + 2\mu)(1 - d_2)^2$	
(damage variables d_1, d_2)	$\epsilon_1 < 0$	$\epsilon_2 > 0$	
	$\lambda + 2\mu$	$\lambda(1 - d_1)(1 - d_2)$	
	$\lambda(1 - d_1)(1 - d_2)$	$(\lambda + 2\mu)(1 - d_2)^2$	
	$\epsilon_1 > 0$	$\epsilon_2 > 0$	
4th rank tensor by	$\lambda + 2\mu + 2(\alpha + 2\beta + \delta)d$	$\lambda + (\alpha + 2\delta)d$	
Halm and Dragon (1996, 1998)	$\lambda + (\alpha + 2\delta)d$	$\lambda + 2\mu + 2\delta d$	
(damage variable d , damage deactivation parameters: α, β, δ)	$\epsilon_1 < 0$	$\epsilon_2 > 0$	
	$\lambda + 2\mu - \frac{\lambda^2}{(\lambda + \mu)^2}\chi d$	$\lambda - \frac{\lambda}{\lambda + \mu}\chi d$	
	$\lambda - \frac{\lambda}{\lambda + \mu}\chi d$	$\lambda + 2\mu - \chi d$	
$\chi = \frac{(\lambda + \mu)^2(\alpha^2 - 8\beta\delta)}{2[2(\lambda + \mu)^2\beta + \mu^2\delta + \mu(\lambda + \mu)\alpha]}$			

completely inactive in further damage process as long as the loading condition can again render them active, see Litewka (1991). A more general approach, where both positive and weighted negative eigenvalues of strain or stress tensors influence damage evolution is due to Murakami and Kamiya (1997) and Hayakawa and Murakami (1997). The positive parts of the strain or stress can also be expressed by the use of the fourth-order positive projection operators written in terms of their eigenvectors, see Krajcinovic (1996) and Hansen and Schreyer (1995). The limitations of the consistent unilateral damage condition applied to the continuum damage theories have been discussed by Chaboche (1992, 1993) and Chaboche et al. (1995). These authors showed that in the existing theories developed by Ramtani (1990) and Ju (1989) or Krajcinovic and Fonseka (1981a, b) either non-symmetries of the elastic stiffness or non-realistic discontinuities of the stress-strain response may occur for general multiaxial non-proportional loading conditions (see Table 1). It is easy to show that if the unilateral condition does affect both the diagonal and the off-diagonal terms of the stiffness or compliance tensor, a stress discontinuity takes place when one of principal strains changes sign and the other remain unchanged, see Skrzypek and Kuna-Ciskal (2003). In the model proposed by Chaboche (1993) only the diagonal components corresponding to negative normal strains are replaced by the initial (undamaged) values. The consistent description of the unilateral effect was recently developed by Halm and Dragon (1996, 1998). These authors introduced a new fourth-rank damage parameter built upon the eigenvectors of second-order damage tensor that controls the crack closure effect with the continuity requirement of the stress-strain response fulfilled.

2 Experiments of Low Cycle Fatigue of Aluminum Alloy Al-2024 by Abdul-Latif and Chadli (2007)

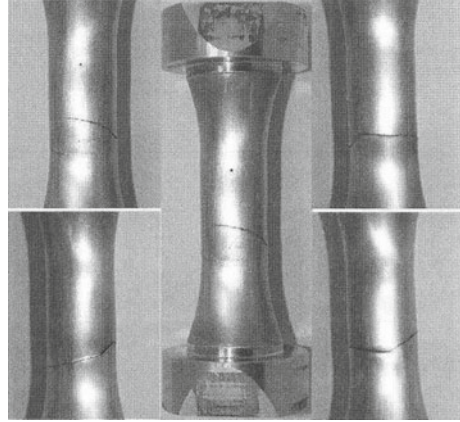
Detailed description of a low cycle fatigue for specimens made of aluminum alloy done by Abdul-Latif and Chadli (2007) whereas later work by Abdul-Latif and Mounounga (2009) contains results of numerical modeling in case of several biaxial loading paths. In experiment the aluminum alloy Al-2024 of chemical composition shown in Table 2 was used. The tests were carried out at room temperature on a servo-hydraulic INSTRON machine type 1,340 using thin-walled tubes of internal diameter 15 mm, external diameter 18 mm. The specimens were machined from a circular bar with an outer diameter of 42 mm in the longitudinal direction. After the machining process all the specimens undergone an over-aging heat treatment consisting of setting them in solution at 495 °C followed by a water quench.

Different uniaxial and biaxial loading paths were conducted up to the final fracture of the specimen, see Fig. 1. Several cyclic tests of constant strain amplitude were carried out. The maximum von-Mises equivalent total strain corresponding to them was defined as follows:

Table 2 Chemical composition of aluminum alloy Al-2024 (% in weight)

Al	Si	Fe	Cu	Mn	Mg	Cr	Ni	Zn	Ti	Zr	Pb
Balance	0.11	0.28	4.33	0.75	1.31	0.01	0.01	0.10	0.03	0.14	0.0021

Fig. 1 General view of a specimen after fracture, after Abdul-Latif and Chadli (2007)



$$\varepsilon_{eq} = \begin{cases} \frac{\varepsilon_{max} - \varepsilon_{min}}{2} & \text{for uniaxial-compression test} \\ \max(\sqrt{\varepsilon^2 + \gamma^2/3}) & \text{for biaxial tension-torsion test} \end{cases} \quad (1)$$

where ε stands for normal strain and γ denotes shear strain. Authors tested following loading paths: uniaxial tension-compression (TC), alternative torsion-torsion (AT), biaxial loading of tension-torsion with 90° out-of-phase angle (TT90) called also diamond test, and butterfly test (Bfly) all represented schematically in Fig. 2. The most interesting and representative results were obtained in case of the uniaxial tension-compression test (TC) and the diamond test (TT-90) at the constant strain amplitude corresponding to the maximum von-Mises equivalent total strain equal to $\varepsilon_{eq} = 1\%$ and to $\varepsilon_{eq} = 0.85\%$, respectively (see Fig. 3). The tests were interrupted at the instant when the specimen failure was achieved after 291 or 81 cycles. Detailed analysis of the subsequent strain-stress loops confirms an elasto-plastic behavior of the material and strong influence of the unilateral damage effect. During the initial cycles the material exhibits plastic hardening leading to the stabilized cycle and, then, asymmetric drop of both the stress amplitude and the modulus of elasticity reveals following damage growth. This process is accompanied by a gradual decrease of the hysteresis area and a change of shape of subsequent hysteresis loops, associated with a formation of the characteristic inflection point on their lower branches.

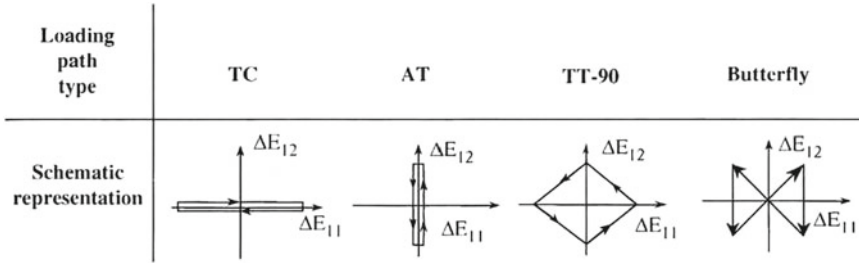


Fig. 2 Loading paths tested by Abdul-Latif and Chadli (2007)

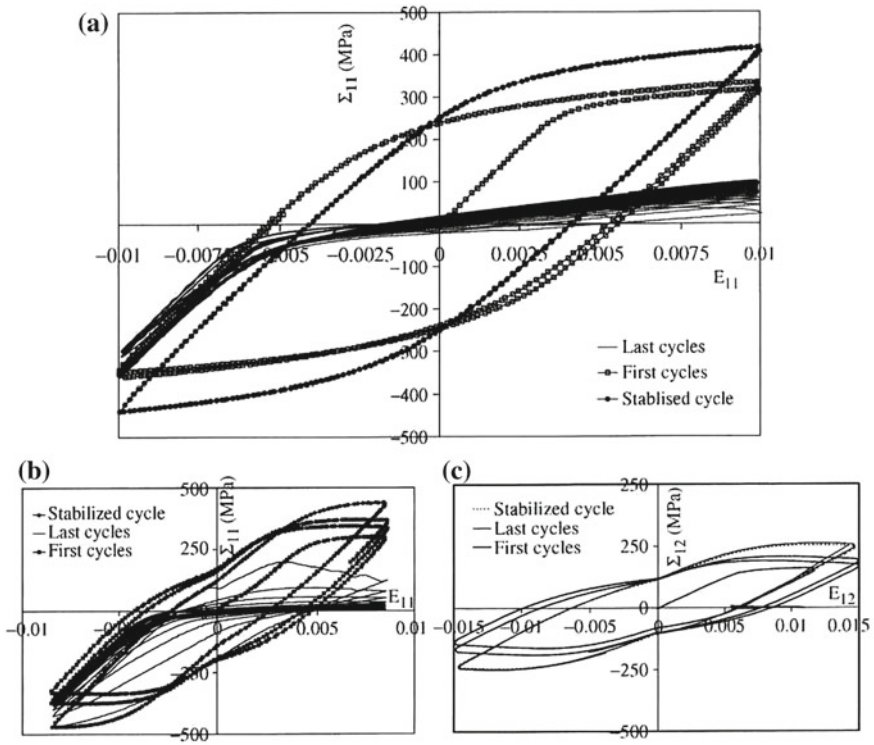


Fig. 3 Experimental tests of aluminum alloy Al-2024: **a** uniaxial tension-compression (TC), **b** biaxial tension-torsion (TT-90), after Abdul-Latif and Chadli (2007)

3 Kinetic Theory of Damage Evolution

The kinetic theory of damage evolution by Lemaitre and Chaboche (1985) and Lemaitre (1992) being extension of the nonlinear Armstrong-Frederick model is based on the dissipation potential

$$F = \sqrt{\frac{3}{2}(\tilde{s}_{ij} - X'_{ij})(\tilde{s}_{ij} - X'_{ij})} - R - \sigma_y + \frac{3}{4X_\infty} X'_{ij} X'_{ij} + \frac{Y^2}{2S(1 - Dh)} H(p - p^D) \quad (2)$$

definition of the elastic strain energy release rate

$$Y = \frac{1}{2} E_{ijkl}^{-1} \tilde{\sigma}_{ij} \tilde{\sigma}_{kl} \quad (3)$$

and the state potential

$$\psi = \frac{1}{\rho} \left\{ \frac{1}{2} E_{ijkl} \varepsilon_{ij}^e \varepsilon_{kl}^e (1 - Dh) + R_\infty \left[r + \frac{1}{b} \exp(-br) \right] + \frac{X_\infty a}{3} \alpha_{ij} \alpha_{ij} \right\} \quad (4)$$

By use of the formalism of classical associated plasticity applied to Eq. (2) we find increments of plastic strain, accumulated plastic strain, isotropic strain hardening, kinematic strain hardening and damage variable

$$\begin{aligned} d\varepsilon_{ij}^p &= \frac{\partial F}{\partial \sigma_{ij}} d\lambda = \frac{3}{2} \frac{\tilde{s}_{ij} - X'_{ij}}{\sqrt{\frac{3}{2}(\tilde{s}_{kl} - X'_{kl})(\tilde{s}_{kl} - X'_{kl})}} \frac{d\lambda}{1 - Dh} \\ dp &= \sqrt{\frac{2}{3}} d\varepsilon_{ij}^p d\varepsilon_{ij}^p = \frac{d\lambda}{1 - Dh} \\ dr &= -\frac{\partial F}{\partial R} d\lambda = (1 - Dh) dp \\ d\alpha_{ij} &= -\frac{\partial F}{\partial X'_{ij}} d\lambda = \frac{3}{2} \left(\frac{\tilde{s}_{ij} - X'_{ij}}{\sqrt{\frac{3}{2}(\tilde{s}_{kl} - X'_{kl})(\tilde{s}_{kl} - X'_{kl})}} - \frac{X'_{ij}}{X_\infty} \right) d\lambda \\ dD &= \frac{\partial F}{\partial Y} d\lambda = \frac{Y}{S(1 - Dh)} H(p - p^D) dp \end{aligned} \quad (5)$$

In next step following inner variables of stress type associated to ε_{ij}^e , r , α_{ij} and D are calculated from the state potential (4):

$$\sigma_{ij} = \rho \frac{\partial \psi}{\partial \varepsilon_{ij}^e} = E_{ijkl} \varepsilon_{kl}^e (1 - Dh) \quad R = \rho \frac{\partial \psi}{\partial r} = R_\infty [1 - \exp(-br)]$$

$$X_{ij} = \rho \frac{\partial \psi}{\partial \alpha_{ij}} = \frac{2}{3} X_{\infty} a \alpha_{ij} \quad Y = -\rho \frac{\partial \psi}{\partial D} = \frac{1}{2} E_{ijkl} \varepsilon_{ij}^e \varepsilon_{kl}^e h \quad (6)$$

Introducing Eqs. (5) and (6) we reduce the inner variables of strain type and arrive at incremental form of the Lemaitre and Chaboche equations

$$\begin{aligned} \sigma_{ij} &= \tilde{E}_{ijkl} (\varepsilon_{kl} - \varepsilon_{kl}^p) \\ d\varepsilon_{ij}^p &= \frac{3}{2} \frac{\tilde{s}_{ij} - X'_{ij}}{\sqrt{\frac{3}{2} (\tilde{s}_{kl} - X'_{kl}) (\tilde{s}_{kl} - X'_{kl})}} \frac{d\lambda}{1 - Dh} \\ dR &= b(R_{\infty} - R) d\lambda \quad (7) \\ dX'_{ij} &= a \left[\frac{2}{3} X_{\infty} d\varepsilon_{ij}^p (1 - Dh) - X'_{ij} \right] \\ dD &= \frac{E_{ijkl}^{-1} \sigma_{ij} \sigma_{kl}}{2S(1 - Dh)^2} H(p - p^D) dp \end{aligned}$$

in which the plastic multiplier derived from the consistency condition is equal to

$$\begin{aligned} d\lambda &= \frac{\frac{3}{2} (\tilde{s}_{ij} - X'_{ij}) \sigma_{ij}}{(1 - Dh) \sqrt{\frac{3}{2} (\tilde{s}_{kl} - X'_{kl}) (\tilde{s}_{kl} - X'_{kl})} \left[X_{\infty} a + b(R_{\infty} - R) \right.} \\ &\quad \left. \dots \frac{3}{2} (\tilde{s}_{mn} - X'_{mn}) \left(\frac{s_{mn}}{1 - Dh} \frac{E_{pqrs} \varepsilon_{pq}^e \varepsilon_{rs}^e h}{2S(1 - Dh)} H(p - p^D) + a X'_{mn} \right) \right]} \quad (8) \end{aligned}$$

4 Continuous Damage Deactivation Effect

In case of uniaxial tensile stress and scalar damage the effective stress the appropriate effective modulus of elasticity are defined as follows

$$\tilde{\sigma} = \frac{\sigma}{1 - D}, \quad \tilde{E} = E(1 - D) \quad (9)$$

Above relations are valid also in case when micro-cracks remain open under uniaxial compression. For certain class of materials and certain conditions of loading the micro-defects may close in compression. This is often case for very brittle materials. If the micro-defects close completely two separate set of conditions must be defined, one for tension and another for compression

$$\tilde{\sigma}^{\pm} = \begin{cases} \sigma^+ / (1 - D) \\ \sigma^- \end{cases} \quad \tilde{E}^{\pm} = \begin{cases} E^+ (1 - D) \\ E^- \end{cases} \quad (10)$$

In the real material, however, the micro-defects have complicated shapes and do not close completely. In order to take into account this effect, so called crack closure parameter h ($0 \leq h \leq 1$) is introduced. The crack closure parameter h depends on a material and loading, however, in practice it is considered to be constant $h_c = 0.2$ and appropriate conditions for tension and compression are given by the following formulas (see Lemaitre 1992)

$$\tilde{\sigma}^{\pm} = \begin{cases} \sigma^+ / (1 - D) \\ \sigma^- / (1 - Dh_c) \end{cases} \quad \tilde{E}^{\pm} = \begin{cases} E^+ (1 - D) \\ E^- (1 - Dh_c) \end{cases} \quad (11)$$

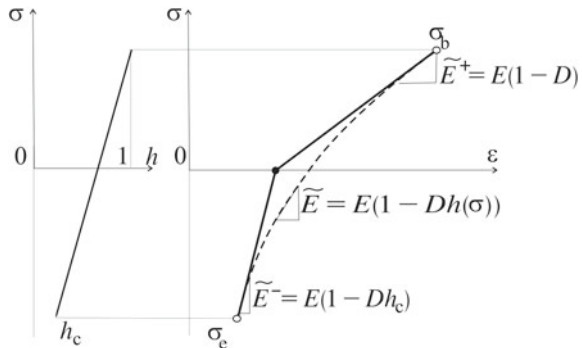
Application of this model for description of unloading path leads to linear relation between the stress decrease and the strain decrease given by E^+ . Entering the compression range the material switches to the path characterized by the modulus of elasticity which is equal to E^- . The real materials do not exhibit such bilinear unloading paths therefore the concept of continuous crack closure that allows to eliminate mentioned switch between E^+ and E^- is introduced. It consists in the replacement of parameter h by a function $h(\sigma)$, being linear in the simplest case, such that (see Ganczarski and Cegielski 2010)

$$h(\sigma) = h_c + (1 - h_c) \frac{\sigma - \sigma_c}{\sigma_b - \sigma_c} \quad (12)$$

According to above relation function $h(\sigma)$ is equal to 1 when $\sigma = \sigma_b$ and h_c when $\sigma = \sigma_c$, see Fig. 4. Three-dimensional generalization of the continuous damage deactivation requires distinction between tension and compression. When the stress tensor is given by its eigenvalues the following decomposition is applied

$$\sigma_{ij} = \sigma_{ij}^+ + \sigma_{ij}^- = \langle \sigma_{ij} \rangle - \langle -\sigma_{ij} \rangle \quad (13)$$

Fig. 4 Concept of the continuous damage deactivation, after Ganczarski and Cegielski (2010)



When the isotropic damage occurs, in accordance with the concept of effective stress, the unilateral conditions are written by means of $(1 - D)$ for the positive part and $(1 - Dh)$ for the negative term, respectively

$$\begin{aligned} \varepsilon_{ij} = & \frac{E_{ijkl}^{-1}}{1 - D} [(1 + \nu)\langle\sigma_{kl}\rangle - \nu\langle\sigma_{mm}\delta_{kl}\rangle] \\ & - \frac{E_{ijkl}^{-1}}{1 - Dh} [(1 + \nu)\langle-\sigma_{kl}\rangle - \nu\langle-\sigma_{mm}\delta_{kl}\rangle] \end{aligned} \quad (14)$$

Application of the principle of strain equivalence imposes certain conditions on the effective stress in the general form of the law of elasticity

$$\varepsilon_{ij} = E_{ijkl}^{-1} [(1 + \nu)\tilde{\sigma}_{kl} - \nu\tilde{\sigma}_{mm}\delta_{kl}] \quad (15)$$

and one may find out (Lemaitre 1992)

$$\tilde{\sigma}_{ij}^+ = \frac{\langle\sigma_{ij}\rangle}{1 - D} + \frac{\nu}{1 - 2\nu} \frac{\langle\sigma_{kk}\rangle\delta_{ij} - \langle\sigma_{kk}\delta_{ij}\rangle}{1 - D} \quad (16)$$

and

$$\tilde{\sigma}_{ij}^- = -\frac{\langle-\sigma_{ij}\rangle}{1 - Dh} - \frac{\nu}{1 - 2\nu} \frac{\langle\sigma_{kk}\rangle\delta_{ij} - \langle-\sigma_{kk}\delta_{ij}\rangle}{1 - Dh} \quad (17)$$

Terms associated to the factor $\nu/(1 - 2\nu)$ introducing coupling disappear if all eigenvalues of stress are of the same sign and in such case simplified effective stresses and the corresponding elastic modules take the form

$$\tilde{\sigma}_{ij}^{\pm} = \begin{cases} \langle\sigma_{ij}\rangle/(1 - D) \\ \langle-\sigma_{ij}\rangle/(1 - Dh) \end{cases} \quad \tilde{E}_{ijkl}^{\pm} = \begin{cases} E_{ijkl}(1 - D) \\ E_{ijkl}(1 - Dh) \end{cases} \quad (18)$$

Application of the concept of continuous crack closure in the case of three-dimensional state of stress turns out a little more sophisticated when compare to the case of uniaxial stress (12) and needs additional hypothesis that introduces the relation between the crack closure magnitude and a scalar function of the stress tensor

$$h(\sigma_{ij}) = h_c + (1 + h_c) \frac{\chi(\sigma_{ij}) - \chi(\sigma_{(e)ij})}{\chi(\sigma_{(b)ij}) - \chi(\sigma_{(e)ij})} \quad (19)$$

here the known Hayhurst function (Hayhurst 1998) dependent on first and second invariants of stress tensor

$$\chi(\sigma_{ij}) = c\sigma_{kk}\delta_{ij}/3 + (1 - c)\sqrt{3s_{kl}s_{kl}}/2 \quad (20)$$

Form tensor algebra point of view the Hayhurst function allows for replacement of the general 3D state of stress by its scalar equivalent which remains in accordance with scalar nature of damage. Original physical meaning of the function (20) refers to the traditional classification of polycrystalline metallic materials with respect to their damage sensitivity: $c = 0$ represents class of aluminium-like materials damage of which is controlled by second invariant of stress tensor, $c = 1$ represents class of copper-like materials damage of which is controlled by first invariant of stress tensor, whereas $c \in (0, 1)$ represents other materials.

5 Examples of Numerical Modeling of LCF Tests

5.1 Uniaxial Tension-Compression (TC)

In case of uniaxial stress simplified forms of the dissipation potential (2)

$$F = |\tilde{\sigma} - X| - R - \sigma_y + 0.75X^2/X_\infty + \frac{Y^2}{2S(1 - Dh)}H(p - p^D) \quad (21)$$

which together with the elastic strain energy release rate (3)

$$Y = \tilde{\sigma}h/2E \quad (22)$$

and the state potential (4)

$$\psi = \frac{1}{\rho} \left\{ \frac{1}{2}E(\varepsilon^e)^2(1 - Dh) + R_\infty \left[r + \frac{1}{b} \exp(-br) \right] + \frac{X_\infty a}{3} \alpha^2 \right\} \quad (23)$$

lead to the following form of the Lemaitre and Chaboche equations (7)

$$\begin{aligned} d\sigma/d\varepsilon &= E(1 - Dh) && \text{elastic range} \\ d\sigma/dp &= (1 - Dh)^2 \{ [X_\infty a + b(R - R_\infty)] \text{sign}(\tilde{\sigma} - X) - aX \} && \text{plastic range} \\ &\quad - \frac{\tilde{\sigma}^3}{2ES} H(p - p^D) \\ dR/dp &= b(R_\infty - R)(1 - Dh) && (24) \\ dX/dp &= a [X_\infty \text{sign}(\varepsilon^p) - X] (1 - Dh) \\ dD/dp &= \frac{\sigma^2}{2ES(1 - Dh)^2} H(p - p^D) \end{aligned}$$

Above system of four ordinary differential equations is numerically integrated for constant strain range $\Delta\varepsilon = \pm 1\%$ by use of the fourth-order Runge-Kutta technique

with the adaptive stepsize control, see Press et al. (1993). Identification of material constants is done partly on the basis of experiments and partly on numerical way. Magnitudes of the Young modulus E and the yield stress σ_y are taken from paper by Abdul-Latif and Chadli (2007) whereas magnitudes of material constants of isotropic and kinematic plastic hardening b , R_∞ , a , X_∞ are chosen in order to minimize discrepancies between initial hysteresis loops corresponding to experiment and numerical simulation. Identification of material parameters kinetic law of damage evolution h_c , S , p^D is based on a procedure by Lemaitre (1992). Magnitude of the stress referring to the end of damage deactivation process σ_e is assumed to be equal to the actual compressive yield stress. Full set of material constants is shown in Table 3. Results of numerical simulation with sampling model of discontinuous damage deactivation (11) are presented in Fig. 5b. Model gives only quantitatively good agreement with experimental data (see Fig. 5d) since it properly maps unilateral damage softening in this sense that ordinates of subsequent hysteresis loops correspond to appropri-

Table 3 Material constants of aluminum alloy Al-2024 in TC test

E (GPa)	σ_y (MPa)	b	R_∞ (MPa)	a	X_∞ (MPa)	h_c	S (MPa)	p^D
70	230	0.1	120	4.0	60	0.2	3,500	0.248

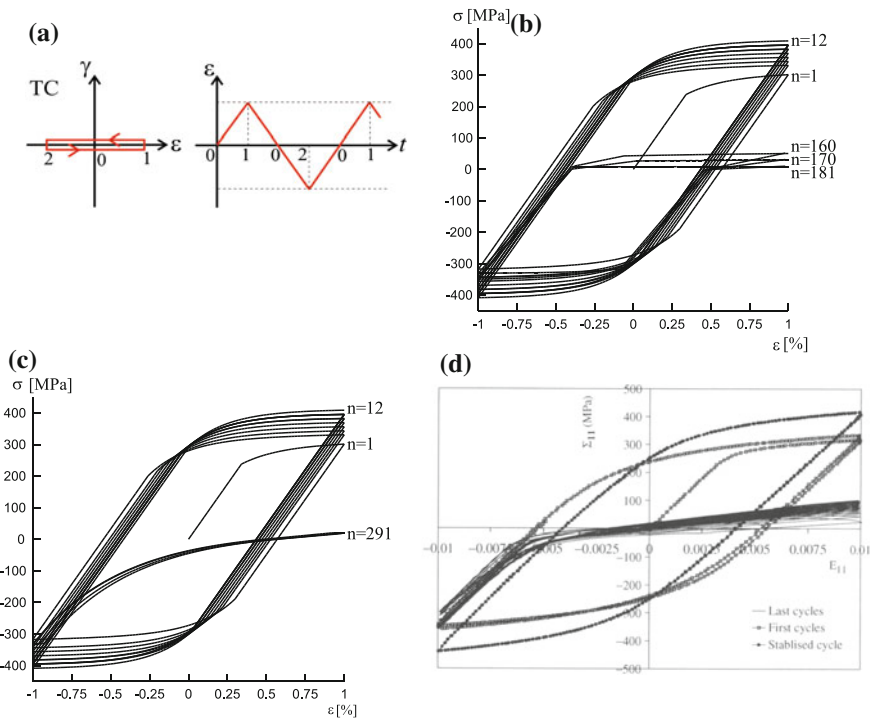


Fig. 5 Results of numerical simulation of uniaxial tension-compression: **a** loading history, evolution of axial stress versus axial strain in case of **b** discontinuous (11), **c** continuous damage deactivation effect (12) and **d** experimental test by Abdul-Latif and Chadli (2007)

ate points at experimental curves. However, the model under consideration exhibits $\partial\sigma/\partial\varepsilon$ discontinuity for $\sigma = 0$ leading to drastic disagreement with experiment in case of final cycles ($n \geq 160$). In contrast to above model, the numerical simulation with model of continuous damage deactivation effect included (12) exhibits not only quantitative but also qualitative proper correctness in comparison with experimental results (Fig. 5c, d). Essential defect of non-smooth and bilinear characteristics that separates ranges of tension and compression is successively eliminated. Additionally effects of a gradual decrease of area bounded by subsequent hysteresis loops and corresponding change of convexity at lower branch of hysteresis are perfectly mapped.

5.2 Alternative Torsion (AT)

In case of simple shear stress state when its principal directions stay materially constant and equal $\pm 45^\circ$ the dissipation potential (2) is assumed in simplified form

$$F = \sqrt{3}|\tilde{\tau} - X| - R - \sigma_y + 0.75X^2/X_\infty + \frac{Y^2}{2S(1 - Dh)}H(p - p^D), \quad (25)$$

whereas corresponding elastic strain energy density release rate (3) is equal to

$$Y = \tilde{\tau}h/2\sqrt{3}G \quad (26)$$

The Lemaitre and Chaboche equations (7) take therefore following form

$$\begin{aligned} d\tau/d\gamma &= G(1 - D_i h) && \text{elastic range} \\ d\tau/dp &= (1 - D_i h)^2 \{2[X_\infty a + b(R - R_\infty)] \\ &\quad \times \text{sign}(\tilde{\tau} - X)/\sqrt{3} - aX\} - \frac{\tilde{\tau}^3}{2\sqrt{3}GS}H(p - p^D) && \text{plastic range} \\ dR/dp &= b(R_\infty - R)(1 - D_i h) && (27) \\ dX/dp &= a \left[X_\infty \text{sign}(\gamma^p)/3 - X/\sqrt{3} \right] (1 - D_i h) \\ dD_i/dp &= \frac{\tau^2}{2\sqrt{3}GS(1 - D_i h)^2}H(p - p^D) \end{aligned}$$

in which D_1, D_2 refer to two damage variables corresponding to two eigendirections inclined $\pm 45^\circ$ to global co-ordinate axis. Above system of five ordinary differential equations is numerically integrated for shear strain $\Delta\gamma = \pm 1.47\%$ by `odeint`. for routine previously applied in case of TC test, see Press et al. (1993). Magnitudes of material constants are the same as in Table 3 except for the Young modulus is replaced by the shear modulus $G = 26.92$ GPa. In order to emphasize influence of unidirectional character of damage the following initial damage advance $D_1 = 0.3, D_2 = 0.0$

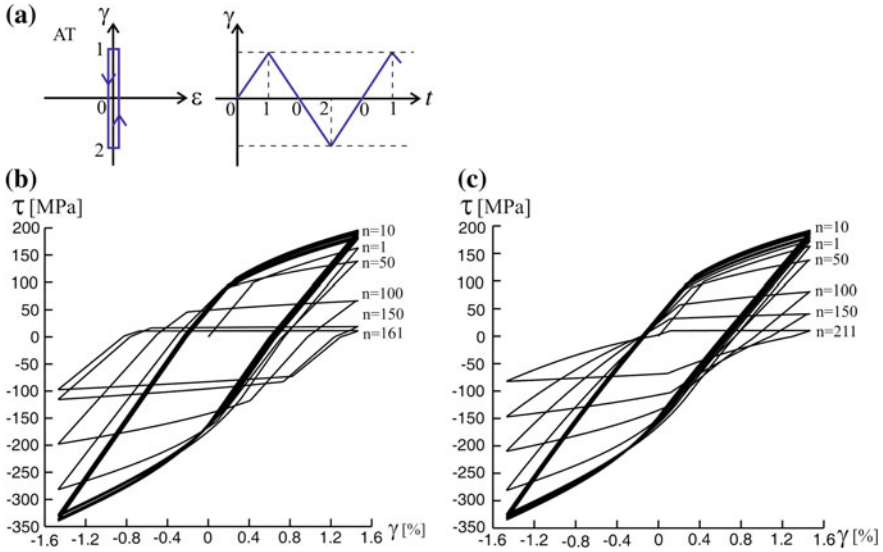


Fig. 6 Results of numerical simulation of alternative torsion: **a** loading history, evolution of shear stress versus shear strain in case of **b** discontinuous and **c** continuous damage deactivation effect

is assumed. Results of numerical simulation with models of discontinuous and continuous damage deactivation are shown in Fig. 6b, c however there is no comparison to experiment since the paper by Abdul-Latif and Chadli (2007) does not comprise it. Although initial hysteresis loops in both cases are identical two essential differences are clearly visible in case of final cycles. Namely, number of cycles to failure for model of continuous damage deactivation ($n = 211$) is greater than analogous number for model of discontinuous damage deactivation ($n = 161$). This effect is strictly associated with the shape of final hysteresis loops which are narrower in case model of continuous damage deactivation. In other words smaller dissipation leads to longer life-time of material. Finally, it is worth to notice that alternative torsion is the last of elementary tests which can be solved by the use of simple algorithm of numerical integration with out necessity of the use any of FEM routines.

5.3 Biaxial Tension-Torsion (TT-90)

The biaxial tension-torsion is the first of non-elementary cases. This means that neither the dissipation potential (2), the elastic strain energy release rate (3) nor system of Eqs. (7), (8) can be reduced to a simplified form and one of FEM routines has to be applied in order to get a solution. A simple finite element code used in this example is a combination of the return mapping algorithm routine proposed by Owen and Hinton (1980) also by Ganczarski and Skrzypek (2009) on one hand and

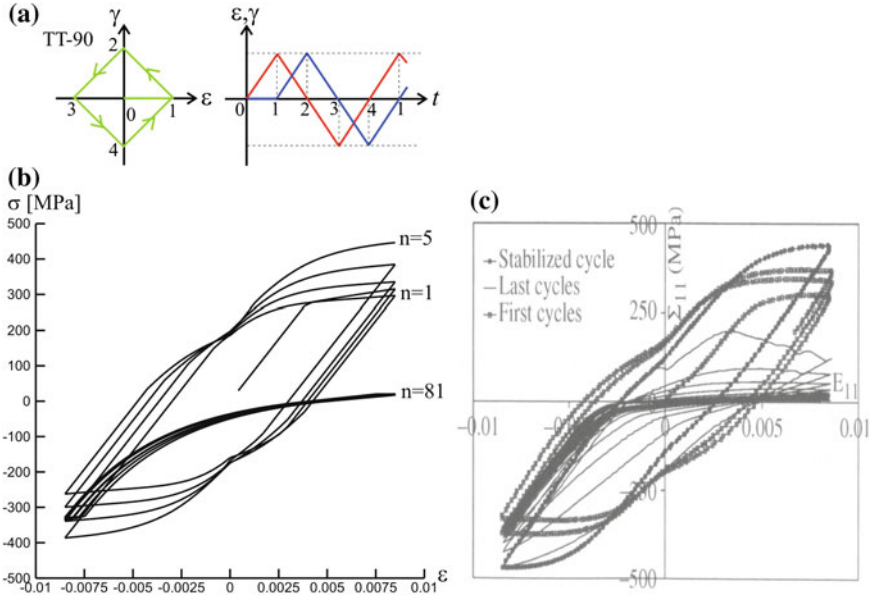


Fig. 7 Results of numerical simulation of biaxial tension-torsion: **a** loading history, **b** evolution of axial stress versus axial strain in case of continuous damage deactivation effect and **c** experimental test by Abdul-Latif and Chadli (2007)

the postprocessor DAMAGE90 proposed by Doghri (1990). It is written in fortran and limited to one finite element which contains only one integration point. Running this code for the biaxial tension-torsion loading history (see Fig. 7a) characterized by $\Delta\epsilon = \pm 0.85\%$, $\Delta\gamma = \pm 0.91\%$ (the maximum von Mises equivalent total strain equal to $\epsilon_{eq} = 1\%$) and material constants presented in Table 3 the results shown in Fig. 7b are obtained and compared with experimental tests by Abdul-Latif and Chadli (2007) (Fig. 7c). Detailed analysis of subsequent hysteresis loops exhibits that both stabilized cycle and cycles preceding failure are attained faster than in case of previously discussed loading paths TC and AT. This is effect of simultaneous acting two independent strains the axial and the shear which are additionally shifted in phase (see points 2, 4 etc. in Fig. 7a). Shifting effect explains existence of characteristic inflection points (see Fig. 7b) corresponding to $\epsilon = 0$ but maximum of absolute value of γ .

5.4 Butterfly Test (Bfly)

Simulation of Butterfly test is done by use of the same code like in case of TT-90 for the loading history (see Fig. 8a) characterized by $\Delta\epsilon = \Delta\gamma = \pm 0.866\%$ (the maximum von Mises equivalent total strain equal to $\epsilon_{eq} = 1\%$) and material constants

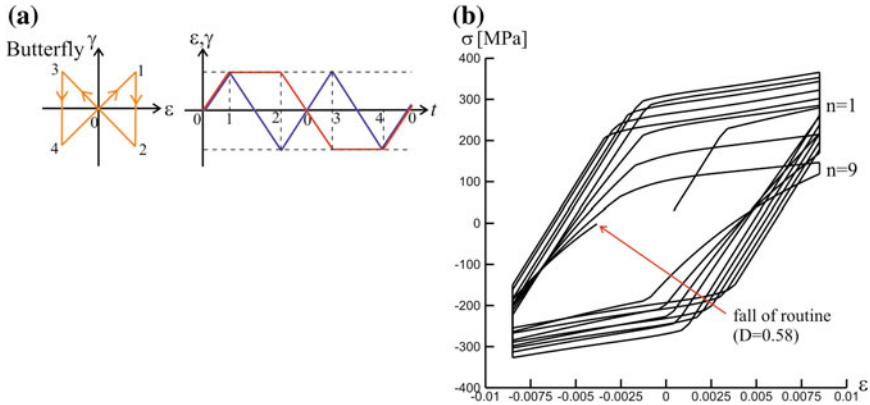


Fig. 8 Results of numerical simulation of Butterfly test: **a** loading history, **b** evolution of axial stress versus axial strain in case of continuous damage deactivation effect

presented in Table 3. Results are shown in Fig. 8b however there is no comparison to experiment because the paper by Abdul-Latif and Chadli (2007) does not contain it. In example under consideration all hysteresis loops exhibit characteristic vertical segments referring to constant value of axial strain (see points 1–2 and 3–4 in Fig. 8a). Number of cycles to failure very low ($n = 9$) in comparison to the previous tests. This is a consequence of relatively broad subsequent hysteresis loops, which means that dissipation of energy is high, in one hand and the fall of numerical routine, when damage advance is equal 0.58, on the other hand. The reason of such a falling is fundamental assumption of return mapping algorithm that actual yield surface always expands during plastic hardening. However, accounting for damage introduces another mechanism associated with material softening. As consequence a combined process of simultaneous hardening and softening may be traced by routine until first effect of is dominant. Obviously, there is in the literature (Casey and Naghdi 1983; Chen and Han 1995; Khan and Huang 1995) the strain-space plasticity formulation however it is not applied in the present work.

6 Conclusions

Modeling of low cycle fatigue by use of sampling model of discontinuous damage deactivation leads to physically unjustified discontinuities of loading-unloading path.

Model of continuous damage deactivation being free from defects of classical models is useful in modeling of low cycle fatigue of alloy Al-2024 for both uniaxial TC, AT and biaxial TT-90, Butterfly tests.

Comparing number of cycles to failure referring to subsequent loading paths TC, AT, TT-90 and Bfly the following decreasing series is observed: 291, 211, 87 and ?, this shows that biaxial tests are more important than uniaxial tests.

Acknowledgments This work was supported by National Science Centre Poland grant Nr UMO-2011/03/B/ST8/05132.

References

- Abdul-Latif A, Chadli M (2007) Modeling of the heterogeneous damage evolution at the granular scale in polycrystals under complex cyclic loadings. *Int J Damage Mech* 16(2):133–158
- Abdul-Latif A, Mounounga TB (2009) Damage-induced anisotropy with damage deactivation. *Int J Damage Mech* 18(2):177–198
- Brocks W, Steglich D (2003) Damage models for cyclic plasticity. In: Buchholtz FG, Richard H, Aliabadi M (eds) *Advances in fracture and damage mechanics*. Trans Tech Publications, Zürich, pp 389–398
- Casey J, Naghdi P (1983) On the nonequivalence of the stress space and strain space formulations of plasticity theory. *Trans ASME J Appl Mech* 50:321–345
- Chaboche JL (1992) Damage induced anisotropy: on the difficulties associated with the active/passive unilateral condition. *Int J Damage Mech* 1(2):148–171
- Chaboche JL (1993) Development of continuum damage mechanics for elastic solids sustaining anisotropic and unilateral damage. *Int J Damage Mech* 2(4):311–329
- Chaboche JL (2006) Constitutive modelling and damage of materials and structures. In: Skoczniński B, Pamin J (eds) *Experimental techniques and modelling of advanced materials*. KMM-NoE Integrated Post-Graduate School Doctoral Path, First Intensive Session, Cracow
- Chaboche JL, Lesne PM, Maire JF (1995) Continuum damage mechanics, anisotropy and damage deactivation for brittle materials like concrete and ceramic composites. *Int J Damage Mech* 4(1):5–22
- Chen W, Han D (1995) *Plasticity for structural engineers*. Springer, Berlin
- Doghri I (1990) Description and listening of the postprocessor DAMAGE90. In: Lemaitre J (ed) *A course on damage mechanics*. Springer, Berlin, pp 170–186
- Ganczarski A, Cegielski M (2010) Continuous damage deactivation in modeling of cycle fatigue of engineering materials. *Procedia Eng* 2(1):1057–1066
- Ganczarski A, Skrzypek J (2009) *Plasticity of engineering materials (in Polish)*. Wydawnictwo, Kraków
- Halm D, Dragon A (1996) A model of anisotropic damage by mesocrack growth; unilateral effect. *Int J Damage Mech* 5(4):384–402
- Halm D, Dragon A (1998) An anisotropic model of damage and frictional sliding for brittle materials. *Eur J Mech—A/Solids* 17(3):439–460
- Hansen N, Schreyer HL (1995) Damage deactivation. *Trans ASME J Appl Mech* 62(2):450–458
- Hayakawa K, Murakami S (1997) Thermodynamical modeling of elastic-plastic damage and experimental validation of damage potential. *Int J Damage Mech* 6(4):333–363
- Hayhurst DR (1998) Data bases and mechanisms-based constitutive equations for use in design. In: Altenbach H, Skrzypek J (eds) *Creep and damage in materials and structures*, Springer, Vienna, no. 187 in CISM Course, pp 167–208
- Ju J (1989) On energy-based coupled elastoplastic damage theories: constitutive modeling and computational aspects. *Int J Solids and Struct* 25(7):803–833
- Khan A, Huang S (1995) *Continuum theory of plasticity*. Wiley, New York
- Krajcinovic D (1996) *A course on damage mechanics*. Elsevier, Amsterdam

- Krajcinovic D, Fonseka G (1981a) The continuous damage theory of brittle materials. Part 1: general theory. *Trans ASME J Appl Mech* 48(4):809–815
- Krajcinovic D, Fonseka G (1981b) The continuous damage theory of brittle materials. Part 2: uniaxial and plane response modes. *Trans ASME J Appl Mech* 48(4):816–824
- Ladeveze PLJ (1992) Damage effective stress in quasi-unilateral conditions. In: *Proceedings of the IUTAM Congress 1984*, Lyngby, Denmark
- Lemaitre J (1992) *A course on damage mechanics*. Springer, Berlin
- Lemaitre J, Chaboche JL (1985) *Mécanique des Matériaux Solides*. Bordas, Paris
- Litewka A (1991) Creep damage and creep rupture of metals (in Polish). *Wyd Polit Poznańskiej*, Poznań
- Mazars J (1986) A model of unilateral elastic damageable material and its application to concrete. In: Wittmann FH (ed) *Energy toughness and fracture energy of concrete*. Elsevier, Amsterdam, pp 61–71
- Murakami S, Kamiya K (1997) Constitutive and damage evolution equations of elastic-brittle materials based on irreversible thermodynamics. *Int J Mech Sci* 39(4):473–486
- Owen DRJ, Hinton E (1980) *Finite elements in plasticity: theory and practice*. Pineridge Press Ltd, Swansea
- Press W, Teukolsky S, Vetterling W, Flannery B (1993) *Numerical recipes in Fortran*. Cambridge Press, Cambridge
- Ramtani S (1990) *Contribution á la modelisation du comportement multiaxial du beton endommagé avec description du caractere unilateral*. PhD thesis, University Paris VI, Paris
- Saanouni K, Abdul-Latif A (1996) Micromechanical modeling of low cycle fatigue under complex loadings—part I. Theoretical formulation. *Int J Plast* 12(9):1111–1121
- Saanouni K, Forster CH, Hatira P (1994) On the anelastic flow with damage. *Int J Damage Mech* 3(2):140–169
- Skrzypek J, Ganczarski A (1999) *Modeling of material damage and failure of structures*. Springer, Berlin
- Skrzypek JJ, Kuna-Ciskał H (2003) Anisotropic elastic-brittle-damage and fracture models based on irreversible thermodynamic. In: Skrzypek JJ, Ganczarski A (eds) *Anisotropic behaviour of damaged materials*. Springer, Berlin, pp 143–184
- Weleman H, Cormery F (2002) Some remarks on the damage unilateral effect modelling for microcracked materials. *Int J Damage Mech* 11(1):65–86

Computational Multiscale Modeling of Nickel-Based Superalloys Containing Gamma-Gamma' Precipitates

Somnath Ghosh, Shahriyar Keshavarz and George Weber

Abstract A hierarchical crystal plasticity constitutive model, comprising three different scales for polycrystalline microstructures of Ni-based superalloys, is developed. Three scales, dominant in models of polycrystalline Ni-based superalloys, are: (i) the sub-grain scale of γ - γ' microstructure, characterized by γ' precipitate size and their spacing; (ii) grain-scale characterized by the size of single crystals; and (iii) the scale of polycrystalline representative volume elements. A homogenized activation energy-based crystal plasticity (AE-CP) FEM model is developed for the grain-scale, accounting for characteristic parameters of the sub-grain scale γ - γ' morphology. A significant advantage of this AE-CP model is that its high efficiency enables it to be effectively incorporated in polycrystalline crystal plasticity FE simulations, while retaining the accuracy of detailed sub-grain level representative volume element (SG-RVE) models. The SG-RVE models are created for variable morphology, e.g. volume fraction, precipitate shape and channel-widths. The sub-grain crystal plasticity model incorporates a dislocation density-based crystal plasticity model augmented with mechanisms of anti-phase boundary (APB) shearing of precipitates. The sub-grain model is homogenized for developing parametric functions of morphological variables in evolution laws of the AE-CP model. Micro-twinning initiation and evolution models are incorporated in the single crystal AE-CP finite element models for manifesting tension-compression asymmetry. In the next ascending scale, a polycrystalline microstructure of Ni-based superalloys is simulated using an augmented AE-CP FE model with micro-twinning. Statistically equivalent virtual polycrystals of the alloy CMSX-4 are created for simulations with the homogenized model. The results of simulations at each scale are compared with experimental data with good agreement.

S. Ghosh (✉) · S. Keshavarz · G. Weber
Departments of Civil and Mechanical Engineering,
Johns Hopkins University, Baltimore, MD, USA
e-mail: sghosh20@jhu.edu

S. Keshavarz
e-mail: skeshav1@jhu.edu

G. Weber
e-mail: george.r.weber@gmail.com

Keywords Ni-based superalloys · Homogenized crystal plasticity · Sub-grain gamma-gamma' · Homogenization · Microtwinning

1 Introduction

Ni-based superalloys are widely used in propulsion components of the aerospace industry such as turbine engine blades, disks, casings and liners. These alloys possess a desirable combination of high temperature strength and toughness, oxidation and creep resistance, and high temperature stability (McLean and Cahn 1996; Sugui et al. 2011), attributed to a sub-grain scale two-phase γ - γ' microstructure as shown in Fig. 1. The continuous γ -matrix phase has a face centered cubic (fcc) lattice structure, and is an alloy of Ni and Cr with a small fraction of other alloying elements. The precipitate phase γ' is a coherent ordered inter-metallic reinforcing phase of $L1_2$ crystal structure of Ni_3Al type, which appears as a distribution of cuboidal precipitates in a solid solution as shown in Fig. 1b.

The shape and size the γ' -phase depend largely on the cooling rate and internal stress gradients during the casting and heat treatment processes (Epishin et al. 2001; Pollock and Sammy 2006; Ignat et al. 1993). Slower cooling rates lead to the formation of bimodal populations of large (>500 nm) secondary and small (<50 nm) tertiary γ' precipitates, while higher cooling rates yield predominantly unimodal distribution of secondary precipitates (300–500 nm) (Pollock and Sammy 2006). The precipitates act as effective obstacles to the motion of dislocations by virtue of their shape and ordered structure. Depending on the temperature range and stress levels, dislocations either bypass or shear precipitates. The volume fraction of γ' precipitates, their mean size and spacing have a major effect on the mechanical properties of these superalloys (Viswanathan et al. 2005; van Sluytman and Pollock 2012). Micro-mechanisms controlling creep in polycrystalline Ni-based superalloys are quite complex (Viswanathan et al. 2005; Kovarik et al. 2009). At intermediate temperatures $650^\circ\text{C} \leq \theta \leq 800^\circ\text{C}$ and moderate stress levels ~ 650 MPa, dominant deformation mechanisms include anti-phase boundary (APB) shearing and micro-twinning. The probability of occurrence of a given mechanism depends on the load, crystal orientation and microstructural morphology. At lower temperatures ($\theta < 650^\circ\text{C}$) and higher stresses, creep is governed by different types of dislocation-based shearing processes, while at higher temperatures ($\theta > 800^\circ\text{C}$), the creep deformation is controlled by Orowan looping and cross-slip mechanisms (Unocic et al. 2011).

Deformation behavior under various loading and temperature conditions has been analyzed both for single crystal (Chatterjee et al. 2010; Cormier et al. 2011) and polycrystalline (Torster et al. 1997; Hong et al. 2009) Ni-based superalloys. Meso-scale modeling of the γ - γ' phases in single crystal Ni-base superalloys with unimodal precipitate sizes and periodic distributions has been conducted in Pollock and Argon (1992), Nouailhas and Cailletaud (1996), Ohashi et al. (1997), Busso et al. (2000) using phenomenological viscoplastic constitutive laws. Crystal plasticity finite element models (CPFEM) have been implemented to model creep and deformation

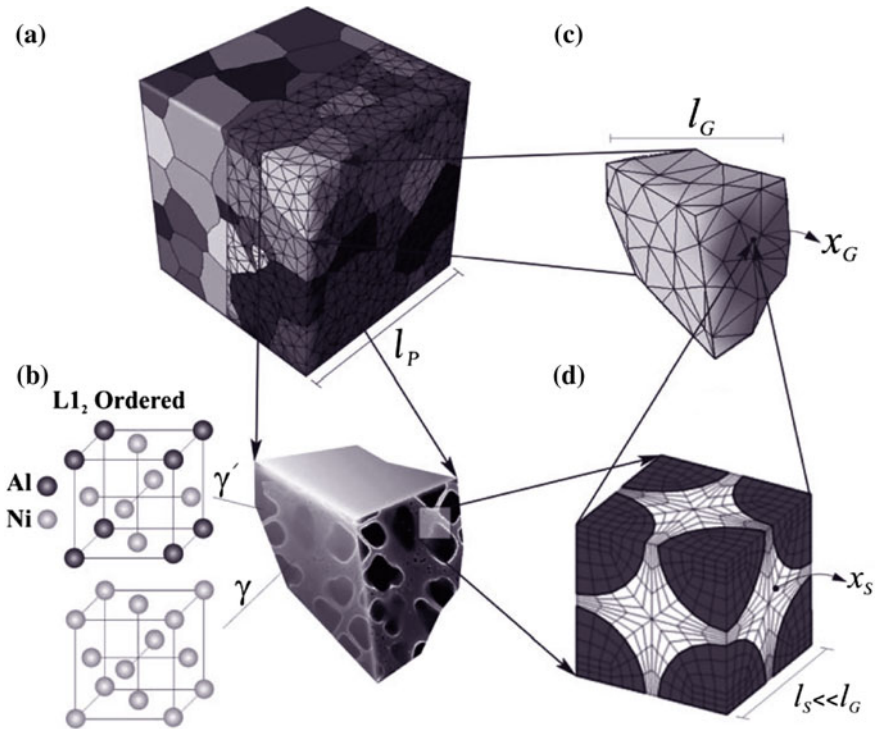


Fig. 1 Schematic representation of multiple scales in the development of a crystal plasticity finite element model for Ni-based superalloys: **a** polycrystalline microstructure showing the CPFEM mesh, **b** subgrain γ - γ' microstructure in a single grain, **c** discretized subgrain γ - γ' microstructural RVE, and **d** homogenized crystal plasticity FE model for a grain

response of single crystal and polycrystalline Ni-based super alloys in Dimiduk et al. (2005), Zambaldi et al. (2007), Roters et al. (2010). In these models, the behavior of single-crystal superalloys with high volume fraction of cuboidal precipitates has been simulated using a gradient-dependent plasticity model. Polycrystalline CPFEM simulations incorporate information on the orientation of grains obtained from EBSD images of the material microstructure. Phenomenological crystal plasticity models are based on the power law description (Asaro and Needleman 1985), or the thermally activated theory of plastic law (Kocks et al. 1975), which accounts for the rate and temperature sensitivity of plastic flow. The latter model has been shown to accurately model a large range of strain rates and temperatures. A limitation of these models is their lack of incorporation of the underlying microstructural characteristics at the sub-grain scale, e.g. γ - γ' volume fraction, shape of the γ' precipitates and the channel-width, which affect single crystal and polycrystalline behavior. Three scales are dominant when modeling polycrystalline behavior of Ni-based superalloys using CPFEM. They are:

- (i) Sub-grain scale, characterized by size of γ precipitates and their spacing or γ channel-width;
- (ii) Grain-scale of single crystals characterized by grain-boundary distance;
- (iii) Scale corresponding to representative volume elements of polycrystalline aggregates.

Crystal plasticity models should hierarchically incorporate information at each scale for generating constitutive models that can be implemented for microstructure-property relations, as well as microstructure design. It is computationally intractable to simulate the behavior of polycrystalline microstructures with explicit representation of the γ - γ' microstructure. In Busso et al. (2000) hardening parameters are expressed as functions of the average size of precipitates. Crystal plasticity models with implicit dependencies on grain and precipitate sizes and volume fraction, have been proposed in Fedelich (2002) by assuming random distribution of precipitate phases. Computational models involving hierarchical approaches for Ni-based superalloys have been proposed in Shenoy (2006), Shenoy et al. (2007). In Shenoy (2006), Shenoy et al. (2007) dislocation-density based crystal plasticity models for creep and fatigue have been developed using artificial neural network algorithm for rate-dependent internal state variable constitutive models, implicitly incorporating effects of averaged grain size, γ' volume fraction and size distribution. The dependence of strength and hardness on microstructural parameters is accommodated by fitting with experimental data.

It is evident that efficient, hierarchical crystal plasticity models with explicit relations to microstructural features are necessary for unraveling the dependence of mechanical behavior and properties on microstructure. The hierarchical framework may be accomplished for Ni-based superalloys through the homogenization of lower (sub-grain) scale response to develop higher (grain) scale constitutive relations. This is achieved by incorporating parametric forms of subgrain-scale morphological characteristics in grain-level constitutive relations. Ghosh and Anahid (2013) have implemented computational homogenization approaches using asymptotic expansion methods to develop reduced order homogenized constitutive models for continuum elasticity of polycrystalline metals, ductile fracture in heterogeneous metals (Ghosh et al. 2009; Ghosh 2011) and damage in composites (Ghosh 2011). These reduced order models with parametric forms, representing microstructural morphologies, have a huge efficiency advantage over explicit micromechanics models. In recent paper (Keshavarz and Ghosh 2013, 2014), the authors have developed a hierarchical model for Ni-based superalloys, where the subgrain-scale model response is homogenized to obtain a grain-scale crystal plasticity constitutive model.

In this chapter a sequence of steps is pursued to systematically create a hierarchical framework for realizing a homogenized crystal plasticity constitutive model for polycrystalline Ni-based superalloys. The crystal plasticity models account for monotonic loading only. A schematic view of the multi-scale problem, ranging from the sub-grain γ - γ' microstructure to the meso-scale polycrystalline ensemble is shown in Fig. 1. The first step involves development of crystal plasticity finite

element (CPFE) model of a sub-grain scale representative volume element or RVE, delineating explicit morphologies of the γ - γ' microstructure shown in Fig. 1c. The CPFE model incorporates a size-dependent dislocation density-based crystal plasticity model together with the mechanism considered in this study of anti-phase boundary (APB) shearing of γ' precipitates. Experimental studies have shown that mechanisms such as APB and micro-twinning are important at the temperature range ($650^\circ\text{C} < \theta < 800^\circ\text{C}$). In this temperature range, dislocation glide on the primary octahedral plane (111) are responsible for plastic deformation and hence cube slip systems on (001) plane are ignored in this study. Section 2 introduces the sub-grain scale dislocation density crystal plasticity constitutive laws with APB shearing of γ' precipitates. The next step involves the development of an activation energy-based crystal plasticity (AE-CP) model at the scale of single crystals, by homogenizing the sub-grain model response. The homogenized model incorporates the sub-grain morphology through critical morphological parameters (Keshavarz and Ghosh 2013, 2014). Section 3 provides a framework for the AE-CP model and homogenization. This section also introduces nucleation and evolution models for micro-twins in the grain. The final step involves augmentation of the homogenized AE-CP model, accounting for the effects of geometrically necessary dislocations or GND's, for analyzing polycrystalline microstructures. This is developed in Sect. 4.

2 Sub-Grain Scale Model γ - γ' for the Microstructural RVE

The two-phase binary Ni-based superalloy consists of a primary matrix γ phase (pure Ni) and a secondary intermetallic γ' (Ni_3Al) phase as shown in Fig. 1b. The primary phase is a solid solution with a face-centered cubic or fcc crystal structure, with four planes of inelastic slip corresponding to the $\{111\}$ family, i.e. $\{111\}[(111), (1\bar{1}\bar{1}), (\bar{1}\bar{1}1), (\bar{1}\bar{1}\bar{1})]$ in Miller indices. The secondary phase has an ordered crystalline lattice of type $L1_2$. Atoms of aluminum are placed at the vertices of the cubic cell, while atoms of Ni are located at centers of the faces as shown in Fig. 1b. For each of slip plane, there are three slip directions of $\langle 110 \rangle$ family along the Burgers vectors. Dislocations dissociate in the γ' -phase, leading to formation of an anti-phase boundary (APB). Ni-based superalloys exhibit anisotropic behavior in the plastic regime due to slip system interactions in the γ - γ' sub-grain microstructure. Plastic deformation is accommodated through crystallographic slip on discrete slip systems and by APB shearing of the γ' phase. A signed dislocation density-based crystal plasticity model proposed in Ma and Roters (2004), Ma et al. (2006) is implemented to model rate-dependent plastic behavior. These models incorporate evolution of statistically stored (SSD) and geometrically necessary dislocations (GND) due to the plastic deformation. Plastic strain gradient at the γ - γ' phase interface and grain boundaries lead to generation of GNDs. The micro-mechanical crystal plasticity model accommodates multiplication and annihilation of SSDs in the γ -channel and also accounts for APB shearing of γ' precipitates by matrix dislocations.

2.1 Dislocation Density-Based Crystal Plasticity Model

Crystal deformation results from a combination of the elastic stretching and rotation of the crystal lattice and plastic slip on different slip systems. Large-strain kinematics is accommodated through a multiplicative decomposition of the total deformation gradient \mathbf{F} into an incompressible, inelastic component \mathbf{F}^p associated with pure slip, and an elastic component \mathbf{F}^e that accounts for elastic stretching and rigid body rotations, expressed as:

$$\mathbf{F} = \mathbf{F}^e \mathbf{F}^p, \quad \text{s.t.} \quad \det \mathbf{F}^e > 1 \quad \text{and} \quad \det \mathbf{F}^p = 1 \quad (1)$$

Evolution of plastic deformation is expressed in terms of the plastic velocity gradient \mathbf{L}^p , the plastic shear rate on $\dot{\gamma}^\alpha$ the slip system α , Schmid tensor $\mathbf{s}_0^\alpha \equiv \mathbf{m}_0^\alpha \otimes \mathbf{n}_0^\alpha$ (in terms of the slip direction \mathbf{m}_0^α and slip plane normal \mathbf{n}_0^α in the reference configuration) as:

$$\mathbf{L}^p = \dot{\mathbf{F}}^p \mathbf{F}^{-p} = \sum_{\alpha=1}^N \dot{\gamma}^\alpha \mathbf{m}_0^\alpha \otimes \mathbf{n}_0^\alpha = \sum_{\alpha=1}^N \dot{\gamma}^\alpha \mathbf{s}_0^\alpha \quad (2)$$

The stress-strain relation invokes the second Piola-Kirchhoff stress \mathbf{S} and its work-conjugate Lagrange-Green strain tensor \mathbf{E}^e in the intermediate configuration as:

$$\mathbf{S} = \det(\mathbf{F}^e) \mathbf{F}^{e-1} \boldsymbol{\sigma} \mathbf{F}^{e-T} = \mathbf{C} : \mathbf{E}^e \quad \text{and} \quad \mathbf{E}^e \equiv \frac{1}{2} \left(\mathbf{F}^{eT} \mathbf{F}^e - \mathbf{I} \right) \quad (3)$$

\mathbf{I} is the identity tensor, \mathbf{C} is a fourth order anisotropic elasticity tensor and $\boldsymbol{\sigma}$ is the Cauchy stress tensor. The plastic shearing rate on a slip system is expressed using the Orowan equation as $\dot{\gamma}^\alpha = \rho_m^\alpha b v^\alpha$, where ρ_m^α is the density of mobile dislocations, b is the Burgers vector and v^α is the velocity of dislocations on the slip system α . The velocity of dislocations, which is a function of the applied shear stress τ^α , the passing stress $\tau_{\text{pass}}^\alpha$ in the slip system and other slip system resistances, is written as:

$$v^\alpha = \lambda \nu \exp \left[-\frac{Q_{\text{act}}}{k_B \theta} \left(1 - \frac{\langle |\tau^\alpha| - \tau_{\text{pass}}^\alpha \rangle}{\tau_{\text{cut}}^\alpha} \right) \right] \text{sgn}(\tau^\alpha), \quad (4)$$

where λ is the distance traversed by dislocations subject to the probability of overcoming barriers, ν is the oscillation frequency of dislocations, Q_{act} the activation free energy required to overcome the obstacles to slip without the aid of an applied shear stress, k_B is the Boltzmann's constant, θ is the absolute temperature and $\langle \bullet \rangle$ is the Macaulay bracket. Slip system resistances are represented in terms of the passing stress $\tau_{\text{pass}}^\alpha$ due to the interaction of mobile dislocations with other dislocations and their networks in the slip plane, and the cutting stress τ_{cut}^α due to the mobile

dislocations cutting the forest dislocations with density perpendicular to the slip plane. The stresses are expressed in Keshavarz and Ghosh (2013, 2014) as:

$$\tau_{\text{pass}}^{\alpha} = c_1 G b \sqrt{\rho_{\text{p}}^{\alpha} + \rho_{\text{m}}^{\alpha}}, \quad \text{and} \quad \tau_{\text{cut}}^{\alpha} = \frac{Q \sqrt{\rho_{\text{F}}^{\alpha}}}{c_2 b^2}, \quad (5)$$

where c_1 and c_2 are material constants and G is the shear modulus and Q is the activation energy. Contributions to the overall slip resistance are assumed to be due to both the density of immobile, statistically stored dislocations, and the vector field of geometrically necessary dislocation density $\rho_{\text{GND}}^{\alpha}$. The rate of evolution of statistically stored dislocation density $\dot{\rho}_{\text{SSD}}^{\alpha}$ has been identified in Ma et al. (2006) as the net effect of components due to lock formation, dipole formation, athermal annihilation and thermal annihilation as:

$$\dot{\rho}_{\text{SSD}}^{\alpha} = \dot{\rho}_{\text{SSD}_{\text{if}}}^{\alpha+} + \dot{\rho}_{\text{SSD}_{\text{df}}}^{\alpha+} + \dot{\rho}_{\text{SSD}_{\text{aa}}}^{\alpha-} + \dot{\rho}_{\text{SSD}_{\text{ta}}}^{\alpha-} \quad (6)$$

Superscripts $+/-$ correspond to multiplication and annihilation respectively. The rate increase due to lock formation, dipole formation, and decrease due to mechanisms of dislocation annihilation due to thermal and athermal annihilation are respectively given as (Ma and Roters 2004):

$$\begin{aligned} \dot{\rho}_{\text{SSD}_{\text{if}}}^{\alpha} &= \frac{c_3}{b} \sqrt{\rho_{\text{F}}^{\alpha}} \dot{\gamma}^{\alpha} \quad \text{and} \quad \dot{\rho}_{\text{SSD}_{\text{df}}}^{\alpha} = \frac{c_4}{b} \frac{\sqrt{3} G b}{16\pi(1-\nu)} (|\tau^{\alpha} - \tau_{\text{pass}}^{\alpha}|)^{-1} \rho_{\text{m}}^{\alpha} \dot{\gamma}^{\alpha}, \\ \dot{\rho}_{\text{SSD}_{\text{aa}}}^{\alpha} &= -c_5 \rho_{\text{SSD}}^{\alpha} \dot{\gamma}^{\alpha} \quad \text{and} \quad \dot{\rho}_{\text{SSD}_{\text{ta}}}^{\alpha} = -c_6 \frac{D_0 b^3}{k_{\text{B}} \theta} \exp\left(\frac{-Q_{\text{bulk}}}{k_{\text{B}} \theta}\right) (\rho_{\text{SSD}}^{\alpha})^2 |\tau^{\alpha}| \left(\frac{\dot{\gamma}^{\alpha}}{\dot{\gamma}_{\text{ref}}^{\alpha}}\right)^{c_7}, \end{aligned} \quad (7)$$

where c_3, c_4, c_5, c_6 and c_7 are material constants, D_0 is the diffusion co-efficient, Q_{bulk} is the activation energy for dislocation climb and $\dot{\gamma}_{\text{ref}}^{\alpha}$ is a reference shear rate. Each of the contributing components in Eq. (7) are functions of the slip rate $\dot{\gamma}^{\alpha}$, forest dislocation density, density of statistically stored dislocations, component of applied shear stress τ^{α} and the absolute temperature θ . Thus, a general form is proposed as $\dot{\rho}_{\text{SSD}}^{\alpha} = \dot{\rho}_{\text{SSD}}^{\alpha}(\dot{\gamma}^{\alpha}, \rho_{\text{F}}^{\alpha}, \tau^{\alpha}, \theta)$. The vector GND density rates depend on the gradient of plastic strain, written in terms of the Nye's dislocation tensor \mathbf{A} . The three scalar components, viz. screw, edge and normal components of the GND density have been derived in Ma et al. (2006). The material time derivative of the Nye's dislocation tensor is decomposed for individual slip systems, i.e.

$$\dot{\mathbf{A}} = \sum_{\alpha=1}^N \dot{\mathbf{A}}^{\alpha}$$

to derive the GND density components as:

$$\begin{aligned}\dot{\rho}_{\text{GND}_s}^\alpha &= \frac{1}{b} [\nabla_{\mathbf{x}} \times (\dot{\gamma}^\alpha \mathbf{F}_p^T \mathbf{n}^\alpha)] \cdot \mathbf{m}^\alpha, \\ \dot{\rho}_{\text{GND}_{\text{et}}}^\alpha &= \frac{1}{b} [\nabla_{\mathbf{x}} \times (\dot{\gamma}^\alpha \mathbf{F}_p^T \mathbf{n}^\alpha)] \cdot \mathbf{t}^\alpha, \\ \dot{\rho}_{\text{GND}_{\text{en}}}^\alpha &= \frac{1}{b} [\nabla_{\mathbf{x}} \times (\dot{\gamma}^\alpha \mathbf{F}_p^T \mathbf{n}^\alpha)] \cdot \mathbf{n}^\alpha,\end{aligned}\quad (8)$$

where \mathbf{m}^α , \mathbf{n}^α and $\mathbf{t}^\alpha = \mathbf{n}^\alpha \times \mathbf{m}^\alpha$, are unit vectors in the slip direction of the Burgers vector, normal to the slip plane α , and tangent to the edge dislocation direction respectively. Correspondingly, $\dot{\rho}_{\text{GND}_s}^\alpha$, $\dot{\rho}_{\text{GND}_{\text{et}}}^\alpha$ and $\dot{\rho}_{\text{GND}_{\text{en}}}^\alpha$ are the screw component and two edge components parallel to \mathbf{n}^α and \mathbf{t}^α respectively. $\nabla_{\mathbf{x}}$ is the gradient operator in the material coordinate system. The forest and parallel dislocation densities are now written as functions of the SSDs and GNDs (Ma and Roters 2004) with an interaction strength coefficient between different slip systems (Arsenlis and Parks 2002) as:

$$\begin{aligned}\rho_{\text{F}}^\alpha &= \sum_{\beta=1}^N \chi^{\alpha\beta} \left[\rho_{\text{SSD}}^\beta |\cos(\mathbf{n}^\alpha, \mathbf{t}^\beta)| + \rho_{\text{GND}_s}^\beta |\cos(\mathbf{n}^\alpha, \mathbf{m}^\beta)| \right. \\ &\quad \left. + \rho_{\text{GND}_{\text{et}}}^\beta |\cos(\mathbf{n}^\alpha, \mathbf{t}^\beta)| + \rho_{\text{GND}_{\text{en}}}^\beta |\cos(\mathbf{n}^\alpha, \mathbf{n}^\beta)| \right], \\ \rho_{\text{P}}^\alpha &= \sum_{\beta=1}^N \chi^{\alpha\beta} \left[\rho_{\text{SSD}}^\beta |\sin(\mathbf{n}^\alpha, \mathbf{t}^\beta)| + \rho_{\text{GND}_s}^\beta |\sin(\mathbf{n}^\alpha, \mathbf{m}^\beta)| \right. \\ &\quad \left. + \rho_{\text{GND}_{\text{et}}}^\beta |\sin(\mathbf{n}^\alpha, \mathbf{t}^\beta)| + \rho_{\text{GND}_{\text{en}}}^\beta |\sin(\mathbf{n}^\alpha, \mathbf{n}^\beta)| \right],\end{aligned}\quad (9)$$

which evolve with the SSDs and GNDs due to plastic deformation and hardening mechanisms. The density of mobile dislocations ρ_{m}^α is computed as a function of forest and parallel dislocation density and the temperature as (Ma and Roters 2004):

$$\rho_{\text{m}}^\alpha = \frac{2k_{\text{B}}\theta\sqrt{\rho_{\text{F}}^\alpha\rho_{\text{P}}^\alpha}}{c_1c_2Gb^3}\quad (10)$$

2.2 Criteria for γ' Phase Anti-phase Boundary (APB) Shearing

Matrix dislocations in the disordered fcc matrix γ phase cannot enter the ordered γ' phase, characterized by crystalline lattice structure $L1_2$, initially. However, the matrix dislocations can form super-dislocations at the γ - γ' interface and enter the γ' phase through the mechanism of anti-phase boundary or APB shearing upon reaching a

critical condition, as shown by TEM analysis in Viswanathan et al. (2005). The γ' phase APB shearing is assumed to take place when the following conditions are met at the interface:

- (i) $\tau^\alpha > \tau_c$ (resolved shear stress on a slip system exceeds a critical value),
 - (ii) $\rho_m^\alpha > \rho_c$ (dislocation density exceeds a critical value)
- (11)

The corresponding flow rule for the γ' phase is expressed as:

$$\dot{\gamma}^\alpha = H(\rho_m^\alpha - \rho_c) \rho_m^\alpha b v^\alpha, \quad (12)$$

where

$$v^\alpha = \lambda v \exp \left[-\frac{Q}{K_B \theta} \left(1 - \frac{\langle \tau^\alpha - \tau_{\text{pass}}^\alpha \rangle H(\tau^\alpha - \tau_c)}{\tau_{\text{cut}}^\alpha} \right) \right] \text{sgn}(\tau^\alpha)$$

with $H(\rho_m^\alpha - \rho_c)$ and $H(\tau^\alpha - \tau_c)$ are Heaviside functions, τ_c is the critical resolved shear stress and ρ_c is the critical density at the interface. Implementation of the constitutive model in a CPFEM code is given in Keshavarz and Ghosh (2013, 2014).

2.3 Parameter Calibration and Validation of the Constitutive Law

Selected constitutive parameters in the crystal plasticity model for γ - γ' phase Ni-based superalloys with APB shearing have been calibrated for the alloy CMSX-4 (Ni, Cr-6.4, Co-9.3, Al-5.45, Ta-6.3, W-6.2, Ti-0.9, Mo-0.5, Re-2.8 in wt%) in Keshavarz and Ghosh (2013, 2014). Calibration of constants c_1 and c_2 in Eq. (5) and constants c_3, c_4, c_5, c_6, c_7 in Eq. (7) are done using experimental data from tensile constant strain-rate tests in Knowles and Gunturi (2002). The critical shear stress τ_c and the threshold dislocation density ρ_c in Eq. (11) are calibrated from the tension creep experimental data in Fleury et al. (1996). These are listed in Table 1. The symmetric, elastic stiffness tensor $C_{\alpha\beta} = C_{\beta\alpha}$, ($\alpha = 1, \dots, 6$, $\beta = 1, \dots, 6$) is considered to be isotropic for both phases, for which the non-zero components are obtained from Kayser and Stassis (1981). In addition, the Burgers vector b and the activation energy Q are handbook values, given in Table 2.

Table 1 Experimentally calibrated parameters for the sub-grain scale crystal plasticity model

Constant	c_1	c_2	c_3	c_4	c_5	c_6	c_7	τ_c	ρ_c
Value	4.0	0.8	1×10^{-3}	1×10^{-4}	10.0	10.0	0.3	110 MPa	1×10^{11}

Table 2 Stiffness and crystal plasticity parameters for the sub-grain model

Phase	$C_{11} = C_{22} = C_{33}$	$C_{44} = C_{55} = C_{66}$	$C_{12} = C_{13} = C_{23}$	b (nm)	Q (J)
γ	201.7 GPa	104.5 GPa	134.4 GPa	2.49	6.5×10^{-19}
γ'	229.7 GPa	110.1 GPa	153.2 GPa	2.49	6.5×10^{-19}

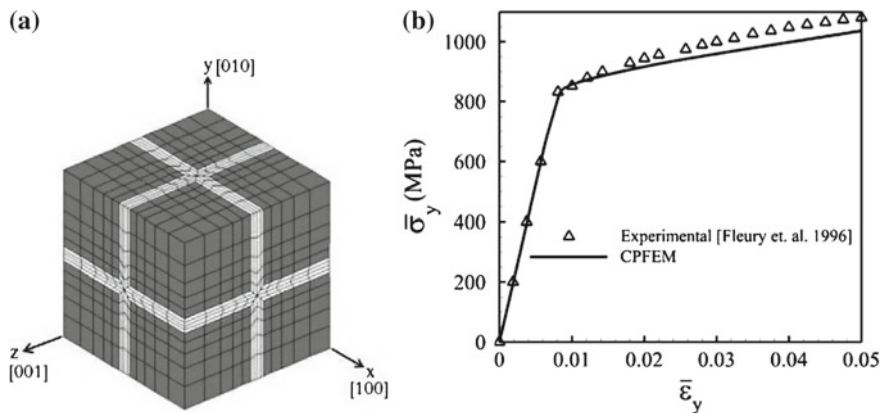


Fig. 2 Comparing CPFEM results with those for tension experiments under a constant strain rate 0.0001 s^{-1} : **a** FEM mesh for cubic precipitates with the volume fraction of 70 % and edge length $x = 0.5 \mu\text{m}$, **b** volume-averaged Cauchy stress-true (logarithmic) strain response

To validate the crystal plasticity constitutive relations with APB shearing, the CPFEM analyses results are compared with experimental data in Knowles and Gunturi (2002), Fleury et al. (1996). The RVE is for a regular array of cubic precipitates with a 70% volume fraction, as shown in Fig. 2a. Its dimensions are $0.5 \mu\text{m} \times 0.5 \mu\text{m} \times 0.5 \mu\text{m}$. The edge length of cubic γ' particles, allocated symmetrically at the eight corners, is $0.45 \mu\text{m}$. The CPFEM model of the microstructural RVE is discretized into 2,200, 8-noded brick elements using selective reduced integration. CPFEM simulations are conducted with an applied strain-rate of 0.0001 s^{-1} in the y -direction at a temperature of $800 \text{ }^\circ\text{C}$. A tensile constant strain-rate is applied to the top y -surface in Fig. 2a, while rigid body modes are suppressed by applying boundary conditions on the bottom y -surface as: $u_y = 0$ on all nodes $u_x = 0$ on nodes on the line $x = 0.25 \mu\text{m}$ and $u_z = 0$ on nodes on the line $z = 0.25 \mu\text{m}$.

The volume-averaged Cauchy stresses

$$\bar{\sigma} = \frac{1}{\Omega_{\text{RVE}}} \int_{\Omega_{\text{RVE}}} \sigma(x, t) dV$$

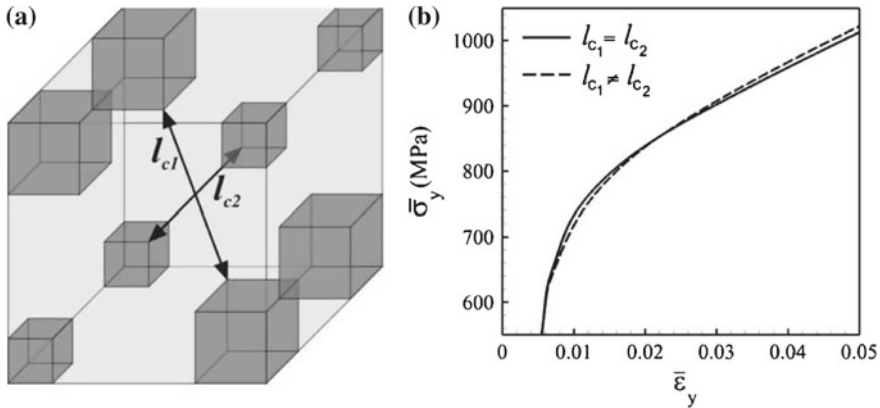


Fig. 3 **a** RVE with non-symmetric diagonal channel widths, and **b** comparison of Cauchy stress-true strain response under tension constant strain rate for cubic precipitates with the same volume fraction (35 %) and RVE size (0.24 μm)

over the RVE Ω_{RVE} and the averaged true (logarithmic) strain expressed as:

$$\bar{\epsilon} = \ln \left(\frac{l_y}{l_{0y}} \right) = \ln \left(\frac{l_{0y} + \bar{u}_y}{l_{0y}} \right)$$

are computed for the RVE where l_{0y} and \bar{u}_y are respectively the initial dimension and the y -direction displacement of the top surface of the RVE. The volume-averaged stress-strain response is compared with experimental data from Fleury et al. (1996) in Fig. 2b. In general there is a good agreement between the experimental and model predictions. The γ -channel-width l_c and shapes can vary significantly in the actual alloy. To explore the effect of γ channel-width, two microstructures are constructed for comparison as shown in Fig. 3a; one with non-symmetrical ($l_{c1} \neq l_{c2}$) γ' channel-width $l_{c1} = 0.069 \mu\text{m}$ and $l_{c2} = 0.139 \mu\text{m}$, and the other with symmetric channel-width, i.e. $l_{c1} = l_{c2} = 0.122 \mu\text{m}$. The volume fraction of cubic γ' precipitates in both the microstructures is 35 %. Simulations are conducted for a constant tensile strain-rate of $5 \times 10^{-5} \text{s}^{-1}$ in the y -direction, corresponding to the [010] slip direction. The stress-strain response in Fig. 3b exhibits some difference in plastic response, with higher hardness for the non-symmetrical RVE.

2.4 Effect of γ' APB Shearing and Precipitate Shape on the Overall Response

Figure 4 plots the volume-averaged stress-strain response by CPFEM simulations for the RVE in the previous section, with and without the activation of APB shearing of γ' precipitates. The figure also shows the response for only the γ' phase. In the absence of the phase, the overall yield strength as well the hardening are considerably

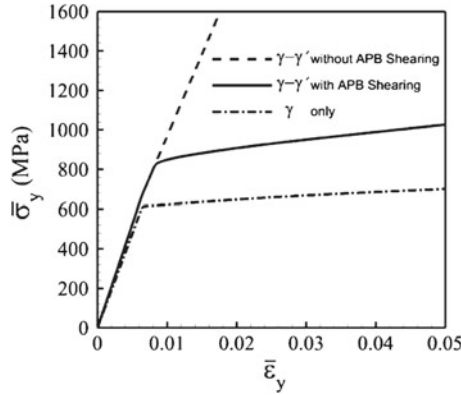


Fig. 4 The effect of activation of APB shearing on stress strain curve under tension constant strain rate at 800 °C

low. The alloy gets its high yield stress and hardening behavior from the γ' phase in the matrix. The stress-strain response is rather stiff if the APB shearing mechanism is not activated in the high volume fraction ($\sim 70\%$) γ' phase that has zero initial dislocation density. Accumulation of dislocation density at the γ - γ' phase interface with high stresses leads to APB shearing, with super-dislocations entering the γ -phase and softening the overall response. Accurate representation of the stress-strain response requires incorporation of APB shearing criteria and associated relations for γ' -phase plastic flow.

Three different stages of deformation are marked by points in the stress-strain response of Fig. 5a. For deformation up to state-point 1, both γ and γ' phases behave elastically and there is no plastic deformation in the domain. From state 1 to state 2, the γ -phase experiences plastic deformation and SSDs start to evolve, with plastic strain gradient building especially near the γ - γ' interfaces. To preserve lattice continuity, the GNDs must evolve causing an increase in mobile dislocation density ρ_m . The distribution of ρ_m along the x -axis at state 2 is plotted in Fig. 5b. There is little difference in ρ_m for the states 1 and 2 in the γ' phase. However this difference is significant in the γ -channel due to evolution of GNDs. In the post APB shearing stage, the γ' -phase experiences plastic deformation with considerable rise in ρ_m . Figure 5c, d shows the ρ_m distribution at states 2 and 3. At state 2, corresponding to the activation of APB shearing, the initial value of ρ_m does not change in the γ' phase. Beyond this state, ρ_m starts to evolve and reaches the distribution in Fig. 5d at 5% strain.

The effect of precipitate shape is explored through another RVE containing a 40% volume fraction of spherical precipitates as shown in Fig. 6a. The channel-width for spherical precipitates is the same as for cubic at the boundary. This corresponds to a precipitate radial edge-length of 0.45 μm . All other conditions are the same as in the constant strain-rate problem of the previous example. The microstructural RVE

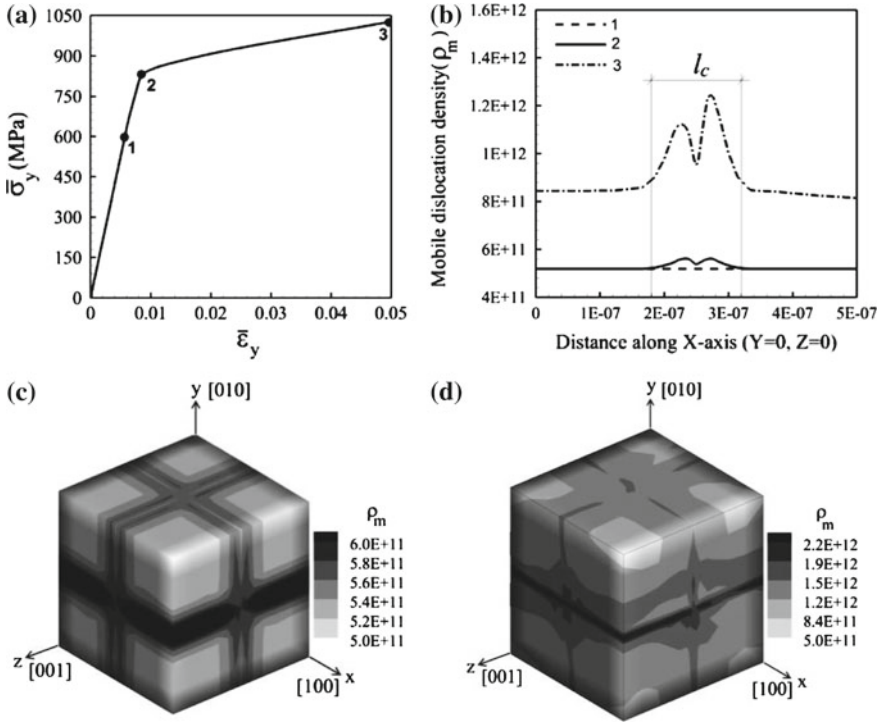


Fig. 5 Effect of APB shearing for RVE with cubic γ' precipitates: **a** stress-strain response with three state-markers, **b** distribution of mobile dislocation density along x -axis for the three states, **c**, **d** mobile dislocation density contour plots at states 2 and 3 respectively

model is discretized into 1,512, 8-noded brick elements. The same state-markers are inserted in stress-strain response plot of Fig. 6b. The distributions of the mobile dislocation density at states 1, 2 and 3 along the x -axis are plotted in Fig. 6c, while Fig. 6d shows the ρ_m distribution at state 3. Responses for the cubic and spherical precipitates are quite different between the states 1 and 2. For the cubic shape, the transition of plastic flow from the γ to γ' phase is sharp. Plastic deformation in the γ channel does not affect the response much, as the channel width is generally small as observed in Fig. 2a. This situation is different for the spherical precipitates where after state 1, nucleated dislocations in the γ phase rapidly evolve in the channel where the round interface between γ and γ' provides more spaces to accommodate higher dislocation densities.

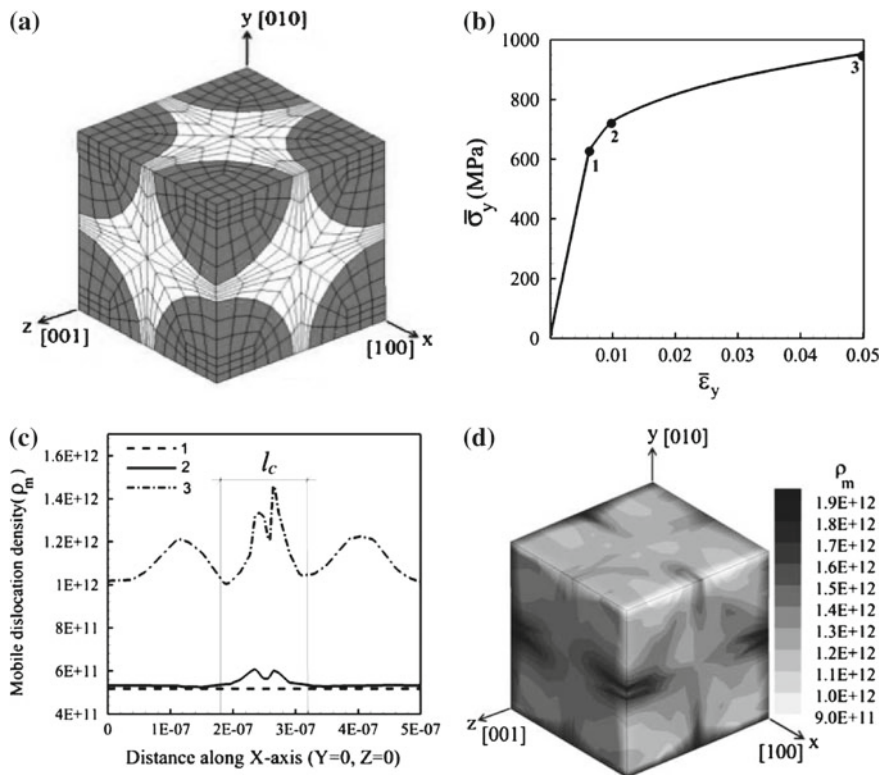


Fig. 6 Effect of APB shearing for RVE with spherical γ' precipitates: **a** CPFEM mesh, **b** stress-strain response with three state-markers, **c** distribution of mobile dislocation density along x -axis for the three states, **d** mobile dislocation density contour plot at state 3

3 Grain-Scale Crystal Plasticity Model with Microtwinning

3.1 Homogenized Activation Energy-Based Crystal Plasticity (AE-CP) Model

Results of simulation of the sub-grain RVE model, discussed in Sect. 2, are homogenized to generate constitutive parameters for a grain-scale activation energy-based crystal plasticity (AE-CP) model. Determination of parameters is assumed to be governed by the Hill-Mandel principle of macro-homogeneity (Hill 1984) expressed as:

$$\langle \mathbf{S} \rangle : \langle \dot{\mathbf{E}} \rangle = \frac{1}{\Omega_{\text{RVE}}} \int_{\text{RVE}} \mathbf{S} dV : \frac{1}{\Omega_{\text{RVE}}} \int_{\text{RVE}} \dot{\mathbf{E}} dV = \frac{1}{\Omega_{\text{RVE}}} \int_{\text{RVE}} \mathbf{S} : \dot{\mathbf{E}} dV = \langle \mathbf{S} : \dot{\mathbf{E}} \rangle \quad (13)$$

Here \mathbf{S} and $\dot{\mathbf{E}}$ correspond to the second Piola-Kirchhoff stress and the Lagrangian strain rate respectively and the symbol $\langle \bullet \rangle$ corresponds to volume averaging over the RVE domain. The constitutive parameters are formulated in terms of morphological variables and are calibrated by computational homogenization.

The proposed grain-scale, homogenized crystal plasticity model for fcc Ni-based superalloys follows the framework of activation energy-based crystal plasticity (AE-CP) models (Kocks et al. 1975; Frost and Ashby 1982; Xie et al. 2004). The homogenized constitutive model incorporates an evolving thermal shear resistance as well as an athermal shear resistance due to plastic deformation. For a slip system, the plastic shearing rate follows from the Orowan equation as:

$$\dot{\gamma}^\alpha = \begin{cases} 0 & \text{if } \tau_{\text{eff}}^\alpha \leq 0, \\ \dot{\gamma}_*^\alpha \exp \left\{ -\frac{Q}{k_B \theta} \left[1 - \left(\frac{\tau_{\text{eff}}^\alpha}{s_*^\alpha} \right)^p \right]^q \right\} \text{sgn}(\tau^\alpha) & \text{if } 0 \leq \tau_{\text{eff}}^\alpha \leq s_*^\alpha \end{cases} \quad (14)$$

Here Q is the activation energy barrier, $k_B (= 1.3807 \times 10^{-23} \text{ J} \cdot \text{K}^{-1})$ is the Boltzmann's constant, θ is the temperature and exponents p, q are material constants. For the slip system α , $\dot{\gamma}_*^\alpha$ is a reference strain-rate, $\tau_{\text{eff}}^\alpha (= |\tau^\alpha| - s_a^\alpha)$ is the effective resolved shear stress. The temperature-dependent critical slip resistance s , (>0) is assumed to be comprised of a thermally activated obstacle to slip s_*^α and a part due to the athermal obstacles s_a^α . The athermal and thermal shear resistances s_a^α and s_*^α correspond to the passing and cutting stress barriers respectively. The difference between the athermal shear resistance and the resolved shear stress is the driving force for dislocation motion on the slip system α . $\dot{\gamma}_*^\alpha$ can evolve with the activation of APB shearing, when the γ -phase experiences plastic deformation with increasing dislocation density, especially near the γ - γ' interfaces. This deformation effect can be significant for some γ' precipitate shapes, e.g. spherical, but not as strong for cuboidal. An yield point phenomenon is applied to introduce a morphology dependent functional form for $\dot{\gamma}_*^\alpha$ (Keshavarz and Ghosh 2013, 2014) as:

$$\dot{\gamma}_*^\alpha = H(\bar{\varepsilon}_p - l_p) \dot{\gamma}_0^\alpha \left(\frac{\tanh(k) + \tanh(kl_p)}{10(\tanh[k_* (\bar{\varepsilon}_p - l_p)] + \tanh(kl_p))} - 1 \right) + \dot{\gamma}_0, \quad (15)$$

where H is the Heaviside step function, $\dot{\gamma}_0$ corresponds to the initial strain rate and l_p, k, k_* are material constants. In this work $l_p = 10^{-10}$, k and k_* are derived in terms of morphological parameters. The equivalent plastic strain

$$\bar{\varepsilon}_p = \sqrt{\frac{2}{3} \varepsilon_{ij}^p \varepsilon_{ij}^p}$$

is defined in terms of the Lagrangian plastic strain

$$\varepsilon_{ij}^p = \frac{1}{2} (F_{ij}^{pT} F_{ij}^p - \delta_{ij})$$

Consequently, evolution laws for thermal and athermal shear resistances, contributing to the overall slip resistance s^α , are proposed in terms of the plastic strain rate. The thermal shear resistance, accounting for forest dislocations normal to the slip plane and the athermal shear resistance reflecting the effect of parallel dislocations in the slip direction \mathbf{m}^α , are expressed as:

$$\dot{s}_a^\alpha = \sum_{\beta=1}^n h_\alpha^{\alpha\beta} |\dot{\gamma}^\beta \sin(\mathbf{n}^\alpha, \mathbf{t}^\beta)|, \quad \dot{s}_*^\alpha = \sum_{\beta=1}^n h_*^{\alpha\beta} |\dot{\gamma}^\beta \cos(\mathbf{n}^\alpha, \mathbf{t}^\beta)|, \quad (16)$$

where \mathbf{n}^α is slip-plane normal, $\mathbf{t}^\alpha = \mathbf{m}^\alpha \times \mathbf{n}^\alpha$, and the total shear resistance is

$$\dot{s}^\alpha = \sqrt{(\dot{s}_a^\alpha)^2 + (\dot{s}_*^\alpha)^2}$$

The initial values of the athermal and thermal shear resistances are respectively \dot{s}_{a0}^α , \dot{s}_{*0}^α . For convenience, coefficients accounting for the interactions between slip systems are taken to be the same i.e. $h_a^{\alpha\beta} = h_*^{\alpha\beta} = h^{\alpha\beta}$. Each component of $h^{\alpha\beta}$ is the deformation resistance on slip system α due to shearing on slip system β . It describes both self and latent hardening as:

$$h^{\alpha\beta} = q^{\alpha\beta} h^\beta, \quad \text{where } h^\beta = \left[h^0 \left(1 - \frac{s^\beta}{s_{\text{sat}}^\beta} \right)^r \right] \text{sign} \left(1 - \frac{s^\beta}{s_{\text{sat}}^\beta} \right) \quad (17)$$

The parameter h^β denotes the resistance dependent self-hardening rate, s_{sat}^β is the saturation value of reference shear stress and r is a constant exponent. The coefficient $q^{\alpha\beta} = q + (1 - q)\delta^{\alpha\beta}$, where q is a latent-hardening parameter chosen as 1.4.

3.1.1 Sub-grain Morphological Parameters

Three characteristic parameters representing the sub-grain microstructural morphology in Fig. 1c, are delineated as:

- (i) γ' volume fraction ν^p ,
- (ii) γ' shape factor n and,
- (iii) minimum limiting channel-width l_c between γ' precipitates.

The volume fraction is expressed as the ratio of the precipitate volume to the RVE volume, i.e.

$$\nu^p = \frac{\Omega_{\gamma'}}{\Omega_{\text{RVE}}}$$

The shape factor is described in terms of the exponent of a generalized ellipsoid:

$$\left(\frac{x}{a} \right)^n + \left(\frac{y}{b} \right)^n + \left(\frac{z}{c} \right)^n = 1,$$

where a, b, c are the dimensions of the three principal axes and n is shape exponent. Here, $a = b = c$ is assumed to represent equiaxed precipitates. A value $n = 2$ corresponds to a sphere while $n \rightarrow \infty$ corresponds to a cube. To avoid a singular value of n , a transformed shape factor $n_1 = \tan^{-1}(n)$ is used in the parameterization.

The effect of these morphological parameters on the volume-averaged stress-strain response of the RVE using the sub-grain dislocation density CPFEM simulations is examined and depicted in Fig. 7. For each simulation conducted at 0.0001s^{-1} and $800\text{ }^\circ\text{C}$, one of the parameters is varied, while the other two are held constant. Variables considered are

- (i) cubic precipitates of volume fractions 75.13 and 57.87 %,
- (ii) shape factors $n = 2.0$, and ∞ and
- (iii) channel-width $l_c = 0.29\text{ }\mu\text{m}$ and $l_c = 0.58\text{ }\mu\text{m}$ for cubic precipitates of 29.63 % volume fraction.

Results in Fig. 7 shows that with increasing volume fraction, the post-yield plastic response does not change too much even though the yield strength increases. The

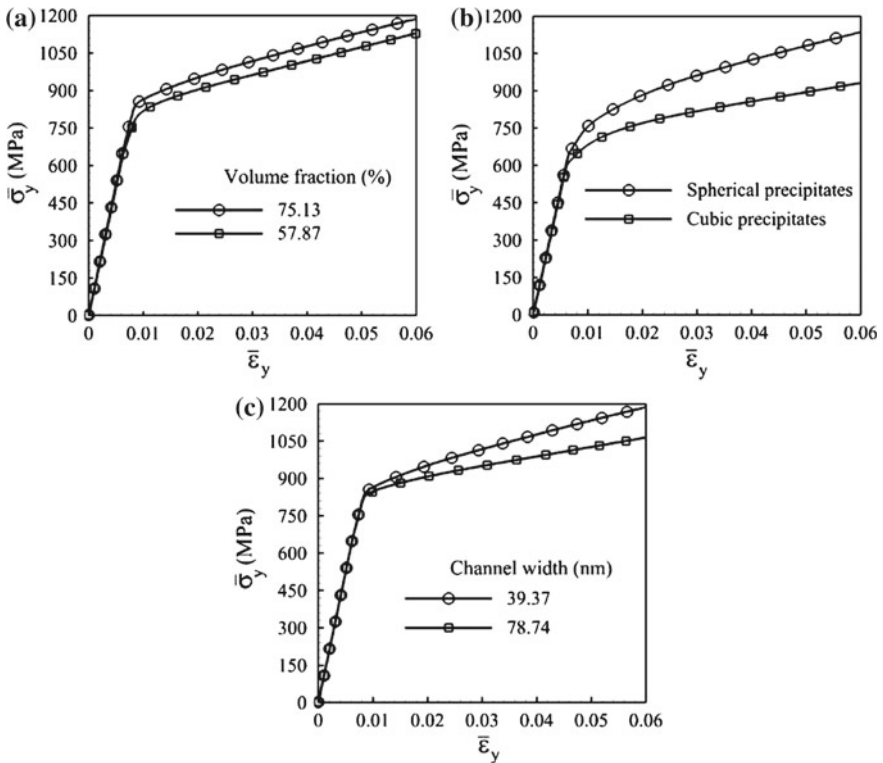


Fig. 7 Effect of γ' precipitate: **a** volume fraction, **b** shape and **c** channel width for cubic precipitates with 29.63 % volume fraction, on the stress-strain response under constant tensile strain-rate of 0.0001 s^{-1} at a temperature of $800\text{ }^\circ\text{C}$

yield strength changes and the plastic response diverges with increasing strain for different shapes. The plastic response changes with increasing channel-width, while the yield strength decreases only slightly.

Plastic slip and hardening parameters in the grain-scale AE-CP model are functions of the SSDs and GNDs. SSDs do not generally change much with morphological variables i.e. they are size independent, but GNDs can vary significantly with precipitate shape and size. Forest and parallel components of dislocation densities may be expressed as:

$$\rho_F(\rho_{SSD}, \rho_{GND}) = \rho_F(\gamma^\alpha, \nabla\gamma^\alpha), \quad \rho_P(\rho_{SSD}, \rho_{GND}) = \rho_P(\gamma^\alpha, \nabla\gamma^\alpha) \quad (18)$$

Crystal plasticity hardening parameters are functions of the plastic slip γ^α due to SSD's. Morphological parameters should also be incorporated in these functions to account for the effect of GNDs or gradient of plastic shear strain $\nabla\gamma^\alpha$. Sensitivity analyses indicate that the initial thermal shear resistance and its rate, the reference slip-rate $\dot{\gamma}_*$ and the saturation shear stress s_{sat}^α are functions of the morphology. Thus, in Eqs. (19)–(21) parameters $s_*^\alpha(n_1, \nu_p, l_c)$, $\dot{\gamma}_*(n_1, \nu_p, l_c)$, $s_{sat}^\alpha(n_1, \nu_p, l_c)$, are derived in terms of morphological parameters as well as $(\gamma^\alpha, \nabla\gamma^\alpha)$ as:

$$\begin{aligned} s_*^\alpha(n_1, \nu_p, l_c) &= \sum_{\beta=1}^n h^{\alpha\beta}(n_1, \nu_p, l_c) |\dot{\gamma}^\beta \cos(\mathbf{n}^\alpha, \mathbf{t}^\beta)| \\ &= \sum_{\beta=1}^n \left[h_0 \left(1 - \frac{s^\beta}{s_{sat}^\beta(n_1, \nu_p, l_c)} \right)^r \right] \operatorname{sgn} \left(1 - \frac{s^\beta}{s_{sat}^\beta} \right) |\dot{\gamma}^\beta \cos(\mathbf{n}^\alpha, \mathbf{t}^\beta)|, \\ \dot{\gamma}_*(n_1, \nu_p, l_c) &= H(\varepsilon_p - l_p) \dot{\gamma}_0 \left\{ \frac{\tanh[k(n_1, \nu_p, l_c)] + \tanh[k(n_1, \nu_p, l_c)l_p]}{10 \tanh[k_*(n_1, \nu_p, l_c)] + \tanh[k(n_1, \nu_p, l_c)l_p]} - 1 \right\} \\ &\quad + \dot{\gamma}_0 \end{aligned} \quad (19)$$

The initial strain rate $\dot{\gamma}_0$ and hardening parameter h_0 are insensitive to the morphology.

3.1.2 Calibrating the Grain Scale AE-CP Model Parameters

Equations (14)–(17), (19) contain a number of material parameters, some of which vary with the morphology while others are independently constant. The constant material parameters that should be experimentally calibrated for the AE-CP model are the activation energy Q and exponents p, q in Eq. (14), $\dot{\gamma}_0$ in Eq. (15) and hardening parameter h_0 and exponent r in Eq. (16). These parameters have been calibrated in Keshavarz and Ghosh (2013, 2014) for single crystal CMSX-4 using experimental data from tensile constant strain-rate and creep tests in Knowles and Gunturi (2002), Fleury et al. (1996). The parameters are listed in Table 3. Subsequently, the morphology-dependent AE-CP parameters $s_{*0}^\alpha(n_1, \nu_p, l_c)$,

Table 3 Experimentally calibrated constant material parameters for the grain scale AE-CP model

Parameters	$Q(J)$	p	q	$\dot{\gamma}_0(s^{-1})$	$h_0(MPa)$	r
Value	6.5×10^{-12}	0.78	1.15	5.0×10^7	1,300	1.115

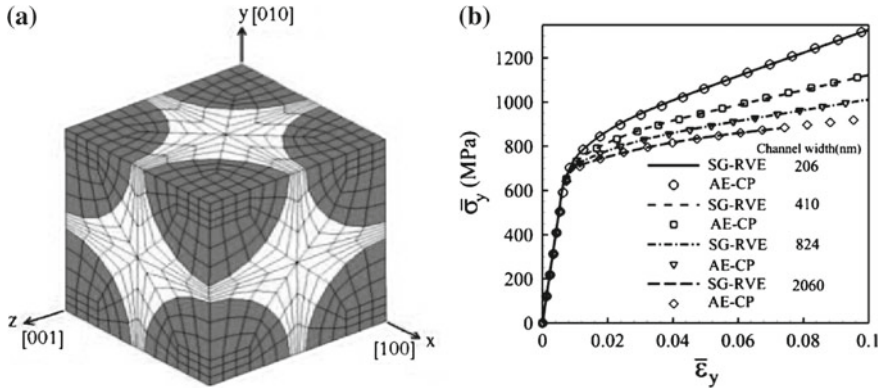


Fig. 8 Calibration of morphology-dependent homogenized crystal plasticity parameters in the grain-scale activation energy-based crystal plasticity (AE-CP) model: **a** FEM model of the sub-grain RVE (SG-RVE) with spherical precipitates of volume fraction 39.16%, and **b** stress-strain response by the SG-RVE and AE-CP FE models

$k_*(n_1, \nu_p, l_c)$, $k(n_1, \nu_p, l_c)$ and $s_{sat}^\beta(n_1, \nu_p, l_c)$ in Eq. (19) are calibrated from the simulated volume-averaged response of the sub-grain RVE model. These simulations are conducted under a constant strain-rate of $0.0001 s^{-1}$ in the [010] direction at $800^\circ C$. The calibration process has involved 37 different RVE microstructures. An example of the sub-grain RVE, FE model containing spherical precipitates of 39.16% volume fraction and different channel-widths, discretized into 8-noded brick elements, is depicted in Fig. 8a. In Fig. 8b, the homogenized AE-CP model parameters are calibrated with the averaged stress-strain responses from the RVE model.

3.1.3 Functional Forms of Homogenized AE-CP Constitutive Parameters

Functional forms of the constitutive parameters $s_{*0}^\alpha(n_1, \nu_p, l_c)$, $k_*(n_1, \nu_p, l_c)$, $k(n_1, \nu_p, l_c)$ and $s_{sat}^\beta(n_1, \nu_p, l_c)$ in Eq. (19) are generated for representing the effect of morphology on the single crystal behavior. To derive these functional forms by computational homogenization, a large number of sub-grain RVE model simulations with varying volume fractions, channel-widths and shapes are conducted (Keshavarz and Ghosh 2013, 2014). These set of simulations yield the following functional forms, where the coefficients are determined by solving a set of least square minimization problems:

$$\begin{aligned}
 1. \quad s_{*0}^\alpha(n_1, \nu_p, l_c) &= a_1(n_1, \nu_p) + \frac{b_1(n_1, \nu_p)}{\sqrt{l_c}} \\
 &= 1039 + 559\nu_p - 99n_1 - 136\nu_p n_1 \\
 &\quad + \frac{-0.1 + 89\nu_p + 53n_1 - 90\nu_p n_1}{\sqrt{l_c}} \quad (20)
 \end{aligned}$$

$$\begin{aligned}
 2. \quad s_{\text{sat}}^\alpha(n_1, \nu_p, l_c) &= a_2(n_1, \nu_p) + \frac{b_2(n_1, \nu_p)}{l_c} \\
 &= 3185 - 8905\nu_p - 1648n_1 + 6680\nu_p n_1 \\
 &\quad + \frac{-0.21 + 5008\nu_p + 363n_1 - 3599\nu_p n_1}{l_c} \quad (21)
 \end{aligned}$$

$$\begin{aligned}
 3. \quad k_*(n_1, \nu_p, l_c) &= 65 - 7500\nu_p + 33n_1 - 2700l_c + 12768\nu_p n_1 \\
 &\quad - 23120\nu_p l_c + 4080n_1 l_c - 19847\nu_p n_1 l_c \quad (22)
 \end{aligned}$$

$$\begin{aligned}
 4. \quad k(n_1, \nu_p, l_c) &= a_3(n_1, \nu_p) + \frac{b_3(n_1, \nu_p)}{\sqrt{l_c}} \\
 &= 5.5 - 327.6\nu_p + 31.5n_1 + 221.4\nu_p n_1 \\
 &\quad + \frac{0.14 + 281.2\nu_p - 2.44n_1 - 176.5\nu_p n_1}{\sqrt{l_c}} \quad (23)
 \end{aligned}$$

The explicit dependence on channel-width l_c reflects the size-effect due to the presence of GNDs in the sub-grain dislocation density CP model. In Eqs. (20)–(23) the unit of l_c is μm , while the units of initial thermal resistance and saturation shear resistance in Eqs. (20), (21) are MPa.

3.1.4 Validation of the Homogenized AE-CP Model

Two sets of validation tests are conducted for the homogenized AE-CP constitutive model. In the first set, the results of a single grain, crystal plasticity FEM analysis with the calibrated homogenized AE-CP constitutive model are compared with the averaged response of a sub-grain RVE (SG-RVE) analysis. Three cases, corresponding to different microstructures, are considered for simulation. These are:

- Case 1: $n = 10$, $\nu_p = 44\%$, $l_c = 0.135 \mu\text{m}$;
- Case 2: $n = 1.5$, $\nu_p = 22\%$, $l_c = 0.260 \mu\text{m}$;
- Case 3: $n = \infty$, $\nu_p = 30\%$, $l_c = 0.576 \mu\text{m}$,

Simulations for both the AE-CP and SG-RVE FE models are conducted for an applied strain-rate of 0.0001s^{-1} in the y -direction at 800°C . The true stress-logarithmic strain response by the AE-CPFE model and the averaged stress-strain response by the SG-RVE FE model are plotted in Fig. 9. Excellent agreement is obtained between the homogenized grain-scale AE-CPFE model with morphological parameters and the explicit sub-grain RVE model. A notable advantage of the homogenized model is

Fig. 9 Validation of the homogenized grain-level activation energy-based crystal plasticity (AE-CPFE) model with a FEM model of the sub-grain RVE (SG-RVE) for three different microstructures

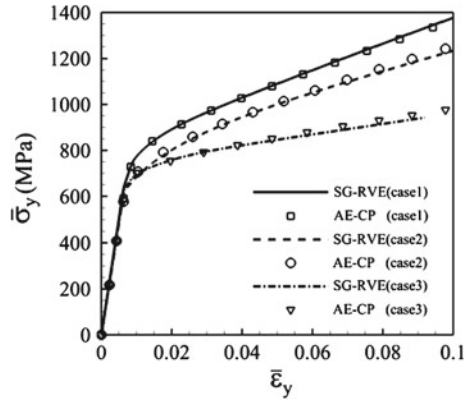
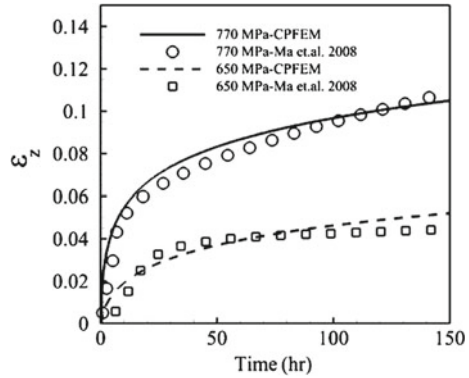


Fig. 10 Creep response by the homogenized AE-CP FEM and experiments in Ma et al. (2008) for tension tests in [001] direction with 750 and 650 MPa respectively at 750 °C



the significant efficiency gain over explicit RVE models. For this example, the gain in efficiency is of the order of 10^4 (few seconds for AE-CPFE model) with identical response.

The second example involves validating the AE-CP constitutive model with results from creep experiments in Ma et al. (2008) for single crystal CMSX-4 with 70% volume fraction of γ' precipitates. In Ma et al. (2008) two tensile loads of 650 and 770 MPa are applied in the [001] direction at 750 °C. CPFEM analyses with the homogenized parameters are conducted for a single grain under these conditions. The simulated logarithmic strain-time response by the simulations is compared with the experimental results in Fig. 10 with good agreement.

3.2 Micro-Twinning in Grain-Scale CP Model: Tension-Compression Asymmetry

Single crystal experiments on Ni-based superalloys show considerable tension-compression asymmetry. Large difference in the creep response for single crystals

loaded in the [001] and [011] directions under tension and compression conditions has been reported in Knowles and Gunturi (2002), Fleury et al. (1996). APB shearing is responsible for the difference in tension and compression tests in the [001] direction. However, transmission electron microscopy observations in Unocic et al. (2011) have reported micro-twinning mechanism for high temperature creep deformation. To account for this tension-compression asymmetry, a microtwinning model developed in Unocic et al. (2011) is incorporated in the grain-scale crystal plasticity formulation. The criterion for micro-twin nucleation is based on the state of dissociation of the leading and trailing partials on a slip system, where the condition for dissociation of a full dislocation $a/2\langle 110 \rangle$ is given as a function of the magnitude and orientation of the in-plane shear stress. With deformation, the leading and trailing Shockley partial experience stresses τ_{lead} and τ_{trail} respectively. From the magnitudes of in-plane resolved shear stress τ^{inplane} , stresses τ_{lead} and τ_{trail} the criterion examines whether the partials will remain together or get dissociated at the interface of the γ - γ' phases. Thus, if $\|\tau^{\text{inplane}}\| > \tau_{\text{lead}}$, $\|\tau^{\text{inplane}}\| < \tau_{\text{trail}}$ the leading partial passes through and hence the leading and trailing partials remain dissociated. The direction of dislocation is also another determinant for dissociation. This condition is applied to yield asymmetry due to the difference in the direction of dislocation motion for tension and compression. The micro-twin evolution model is based on the premise that γ' precipitate shearing and subsequent re-ordering is the predecessor to the movement of partials that cause plastic slip. The thermal re-ordering rate by diffusion depends on the activation energy barrier, i.e.

$$R_{\text{reorder}} \propto \exp\left(-\frac{\Delta E + p\Delta V_{\text{act}} - \theta\Delta S}{k_B\theta}\right),$$

where ΔE is the internal energy barrier, p is the pressure, ΔV_{act} is the activation volume for pressure dependent diffusion, ΔS is the change in entropy, k_B is Boltzmann's constant and θ is the absolute temperature. For solids, the pressure dependent activation volume ΔV_{act} is small and is hence ignored. Change in entropy occurs due to irreversible dissipation such as plastic work and is expressed as: $\theta\Delta S = W_P = \tau_{\text{eff}}A_p b_{\text{tp}}$, where τ_{eff} is the effective shear stress, A_p is the shearing area during plastic deformation and b_{tp} is the Burgers vector of the twin partials. The velocity of twin partials may be written as:

$$v_{\text{tp}} = f_{\text{reorder}}\lambda_{\text{reorder}}P_{\text{reorder}}(\Delta E, \theta\Delta S), \quad (24)$$

where f_{reorder} is the frequency of re-ordering, λ_{reorder} is the reordering distance and P_{reorder} is the probability of re-ordering against the energy barrier, which is a function of plastic dissipation and internal energy barrier. The internal energy barrier is expressed as $\Delta E = \Gamma(t)A_{\text{eff}}$, where $\Gamma(t) = (\Gamma_{\text{pt}} - \Gamma_{\text{tt}})\exp(-Kt) + \Gamma_{\text{tt}}$ is the energy drop, which decreases exponentially with time from pseudo-twin energy Γ_{pt} to true twin energy Γ_{tt} . The effective shear stress including the effect of tertiary γ' precipitates is expressed in Karthikeyan et al. (2006) as

$$\tau_{\text{eff}} = \tau - \frac{f_3}{2} \frac{\Gamma_{\text{pt}}}{b_{\text{tp}}},$$

where f_3 is the volume fraction of the tertiary γ' precipitates. Thus, the plastic shear strain-rate due to micro-twinning is written from the Orowan equation as:

$$\dot{\gamma} = \rho_{\text{tp}} b_{\text{tp}} \lambda_{\text{reorder}} f_{\text{reorder}} \exp\left(-\frac{A_{\text{eff}} \Gamma(t) - V_{\text{act}} \tau_{\text{eff}}}{k_B \theta}\right), \quad (25)$$

where ρ_{tp} is the density of partials which is a function of applied stress and time.

The homogenized AE-CP model, along with the grain-scale micro-twin nucleation and evolution models in Eqs. (14)–(25), are employed to simulate creep response of single crystal superalloys. Significant tension-compression asymmetry is observed in the experimental data plotted in Fig. 11 for single crystal CMSX-4 specimen (Xie et al. 2004). Micro-twin formation is not seen for tension loading in the [001] direction. However, significant micro-twin has been seen to develop for compression in this direction in the TEM studies of Kakehi (1999). Deformation is dominated by strain due to micro-twin evolution as shown in Fig. 11a. Similar observations have also been made in experiments with loading in the [011] direction. For tensile and compressive creep tests, the observed trend shown in Fig. 11b, is opposite to that for the [001] direction. Micro-twins in the deformed micro-structure are observed for tension loading in the [011] direction, whereas no micro-twin induced deformation is seen for compression loading. Results of compression creep experiments with single crystals containing 70% volume fraction of cubic precipitates Fleury et al. (1996), Karthikeyan et al. (2006) are used to calibrate material constants in Eq. (25). For compression tests, the loading conditions and microstructures are the same as in the tensile tests of Sect. 3.1. Experimentally calibrated material constants are:

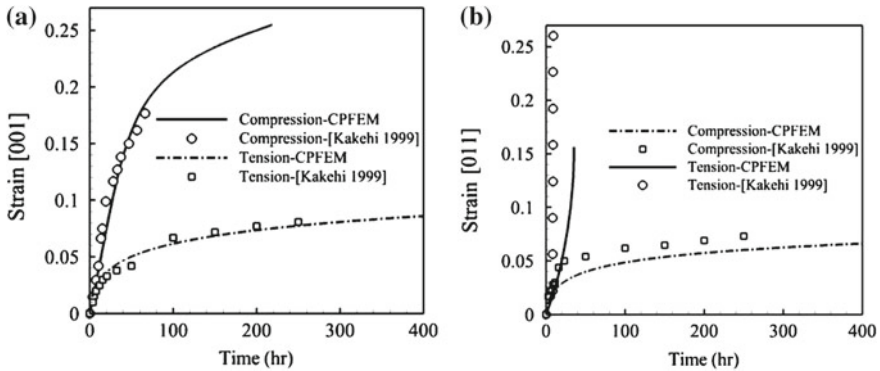


Fig. 11 Logarithmic strain-time response by the homogenized AE-CPFE model including micro-twin nucleation and evolution, with experimental data (Kakehi 1999), for tension and compression creep in **a** [001] and **b** [011] directions

$\rho_{\text{tp}} = 1.0^{11} \text{ m}^{-2}$, $b_{\text{tp}} = 0.145 \text{ } \mu\text{m}$, $\lambda_{\text{reorder}} = 0.3$, $f_{\text{reorder}} = 0.1$, $\Gamma_{\text{pt}} = 0.7 \text{ J m}^{-2}$, and $\Gamma_{\text{tt}} = 0.02 \text{ J m}^{-2}$. Results of CPFЕ simulations are compared with experimental data (Xie et al. 2004) in Fig. 11 for validation. The grain-scale crystal plasticity FE model satisfactorily predicts single crystal experimental data, including micro-twin induced tension-compression asymmetry.

4 AE-CP Model for Polycrystalline Microstructures

Polycrystalline microstructures of Nickel-based superalloys are modeled in this section using the homogenized AE-CP model with parametric representation of the γ - γ' microstructure, together with the micro-twin nucleation and evolution models. For modeling polycrystalline microstructures however, the AE-CP model should be modified to account for grain boundary lattice incompatibility. Hardening laws, accounting for GNDs, have been proposed to address lattice incompatibility in Acharya and Beaudoin (2000) using the Nye tensor along slip plane normal. In the present study, the dislocation density-based slip relations have been extended to take into account lattice incompatibility. The hardening parameters in Eq. (16) are augmented to account for lattice deformation incompatibility at grain boundaries due to plastic strain gradients leading to dislocation pileup. The athermal and thermal shear resistances in Eq. (16) are each divided into two parts, corresponding to SSDs and GNDs as:

$$s_{\text{a}}^{\alpha} = s_{\text{a,SSD}}^{\alpha} + s_{\text{a,GND}}^{\alpha}, \quad s_{*}^{\alpha} = s_{*,\text{SSD}}^{\alpha} + s_{*,\text{GND}}^{\alpha}, \quad (26)$$

where

$$s_{\text{a,GND}}^{\alpha} = \bar{c}_1 G b \sqrt{\rho_{\text{GP}}^{\alpha}}, \quad s_{*,\text{GND}}^{\alpha} = \frac{Q}{\bar{c}_2 b^2} \sqrt{\rho_{\text{GF}}^{\alpha}} \quad (27)$$

These relations are consistent with those in the sub-grain scale model in Eq. (5), where the cutting and passing shear resistances are expressed as functions of parallel and forest dislocation densities. In Eq. (27) \bar{c}_1 and \bar{c}_2 are material constants, and $\rho_{\text{GP}}^{\alpha}$, $\rho_{\text{GF}}^{\alpha}$ are parallel and forest dislocation densities resulting from GNDs corresponding to Eq. (9). They may be written as:

$$\begin{aligned} \rho_{\text{GP}}^{\alpha} &= \sum_{\beta=1}^N \chi^{\alpha\beta} [\rho_{\text{GNDs}}^{\beta} |\sin(\mathbf{n}^{\alpha}, \mathbf{m}^{\beta})| + \rho_{\text{GNDet}}^{\beta} |\sin(\mathbf{n}^{\alpha}, \mathbf{t}^{\beta})| + \rho_{\text{GNDen}}^{\beta} |\sin(\mathbf{n}^{\alpha}, \mathbf{n}^{\beta})|], \\ \rho_{\text{GF}}^{\alpha} &= \sum_{\beta=1}^N \chi^{\alpha\beta} [\rho_{\text{GNDs}}^{\beta} |\sin(\mathbf{n}^{\alpha}, \mathbf{m}^{\beta})| + \rho_{\text{GNDet}}^{\beta} |\sin(\mathbf{n}^{\alpha}, \mathbf{t}^{\beta})| + \rho_{\text{GNDen}}^{\beta} |\sin(\mathbf{n}^{\alpha}, \mathbf{n}^{\beta})|] \end{aligned} \quad (28)$$

where $\chi^{\alpha\beta}$ is the interaction strength coefficient and ρ_{GNDs} , ρ_{GNDet} , ρ_{GNDen} are a screw and two edge components of the GND densities respectively. Implementation of GND based hardness in the polycrystalline AE-CP model is discussed in Keshavarz and Ghosh (2014).

4.1 3D Virtual Polycrystalline Microstructure Simulation and Mesh Generation

Virtual polycrystalline microstructures have been generated by the author’s group using methods and codes described in Groeber et al. (2008a, b), Thomas et al. (2012), by matching morphological and crystallographic statistics obtained from electron back-scattered diffraction or EBSD data of microstructural sections. An image based CPFE model is developed for the superalloy René-88 DT, dominated by annealing $\Sigma 3$ twin boundaries with a specific misorientation angle for $\{111\}$ planes (Miao et al. 2012). The annealing twins that develop during processing have large aspect ratios as shown in Fig. 12a. The geometric disparity of these twins requires mesh localization at these areas relative to the remainder of the polycrystalline structure. In resolving the twin bands and maintaining a large sample size, the voxelized 3D reconstruction often contains flaws like disconnected defects or hooked features near grain boundaries, due to resolution. These flaws are eliminated through filtration and smoothing techniques as shown in Fig. 12.

Two methods are pursued for developing virtual images and finite element models of the actual microstructures. The first method shown in Fig. 12 uses a code Symmetrix (Simmetrix Inc. 2014) method to directly implement the actual microstructure derived from EBSD and serial sectioning-based reconstruction in the FE model. The structural data is filtered with minimal data treatment. A significant percentage of annealing twins is preserved in this method. The primary steps in transforming a voxel dataset into a finite element mesh include volume thresholding, erosion,

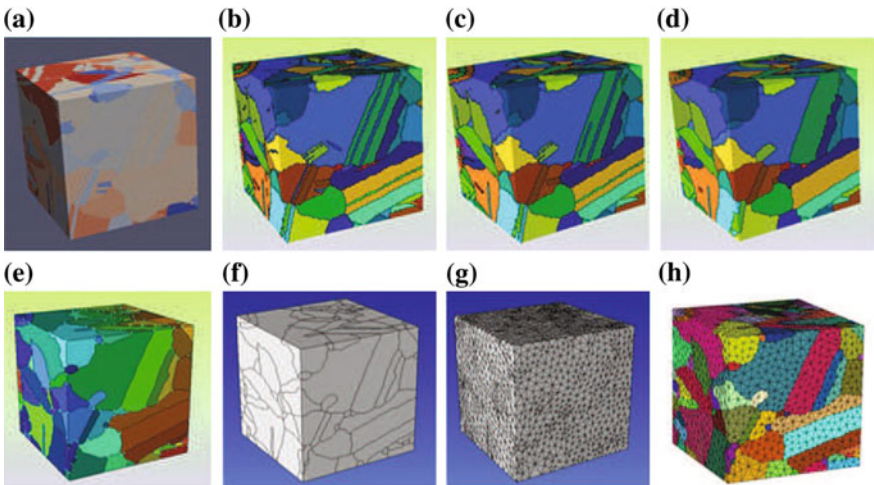


Fig. 12 Reconstructing a virtual microstructure of polycrystalline René-88 DT: **a** 3D EBSD data, **b** fine scale features, **c** “hooked” grain boundaries, **d** isolated defects within grains **e**, **f** filtering and smoothing process, **g**, **h** transformation of the EBSD to a FE mesh

dilation, edge refinement, boundary smoothing, vertex repositioning, and curvature refined meshing. The steps and the final polycrystalline model are shown sequentially in Fig. 12.

Another methodology uses the code DREAM.3D (Groeber and Jackson 2014) to generate synthetic representation of the microstructure, based on the statistical features of the 3D reconstruction. The primary structural and crystallographic characteristics such as grain size, number of neighboring grains, orientation, and misorientation are matched to the corresponding statistical distributions of the data.

4.2 Results of Polycrystalline Microstructure Simulation

The virtual polycrystalline microstructures developed by the codes SIMMETRIX and DREAM.3D are next incorporated for crystal plasticity finite element simulations using the homogenized crystal plasticity constitutive models.

A constant strain-rate tension test is simulated for each microstructure and for various sub-grain morphological conditions. The competing activation of microstructural mechanisms controls the volumetric elastic-plastic response of the polycrystalline material. Local variations in stress and plastic strain are observed to be highly dependent on the grain structure and concentrate near twin bands, where favorably oriented grains reside. The stress-strain response of the polycrystalline microstructure for the two models is compared in Fig. 13c with good agreement. The figure also shows the response in the absence of the annealing twins. Removal of twins reduces the elastic modulus of the superalloy as well as softens the material in the plastic region. This reduction in strength is solely due to the variation of microstructural features. The simulation reveals that the effects of morphology and crystallography can be captured by the statistics of the EBSD scans and reliably controlled within bounds through error quantification. The implementation of statistically equivalent microstructures can thus greatly reduce the time and effort required for material characterization and mechanical experiments.

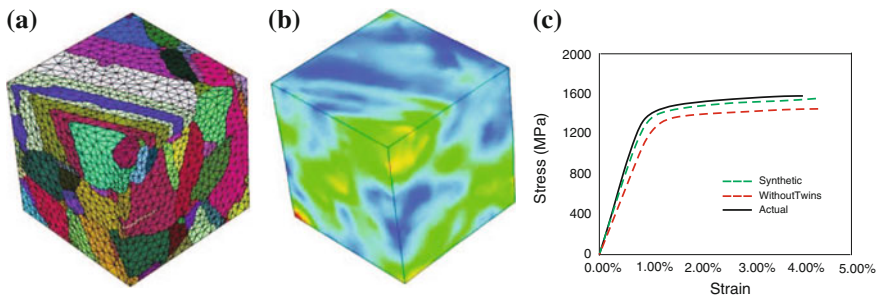


Fig. 13 Virtual polycrystalline microstructures of René-88 DT including twins: **a** generated by direct implementation, **b** generated by equivalence of statistical data, and **c** stress-strain response

5 Summary and Conclusion

This chapter creates a hierarchical framework for realizing a homogenized grain-scale crystal plasticity model that can be used for modeling polycrystalline microstructures of Ni-based superalloys. Specifically, an activation energy-based crystal plasticity (AE-CP) FEM model is developed that incorporates characteristic parameters of the sub-grain scale γ - γ' morphology. Hardening evolution laws are developed to reflect the effect of dislocation density distributions from the sub-grain RVE model, which represents deformation mechanisms in the temperature range $650^\circ\text{C} \leq \theta \leq 800^\circ\text{C}$. A significant advantage of this homogenized AE-CP model is that its high efficiency enables it to be effectively incorporated in polycrystalline crystal plasticity FE simulations, while retaining the accuracy of detailed RVE models. It would be impossible to simulate polycrystalline microstructures with direct numerical simulation of the subgrain morphology otherwise. The homogenized model incorporates the effect of important characteristics of the sub-grain γ - γ' morphology, viz. the volume fraction and shape of the γ' precipitates and the γ channel-width. Parametric representations of these sub-grain morphology variables are incorporated in evolution laws of the homogenized AE-CP model that include both thermal and athermal shear resistance. The simplified RVEs with uniformly distributed generalized ellipsoidal particles provide a demonstrative platform for modeling framework connecting three-scales, one with explicit representation and the others with their respective parametric forms. Three homogenized parameters, viz. the thermal shear resistance, the saturation shear resistance and the reference slip-rate $\dot{\gamma}_*$ are expressed as functions of the sub-grain morphology variables. Size dependence that is explicitly represented in the sub-grain dislocation density crystal plasticity model through the presence of geometrically necessary dislocations or GNDs, is reflected in the homogenized AE-CP model through the explicit dependence on the channel-width. The homogenized AE-CP model is found to accurately reproduce the stress-strain response of the detailed γ - γ' RVE for a range of microstructural variations. It is also found to agree quite well with results of experimental studies on single crystal superalloys in the literature.

The other dominant mechanism at the grain-scale is micro-twinning, which is taken into account through a micro-twin nucleation and evolution model that is incorporated alongside the homogenized AE-CP model. Tension-compression asymmetry, observed in creep experiments, is very well represented by this model. In the final ascending scale, a polycrystalline microstructure of Ni-based superalloys is modeled using the homogenized CPFEM model together with microtwinning. The grain-scale model is augmented through the accommodation of GNDs in the hardness formulations to compensate for lattice incompatibility. Virtual polycrystalline microstructural models of the superalloy René-88 DT are created for simulating polycrystalline behavior. This polycrystalline constitutive model implicitly retains the effect of microstructure morphology while reducing computational cost by several orders of magnitude without significant loss of accuracy. This is necessary for meaningful simulations that can be corroborated by experiments.

Acknowledgments This work has been partially supported by the National Science Foundation, Civil and Mechanical Systems Division through Grant No. CMMI-0800587 (program manager: Dr. Clark Cooper), and by Air Force Office of Scientific Research through Grant No. FA9550-13-1-0062 (program manager: Dr. David Stargel). This sponsorship is gratefully acknowledged. Computer use of the Hopkins High Performance Computing facilities is gratefully acknowledged.

References

- Acharya A, Beaudoin AJ (2000) Grain-size effect in viscoplastic polycrystals at moderate strains. *J Mech Phys Solids* 48(10):2213–2230
- Arsenlis A, Parks DM (2002) Modeling the evolution of crystallographic dislocation density in crystal plasticity. *J Mech Phys Solids* 50(9):1979–2009
- Asaro R, Needleman A (1985) Texture development and strain hardening in rate dependent polycrystals. *Acta Mater* 33:923–953
- Busso E, Meissonier F, O’Dowd N (2000) Gradient-dependent deformation of two-phase single crystals. *J Mech Phys Solids* 48:2333–2361
- Chatterjee D, Hazari N, Das N, Mitra R (2010) Microstructure and creep behavior of DMS4-type nickel based superalloy single crystals with orientations near $\langle 001 \rangle$ and $\langle 011 \rangle$. *Mater Sci Eng: A* 528:604–613
- Cormier J, Milhet X, Mendez J (2011) Non-isothermal creep at very high temperature of the nickel-based single crystal superalloy. *Acta Mater* 55:6250–6259
- Dimiduk DM, Uchic MD, Parathasarathy TA (2005) Size-affected single-slip behavior of pure nickel microcrystals. *Acta Mater* 53:4065–4077
- Epishin A, Link T, Brückner U, Portella PD (2001) Kinetics of the topological inversion of the γ/γ' -microstructure during creep of a nickel-based superalloy. *Acta Mater* 49:4017–4023
- Fedelich B (2002) A microstructural model for the monotonic and the cyclic mechanical behavior of single crystals of superalloys at high temperatures. *Int J Plast* 18:1–49
- Fleury G, Schubert F, Nickel H (1996) Modelling of the thermo-mechanical behaviour of the single crystal superalloy CMSX-4. *Comput Mater Sci* 7(1–2):187–193
- Frost HJ, Ashby MF (1982) Deformation-mechanism-map. The plasticity and creep of metals and ceramics. Pergamon Press, Oxford
- Ghosh S (2011) Micromechanical analysis and multi-scale modeling using the Voronoi cell finite element method. CRC Press/Taylor & Francis, Boca Raton
- Ghosh S, Anahid M (2013) Homogenized constitutive and fatigue nucleation models from crystal plasticity FE simulations of Ti alloys. Part 1: macroscopic anisotropic yield function. *Int J Plast* 47:182–201
- Ghosh S, Bai J, Paquet D (2009) Homogenization-based continuum plasticity-damage model for ductile failure of materials containing heterogeneities. *J Mech Phys Solids* 57(7):1017–1044
- Groeber M, Ghosh S, Uchic MD, Dimiduk DM (2008a) A framework for automated analysis and simulation of 3d polycrystalline microstructures. Part 1: statistical characterization. *Acta Mater* 56(6):1257–1273
- Groeber M, Ghosh S, Uchic MD, Dimiduk DM (2008b) A framework for automated analysis and simulation of 3d polycrystalline microstructures. Part 2: synthetic structure generation. *Acta Mater* 56(6):1274–1287
- Groeber MA, Jackson MA (2014) DREAM.3D: a digital representation environment for the analysis of microstructure in 3D. *Integr Mater Manuf Innov* 3(5):1–17
- Hill R (1984) On macroscopic effects of heterogeneity in elastoplastic media at finite strain. *Math Proc Camb Philos Soc* 95:481–494
- Hong HU, Kim IS, Choi BG, Kim MY, Jo CY (2009) The effect of grain boundary serration on creep resistance in a wrought nickel-based superalloy. *Mater Sci Eng: A* 517:125–131

- Ignat M, Buffiere JY, Chaix JM (1993) Microstructures induced by a stress gradient in a nickel-based superalloy. *Acta Mater* 41:855–862
- Kakehi K (1999) Tension/compression asymmetry in creep behavior of a Ni-based superalloy. *Scr Mater* 41(5):461–465
- Karthikeyan S, Unocic R, Sarosi P, Viswanathan G, Whitis D, Mills M (2006) Modeling microtwinning during creep in Ni-based superalloys. *Scr Mater* 54(6):1157–1162
- Kayser FX, Stassis C (1981) The elastic constants of Ni₃Al at 0 and 23.5 °C. *Phys Stat Sol (a)* 64(1):335–342
- Keshavarz S, Ghosh S (2013) Multi-scale crystal plasticity finite element model approach to modeling nickel-based superalloys. *Acta Mater* 61(17):6549–6561
- Keshavarz S, Ghosh S (2014) Hierarchical crystal plasticity FE model for nickel-based superalloys: sub-grain microstructures to polycrystalline aggregates. *Int J Solids Struct*. doi:10.1016/j.ijsolstr.2014.03.037
- Knowles D, Gunturi S (2002) The role of $\langle 112 \rangle_{111}$ slip in the asymmetric nature of creep of single crystal superalloy CMSX-4. *Mater Sci Eng: A* 328(1–2):223–237
- Kocks UF, Argon AS, Ashby MF (1975) Thermodynamics and kinetics of slip, vol 19. Progress in Materials Science Pergamon Press, Oxford
- Kovarik L, Unocic R, Li J, Sarosi P, Shen C, Wang Y, Mills M (2009) Microtwinning and other shearing mechanisms at intermediate temperatures in Ni-based superalloys. *Prog Mater Sci* 54:839–873
- Ma A, Roters F (2004) A constitutive model for fcc single crystals based on dislocation densities and its application to uniaxial compression of aluminium single crystals. *Acta Mater* 52(12):3603–3612
- Ma A, Roters F, Raabe D (2006) A dislocation density based constitutive model for crystal plasticity FEM including geometrically necessary dislocations. *Acta Mater* 54(8):2169–2179
- Ma A, Dye D, Reed R (2008) A model for the creep deformation behaviour of single-crystal superalloy CMSX-4. *Acta Mater* 56(8):1657–1670
- McLean M, Cahn R (1996) Nickel-base superalloys: current status and potential. High Temperature Structural Materials. Chapman and Hall, London
- Miao J, Pollock TM, Jones JW (2012) Microstructural extremes and the transition from fatigue crack initiation to small crack growth in a polycrystalline nickel-base superalloy. *Acta Mater* 60(6–7):2840–2854
- Nouailhas D, Cailletaud G (1996) Multiaxial behaviour of Ni-base single crystals. *Scr Mater* 34(4):565–571
- Ohashi T, Hidaka K, Saito M (1997) Quantitative study of the plastic slip deformation and formation of internal stresses in Ni-base superalloys. *Mater Sci Eng: A* 238:42–49
- Pollock TM, Argon A (1992) Creep resistance of CMSX-3 nickel-base superalloy single-crystals. *Acta Metall* 40:1–30
- Pollock TM, Sammy T (2006) Nickel-based superalloys for advanced turbine engines: chemistry, microstructure, and properties. *J Prop Power* 22(2):361–375
- Roters F, Eisenlohr P, Hantcherli L, Tjahjantoa DD, Bieler TR, Raabe D (2010) Overview of constitutive laws, kinematics, homogenization and multiscale methods in crystal plasticity finite-element modeling: theory, experiments, applications. *Acta Mater* 58:1152–1211
- Shenoy M (2006) Constitutive modeling and life prediction in Ni-base superalloys. PhD thesis, Georgia Institute of Technology, Atlanta
- Shenoy M, Zhang J, McDowell D (2007) Estimating fatigue sensitivity to polycrystalline Ni-base superalloy microstructures using a computational approach. *Fatigue Fract Eng Mater Struct* 30(10):889–904
- Simmetrix Inc (2014) Simmetrix, <http://www.simmetrix.com/>
- Sugui T, Jun X, Xiaoming Z, Benjiang Q, Jianwei L, Lili Y, Wuxiang W (2011) Microstructure and creep behavior of FGH95 nickel-base superalloy. *Mater Sci Eng: A* 528:2076–2084
- Thomas J, Groeber M, Ghosh S (2012) Image-based crystal plasticity FE framework for microstructure dependent properties of Ti-6Al-4V alloys. *Mater Sci Eng: A* 553:164–175

- Torster F, Baumeister G, Albrecht J, Lütjering G, Helm D, Daeubler MA (1997) Influence of grain size and heat treatment on the microstructure and mechanical properties of the nickel-base superalloy U 720 LI. *Mater Sci Eng: A* 234–236:189–192
- Unocic RR, Zhou N, Kovarik L, Shen C, Wang Y, Mills MJ (2011) Dislocation decorrelation and relationship to deformation microtwins during creep of a γ' precipitate strengthened Ni-based superalloy. *Acta Mater* 59:7325–7339
- van Sluytman JS, Pollock TM (2012) Optimal precipitate shapes in nickel-base $\gamma - \gamma'$ alloys. *Acta Mater* 60(4):855–862
- Viswanathan GB, SP M, Whitis DH, Mills MJ (2005) Deformation mechanisms at intermediate creep temperatures in the Ni-base superalloy René 88 DT. *Mater Sci Eng: A* 400–401:489–495
- Xie CL, Ghosh S, Groeber M (2004) Modeling cyclic deformation of HSLA steels using crystal plasticity. *J Eng Mater Technol* 126(4):339–352
- Zambaldi C, Roters F, Raabe D, Glatzel U (2007) Modeling and experiments on the indentation deformation and recrystallization of a single-crystal nickel-base superalloy. *Mater Sci Eng: A* 454–455:433–440

Homogenized Elastic-Viscoplastic Behavior of Thick Perforated Plates with Pore Pressure

Kazutaka Ikenoya, Nobutada Ohno and Naoto Kasahara

Abstract The homogenized elastic-viscoplastic behavior of thick perforated plates with pore pressure is investigated for macro-material modeling. To this end, homogenized stress-strain relations of a periodic unit cell of pore-pressurized thick perforated plates under uniaxial and multiaxial loadings are analyzed using a finite element method with periodic boundary conditions. It is assumed in the analysis that the base metal of the perforated plates exhibits elastic-viscoplasticity based on Hooke's law and Norton's power law and has the material parameters of Mod. 9Cr-1Mo steel at 550 °C. The resulting homogenized stress-strain relations are simulated using a macro-material model in which the pore-viscoplastic macro-strain rate is represented as an anisotropic power function of Terzaghi's effective stress. It is demonstrated that this macro-material model suitably represents the macro-anisotropy, macro-volumetric compressibility, and pore pressure effect revealed in the viscoplastic range in the finite element homogenization analysis.

Keywords Homogenized behavior · Macro-material model · Thick perforated plates · Pore pressure · Viscoplasticity

1 Introduction

Perforated plates used as tubesheets in heat exchangers contain straight circular holes arranged in a triangular pattern. Full-scale finite element meshing of such perforated plates necessarily results in significantly high computational costs because of the very

K. Ikenoya · N. Ohno (✉)
Department of Mechanical Science and Engineering, School of Engineering,
Nagoya University, Chikusa-ku, Nagoya 464-8603, Japan
e-mail: ohno@mech.nagoya-u.ac.jp

K. Ikenoya
e-mail: ikenoya@mml.mech.nagoya-u.ac.jp

N. Kasahara
Department of Nuclear Engineering and Management, School of Engineering,
The University of Tokyo, 7-3-1, Hongo, Bunkyo-ku, Tokyo 113-8656, Japan
e-mail: kasahara@n.t.u-tokyo.ac.jp

© Springer International Publishing Switzerland 2015
H. Altenbach and M. Brünig (eds.), *Inelastic Behavior of Materials
and Structures Under Monotonic and Cyclic Loading*, Advanced
Structured Materials 57, DOI 10.1007/978-3-319-14660-7_6

large number of straight circular holes. If homogenized material properties/models could be made available for perforated plates, finite element analysis could be performed without full-scale meshing and computational costs would be highly reduced as a result. Therefore, Appendix A-8000 in the ASME Boiler and Pressure Vessel Code Sec. III provides homogenized elastic material properties for perforated plates (ASME 2007). For the homogenized plastic properties of perforated plates, several studies have been devoted to investigating macro-yield surfaces and conditions in plane stress states (O'Donnell and Porowski 1973; Porowski and O'Donnell 1974; Reinhardt 2001; Gordon et al. 2002; Khatam et al. 2009; Khatam and Pindera 2011).

The operating temperatures of perforated plates are considerably high in fast breeder reactors and high temperature gas cooled reactors. Accordingly, homogenized creep properties and models of perforated plates have been investigated under plane stress conditions. By assuming Norton's creep equation for base metals and by performing finite element analysis of a periodic unit cell, Uragami et al. (1981) computationally demonstrated that the homogenized creep behavior of thin perforated plates in plane stress states has the same stress exponent as the creep behavior of base metals. Igari et al. (1986, 2001) then developed homogenized creep models for perforated plates in plane stress states by introducing a geometrical parameter into the creep equations of base metals, although the material isotropy and inelastic volume-incompressibility of base metals were assumed to remain valid for the homogenized creep behavior.

Semispherical tubesheets are now under development for heat exchangers in the next generation of fast breeder reactors in Japan (Kasahara et al. 2008; Ando et al. 2013). Since these tubesheets are noticeably thick, three dimensional solid elements are inevitably required for their finite element models. Consequently, out-of-plane as well as in-plane homogenized properties need to be correctly taken into account when developing inelastic macro-material models for such thick tubesheets. Moreover, semispherical tubesheets are designed to be subjected to considerably high pore pressure (Ando et al. 2013). Therefore, it is worthwhile to investigate the macro-anisotropy, macro-volumetric compressibility, and pore pressure effect caused, in the inelastic range, by the circular holes distributed in thick perforated plates.

Ohno et al. (2012) described micro-macro relations relevant to periodic anisotropic open-porous bodies subjected to pore pressure, and showed the following constitutive features as consequences of the macro-homogeneity equation of Hill (1967): the effective stress of Terzaghi (1943) is work-conjugate to the pore-viscoplastic macro-strain rate, and the constitutive relation of this work-conjugate pair has the same stress exponent as Norton's power law assumed for the base metals of open-porous bodies. Ohno et al. (2012) thus developed a macro-material model in which the pore-viscoplastic macro-strain rate is represented as an anisotropic power function of Terzaghi's effective stress. The resulting macro-material model was applied to an ultrafine plate-fin structure with pore pressure. The corresponding finite element homogenization analysis was also performed for comparison. It was thus demonstrated that the developed macro-material model well simulates the homogenization analysis results in spite of there being no fitting parameter for the effect of pore pressure.

In this study, the homogenized elastic-viscoplastic behavior of thick perforated plates under uniaxial and multiaxial loadings with pore pressure is investigated to examine the macro-material model developed by Ohno et al. (2012). For this purpose, the homogenized pore-elastic-viscoplastic behavior is analyzed using the finite element homogenization method based on periodic boundary conditions. It is assumed in the analysis that the base metal of the perforated plates exhibits elastic-viscoplasticity based on Hooke's law and Norton's power law and has the material parameters of Mod. 9Cr-1Mo steel at 550 °C. It is shown that the pore-elastic-viscoplastic macro-material model by Ohno et al. (2012) properly represents the macro-anisotropy, macro-volumetric compressibility, and pore pressure effect found in the viscoplastic range in the finite element homogenization analysis.

In this paper, direct notations are used for vectors and tensors, and inner products between them are indicated by middle dots or colons (e.g., $\mathbf{u} \cdot \mathbf{v} = u_i v_i$, $\mathbf{D} : \boldsymbol{\varepsilon} = D_{ijkl} \varepsilon_{kl}$). In addition, the second-rank and fourth-rank unit tensors are denoted by $\mathbf{1}$ and \mathbf{I} , respectively.

2 Periodic Unit Cell of Thick Perforated Plates

Figure 1a illustrates a portion of the thick perforated plates considered in this study. As shown in the figure, straight circular holes are arranged in a triangular pattern in the thick perforated plates. Figure 1b shows the top view of a periodic unit cell Y of the perforated plates: the unit cell Y consists of solid and pore regions, V_s and V_ω , and its boundary ∂Y is partitioned into solid and pore parts, ∂Y_s and ∂Y_ω .

2.1 Microscopic Material Properties

We suppose that the medium in V_ω has neither rigidity nor viscosity, and that pore pressure p acts uniformly in V_ω (Fig. 1c):

$$\boldsymbol{\sigma} = -p\mathbf{1} \quad \text{in} \quad V_\omega, \quad (1)$$

where $\boldsymbol{\sigma}$ denotes stress in Y .

We assume that the solid region V_s undergoes isothermal small deformation at a high temperature, and consequently that the strain $\boldsymbol{\varepsilon}$ in V_s is additively decomposed into elastic and viscoplastic parts:

$$\boldsymbol{\varepsilon} = \boldsymbol{\varepsilon}_e + \boldsymbol{\varepsilon}_{vp} \quad \text{in} \quad V_s \quad (2)$$

We further assume that $\boldsymbol{\varepsilon}_e$ and $\boldsymbol{\varepsilon}_{vp}$ obey Hooke's law and Norton's power law, respectively:

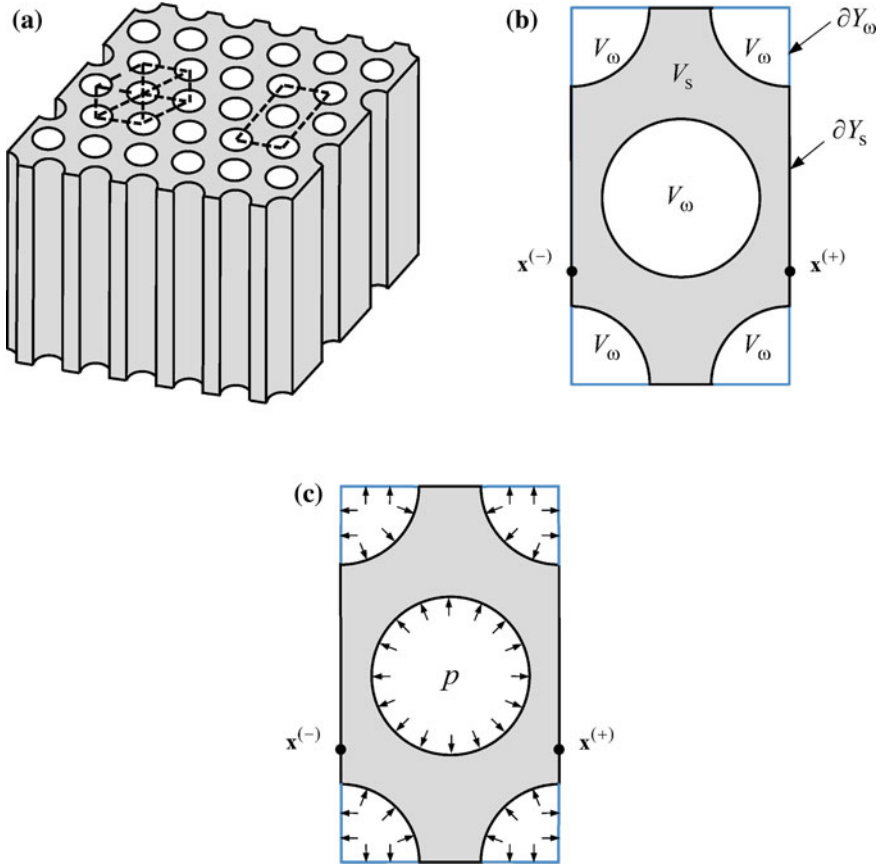


Fig. 1 **a** Portion of the thick perforated plates considered in this study, **b** top view of periodic unit cell Y , and **c** top view of periodic unit cell Y subjected to pore pressure p

$$\boldsymbol{\varepsilon}_e = \frac{1 + \nu}{E} \boldsymbol{\sigma} - \frac{\nu}{E} (\text{tr} \boldsymbol{\sigma}) \mathbf{1}, \quad (3)$$

$$\dot{\boldsymbol{\varepsilon}}_{vp} = \frac{3}{2} \dot{\varepsilon}_0 \left(\frac{\sigma_{eq}}{\sigma_0} \right)^{n-1} \frac{\boldsymbol{\sigma}_d}{\sigma_0}, \quad (4)$$

where E and ν are elastic constants, tr indicates the trace, the superposed dot represents differentiation with respect to time, $\dot{\varepsilon}_0$, σ_0 and n are the material parameters of viscoplasticity, $\boldsymbol{\sigma}_d$ denotes the deviatoric part of $\boldsymbol{\sigma}$, and σ_{eq} expresses the von Mises equivalent stress defined as

$$\sigma_{eq} = \left(\frac{3}{2} \boldsymbol{\sigma}_d : \boldsymbol{\sigma}_d \right)^{1/2}. \quad (5)$$

2.2 Macro-Strain and Macro-Stress

Because Y is a periodic unit cell, the affine deformation part of displacement \mathbf{u} in Y is considered to be due to the macro-strain \mathbf{E} of Y (Suquet 1987; Michel et al. 1999):

$$\mathbf{u} = \mathbf{E} \cdot \mathbf{x} + \tilde{\mathbf{u}}, \quad (6)$$

where \mathbf{x} is the position of a point, and $\tilde{\mathbf{u}}$ indicates the perturbed part of \mathbf{u} that satisfies Y -periodic boundary conditions:

$$\tilde{\mathbf{u}}(\mathbf{x}^{(+)}) = \tilde{\mathbf{u}}(\mathbf{x}^{(-)}). \quad (7)$$

Here, $\mathbf{x}^{(+)}$ and $\mathbf{x}^{(-)}$ are a pair of points on the opposite boundary planes of Y (Fig. 1b).

We suppose that $\partial\tilde{\mathbf{u}}/\partial\mathbf{x}$ exists everywhere in V_s . The strain $\boldsymbol{\varepsilon}$ in V_s is then represented as

$$\boldsymbol{\varepsilon} = \mathbf{E} + \tilde{\boldsymbol{\varepsilon}}, \quad \tilde{\boldsymbol{\varepsilon}} = \frac{1}{2} \left[\frac{\partial\tilde{\mathbf{u}}}{\partial\mathbf{x}} + \left(\frac{\partial\tilde{\mathbf{u}}}{\partial\mathbf{x}} \right)^T \right], \quad (8)$$

where the superscript T indicates the transpose. Equation (8), however, cannot hold in V_ω because $\tilde{\mathbf{u}}$ can be arbitrary and discontinuous due to no rigidity and no viscosity in V_ω .

The macro-stress $\boldsymbol{\Sigma}$ of Y is defined to be the volume average of $\boldsymbol{\sigma}$ in V :

$$\boldsymbol{\Sigma} = \frac{1}{|Y|} \int_Y \boldsymbol{\sigma} \, dV, \quad (9)$$

where $|Y|$ indicates the volume of Y . In contrast, \mathbf{E} cannot be the volume average of $\boldsymbol{\varepsilon}$ in Y (Suquet 1987; Michel et al. 1999; Ohno et al. 2012), because $\tilde{\mathbf{u}}$ can be arbitrary and discontinuous in V_ω , as already stated. Here it is noted that \mathbf{E} depends only on the displacement \mathbf{u} on ∂Y_s (Ohno et al. 2012):

$$\mathbf{E} = \frac{1}{2} \left(\int_{\partial Y_s} \mathbf{u} \otimes \mathbf{n} \, dS \cdot \mathbf{G}^{-1} + \mathbf{G}^{-T} \cdot \int_{\partial Y_s} \mathbf{n} \otimes \mathbf{u} \, dS \right), \quad (10)$$

where \mathbf{n} denotes the outward unit normal to ∂Y_s , and

$$\mathbf{G} = \int_{\partial Y_s} \mathbf{x} \otimes \mathbf{n} \, dS. \quad (11)$$

3 Macro-Material Model

This section outlines the theoretical basis and macro-material modeling studied for the elastic-viscoplastic behavior of anisotropic open-porous bodies with pore pressure (Ohno et al. 2012).

3.1 Constitutive Features

If the macro-homogeneity equation of Hill (1967) is satisfied, one can state that the macroscopic work rate due to Σ and $\dot{\mathbf{E}}$ is equal to the volume average of microscopic work rate $\sigma : \dot{\epsilon}$ in Y . Here it is noted that the microscopic work in V_ω is done by pore pressure p and the volume change in V_ω . It is then shown that the macro-homogeneity equation provides

$$(\Sigma + p\mathbf{1}) : \dot{\mathbf{E}} = \frac{1}{|Y|} \int_{V_s} (\sigma + p\mathbf{1}) : \dot{\epsilon} dV, \quad (12)$$

where $\Sigma + p\mathbf{1}$ is called Terzaghi's effective stress (Terzaghi 1943). The above equation is proved using Eqs. (1), (7), (8) and (9).

We now consider a steady state in which $\dot{\sigma} = \mathbf{0}$ everywhere in Y and $\dot{\Sigma} = \mathbf{0}$. In the steady state, $\dot{\epsilon} = \dot{\epsilon}_{vp}$ because $\dot{\sigma} = \mathbf{0}$ everywhere in V_s , and hence $\dot{\mathbf{E}}$ is regarded as pore-viscoplastic (i.e., $\dot{\mathbf{E}} = \dot{\mathbf{E}}_{vp}$). Then, applying Eq. (12) to the steady state and using Eq. (4), we obtain

$$(\Sigma + p\mathbf{1}) : \dot{\mathbf{E}}_{vp} = \frac{1}{|Y|} \int_{V_s} \dot{w}_{vp} dV, \quad (13)$$

where \dot{w}_{vp} denotes the energy dissipation rate due to $\sigma_d : \dot{\epsilon}_{vp}$ in V_s :

$$\dot{w}_{vp} = \sigma_0 \dot{\epsilon}_0 \left(\frac{\sigma_{eq}}{\sigma_0} \right)^{n+1}. \quad (14)$$

It is thus seen that *Terzaghi's effective stress $\Sigma + p\mathbf{1}$ and the pore-viscoplastic macro-strain rate $\dot{\mathbf{E}}_{vp}$ are a work-conjugate pair for the homogenized energy dissipation rate due to \dot{w}_{vp} in V_s .*

We consider another steady state in which the stress σ in V_s and the pore pressure p in V_ω are multiplied by an arbitrary constant c . Then, $\Sigma + p\mathbf{1}$ and \dot{w}_{vp} are multiplied by c and c^{n+1} , respectively, as seen from Eqs. (9) and (14). Hence, Eq. (13) is satisfied irrespective of the value of c if $\dot{\mathbf{E}}_{vp}$ is replaced by $c^n \dot{\mathbf{E}}_{vp}$. This means that $\dot{\mathbf{E}}_{vp}$ becomes $c^n \dot{\mathbf{E}}_{vp}$ if Terzaghi's effective stress $\Sigma + p\mathbf{1}$ is multiplied by c . In other words, $\dot{\mathbf{E}}_{vp}$ has n th-power dependence on $\Sigma + p\mathbf{1}$.

3.2 Constitutive Relations

The Biot pore-elastic law (Biot 1941) is extended by taking account of the pore-viscoplastic constitutive features described in Sect. 3.1.

We assume that the macro-strain \mathbf{E} is additively decomposed into pore-elastic and pore-viscoplastic parts (i.e., $\mathbf{E} = \mathbf{E}_e + \mathbf{E}_{vp}$). We further assume that the pore-elastic part $\mathbf{E} - \mathbf{E}_{vp}$ is related with the macro-stress $\boldsymbol{\Sigma}$ by the Biot law:

$$\boldsymbol{\Sigma} = \mathbf{D}_{eH} : (\mathbf{E} - \mathbf{E}_{vp}) - p\mathbf{B}, \quad (15)$$

where \mathbf{D}_{eH} is the fourth-rank tensor standing for the homogenized elastic stiffness of Y , and \mathbf{B} is the second-rank tensor called Biot's coefficient. Dormieux et al. (2002, 2006) and Vincent et al. (2009) showed that \mathbf{B} is analytically expressed as

$$\mathbf{B} = (\mathbf{I} - \mathbf{D}_{eH} : \mathbf{D}_{es}^{-1}) : \mathbf{1}, \quad (16)$$

where \mathbf{D}_{es} indicates the elastic stiffness of base solids.

To develop a constitutive relation for $\dot{\mathbf{E}}_{vp}$, let us remember that, in steady states, $\boldsymbol{\Sigma} + p\mathbf{1}$ and $\dot{\mathbf{E}}_{vp}$ are a work-conjugate pair for the energy dissipation in V_s (Sect. 3.1). This suggests that $\dot{\mathbf{E}}_{vp}$ is represented as a function of $\boldsymbol{\Sigma} + p\mathbf{1}$, and that the effect of p on $\dot{\mathbf{E}}_{vp}$ appears through $\boldsymbol{\Sigma} + p\mathbf{1}$. Hence, we consider the following type of quadratic anisotropic equivalent stress, which was, in the case of $p = 0$, proposed by Mises (1928) and used for the rate-independent plasticity of cellular solids (Badiche et al. 2000; Deshpande et al. 2001; Xue and Hutchinson 2004):

$$\Sigma_{eq} = \sqrt{\frac{3}{2}(\boldsymbol{\Sigma} + p\mathbf{1}) : \mathbf{M} : (\boldsymbol{\Sigma} + p\mathbf{1})}, \quad (17)$$

where \mathbf{M} is a positive-definite symmetric fourth-rank tensor. Then, assuming the normality of $\dot{\mathbf{E}}_{vp}$ to a viscoplastic potential $f = \Sigma_{eq}^2$ leads to

$$\dot{\mathbf{E}}_{vp} = \lambda \frac{\partial f}{\partial \boldsymbol{\Sigma}} = 3\lambda \mathbf{M} : (\boldsymbol{\Sigma} + p\mathbf{1}), \quad (18)$$

where λ is a scalar function of $\boldsymbol{\Sigma} + p\mathbf{1}$.

To specify the scalar function λ , we remember further that, in steady states, $\dot{\mathbf{E}}_{vp}$ becomes $c^n \dot{\mathbf{E}}_{vp}$ if Terzaghi's effective stress $\boldsymbol{\Sigma} + p\mathbf{1}$ is multiplied by an arbitrary constant c (Sect. 3.1). This constitutive feature is satisfied if Eq. (18) has the same stress exponent n as that in Eq. (4). Equation (18) can thus be shaped as

$$\dot{\mathbf{E}}_{vp} = \frac{3}{2} \dot{\varepsilon}_0 \left(\frac{\Sigma_{eq}}{\sigma_0} \right)^{n-1} \frac{\mathbf{M} : (\boldsymbol{\Sigma} + p\mathbf{1})}{\sigma_0}, \quad (19)$$

where $\dot{\varepsilon}_0$, σ_0 and n are the same material parameters as those in Eq. (4). The above equation with $p = 0$ has been previously used to simulate the elastic-viscoplastic behavior of an ultrafine plate-fin structure in the absence of p (Tsuda et al. 2010; Tsuda and Ohno 2011).

The macro-material model described above is implemented in a finite element code Abaqus with a user subroutine UMAT by taking into account pore pressure p in the implicit stress integration algorithm and the consistent tangent modulus derived by Tsuda et al. (2010).

4 Finite Element Homogenization Analysis

To examine the macro-material model outlined in Sect. 3.2, the homogenized elastic-viscoplastic behavior of a periodic unit cell Y of pore-pressurized thick perforated plates is analyzed using a finite element homogenization method valid for periodic solids. This section describes the finite element model and method used for the homogenization analysis.

4.1 Finite Element Model and Base Solid Property

Figure 2a depicts the finite element division of V_s in the periodic unit cell Y analyzed in this study. Cartesian coordinates x , y and z are used hereafter, as shown in the figure. The periodic unit cell Y has $h/P = 0.2$, and is divided into 20-node quadratic brick elements with reduced integration. Here, h and P denote the minimum thickness

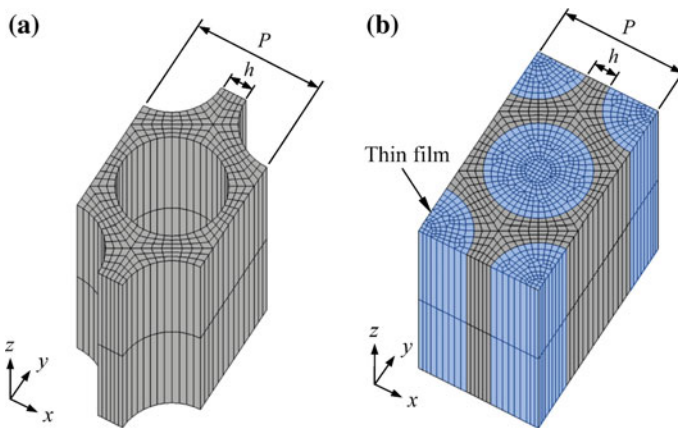


Fig. 2 Finite element model of periodic unit cell Y : **a** solid part V_s , and **b** solid part V_s and fictitious thin films covering pore part V_w

of ligaments and the pitch of holes, respectively. The circular holes penetrate Y in the z -direction. It is noted that the thickness of Y in the z -direction is arbitrary, because no dependence of micro-stress σ and micro-strain ϵ on z is assumed in Y .

Since pore pressure p uniformly acts in V_ω (Fig. 1c), thin flexible fictitious films are placed at the boundary ∂Y_ω , as illustrated in Fig. 2b. The thin flexible films are modeled using elastic shell elements with a very small thickness of $P/10^3$ and an extremely low Young's modulus of 1.0 MPa. It is emphasized that the pore region V_ω inside ∂Y_ω is empty and is not divided into finite elements, and also that the inner surface of ∂Y_ω and the interfacial boundary of V_s are subjected to p (see Fig. 1c). The pore pressure p is taken to be 20 MPa (Ando et al. 2013) when p is considered in the analysis.

The base solid of Y is assumed to be Mod. 9Cr-1Mo steel at 550 °C. This metal exhibits significant rate-dependence but only shows minor strain hardening under uniaxial tensile loading at 550 °C (Ohno and Wang 1993; Yaguchi and Takahashi 2005). Hence, by power-law fitting of the proof stress versus strain rate data shown in Fig. 3, the viscoplastic material parameters $\dot{\epsilon}_0$, σ_0 and n in Eq. (4) are determined (Table 1).

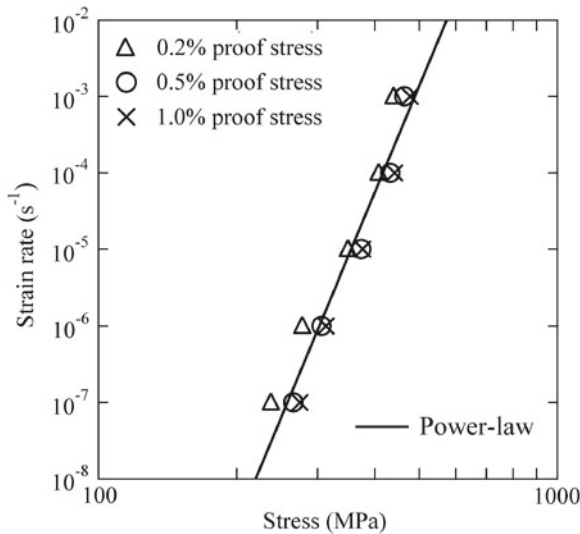


Fig. 3 Stress versus strain rate relation of Mod. 9Cr-1Mo steel under uniaxial tension at 550 °C: power-law fitting of experimental data taken by Yaguchi and Takahashi (2005)

Table 1 Material parameters of Mod. 9Cr-1Mo steel at 550 °C

Elastic	Young's modulus E (GPa)	175.0
	Poisson's ratio ν	0.31
Viscoplastic	Reference strain rate $\dot{\epsilon}_0$ (s ⁻¹)	1.0×10^{-4}
	Reference stress σ_0 (MPa)	416.6
	Stress exponent n	14.4

4.2 Method of Homogenization Analysis

Equations (6) and (7) can be used to perform the elastic-viscoplastic finite element homogenization analysis of periodic solids (Wu and Ohno 1999; Ohno et al. 2000, 2001). Alternatively, we can use the following equation for Y -periodic boundary conditions, which is derived from Eqs. (6) and (7) (Feyel and Chaboche 2000):

$$\mathbf{u}(\mathbf{x}^{(+)}) - \mathbf{u}(\mathbf{x}^{(-)}) = \mathbf{E} \cdot (\mathbf{x}^{(+)} - \mathbf{x}^{(-)}). \quad (20)$$

The homogenization analysis in this study is performed using Abaqus. The above equation is imposed on $\mathbf{u}(\mathbf{x})$ with the help of the Equation command available in Abaqus. It is noted that Eq. (20) is applied to the fictitious thin films as well as to the solid part ∂Y_s of ∂Y .

When p is considered, the finite element model of Y illustrated in Fig. 2b is pore-pressurized before subjection to prescribed loading. In this study, pore pressurization is performed almost instantaneously under the condition of free macro-stress, resulting in a macro-strain $\mathbf{E}^{(p)}$ prior to prescribed loading. This macro-strain $\mathbf{E}^{(p)}$ is almost equal to the macro-strain evaluated from Eq. (15) with $\boldsymbol{\Sigma} = \mathbf{0}$:

$$\mathbf{E}^{(p)} = p \mathbf{D}_{\text{eH}}^{-1} : \mathbf{B}. \quad (21)$$

Then, $\mathbf{E} - \mathbf{E}^{(p)}$ is regarded as the macro-strain $\mathbf{E}^{(\ell)}$ occurring under prescribed loading after pore pressurization:

$$\mathbf{E}^{(\ell)} = \mathbf{E} - \mathbf{E}^{(p)}. \quad (22)$$

5 Verification of Macro-Material Model

In this section, the macro-material model described in Sect. 3.2 is verified on the basis of the finite element homogenization analysis explained in Sect. 4.

Tables 1 and 2 give the material parameters used for the macro-material model in this study. The components of \mathbf{D}_{eH} and \mathbf{M} in Table 2 are based on the assumption of transverse isotropy owing to the 6-fold rotational symmetry on the xy -plane, as described in detail in a different case of h/P (Ikenoya et al. 2012). This assumption is satisfied exactly in the elastic range but approximately in the viscoplastic range in the homogenization analysis, as previously shown for composites and honeycombs (Michel et al. 1999; Asada et al. 2009). It is emphasized that all material parameters have been determined by fitting the homogenization analysis results under uniaxial tensions and simple shears in the absence of pore pressure p .

Table 2 Components of \mathbf{D}_{eH} and \mathbf{M} using Voigt's notation with component order xx, yy, zz, xy, yz and zx

Macro-elastic stiffness (GPa)	$\mathbf{D}_{eH} =$	$\begin{bmatrix} 38.50 & 19.60 & 18.03 & 0 & 0 & 0 \\ 19.60 & 38.50 & 18.03 & 0 & 0 & 0 \\ 18.03 & 18.03 & 84.88 & 0 & 0 & 0 \\ 0 & 0 & 0 & 9.45 & 0 & 0 \\ 0 & 0 & 0 & 0 & 17.68 & 0 \\ 0 & 0 & 0 & 0 & 0 & 17.68 \end{bmatrix}$
Macro-viscoplastic anisotropy	$\mathbf{M} =$	$\begin{bmatrix} 12.40 & -6.76 & -1.68 & 0 & 0 & 0 \\ -6.76 & 12.40 & -1.68 & 0 & 0 & 0 \\ -1.68 & -1.68 & 3.36 & 0 & 0 & 0 \\ 0 & 0 & 0 & 38.20 & 0 & 0 \\ 0 & 0 & 0 & 0 & 28.94 & 0 \\ 0 & 0 & 0 & 0 & 0 & 28.94 \end{bmatrix}$

5.1 Uniaxial Tensile Behavior

Figure 4a, b show macro-stress versus macro-strain relations under three uniaxial tensions at $\dot{E}_{xx}^{(\ell)} = 10^{-4} \text{ s}^{-1}$, $\dot{E}_{yy}^{(\ell)} = 10^{-4} \text{ s}^{-1}$ and $\dot{E}_{zz}^{(\ell)} = 10^{-4} \text{ s}^{-1}$ under $p = 0$ and $p = 20 \text{ MPa}$. First, let us see the homogenization analysis results in the figures, which show that macro-anisotropy is considerable in both the elastic and the viscoplastic range. In the steady-states under the uniaxial tensions, Σ_{zz} is about twice as large as Σ_{xx} and Σ_{yy} , whereas Σ_{xx} and Σ_{yy} differ from each other by only 20%. Therefore, the perforated plate has significant polar macro-anisotropy owing to the straight circular holes that penetrate in the z -direction. Next, let us compare the homogenization analysis results in Fig. 4b to those in Fig. 4a. It is seen that the pore pressure of $p = 20 \text{ MPa}$ lowers the steady-state values of Σ_{xx} and Σ_{yy} by about 10 MPa, but has almost no influence on the steady-state value of Σ_{zz} . Macro-anisotropy is thus seen with respect to the effect of pore pressure on the viscoplastic macro-flow stresses under uniaxial tensions.

The two kinds of macro-anisotropy mentioned above are well simulated by the macro-material model, as shown in Fig. 4a, b. The success in simulating the polar macro-anisotropy in steady states is a consequence of the determination of \mathbf{M} ; i.e., the tension-related components of \mathbf{M} have been determined by fitting the homogenization analysis results in steady states under uniaxial tensions within the assumption of the transverse isotropy on the xy -plane. On the other hand, the success in simulating the macro-anisotropy in the effect of pore pressure on the uniaxial tensile viscoplastic macro-flow stresses is a consequence of the following theoretical feature described in Sect. 3. The effect of p on $\dot{\mathbf{E}}_{vp}$ appears only through Terzaghi's effective stress $\boldsymbol{\Sigma} + p\mathbf{1}$, which has no anisotropic factor. Consequently, the macro-anisotropy in the pore pressure effect in the viscoplastic range is simulated by the presence of \mathbf{M} , which has been determined in the absence of p .

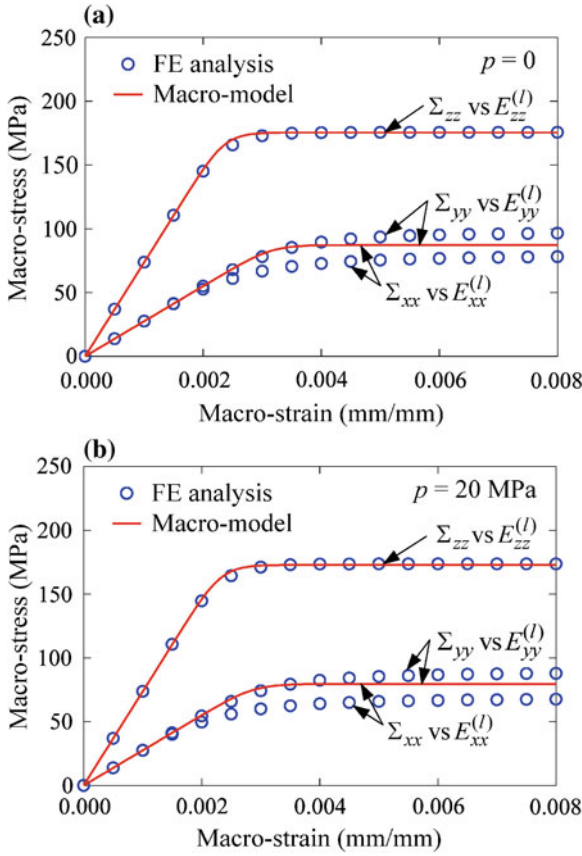


Fig. 4 Macro-stress versus macro-strain relation under uniaxial tension at a macro-strain rate of 10^{-4} s^{-1} : **a** $p = 0$ and **b** $p = 20 \text{ MPa}$

Figure 5a–c depict macro-strain trajectories under the three uniaxial tensions at $\dot{E}_{xx}^{(l)} = 10^{-4} \text{ s}^{-1}$, $\dot{E}_{yy}^{(l)} = 10^{-4} \text{ s}^{-1}$ and $\dot{E}_{zz}^{(l)} = 10^{-4} \text{ s}^{-1}$ under $p = 0$ and $p = 20 \text{ MPa}$. The dashed lines in the figures indicate strain trajectories for volume-incompressible isotropic solids. The homogenization analysis results in the figures show that the macro-strain trajectories concerning $E_{zz}^{(l)}$ under uniaxial tensions in the x - and y -directions noticeably deviate from the dashed lines over the whole macro-strain range (Fig. 5a, b). In other words, macro-volumetric compressibility is evident even in the viscoplastic range under uniaxial tensions in the x - and y -directions. This volumetric compressibility obviously comes from the straight circular holes penetrating in the z -direction. In contrast, under uniaxial tension in the z -direction, no noticeable deviation from the dashed line occurs (Fig. 5c). This is because the straight circular holes penetrating in the z -direction allow all solid elements in Y to be uniformly deformed under uniaxial tension in the z -direction if $p = 0$. The

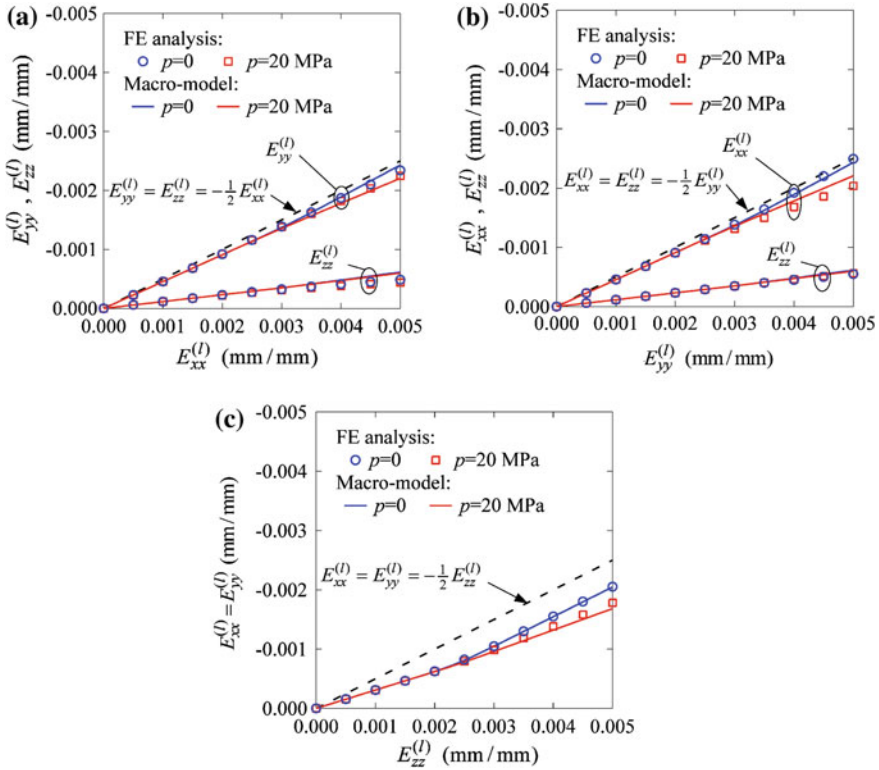


Fig. 5 Macro-strain trajectory under uniaxial tension at a macro-strain rate of 10^{-4} s^{-1} under $p = 0$ and $p = 20 \text{ MPa}$: **a** tension in x -direction, **b** tension in y -direction, and **c** tension in z -direction

straight circular holes penetrating in the z -direction thus cause considerable macro-anisotropy and macro-volumetric compressibility even in the viscoplastic range. As seen from Fig. 5a–c, these macroscopic characteristics are slightly affected by the pore pressure of $p = 20 \text{ MPa}$, and are well simulated by the macro-material model.

5.2 Simple Shear Behavior

Figure 6 shows macro-stress versus macro-strain relations under three simple shears at $\dot{\Gamma}_{xy}^{(\ell)} = 10^{-4} \text{ s}^{-1}$, $\dot{\Gamma}_{yz}^{(\ell)} = 10^{-4} \text{ s}^{-1}$ and $\dot{\Gamma}_{zx}^{(\ell)} = 10^{-4} \text{ s}^{-1}$ under $p = 0$ and $p = 20 \text{ MPa}$. Here $\Gamma_{ij}^{(\ell)} = 2E_{ij}^{(\ell)}$ ($i \neq j$). As seen from the figure, the homogenization analysis reveals the following two features. First, macro-anisotropy is considerably large in the elastic range, but becomes relatively small in the viscoplastic range. This feature is well simulated by the macro-material model, simply because the shear-related components of \mathbf{D}_{cH} and \mathbf{M} have been determined by fitting the

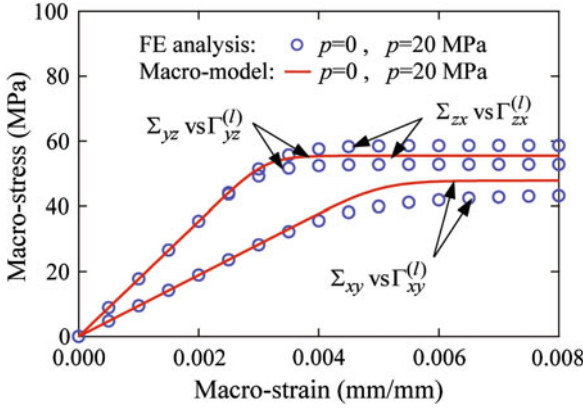


Fig. 6 Macro-stress versus macro-strain relation under simple shear at an engineering shear macro-strain rate of 10^{-4} s^{-1} under $p = 0 \text{ MPa}$ and $p = 20 \text{ MPa}$

homogenization analysis results in the figure within the assumption of transverse isotropy on the xy -plane. Second, the pore pressure of $p = 20 \text{ MPa}$ has no visible influence on the simple shear behavior, as expected. This feature is well represented by the macro-material model, because \mathbf{D}_{eH} and \mathbf{M} have no nonzero components in their tension-shear interaction parts (Table 2).

5.3 Multiaxial Behavior

Figures 7 and 8 depict the steady-state macro-stress surfaces provided by the homogenization analysis and the macro-material model under the following biaxial and triaxial loadings under $p = 0$ and $p = 20 \text{ MPa}$:

$$\dot{E}_{xx}^{(\ell)} = \dot{E}^* \cos \theta, \quad \dot{E}_{yy}^{(\ell)} = \dot{E}^* \sin \theta, \quad \Sigma_{zz} = 0, \quad (23)$$

$$\dot{E}_{xx}^{(\ell)} = \dot{E}_{yy}^{(\ell)} = \frac{\dot{E}^*}{\sqrt{2}} \cos \theta, \quad \dot{E}_{zz}^{(\ell)} = \dot{E}^* \sin \theta, \quad (24)$$

where \dot{E}^* and θ are loading parameters, and $\Sigma_{xy} = \Sigma_{yz} = \Sigma_{zx} = 0$. The macro-stresses in the steady states at $\dot{E}^* = 10^{-4}$ and 10^{-6} s^{-1} at $\theta = (\pi/12)k$ ($k = 0, 1, 2, \dots, 23$) are plotted in the figures. It is seen from Figs. 7a and 8a that the macro-material model properly predicts the steady-state macro-stress surfaces attained in the homogenization analysis under $p = 0$. Here it is recalled that the macro-material model is based on the quadratic equivalent stress defined by Eq. (17). This equivalent stress gives elliptic shapes to the steady-state macro-stress surfaces if $p = 0$. The elliptic shapes are fairly close to those provided by the homogenization

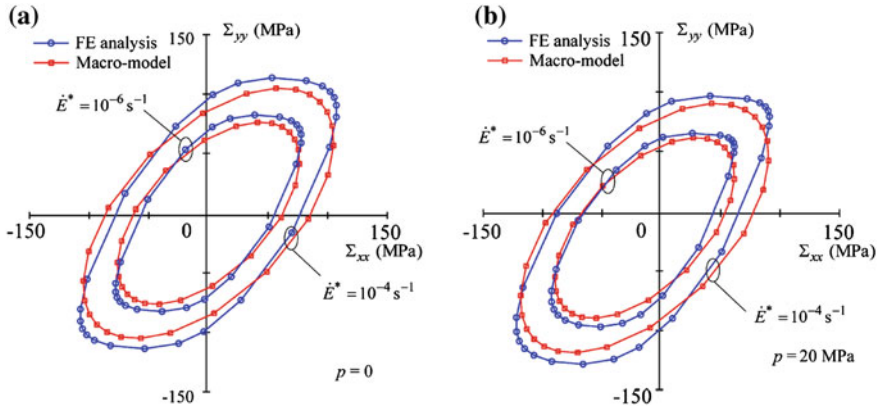


Fig. 7 Steady-state macro-stress surface of periodic unit cell Y under biaxial loading condition (23): **a** $p = 0$ MPa and **b** $p = 20$ MPa

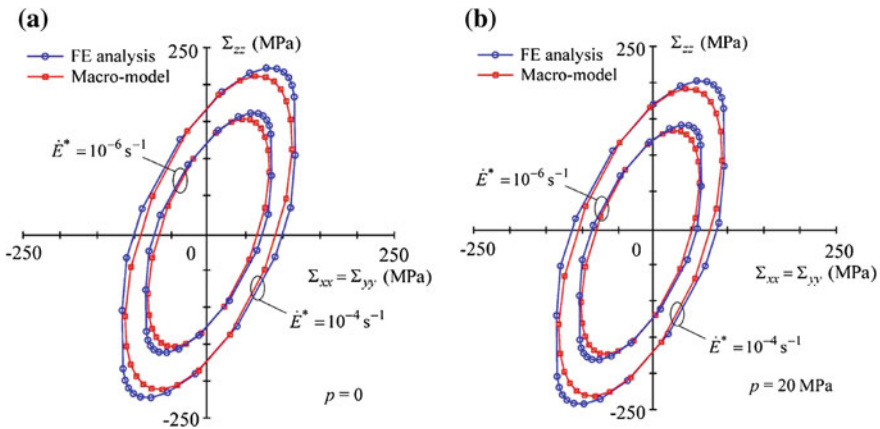


Fig. 8 Steady-state macro-stress surface of periodic unit cell Y under triaxial loading condition (24): **a** $p = 0$ MPa and **b** $p = 20$ MPa

analysis. The pore pressure of $p = 20$ MPa changes the steady-state macro-stress surfaces shown in Figs. 7a and 8a to those in Figs. 7b and 8b. Comparing them, we see that the pore pressure causes translations of the steady-state macro-stress surfaces, and also that the macro-material model closely predicts the translations found in the homogenization analysis. The macro-material model is thus validated for the biaxial and triaxial loadings expressed in Eqs. (23) and (24) under $p = 20$ MPa.

Figures 9 and 10 show the variations in macro-stress and macro-strain in the following two representative cases of multiaxial loading under $p = 0$ MPa and $p = 20$ MPa:

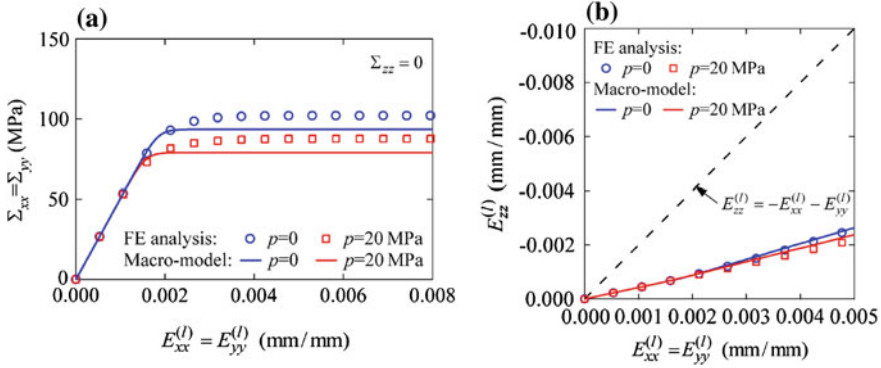


Fig. 9 **a** Macro-stress versus macro-strain relation and **b** macro-strain trajectory under plane-stress equi-biaxial loading condition (25) with $p = 0$ MPa and $p = 20$ MPa

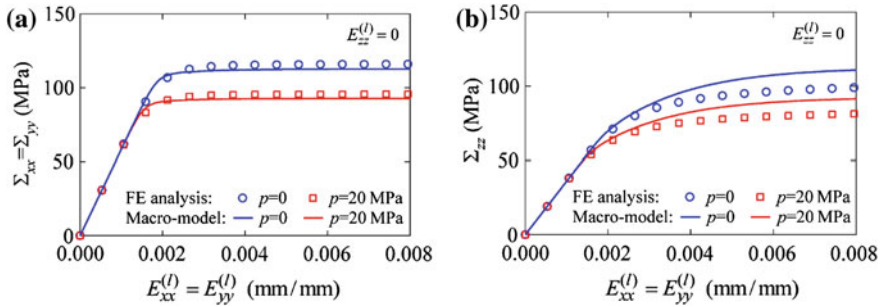


Fig. 10 Macro-stress versus macro-strain relation under plane-strain equi-biaxial loading condition (26) with $p = 0$ MPa and $p = 20$ MPa: **a** in-plane relation and **b** out-of-plane relation

$$\dot{E}_{xx}^{(\ell)} = \dot{E}_{yy}^{(\ell)} = \frac{\dot{E}^*}{\sqrt{2}}, \quad \Sigma_{zz} = 0, \quad (25)$$

$$\dot{E}_{xx}^{(\ell)} = \dot{E}_{yy}^{(\ell)} = \frac{\dot{E}^*}{\sqrt{2}}, \quad \dot{E}_{zz}^{(\ell)} = 0, \quad (26)$$

where $\dot{E}^* = \pm 10^{-4} \text{ s}^{-1}$, and $\Sigma_{xy} = \Sigma_{yz} = \Sigma_{zx} = 0$. Equations (25) and (26) are special cases of Eqs. (23) and (24), and represent plane-stress and plane-strain types of equi-biaxial tensile loading, respectively. As seen from Figs. 9a and 10, the pore pressure of $p = 20$ MPa decreases Σ_{xx} ($=\Sigma_{yy}$) by about 15 MPa in the steady state under plane-stress equi-biaxial tensile loading, whereas the same pore pressure decreases not only Σ_{xx} ($=\Sigma_{yy}$) but also Σ_{zz} by about 20 MPa in the steady state under plane-strain equi-biaxial tensile loading. The effect of pore pressure on the equi-biaxial tensile viscoplastic macro-flow stresses is thus noticeable. In contrast, the variation in $E_{zz}^{(\ell)}$ under plane-stress equi-biaxial tensile loading is slightly affected

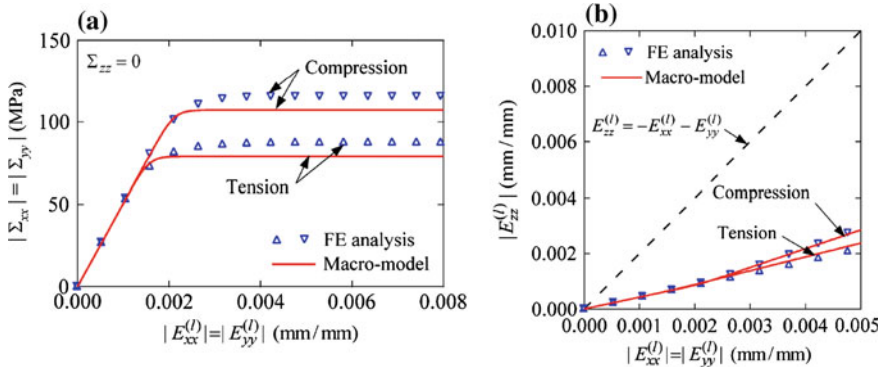


Fig. 11 Tension-compression asymmetry under plane-stress equi-biaxial loading condition (25) with $\dot{E}^* = \pm 10^{-4} \text{ s}^{-1}$ under $p = 20 \text{ MPa}$: **a** macro-stress versus macro-strain relation and **b** macro-strain trajectory

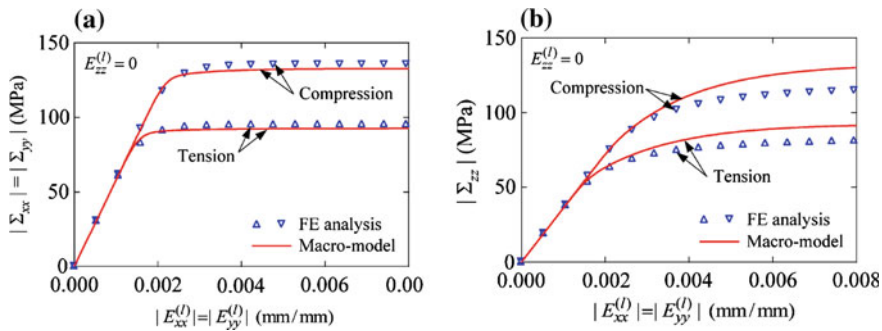


Fig. 12 Tension-compression asymmetry in macro-stress versus macro-strain relation under plane-strain equi-biaxial loading condition (26) with $\dot{E}^* = \pm 10^{-4} \text{ s}^{-1}$ under $p = 20 \text{ MPa}$: **a** in-plane relation and **b** out-of-plane relation

by $p = 20 \text{ MPa}$, as shown in Fig. 9b. It is emphasized that the macro-material model closely simulates the variations in macro-stress and macro-strain under both types of equi-biaxial tensile loading in the presence and absence of $p = 20 \text{ MPa}$.

Figures 11 and 12 are concerned with tension-compression asymmetry under the two types of equi-biaxial loading conditions (25) and (26) with $\dot{E}^* = \pm 10^{-4} \text{ s}^{-1}$ in the presence of $p = 20 \text{ MPa}$. As seen from the figures, the viscoplastic macro-flow stresses have much larger absolute values under equi-biaxial compression than under equi-biaxial tension. This tension-compression asymmetry is a consequence of the pore pressure induced translations of steady-state macro-stress surfaces shown in Figs. 7 and 8, and is again well predicted by the macro-material model.

6 Conclusions

In this study, the homogenized elastic-viscoplastic behavior of thick perforated plates with pore pressure was investigated to examine the macro-material model developed by Ohno et al. (2012). To this end, homogenized stress-strain relations of a periodic unit cell of pore-pressurized thick perforated plates under uniaxial and multiaxial loadings were analyzed using a finite element homogenization method for periodic solids. It was assumed in the analysis that the base metal of the perforated plates exhibited elastic-viscoplasticity based on Hooke's law and Norton's power law and had the material parameters of Mod. 9Cr-1Mo steel at 550 °C. The corresponding macro-material model simulation was performed using the material parameters determined by fitting the homogenization analysis results under uniaxial tensions and simple shears. The finite element homogenization analysis and the macro-material model simulation led to the following main findings:

1. The straight circular holes in the thick perforated plates caused significant macro-anisotropy and macro-volumetric compressibility in the viscoplastic range, as well as in the elastic range.
2. Pore pressure affected viscoplastic macro-flow stress more noticeably under multiaxial loading than under uniaxial loading. Pore pressure thus induced appreciable translations of steady-state macro-stress surfaces and marked tension-compression asymmetry of viscoplastic macro-flow stress under multiaxial loading.
3. The macro-material model properly simulated the homogenization analysis results under uniaxial and multiaxial loadings in the presence and absence of pore pressure in spite of there being no fitting parameter for the effect of pore pressure.

The macro-material model was shown to be suitable under equi-biaxial loading conditions (25) and (26). These loading conditions are actually important for designing the spherical thick perforated plates currently under development for heat exchangers in the next generation of fast breeder reactors in Japan (Kasahara et al. 2008; Ando et al. 2013). Hence, the present macro-material model is expected to be effectively used for their finite element models in their design stages.

Acknowledgments This study was partially supported by a JSPS Grant-in-Aid for Scientific Research (B) (No. 24360045) and the Micro-Nano Global COE project of Nagoya University.

References

- Ando M, Takasho H, Kawasaki N, Kasahara N (2013) Stress mitigation design of a tubesheet by considering the thermal stress inducement mechanism. *J Press Vessel Technol* 135(6):061207 (10 pages)
- Asada T, Tanaka Y, Ohno N (2009) Two-scale and full-scale analyses of elastoplastic honeycomb blocks subjected to flat-punch indentation. *Int J Solids Struct* 46(7–8):1755–1763

- ASME (2007) Appendix A-8000. Stresses in perforated flat plates. In: 2007 ASME boiler and pressure vessel code, Section III, Rules for construction of nuclear facility components, Division 1
- Badiche X, Forest S, Guibert T, Bienvenu Y, Bartout JD, Ienny P, Croset M, Bernet H (2000) Mechanical properties and non-homogeneous deformation of open-cell nickel foams: application of the mechanics of cellular solids and of porous materials. *Mater Sci Eng A* 289(1–2):276–288
- Biot MA (1941) General theory of three-dimensional consolidation. *J Appl Phys* 12(2):155–164
- Deshpande VS, Fleck NA, Ashby MF (2001) Effective properties of the octet-truss lattice material. *J Mech Phys Solids* 49(8):1747–1769
- Dormieux L, Molinari A, Kondo D (2002) Micromechanical approach to the behavior of poroelastic materials. *J Mech Phys Solids* 50(10):2203–2231
- Dormieux L, Kondo D, Ulm FJ (2006) *Microporomechanics*. Wiley, Chichester
- Feyel F, Chaboche JL (2000) FE² multiscale approach for modelling the elastoviscoplastic behaviour of long fibre SiC/Ti composite materials. *Comput Methods Appl Mech Eng* 183(3–4):309–330
- Gordon JL, Jones DP, Banas D, Hutula DN (2002) A collapse surface for a perforated plate with an equilateral triangular array of penetrations. *J Press Vessel Technol* 124(2):201–206
- Hill R (1967) The essential structure of constitutive laws for metal composites and polycrystals. *J Mech Phys Solids* 15(2):79–95
- Igari T, Setoguchi K, Nomura S (1986) Simplified creep analysis of perforated plates under steady creep condition. *Nucl Eng Des* 97(2):161–166
- Igari T, Tokiyoshi T, Mizokami Y (2001) Prediction of macroscopic and local stress-strain behavior of perforated plates under primary and secondary creep conditions. *JSME Int J, Ser A* 44(2):237–245
- Ikenoya K, Ohno N, Kasahara N (2012) Homogenized elasto-viscoplastic material modeling of thick perforated plates at high temperature. *Mater High Temp* 29(4):322–329
- Kasahara N, Takasho H, Kawasaki N, Ando M (2008) Effective stress ratio of triangular pattern perforated plates. In: Proceedings of ASME 2008 pressure vessels and piping conference. American Society of Mechanical Engineers, vol 2, New York, pp 295–303
- Khatam H, Pindera MJ (2011) Plastic deformation modes in perforated sheets and their relation to yield and limit surfaces. *Int J Plast* 27(10):1537–1559
- Khatam H, Chen L, Pindera MJ (2009) Elastic and plastic response of perforated metal sheets with different porosity architectures. *J Eng Mater Technol* 131(3):031015 (14 pages)
- Michel JC, Moulinec H, Suquet P (1999) Effective properties of composite materials with periodic microstructure: a computational approach. *Comput Methods Appl Mech Eng* 172(1–4):109–143
- O'Donnell WJ, Porowski J (1973) Yield surfaces for perforated materials. *J Appl Mech* 40(1):263–270
- Ohno N, Wang JD (1993) Kinematic hardening rules with critical state of dynamic recovery, part ii: application to experiments of ratchetting behavior. *Int J Plast* 9(3):391–403
- Ohno N, Wu X, Matsuda T (2000) Homogenized properties of elastic-viscoplastic composites with periodic internal structures. *Int J Mech Sci* 42(8):1519–1536
- Ohno N, Matsuda T, Wu X (2001) A homogenization theory for elastic-viscoplastic composites with point symmetry of internal distributions. *Int J Solids Struct* 38(16):2867–2878
- Ohno N, Ikenoya K, Okumura D, Matsuda T (2012) Homogenized elastic-viscoplastic behavior of anisotropic open-porous bodies with pore pressure. *Int J Solids Struct* 49(19–20):2799–2806
- Porowski J, O'Donnell WJ (1974) Effective plastic constants for perforated materials. *J Press Vessel Technol* 96(3):234–241
- Reinhardt WD (2001) Yield criteria for the elastic-plastic design of tubesheets with triangular penetration pattern. *J Press Vessel Technol* 123(1):118–123
- Suquet PM (1987) Elements of homogenization for inelastic solid mechanics. In: Sanchez-Palencia E, Zaoui A (eds) *Homogenization techniques for composite media*. Lecture Notes in Physics, vol 272. Springer, Berlin, pp 193–278
- Terzaghi K (1943) *Theoretical soil mechanics*. Wiley, New York

- Tsuda M, Ohno N (2011) Duplex model for homogenized elastic-viscoplastic behavior of plate-fin structures at high temperatures. *Int J Plast* 27(10):1560–1576
- Tsuda M, Takemura E, Asada T, Ohno N, Igari T (2010) Homogenized elastic-viscoplastic behavior of plate-fin structures at high temperatures: Numerical analysis and macroscopic constitutive modeling. *Int J Mech Sci* 52(5):648–656
- Uragami K, Nakamura K, Asada K, Kano T (1981) Simplified inelastic analysis method of ligament plates (in Japanese). *J High Press Inst Jpn* 19(2):57–65
- Vincent PG, Monerie Y, Suquet P (2009) Porous materials with two populations of voids under internal pressure: I. instantaneous constitutive relations. *Int J Solids Struct* 46(3–4):480–506
- von Mises R (1928) Mechanik der plastischen Formänderung von Kristallen. *Zeitschrift für Angewandte Mathematik und Mechanik* 8(3):161–185
- Wu X, Ohno N (1999) A homogenization theory for time-dependent nonlinear composites with periodic internal structures. *Int J Solids Struct* 36(33):4991–5012
- Xue ZY, Hutchinson JW (2004) Constitutive model for quasi-static deformation of metallic sandwich cores. *Int J Numer Methods Eng* 61(13):2205–2238
- Yaguchi M, Takahashi Y (2005) Ratchetting of viscoplastic material with cyclic softening. Part 1: experiments on modified 9Cr-1Mo steel. *Int J Plast* 21(1):43–65

Experimental and Numerical Investigations of the Effects Associated to Complex Loading Combinations

Zbigniew L. Kowalewski, Tadeusz Szymczak and Jan Maciejewski

Abstract The paper presents experimental results concerning evaluation of an influence of cyclic torsion on stress variations during monotonic deformation carried out on the X10CrMoVNb9-1 steel. All strain controlled tests were performed at room temperature using thin-walled tubular specimens. The experimental programme contained selected combinations of monotonic and cyclic loadings, i.e. the torsion-reverse-torsion cycles were superimposed on the monotonic tension. It is shown that such cycles associated with monotonic tension caused essential variations of tensile stress. A significant decrease of the axial stress was visible. A single specimen method for yield surface determination was used to evaluate variations of yield point at different combinations of tension and torsion. The yield surface concept was also used to check permanency of the stress reduction during tension assisted by cyclic torsion. The effects observed during monotonic and cyclic loading combinations were theoretically described using the Maciejewski-Mróz model. It enabled to predict kinematic and isotropic softening or hardening of the material in question. The results exhibited that the model can be used successfully to simulate material behaviour during various combinations of monotonic and cyclic loadings.

Keywords Complex loading · Monotonic tension · Cyclic torsion · Yield condition · Yield surface · Modelling · Isotropic hardening · Kinematic hardening and softening

Z.L. Kowalewski (✉)

Institute of Fundamental Technological Research, Pawińskiego 5B, 02-106 Warsaw, Poland
e-mail: zkowalew@ippt.pan.pl; zbigniew.kowalewski@its.waw.pl

Z.L. Kowalewski · T. Szymczak

Motor Transport Institute, Jagiellońska 80, 03-301 Warsaw, Poland
e-mail: tadeusz.szymczak@its.waw.pl

J. Maciejewski

Warsaw University of Technology, Narbutta 84, 02-524 Warsaw, Poland
e-mail: jmaciejewski@simr.pw.edu.pl

© Springer International Publishing Switzerland 2015

H. Altenbach and M. Brünig (eds.), *Inelastic Behavior of Materials and Structures Under Monotonic and Cyclic Loading*, Advanced Structured Materials 57, DOI 10.1007/978-3-319-14660-7_7

1 Introduction

Investigations of the material behaviour under biaxial stress state have recently attracted interest of many researchers and engineers. This is directly related to the rapid progress in material science, numerical calculations and metal forming processes. Among a wide range of contemporary problems analysed by a number of research centres one can distinguished the so called KOBO effect taking place during an application of a unique method of material forming, proposed by Bochniak et al. (2001, 2006) and Bochniak and Korbel (2003).

In this method, cyclic torsional loading is applied to the moving parts of technological machines, i.e. dies or rollers. The KOBO technique has been employed by Korbel and Bochniak (two first letters of their surnames create the acronym KOBO) to modify extrusion processes of tubes and wires. It provides essential advantages in comparison to the typical forming techniques. A significant reduction of technological forces due to application of the twisting moment is the main beneficial factor of the KOBO method. Although this fact plays a significant role in modifications of technological processes, a number of the results presenting the variations of stress-strain relationship obtained from tests under combination of monotonic loading assisted by cyclic torsion is still far from current need. In the last decade the works of Correa et al. (2003), Kowalewski et al. (2011, 2014) and Szymczak and Kowalewski (2012) were devoted to experimental or numerical analysis of this issue. In the first paper, the authors have illustrated variations of effective stress in low carbon steel due to the presence of delayed torsion cycles with respect to monotonic tension. These results exhibited an immediate drop of stress equal to 150 MPa when the cycles were activated. Kowalewski et al. (2011) have observed the same effect for the 2024 aluminum alloy, applying shear strain amplitude equal to $\pm 0.9\%$. In this case, a tensile stress reduction of 220 MPa was achieved. In addition, the variations of typical mechanical parameters; i.e. proportional limit and yield point versus value of shear strain amplitude were examined. Other aspects associated with this type of loading combination are discussed in the paper by Szymczak and Kowalewski (2012), namely, analysis of strain energy variations during monotonic tension assisted by cyclic torsion of the 2024 aluminum alloy, M1E copper and X10CrMoVNb9-1 steel. Changes of the strain energy were illustrated as a function of shear strain amplitude. As it has been shown, a decrease of plastic energy during tension with an increase of torsion cycles amplitude slightly increased the total plastic strain energy.

The phenomena mentioned above are also important for development of many plasticity theories where various models have been considered (i.e. Mróz 1967; Dafailas and Popov 1976; Wang and Dafailas 1990). Implementation of multi-surface theories involves the following equations: yield surface equation, flow rule, bounding surface and kinematic or hardening rules. In many cases, the plastic strain increment is expressed as a non-linear function of the plastic potential, determined on the basis of the flow rule, while the yield and bounding surfaces are dependent upon the deviatoric stress tensor. In order to identify the kinematic or isotropic hardening rules the stress state components, plastic strain components, stress component increments, and others are required. Moreover, for the correct description of a material behaviour

applying many plastic theories there is a need to use various mechanical parameters like the plastic modulus (Dafailas and Popov 1976; Mayama et al. 2007), tangent modulus of plasticity (Chaboche 1991), saturated value of hardening at infinitely large strain (Yoshida and Uemori 2002), translation modulus of bounding surface center (Hassan and Kyriakides 1992) or elastic-plastic stiffness modulus (Hashiguchi 2005). This issue will be reflected in this paper by the Mróz and Maciejewski's three-yield surface model to be used for description of experimental data from tests carried out under combination of monotonic tension and cyclic torsion.

The main objective of this paper is to show how the torsion cycles may affect tensile characteristic of the X10CrMoVNb9-1 steel, and which parameters play the dominant role in this process. The results achieved from such investigations are significant not only from theoretical point of view, but more importantly from technological reasons, since they are providing a knowledge necessary for modification of some metal forming processes, such as drawing, extrusion or forging (Bochniak and Korbel 1999, 2000, 2003; Kong and Hodgson 2000; Bochniak et al. 2006).

Furthermore, the yield surface concept was applied to check how a prior combined deformation (due to monotonic tension plus cyclic torsion) may change material properties, and whether the effects observed during simultaneous monotonic tension and cyclic torsion have the permanent character.

2 Details of Experimental Procedure

2.1 Material and Specimen

The material used was X10CrMoVNb9-1 steel (manufactured according to Polish Standards). Its chemical composition is shown in Table 1. The specimens used were thin-walled tubes. Nominal dimensions were: total length 122 mm, gauge length 60 mm, outside diameter 19.0 mm, and wall thickness 1.5 mm, Fig. 1.

2.2 Testing Device

The model 1343 INSTRON electrohydraulic, closed-loop, servo-controlled, biaxial testing machine enabling combined loading in tension-compression-torsion-reverse torsion was used in all experiments reported in this paper. The maximum axial and

Table 1 Chemical composition of the X10CrMoVNb9-1 steel

C	Mn	Nb	P	S	Cr	Ni	Mo	V	Cu
0.08	0.50	0.06	Max	Max	8.00	Max	0.85	0.18	Max
0.12	0.80	0.10	0.02	0.015	9.00	0.40	1.05	0.25	0.25

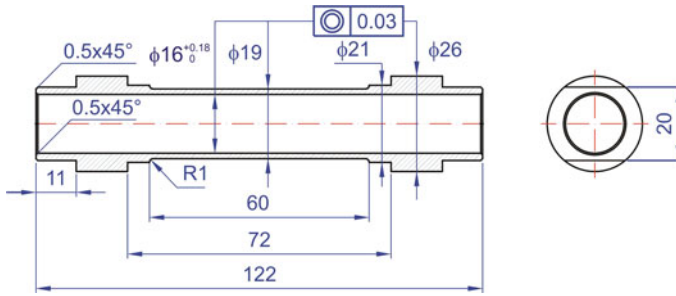


Fig. 1 Thin-walled tubular specimen for material tested under biaxial stress states

torsional load capacities are rated at ± 100 kN and $\pm 1,000$ Nm, respectively. Two separate servo-controller units connected to the computer of the INSTRON loading system can independently apply controlled axial loads and torsional moments. The hydraulic pressure in the actuators comes from two servo-valves operated by servo-controllers provided with set-point control signals from the computer. A multiple analogue-to-digital converter feeds the computer with the signals of: axial displacement of machine piston, rotation of the grip fixture of a specimen, axial force, twisting moment, axial strain and torsional strain. The axial force and the torque applied to the specimen were measured using load cells incorporated in the machine. The software which had been specially developed for these tests enabled the maintenance of constant effective strain rates during plastic loading and the resulting stress-strain responses were recorded by acquisition unit. It was connected to the control computer enabling both direct on-line observations of the experimental results and also their saving onto the hard disk of the computer during each test.

2.3 Strain Measurement

The strains during tests were measured with foil strain gauges bonded to the outer surface of the specimen in the middle of gauge length. Axial strains were measured by a full bridge circuit of four strain gauges of which two, located on the opposite sides of the specimen gauge length, were active, while other two, located on a specially designed semi-ring, were used for temperature compensation. The shear strains circuit also contained a full bridge of four strain gauges. They were bonded to the specimen surface under 45° to the specimen axis. Both strain measurement circuits were connected to the INSTRON measurement system and used for control all tests. Before the start of each test both circuits were calibrated using a highly sensitive tensometric bridge.

2.4 Experimental Procedure

Experimental procedure comprised several steps. At first, the yield surface for virgin material has been determined. Yield loci are typically determined by one of the following techniques (Ikegami 1975a,b; Hecker 1976; Szczepiński et al. 1990):

- (a) method of many specimens testing—in this technique a number of specimens are loaded up to the plastic range along different stress directions. The yield stresses for a chosen definition are determined from each stress-strain curve and plotted in stress space to give the yield locus,
- (b) single specimen method—in this technique a single specimen is loaded in many different stress directions, each time until some measurable and limited plastic strain is observed. At each point it is unloaded and reloaded in different direction until the entire yield locus is obtained. These directions differ from each other by a chosen angular increment, proceeding clockwise or anti-clockwise in individual cases.

According to previous experiments the first method gives results which are qualitatively best, since in this case the shape of the yield surface is not disturbed by the history of the previous probes performed on the same specimen in order to determine the other points of the yield locus. It has been found, however, that under certain conditions single-specimen methods can be successfully used to determine yield surface. In such technique small plastic strains are needed to define yielding and they have to use a specific sequence of loading which should be the same for the whole experimental procedure. Moreover, the use of different variants of the single-specimen method overcomes the disadvantages of the first method, such as having to use a number of expensive specimens to determine each yield locus, and also having to deal with errors due to possible specimen-to-specimen variations. These effects have been previously studied in detail by a number of researchers (Ikegami 1975a,b; Hecker 1976; Kowalewski 1997). Taking into account these considerations the single specimen method was adopted for determination of a yield surface.

The definition of the yield point may have a remarkable effect on the resulting shape and dimensions of the yield surface. Generally, the yield point may be defined by different points in the stress-strain diagram (Phillips and Tang 1972; Hecker 1976), e.g.:

- the point of the proportional limit,
- the point by the back extrapolation,
- the point by the proof stress,
- and some other points.

Since in the case of the material tested in this research the yield point determined by the first two definitions was not clear-cut enough, the yield point was defined here by the proof stress. In all tests for determination of the yield loci at the beginning of loading phase the Young's modulus was determined by the test controlling programme. Such calculations were carried out on the basis of experimental points

captured for the assumed stress limits. The loading of the specimen was stopped when the difference between the total effective strain and elastic effective strain calculated as the quotient of the effective stress and earlier calculated Young's modulus reached the chosen yield offset (in our case it was 5×10^{-5}). Subsequently, the strain control mode was changed to the stress control mode, and the unloading process was carried out until zero force and zero torque were reached. The entire loading and unloading processes were recorded. In the considered range of strain the unloading process was linear for all directions in the stress space.

The experimental procedure comprised 16 successive steps for determining 16 points from the selected proportional (or radial) loading paths as shown in Fig. 2. The angular spacing of the radial paths was equal to 22.5° . Starting from the origin, the specimen was first loaded in tension direction to point 1 where yielding occurred, as defined above, and then the specimen was completely unloaded and again loaded in reversed direction up to point 2 where again yielding occurred. The sequence so described was repeated until all 16 yield points were determined. In Fig. 2 the increasing numbers at the yield points indicate the loading sequence. In all tests the stress state components were defined by the commonly used relations for thin-walled tubes. Namely, the axial stress was expressed by the following formula:

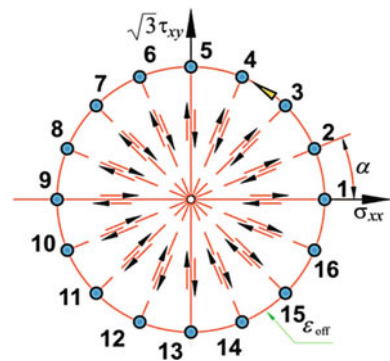
$$\sigma_{xx} = \frac{4F}{\pi(D_0^2 - d_0^2)}, \quad (1)$$

where: F —axial force, D_0 —initial outside diameter measured within gauge length of the specimen, d_0 —initial inside diameter measured within gauge length of the specimen, whereas the shear stress was defined in the form:

$$\tau_{xy} = \frac{16M_s D_0}{\pi(D_0^4 - d_0^4)}, \quad (2)$$

where M_s —twisting moment.

Fig. 2 Loading sequence for yield locus determination using single-specimen method (Kowalewski 1997)



The magnitude of the effective stress in the stress state considered was expressed by the well known relationship:

$$\sigma_e = \sqrt{\sigma_{xx}^2 + 3\tau_{xy}^2}, \tag{3}$$

while the effective strain was determined from the formula involving Poisson’s ratio:

$$\varepsilon_e = \sqrt{\varepsilon_{xx}^2 + \frac{3}{(1 + \nu)^2} \varepsilon_{xy}^2}, \tag{4}$$

where: ν is the Poisson’s ratio, ε_{xx} —axial strain, $\varepsilon_{xy} = \gamma_{xy}/2$ —shear strain. When $\nu = 0.5$ then this equation simplifies to the form:

$$\varepsilon_e = \sqrt{\varepsilon_{xx}^2 + \frac{1}{3} \gamma_{xy}^2}. \tag{5}$$

The experimentally determined Poisson’s ratio ν for the steel tested was equal to 0.30 in the considered range of strain, i.e. up to 5×10^{-5} . Thus, in all tests for yield locus determination the Eq.(4) was used to calculate effective strain.

3 Results of Preliminary Tests

3.1 Results of Investigations of the Basic Mechanical Properties

In order to determine mechanical properties of the tested material the standard tension test was carried out on the thin-walled tubular specimen at room temperature. This experiment was conducted on the INSTRON testing machine under constant strain rate equal to 3.5×10^{-4} 1/s. All typical mechanical properties were determined from the stress-strain curve for the steel tested. These data are summarized in Table 2.

Table 2 Mechanical properties of tested steel

Mechanical properties at room temperature	Value
Young’s modulus E	2.19×10^5 N/mm ²
Conventional yield limit $R_{0.2}$	490 N/mm ²
Ultimate tensile stress R_m	640 N/mm ²
Elongation	30 %

3.2 Validation of the Specimen Geometry

The main aim of the first part of experimental programme was to check whether the specimen geometry provides sufficient range of homogeneous stress distribution. It has been done using Finite Element Method (FEM). A scheme of loading conditions for the specimen taken into account is presented in Fig. 3. The specimen was modelled as a full elastic material. It was covered by the 43567 3D hexagonal elements, Fig. 4. The Multipoint Constraint was used to apply an axial force and twisting moment by coaxial vectors of displacement and rotation with z axis, Figs. 3 and 4.

The results of FEM analysis are illustrated in Fig. 5. Figure 5a presents variations of the axial stress σ_{zz} . The uniform distribution of this stress component along 40 mm measurement zone was achieved. This is important for selection of extensometers or localization of strain gauges for determination of strain components. Having the results of analysis for specimen geometry validation under torsional loading, it is easy to notice a typical gradient of shear stress along the specimen thickness, Fig. 5b, however, since it is relatively small we assumed that such stress distribution can be treated as sufficiently homogeneous.

Fig. 3 Thin-walled tubular specimen subjected to the combination of axial force (F_z) and twisting moment (M_s)

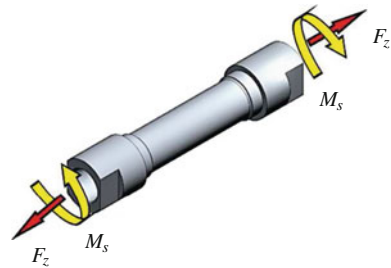
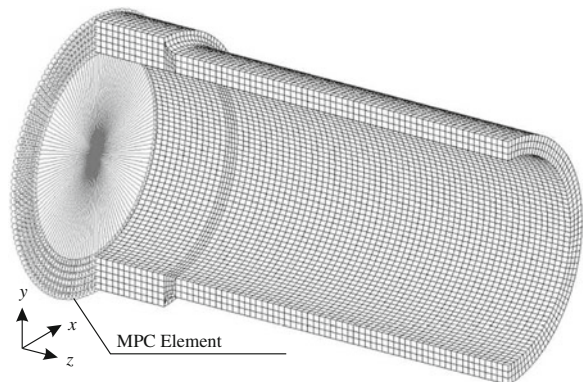


Fig. 4 3D mesh specimen and Multipoint Constraint



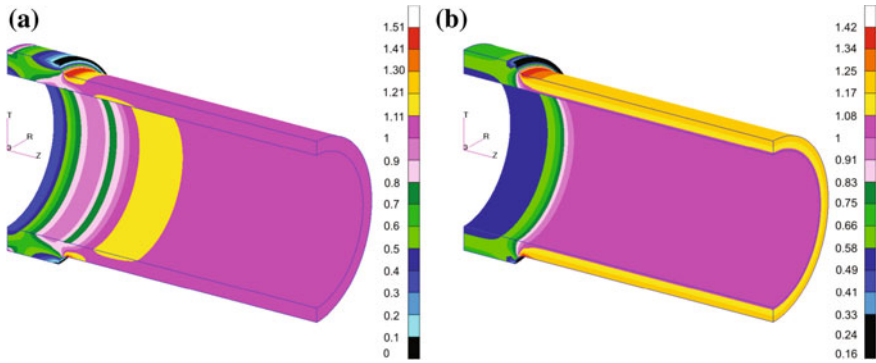


Fig. 5 Distribution of stress state components: **a** axial, **b** shear

4 Yield Condition

The yield condition represents a relationship between stresses which are used to describe the transition of a body from the elastic state to the plastic range. In practice, many of engineering materials are not isotropic. In such cases investigation of a yield surface evolution is regarded as one of the most effective methods to study anisotropic properties of materials. Yield loci can be represented in a stress space by the experimental points determined on the basis of stress-strain diagrams for the magnitude of the effective strain assumed as a yield definition. These points determine a shape, dimensions and location of the yield surface. On the basis of the experimental points, all coefficients in a proposed anisotropic yield condition can be calculated using the least squares technique. Since numerous experimental data show that plastic anisotropy induced in metals by plastic forming processes is very complicated, it is difficult to expect that it can be described by an universal theory. All the forms of yield conditions discussed in many papers are based on certain simplifications and, therefore, they should be treated as approximate conditions only. In order to find the most accurate evaluation of anisotropic properties of a material the yield condition used should possibly respect all the most important phenomena associated with a plastic deformation such as for example the Bauschinger effect, shift and rotation of the yield locus.

von Mises (1928) proposed the general yield function for crystals being quadratic function with respect to stress components which contains 21 various coefficients of anisotropy. This function remains unchanged when the sign of all stress components are changed. It means that when using it, we cannot take into account the Bauschinger effect. If the Bauschinger effect in metals with deformation-induced anisotropy is to be accounted for, linear terms with respect to stress components should be introduced in the yield condition. Goldenblat and Kopnov (1965) considered combination of the stress state components with respect to material axes to propose criterion in the form of a polynomial function. Szczepiński (1993) has elaborated on the basis

of the Mises anisotropic yield condition (von Mises 1928) more general form of the yield condition for materials displaying the Bauschinger effect. This yield condition has been adopted in numerical calculations presented in this paper since it reflects all effects mentioned above, and moreover, it can be easily transformed into the other well known yield conditions, such as Hill's yield condition (Hill 1956) or the yield condition proposed by Ota et al. (1959), under adequate assumptions.

Generally, the Mises anisotropic yield condition (von Mises 1928) in form derived by Szczepiński (1993) can be expressed by the following relationship:

$$\begin{aligned}
 f(\sigma_{ij}) = & k_{12}(\sigma_{xx} - \sigma_{yy})^2 + k_{23}(\sigma_{yy} - \sigma_{zz})^2 + k_{31}(\sigma_{zz} - \sigma_{xx})^2 \\
 & + 2\tau_{xy}[k_{16}(\sigma_{zz} - \sigma_{xx}) + k_{26}(\sigma_{zz} - \sigma_{yy})] \\
 & + 2\tau_{yz}[k_{24}(\sigma_{xx} - \sigma_{yy}) + k_{34}(\sigma_{xx} - \sigma_{zz})] \\
 & + 2\tau_{zx}[k_{35}(\sigma_{yy} - \sigma_{zz}) + k_{15}(\sigma_{yy} - \sigma_{xx})] \\
 & - 2k_{45}\tau_{yz}\tau_{zx} - 2k_{56}\tau_{zx}\tau_{xy} - 2k_{64}\tau_{xy}\tau_{yz} \\
 & + k_{44}\tau_{yz}^2 + k_{55}\tau_{zx}^2 + k_{66}\tau_{xy}^2 \\
 & - b_{12}(\sigma_{xx} - \sigma_{yy}) - b_{23}(\sigma_{yy} - \sigma_{zz}) - b_{31}(\sigma_{zz} - \sigma_{xx}) \\
 & + b_{44}\tau_{yz} + b_{55}\tau_{zx} + b_{66}\tau_{xy}.
 \end{aligned} \tag{6}$$

In the experiments carried out in this research only σ_{xx} and τ_{xy} took nonzero values. When this is substituted into the relation (6) the yield condition is simplified as follows:

$$f(\sigma_{ij}) = (k_{12} + k_{31})\sigma_{xx}^2 - 2k_{16}\tau_{xy}\sigma_{xx} + k_{66}\tau_{xy}^2 + (b_{31} - b_{12})\sigma_{xx} + b_{66}\tau_{xy} = 1. \tag{7}$$

This expression represents the equation of a curve of a second order, usually written in the form:

$$A\sigma_{xx}^2 + 2B\sigma_{xx}\tau_{xy} + C\tau_{xy}^2 + 2D\sigma_{xx} + 2F\tau_{xy} = 1, \tag{8}$$

where coefficients A and D denote functions of yield limits for tension and compression, respectively. They can be expressed as follows:

$$A = \frac{1}{Y_{xx}Z_{xx}}, \quad 2D = \frac{1}{Y_{xx}} - \frac{1}{Z_{xx}}, \tag{9}$$

where Y_{xx} and Z_{xx} are the yield limits for tension and for compression, respectively. The coefficients C and F are related to the shear yield limits obtained from tests under torsion and reverse torsion, respectively. They can be written in the following simple form:

$$C = \frac{1}{R_{xy}S_{xy}}, \quad 2F = \frac{1}{R_{xy}} - \frac{1}{S_{xy}}, \tag{10}$$

where R_{xy} denotes the yield limit obtained under positive oriented shear stress and S_{xy} denotes the yield limit obtained under negative oriented shear stress.

The B coefficient, which is proportional to the rotation of a yield surface with respect to (σ_{xx}, τ_{xy}) co-ordinate system, has no such simple physical interpretation as the coefficients described above and it cannot be deduced from uniaxial tests. In order to find its value it is necessary to carry out at least a single test in a complex stress state.

The main dimensions of the ellipse for the anisotropic yield condition are expressed in the form of functions of parameters of a second order curve, i.e.:

- co-ordinates of the ellipse centre:

$$\alpha_\sigma = \frac{B \cdot F - C \cdot D}{\delta}; \quad \alpha_\tau = \frac{B \cdot D - A \cdot F}{\delta}, \quad (11)$$

- rotation angle of the ellipse axes with respect of σ_{xx}, τ_{xy} co-ordinate system:

$$\Phi = \frac{1}{2} \cdot \arctan \left(\frac{2B}{A - C} \right) \quad (12)$$

- major (a) and minor (b) ellipse semi-axes:

$$a = \sqrt{-\frac{\Delta}{a' \cdot \delta}}, \quad b = \sqrt{-\frac{\Delta}{b' \cdot \delta'}}, \quad (13)$$

where:

$$\Delta = -A \cdot C + 2 \cdot B \cdot D \cdot F - C \cdot D^2 - A \cdot F^2 + B^2, \quad \delta = A \cdot C - B^2, \quad (14)$$

and:

$$a' = \frac{1}{2}(A + C + \sqrt{(A - C)^2 + 4B^2}), \quad b' = \frac{1}{2}(A + C - \sqrt{(A - C)^2 + 4B^2}). \quad (15)$$

The coefficients of the equation for the ellipse, to fit the experimental data, are calculated by the least squares method. Such a procedure enables the determination of all values of the coefficients in general form and, as a consequence, it provides information about the anisotropic properties of the tested material.

The yield condition for anisotropic materials in form (8) is determined by five material parameters. From a geometrical point of view they can be identified with the five ellipse parameters, i.e. the lengths of the axes, its centre co-ordinates and its rotation angle with respect to the co-ordinate system.

It has to be noted that besides of the quadratic yield functions, the non-quadratic yield functions have been also proposed, e.g. Gotoh (1977), Hill (1990), Barlat et al. (1988; 1991). Their yield conditions have been formulated in connection with the sheet forming problems and are restricted to the special case of anisotropy. Such approaches are not considered in this paper.

5 Results of Investigations

5.1 Results for the Material in the As-Received State

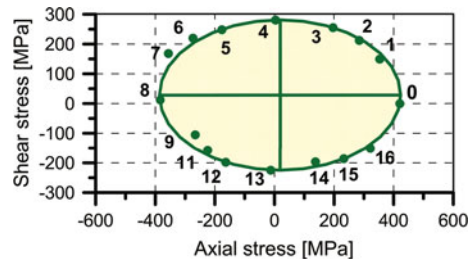
Yield surface for the non-deformed steel determined for the offset strain $\varepsilon_{\text{off}} = 5 \times 10^{-5}$ is shown in Fig. 6. Points in this figure represent experimental results while ellipses are obtained by the least squares evaluation of the A, B, C, D, F coefficients in Eq. (8). The ratio of the tension-compression and torsion-reverse torsion ellipse axes (13) is close to that resulting from the Huber-von Mises yield condition for isotropic materials.

In order to determine each single point of the yield surface two diagrams have to be elaborated first, namely, axial stress and shear stress versus effective plastic strain, Fig. 7. Having them subsequent points of the yield surface can be found.

5.2 Results for the Material After Prior Cyclic Deformation

In the main part of the experimental programme the steel was tested under cyclic tension-compression or cyclic torsion-reverse torsion in order to find necessary parameters for theoretical simulations of cyclic phenomena related to the planned loading programme using Maciejewski-Mróz model. After these tests the yield surfaces were determined in order to check an effect of prior loading history on the initial yield locus evolution. As it is shown in Fig. 8 an essential changes of the yield surface were obtained. Prior cyclic loading along tension-compression strain path induced significant softening of the material, reflected by decrease of the yield surface dimensions, especially in the direction coinciding with that of prior cycles. In the directions perpendicular with respect to the prior cyclic deformation the magnitudes of yield point remained almost the same as those for the material in the as-received state achieved.

Fig. 6 Initial yield locus for the X10CrMoVNb9-1 steel



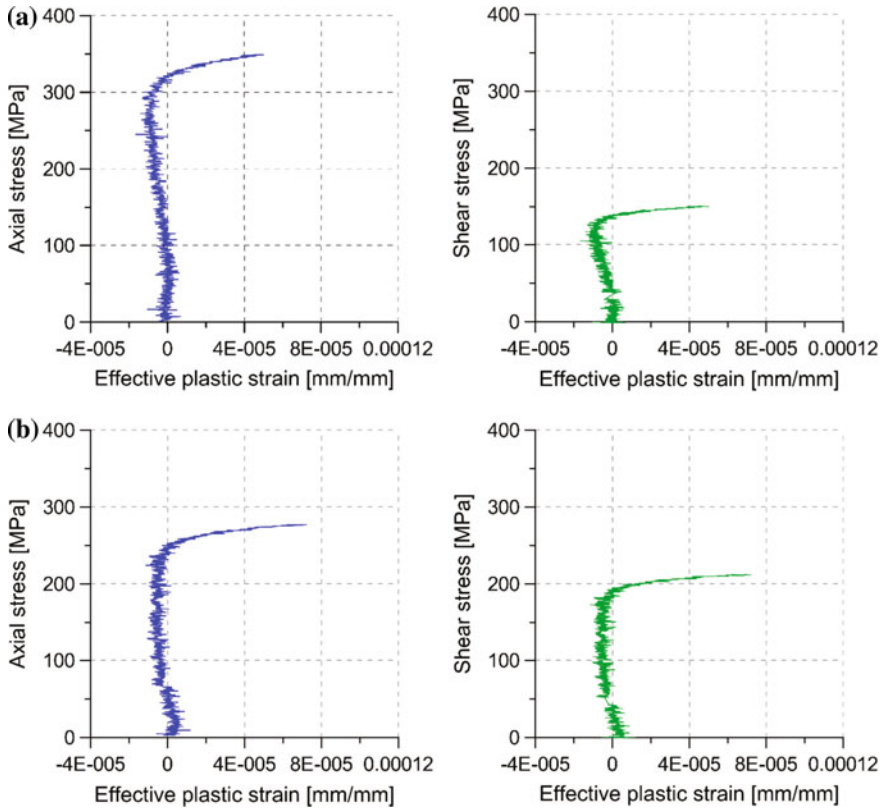


Fig. 7 Stress state components versus effective plastic strain for the yield point to be determined for the loading paths oriented by the angular increment equal to 22.5° (a) and 67.5° (b)

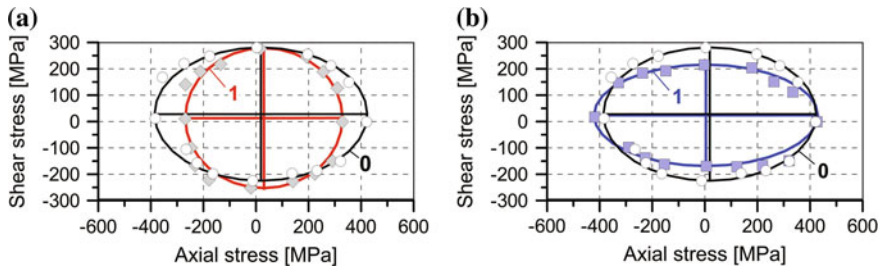


Fig. 8 Comparison of the initial yield surface (0) and subsequent locus (1) were examined after tension-compression (a) and torsion-reverse-torsion cycles (b) conducted at the strain amplitude equal to $\pm 0.8\%$

5.3 Results for the Material Tested Under Combination of Monotonic Tension and Cyclic Torsion

In the next part of the experimental programme the steel was subjected to combination of monotonic tension and cyclic torsion. The main aim of these tests was to investigate whether the presence of torsion cycles can influence an axial stress.

All tests were carried out at room temperature under strain control of the servo-hydraulic testing machine. Axial, shear and hoop strains were measured by means of the strain gauges bonded to the outer surface of the specimen and located near the terminal with strain gauges wired to form three temperature compensated bridge circuits corresponding to the appropriate strain components measurements.

The tests of monotonic tension assisted by cyclic torsion were carried out for cyclic strain amplitudes equal to ± 0.3 , ± 0.5 and $\pm 0.7\%$, and frequency of 0.5 Hz, Fig. 9a. For all experiments, variations of axial and shear stresses were registered versus time, Fig. 9b. After unloading an analysis of mechanical properties variations due to complex loading history induced was performed using again the concept of yield surface determined in the two-dimensional stress space (σ , τ). All yield surfaces were determined using the single specimen method (Kowalewski 1997; Kowalewski and Śliwowski 1997) for the offset strain equal to 0.005 %.

The experimental results from tests carried out according to the loading programme illustrated in Fig. 9a, are presented in Figs. 10, 11, 12, 13 and 14. Figure 10a shows a comparison of the standard tensile characteristic of the steel with stress-strain curves determined during tension assisted by torsion-reverse-torsion cycles for three values of the shear strain amplitude. As it is shown in Fig. 10, the torsion-reverse-torsion cycles associated with monotonic tension caused variations of the tensile characteristics. A significant decrease of the axial stress can be observed. An increase of the cyclic shear strain amplitude led to the further decrease of the

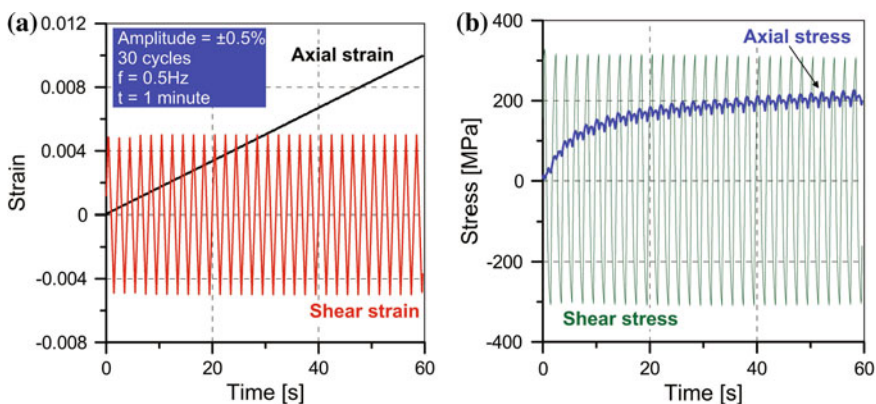


Fig. 9 Details of the experiment: strain signals (a), stress response (b) into the loading program shown in (a)

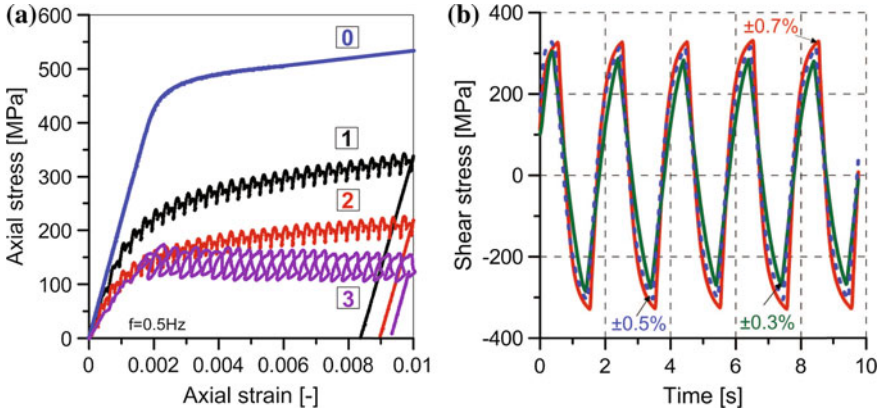


Fig. 10 Results of tests for the steel subjected to monotonic tension assisted by cyclic torsion: **a** Comparison of tensile curves; **b** Shear stress variations versus time; numbers denote: tensile characteristic (0); 1, 2, 3—tensile curves determined in assistance of torsion-reverse-torsion cycles at shear strain amplitude equal to: ± 0.3 , ± 0.5 , $\pm 0.7\%$, respectively

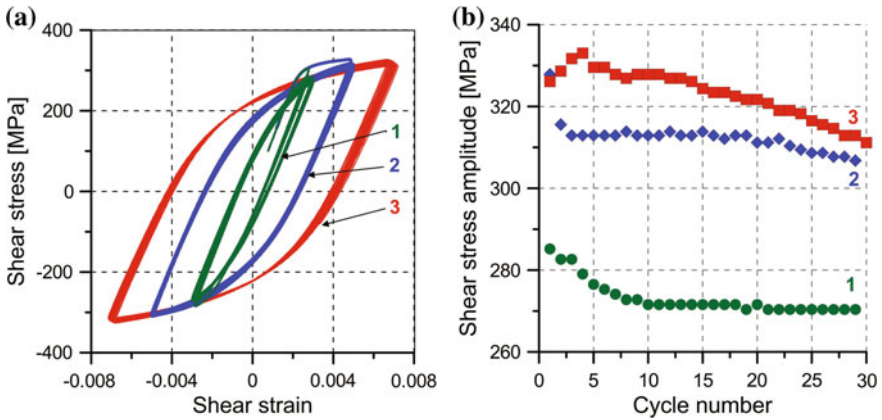
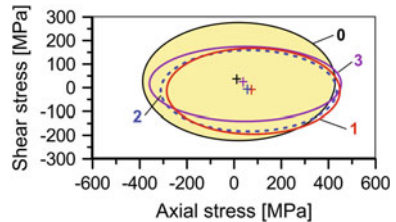


Fig. 11 Evolution of hysteresis loops **(a)** and variations of maximum values of shear stress versus cycle number **(b)** for cyclic strain amplitude equal to: $\pm 0.3\%$ (1), $\pm 0.5\%$ (2), $\pm 0.7\%$ (3)

Fig. 12 Initial yield surface(0) and subsequent yield loci after monotonic tension assisted by torsion cycles for shear strain amplitude equal to: $\pm 0.3\%$ (1), $\pm 0.5\%$ (2), $\pm 0.7\%$ (3)



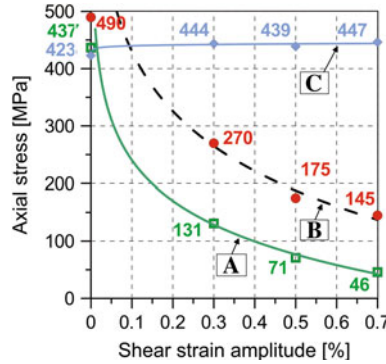


Fig. 13 Comparison of tensile stress variations determined during torsion cycles assistance for the offset strain equal to: (A) $- 5 \times 10^{-5}$, (B) $- 0.002$, and obtained during yield surface investigation (C) for the offset strain of 5×10^{-5}

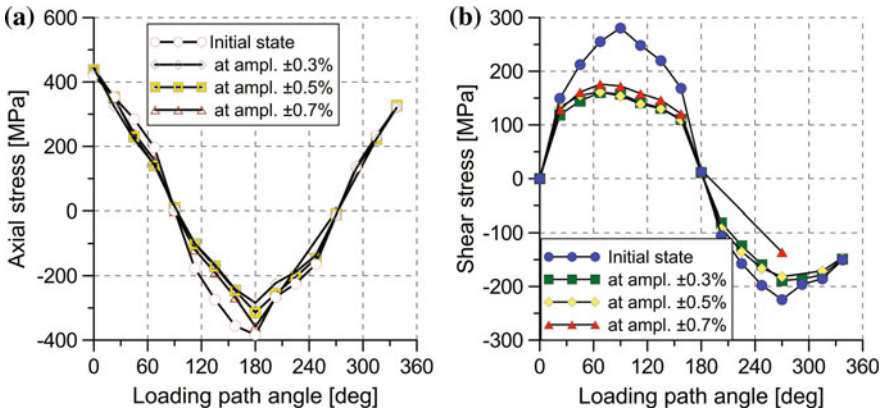


Fig. 14 Comparison of stress state components variations during yield surface investigations of the steel in the as-received state and after monotonic-cyclic loading combination for the shear strain amplitude being within a range from ± 0.3 to $\pm 0.7\%$

tensile stress. It is expressed for example by an axial stress drop corresponding to the axial plastic strain equal to 0.3 %, from 475 to 125 MPa. It has been shown that the effect can be much stronger for the copper, since such reduction was almost three times higher than that for the steel achieved (Kowalewski et al. 2014). In Fig. 10b the results of shear stress component variations are presented. Differences between maximum values of shear stress amplitude were rather small and did not exceed 50 MPa, despite of various shear strain amplitude levels used in the tests. The data presented in Fig. 10b was also used to elaborate hysteresis loop variations enabling an analysis of the material hardening or softening effects, Fig. 11. Variations of the peak values of hysteresis loops were shown in Fig. 11b. A character of their changes was not the same for each strain amplitude considered. In the case of the lowest strain

amplitude ($\pm 0.3\%$) the material exhibited softening effect expressed by gradual decrease of the maximum value of shear stress amplitude tending to the asymptotic level equal to 270 MPa. For higher shear strain amplitude ($\pm 0.5\%$) the saturation state was not achieved for the number of cycles applied in the test. The same situation was observed for the highest shear strain amplitude ($\pm 0.7\%$). Additionally in this case a shear stress variation was different than for the lower strain amplitudes. At the beginning of torsion cycles the hardening effect was evident, however, after five cycles the material exhibited a gradual softening effect.

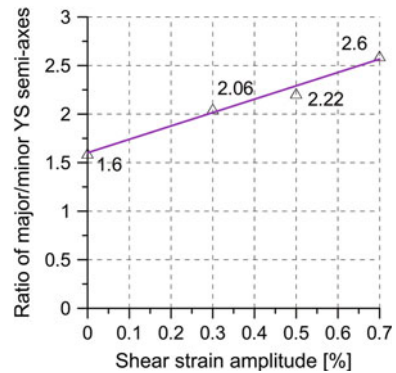
The experimental programme comprised also tests the aim of which was to check whether the axial stress reduction during tension assisted by cyclic torsion had the permanent character. The yield surface concept was again applied. It was conducted after examination of the steel under monotonic tension and torsion-reverse-torsion cycles. For each yield surface determined in the experimental programme the same offset strain equal to 0.005% was assumed. The representative results for the X10CrMoVNb9-1 steel are presented in Fig. 12. As it is clearly seen, the subsequent yield surfaces for the steel proved that the axial force reduction is only related to torsion cycles during monotonic tension. Looking at the magnitudes of tension stress instead of reduction a little increase can be observed. Therefore, it can be concluded that the comparison of the subsequent yield loci with the initial yield surface exhibits only an influence of the loading history applied, and moreover, proves a transient character of the axial stress drop, which can be solely attributed to cycles acting simultaneously.

This fact is more clearly reflected in Fig. 13 that presents the differences between tensile stresses determined at various levels of the shear strain amplitude. The curves A and B represent yield point variations determined on the basis of stress-strain curve from monotonic-cyclic loading test (Fig. 10) for plastic offset strain equal to 0.005 and 0.2%, respectively. The results denoted by C illustrate the yield points for tension determined after termination of monotonic tension assisted by cyclic torsion and taken from yield loci presented in Fig. 12. It is easy to notice that the yield point for tension, determined after loading history induced (curve C), achieved the average level close to 440 MPa. It is significantly higher than the yield points calculated on the basis of tensile curves obtained during tension tests assisted by torsion cycles (curve A).

Larger changes of yield loci were visible in the torsion direction (Figs. 12 and 13). The softening occurred for the positive shear stress is reflected by a reduction of the yield point around 100 MPa independently on the amplitude of torsion cycles. In the case of negative shear stress the same effect can be observed, however, a drop of yield point was dependent on the shear strain amplitude. For the strain amplitudes ± 0.3 , ± 0.5 , $\pm 0.7\%$ it attained magnitudes equal to 20, 25 and 100 MPa, respectively.

Some important effects are well reflected in Fig. 14 presenting variations of stress components versus loading paths orientation applied in the procedure for the yield surface determination. The axial stress component takes almost the same magnitudes independently on the loading history induced. There are also very close to the values obtained for the material in the as-received state. The shear stress component variations are sensitive into the loading path orientation. In the case of pure torsion

Fig. 15 The ratio of major/minor yield surface semi-axes versus shear strain amplitude



(90° and 270°) the greatest difference can be observed between shear stress for material in the as-received state and the same material pre-stressed by means of tension combined with cyclic torsion.

An interesting presentation of the results is shown in Fig. 15. It illustrates variations of the ratio between the major and minor axes of the yield surfaces as a function of the shear strain amplitude. As it is shown, in all cases we have material exhibiting an anisotropy in the sense of the isotropic Huber-von Mises yield condition. The ratio obtained for the steel in the as-received state was the nearest to that representing isotropic material. It is seen that for higher magnitudes of shear strain amplitude a degree of anisotropy became greater.

The results of tests containing combination of monotonic and cyclic loading can be modelled using Maciejewski and Mróz (2007, 2008) approach. In order to demonstrate opportunities of this model, the experimental data for the X10CrMoVNb9-1 steel will be used.

6 Simulation of Tensile Curve Variations Due to Application of Torsion Cycles Using the Maciejewski-Mróz Model

The Maciejewski-Mróz model may be applied for theoretical analysis of the elastic-plastic materials subjected to biaxial stress states realized on thin-walled tubular specimens loaded by combination of tension and torsion.

In order to demonstrate opportunities of this model, the experimental data for the X10CrMoVNb9-1 steel will be used. To discuss the process for determining necessary parameters in the combined tension and cyclic torsion, a thin walled tube of initial radius r_0 , length l_0 and wall thickness t_0 was considered. The alternating torsion was applied in order to reduce the axial stress and the axial force used, required to execute the process. To obtain uniform length variation, the axial strain and strain rate were $|\dot{\epsilon}_x| = \dot{\alpha}t$, $|\dot{\epsilon}_x| = \dot{\alpha}$, where $|\dot{\alpha}| = |\dot{i}|/l_0$. For the logarithmic strain measure there is $\epsilon_x = \ln(1 \pm l_0\dot{\alpha}t)$ and $|\dot{\epsilon}_x| = |\dot{i}|/l = \dot{\alpha}l/(1 \pm \dot{\alpha}t)$.

The shear strain is assumed to oscillate within the range $2\gamma_m$ and the period T . For piecewise linear oscillation, we have $\dot{\beta} = \dot{\gamma}_{xy} = 4\gamma_m/T$. Marking the ratio of rates of shear and axial strains by η gives

$$\eta = \frac{\dot{\beta}}{\dot{\alpha}} = \text{const}, \quad \dot{\beta} = \frac{4\gamma_m}{T}, \quad \dot{\beta} > 0, \quad \dot{\alpha} > 0. \quad (16)$$

For the piecewise linear shear strain control (Fig. 9a) there are two essential parameters controlling the process, namely the strain rate ratio η and the torsion amplitude $2\gamma_m$.

Maciejewski and Mróz (2008) studied the cyclic deformation process for different values of η and γ_m after initial model calibration and verification for uniaxial cyclic loading. The cyclic hardening model based on the classical Huber-von Mises yield function and the kinematic hardening rule proposed by Armstrong and Frederick (1966). The small strain framework is assumed. This is justified by the domain of application to cyclic loading conditions applied in the experimental programme. A partition of the total strain tensor into elastic strain and plastic strain is assumed, where elasticity is described by the linear Hooke's Law. The yield condition and the plastic flow rule are expressed by the following equations:

$$\begin{aligned} f_p &= \sqrt{\frac{3}{2} (\mathbf{S} - \mathbf{X}) (\mathbf{S} - \mathbf{X})} - \sigma_p(\xi) = 0, \\ \dot{\boldsymbol{\varepsilon}}^p &= \dot{\lambda} \frac{\partial f_p}{\boldsymbol{\sigma}} = \dot{\lambda} \frac{\frac{3}{2} (\mathbf{S} - \mathbf{X})}{\sigma_p}, \quad \dot{\lambda} \geq 0, \quad f_p \leq 0, \quad \dot{\lambda} f_p = 0, \end{aligned} \quad (17)$$

where

$$\dot{\lambda} = \sqrt{\frac{2}{3} \dot{\boldsymbol{\varepsilon}}^p \dot{\boldsymbol{\varepsilon}}^p},$$

\mathbf{S} is the stress deviator

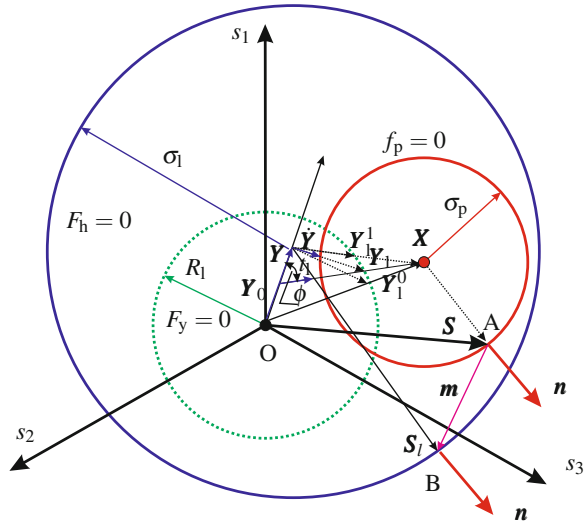
$$\mathbf{S} = \boldsymbol{\sigma} - \frac{1}{3} \text{tr} \boldsymbol{\sigma} \mathbf{1},$$

\mathbf{X} is the back stress deviator and σ_p is the yield stress. Here \cdot denotes the scalar product and $(\dot{\cdot})$ over a symbol denotes the rate with respect to a process evolution parameter. The back stress evolution rule can be written in the form

$$\dot{\mathbf{X}} = \dot{\lambda} \gamma (\mathbf{S}_1 - \mathbf{S}) = \dot{\lambda} \gamma (\mathbf{X}_1 - \mathbf{X}) = \dot{\lambda} \gamma \boldsymbol{\rho} \Delta, \quad (18)$$

where γ is material parameter and \mathbf{S}_1 and \mathbf{X}_1 are the saturation states associated with the instantaneous plastic strain rate orientation. Considering a deformation process with constant orientation of the plastic strain rate vector, the stress \mathbf{S} tends to its limiting value \mathbf{S}_1 (on the hardening surfaces $F_h = 0$) coaxial with the plastic strain trajectory for specified $\dot{\boldsymbol{\varepsilon}}^p$ of constant orientation, Fig. 16.

Fig. 16 Concept of the three-surface model of Maciejewski-Mróz



Consider now a more general model for which the hardening surface is allowed to translate and expand. The hardening surface equation is assumed in the following form

$$F_h = \sqrt{\frac{3}{2} (\mathbf{S}_1 - \mathbf{Y}) (\mathbf{S}_1 - \mathbf{Y})} - \sigma_1(\xi) = 0, \quad (19)$$

where $\sigma_1(\xi)$ is the hardening of the surface radius, and its translation rule in similar form to (18) as the Eq. (20), where \mathbf{Y} is the second level back stress, γ_1 is the material parameter, and \mathbf{Y}_l is the limit convergence point

$$\begin{aligned} \dot{\mathbf{Y}} &= \dot{\lambda} \gamma_1 (\mathbf{Y}_l - \mathbf{Y}) \quad \text{for } r = \sqrt{\frac{3}{2} \mathbf{X} \mathbf{X}} > R_l, \\ \dot{\mathbf{Y}} &= \dot{\lambda} \gamma_1 (\mathbf{X} - \mathbf{Y}) \quad \text{for } r \leq R_l \end{aligned} \quad (20)$$

Assume that \mathbf{Y}_l lies on the limit surface whose equation can be written in the form

$$F_y = \sqrt{\frac{3}{2} \mathbf{Y}_l \mathbf{Y}_l} - R_l(\xi) = R - R_l = 0, \quad (21)$$

where R_l is the limit surface radius.

The back stress \mathbf{Y} evolution rule is obtained by assuming that \mathbf{Y} tends to the radial state \mathbf{Y}_1 on the limit surface F_y . The limit state \mathbf{Y}_1 is specified by the vector $\mathbf{X} - \mathbf{Y}_0$, where $\mathbf{Y}_0 = f \mathbf{Y}$, $0 \leq f \leq 1$, so we have

$$\mathbf{Y}_1 = \mathbf{Y}_0 + t_1 \rho, \quad t_1 = \frac{\mathbf{X} - \mathbf{Y}_0}{\|\mathbf{X} - \mathbf{Y}_0\|}, \quad \mathbf{Y}_0 = f \mathbf{Y}, \quad 0 \leq f \leq 1. \quad (22)$$

Here t_1 is the unit vector along $\mathbf{X} - \mathbf{Y}_0$, and the scalar factor ρ . The fraction factor f is identified from the multiaxial ratcheting tests, for instance from combined monotonic tension—cyclic torsion tests. It turns out that the position of the limit state t_1 is very essential in accurate prediction of the ratcheting strain. When the back stress \mathbf{X} is represented by the point inside the limit surface $F_y = 0$, then according to (19) we set $\mathbf{Y}_1 = \mathbf{X}$. The translation rule of the first level back stress \mathbf{X} is now modified and instead of (18) the following formula can be written

$$\dot{\mathbf{X}} = \dot{\lambda} \gamma (\mathbf{X}_1 - \mathbf{X}) + \dot{\mathbf{Y}}, \tag{23}$$

where $\dot{\mathbf{Y}}$ is now the convective rate.

It is assumed that both limit, hardening and yield surfaces may expand, but the ratio of their diameters is constant, thus:

$$k_l = \frac{\sigma_l}{R_l} = \text{const}, \quad k_p = \frac{\sigma_l}{\sigma_p} = \text{const}. \tag{24}$$

The isotropic expansion of surfaces $F_h = 0$, $f_p = 0$, $F_y = 0$ are dependent on the amplitude of cyclic stress. Assumption that there is no isotropic hardening effect for $l \leq l_0$ (Fig. 17), leads to

$$\dot{\xi} = \begin{cases} \dot{\lambda} \left(\frac{l - l_0}{1 - l_0} \right)^k = L^k, & l > l_0, \\ 0, & l \leq l_0, \end{cases} \tag{25}$$

$$l = 1 - \frac{|\Delta|}{2(\sigma_l - \sigma_p)}, \quad \Delta = |AB| = |\mathbf{S}_1 - \mathbf{S}|.$$

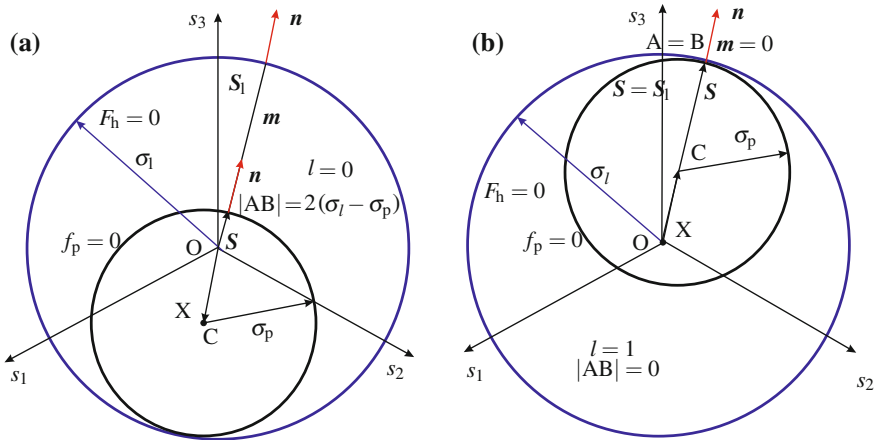


Fig. 17 Translation of the yield surface along the AB path: **a** initial position: $l = 0$, $|AB| = 2(\sigma_l - \sigma_p)$, **b** ultimate position: $l = 1$, $|AB| = 0$

The weighting parameter l depends on the distance of the stress point to the hardening surface. When the yield surface approaches the hardening surface, then $l \rightarrow 1$, but for the other cases there is $0 \leq l \leq 1$. Thus, the deformation paths more distant from the hardening surface induce lower hardening than the paths approaching the surface $F_h = 0$. Similarly, the cycles of lower stress or strain amplitudes correspond to lower hardening rates than those of higher amplitudes.

Similar notion for the evolution of isotropic hardening was introduced first by Chaboche et al. (1979), where the strain range dependence of cyclic hardening was incorporated into constitutive modeling of isotropic hardening. Later, Ohno (1982) proposed the cyclic non-hardening region in the plastic strain space and assumed that when plastic strain changes inside the region under cyclic loading, no evolution of isotropic hardening occurs, leading to the dependence of cyclic hardening on strain range. Such concept has been used and further developed in other works (e.g., Ohno and Kachi 1986; Ohno et al. 1986; Chaboche 1986, 1989; Kang et al. 2002). Instead of plastic strain space Yoshida and Uemori (2002) specified the cyclic non-hardening region in the deviatoric stress space for formulating a large-strain cyclic plasticity model. The extensive review of plastic and viscoplastic hardening models applicable for simulation of cyclic deformation was presented by Kang et al. (2008).

In our analysis the isotropic hardening rule is assumed in a form

$$\sigma_l = \sigma_{l0} + (\sigma_{lf} - \sigma_{l0}) (1 - e^{-w\xi}), \quad (26)$$

where σ_{l0} is the initial radius of the hardening surface and σ_{lf} is the asymptotic value, w is the constant hardening parameter.

In the case of the X10CrMoVNb9-1 steel the model was used to simulate its cyclic response on the basis of tests presented in Figs. 9 and 10. The material parameters have been calibrated from cyclic pure tension and torsion tests. The model parameters for three-surface models are: the elasticity moduli $E = 200$ GPa, $n = 0.30$, hardening surface radius is $\sigma_{l0} = 520$ MPa, $\sigma_{lf} = 540$ MPa, $l_0 = 0.5$, $\kappa = 1$, $w = 1$, $k_p = 1.81$, $k_l = 4.0$, and translation rule parameters $\gamma = 550$, $\gamma_l = 55$, $f = 1$.

The results of uniaxial tests in simple cyclic tension-compression and cyclic torsion are presented in Fig. 18 and experimental data for axial tension combined with cyclic torsion are shown in Fig. 19. For the piecewise linear shear strain control (Fig. 9a) there are two essential parameters controlling the process, namely the strain rate ratio $\eta = \dot{\gamma}_{xy}/\dot{\epsilon}_x$ and the torsion amplitude.

The experimental results in Fig. 19 are compared with predictions obtained using the three-surface model for torsion strain amplitude equal to 0.3%, ($\eta = 72$) and 0.7%, ($\eta = 168$). It can be observed that the model predictions are close to experimental curves for all values of shear strain amplitude considered. Since the three-surface model provides realistic predictions, it seems to be reasonable to use it in a further planned analysis of the X10CrMoVNb9-1 steel under combined loading.

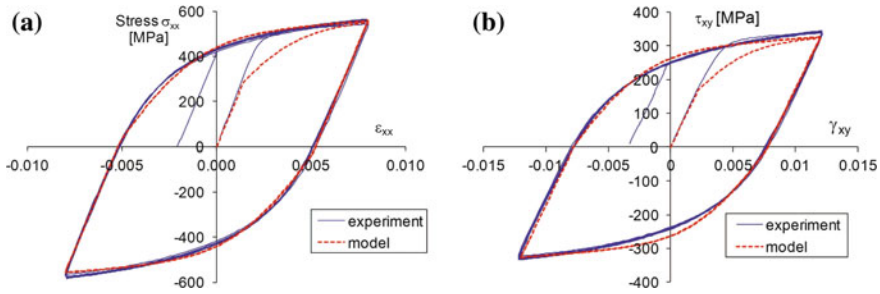
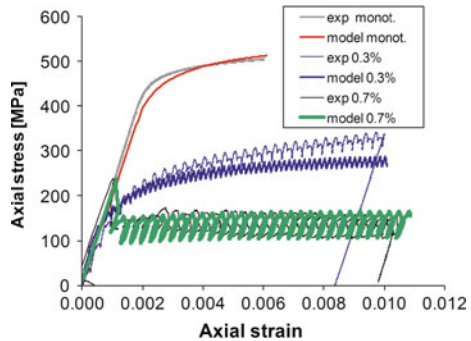


Fig. 18 Experimental and numerical hysteresis loops of the X10CrMoVNb9-1 steel: **a** cyclic tension-compression; **b** cyclic torsion

Fig. 19 Comparison of the three-surface model predictions with experimental data for the X10CrMoVNb9-1 steel subjected to monotonic tension assisted by torsion-reverse-torsion cycles at various processing parameters



7 Summary and Concluding Remarks

The experimental programme carried out on the X10CrMoVNb9-1 steel had to provide a knowledge necessary for better understanding of phenomena taking place during combination of monotonic and cyclic loading in the range of small deformations. The results exhibited that superimposing cyclic torsion on monotonic tension reduces the axial stress significantly. In many industrial applications such effect would extend the lifetimes of some engineering components. This is especially important when considering the manufacturing costs of these elements which are extremely high. The applied loading combinations considered in this paper give a promising tool for reduction of an acting axial force, and therefore, ensure more beneficial working conditions in comparison to similar loading conditions but realized within large deformation range. This may lead to the lifetime extension of some working elements of machines used to fabricate many products in the form of rods, tubes, etc. applying less energy, and as a consequence, generating less costs.

In order to gain a more thorough knowledge of the effects related to various combinations of monotonic and cyclic loading the microscopic observations are necessary. They should be carrying out “on line” with the loading process, what is

difficult and requires adequate equipment. Our current experimental facility does not enable a performance of such investigations at the moment.

Experimental evaluation of the influence of prior loading history in the steel due to tension assisted by cyclic torsion at ambient temperature on the shape and dimensions of yield surfaces are also reported in this paper. An increase of torsion cycles amplitude caused essential variations of the yield surface dimensions measured by the ratio of the major to minor axes. The ratio changed from 1.6 for the material in the as-received state to 2.6 for the material pre-stressed due to combination of monotonic tension and cyclic torsion for the highest shear strain amplitude applied in this research. It means that the tested steel became more anisotropic due to cycles under higher strain amplitudes.

The theoretical results presented in the paper show that phenomena observed during combination of monotonic and cyclic loading can be successfully simulated applying the Maciejewski-Mróz three-surface model.

References

- Armstrong PJ, Frederick CO (1966) A mathematical representation of the multiaxial Bauschinger effect. CEGB report RD/B/N731, Berkeley Nuclear Laboratories
- Barlat F, Lian J, Baudalet B (1988) A yield function for orthotropic sheets under plane stress conditions. In: Proceedings 8th international conference strength of metals and alloys, Tampere, Finland, August 1988, vol 1. Pergamon Press, New York, pp 283–288
- Barlat F, Lege DJ, Brem JC (1991) A six-component yield function for anisotropic materials. *Int J Plast* 7(7):693–712
- Bochniak W, Korbel A (1999) Extrusion of CuZn39Pb2 alloy by the KOBO method. *Eng Trans* 47(3):351–367
- Bochniak W, Korbel A (2000) Plastic flow of aluminium extruded under complex conditions. *Mater Sci Technol* 16:664–699
- Bochniak W, Korbel A (2003) KOBO type forming: forging of metals under complex conditions of process. *J Mater Process Technol* 134(1):120–134
- Bochniak W, Korbel A, Szyndler R (2001) Innovative solutions for metal forming. In: Proceedings international conference MEFORM 2001, vol 239. Institut für Metallformung, Freiberg/Riesa
- Bochniak W, Korbel A, Szyndler R, Hanarz R, Stalony-Dobrzanski F, Błaz L, Snarski P (2006) New forging method of bevel gears from structural steel. *J Mater Process Technol* 173(1):75–83
- Chaboche J, Van Dang K, Cordier G (1979) Modelization of the strain memory effect on the cyclic hardening of 316 stainless steel. In: Transactions of SMiRT 5, vol L, paper L11/3
- Chaboche JL (1986) Time-independent constitutive theories for cyclic plasticity. *Int J Plast* 2:149–188
- Chaboche JL (1989) Constitutive equations for cyclic plasticity and cyclic viscoplasticity. *Int J Plast* 5:247–302
- Chaboche JL (1991) On some modifications of kinematic hardening to improve the description of ratcheting effects. *Int J Plast* 7:661–678
- Correa ECS, Aguilar MTP, Silva EMP, Cetlin PR (2003) The effect of sequential tensile and cyclic torsion straining on work hardening of steel and brass. *J Mater Process Technol* 142(1):282–288
- Dafailas YF, Popov EP (1976) Plastic internal variables formalism of cyclic plasticity. *Trans ASME J Appl Mech* 43:645–651
- Goldenblat II, Kopnov VA (1965) Strength of glass-reinforced plastics in the complex stress state. *Mech Polym* 1(2):54–59

- Gotoh M (1977) A theory of plastic anisotropy based on a yield function of fourth order (plane stress)—part I and II. *Int J Mech Sci* 19:505–512
- Hashiguchi K (2005) Generalized plastic flow rule. *Int J Plast* 21:321–351
- Hassan T, Kyriakides S (1992) Ratcheting in cyclic plasticity, part I: uniaxial behavior. *Int J Plast* 8:117–146
- Hecker SS (1976) Experimental studies of yield phenomena in biaxially loaded metals. In: Stricklin A, Saczalski KC (eds) *Constitutive equations in viscoplasticity: computational and engineering aspects*. Proceedings of the winter annual meeting of the American Society of Mechanical Engineers, vol 20. ASME, AMD, New York, pp 1–33
- Hill R (1956) *The mathematical theory of plasticity*. Clarendon Press, Oxford
- Hill R (1990) Constitutive modelling of orthotropic plasticity in sheet metals. *J Mech Phys Solids* 38:405–417
- Ikegami K (1975a) An historical perspective of the experimental study of subsequent yield surfaces for metal I. *P Soc Mater Sci* 24:491–505
- Ikegami K (1975b) An historical perspective of the experimental study of subsequent yield surfaces for metal II. *P Soc Mater Sci* 24:709–719
- Kang G, Gao Q, Yang X (2002) A visco-plastic constitutive model incorporated with cyclic hardening for uniaxial/multiaxial ratcheting of SS304 stainless steel at room temperature. *Mech Mater* 34:521–531
- Kang G, Gao Q, Yang X (2008) Ratcheting: recent progresses in phenomenon observation, constitutive modelling and application. *Int J Fatigue* 30(8):1448–1472
- Kong LX, Hodgson PD (2000) Constitutive modeling of extrusion of lead with cyclic torsion. *Mater Sci Eng: A* 276:32–38
- Kowalewski ZL (1997) Assessment of cyclic properties of 18G2A low-alloy steel at biaxial stress state. *Acta Mech* 120:71–89
- Kowalewski ZL, Śliwowski M (1997) Effect of cyclic loading on the yield surface evolution of 18G2A low-alloy steel. *Int J Mech Sci* 39(1):51–68
- Kowalewski ZL, Szymczak T, Rutecka A (2011) Variations of mechanical parameters during monotonic deformation conducted at presence of torsion-reverse-torsion cycles (in Polish). *Mech Rev* 2:27–33
- Kowalewski ZL, Szymczak T, Maciejewski J (2014) Material effects during monotonic-cyclic loading. *Int J Solids Struct* 51(3–4):740–753
- Maciejewski J, Mróz Z (2007) Modelling of plastic deformation of metals at complex loading paths (in Polish). In: *I congress of polish mechanics*, Warsaw, Poland, 28–31 August 2007
- Maciejewski J, Mróz Z (2008) An upper-bound analysis of axisymmetric extrusion assisted by cyclic torsion. *J Mater Proc Technol* 206:333–344
- Mayama T, Sasaki K, Ishikawa H (2007) A constitutive model of cyclic viscoplasticity considering changes in subsequent viscoplastic deformation due to the evolution of dislocation structures. *Int J Plast* 23:915–930
- Mróz Z (1967) On the description of anisotropic workhardening. *J Mech Phys Solids* 15:163–175
- Ohno N (1982) A constitutive model of cyclic plasticity with a nonhardening strain region. *ASME J Appl Mech* 49:721–727
- Ohno N, Kachi Y (1986) A constitutive model of cyclic plasticity for nonlinear hardening materials. *ASME J Appl Mech* 53:395–403
- Ohno N, Takahashi Y, Kuwabara K (1986) Constitutive modeling of anisothermal cyclic plasticity of 304 stainless steel. *ASME J Eng Mater Tech* 11:106–114
- Ota T, Shindo A, Fukuoka H (1959) A consideration on anisotropic yield criterion. In: *Proceedings of the 9th Japan national congress for applied mechanics*, pp 117–120
- Phillips A, Tang JL (1972) The effect of loading path on the yield surface at elevated temperatures. *Int J Solids Struct* 8:463–474
- Szczepiński W (1993) On deformation-induced plastic anisotropy of sheet metals. *Arch Mech* 45:3–38

- Szczepiński W, Dietrich L, Miastkowski J (1990) *Experimental methods in mechanics of solids*, Elsevier, New York (Chap. Plastic properties of metals)
- Szymczak T, Kowalewski ZL (2012) Variations of mechanical parameters and strain energy dissipated during tension-torsion loading. *Arch Metall Mater* 57(1):193–197
- von Mises R (1928) Mechanik der plastischen Formänderung von Kristallen. *Zeitschrift für Angewandte Mathematik und Mechanik* 8(3):161–185
- Wang ZL, Dafailas YF, Shen CK (1990) Bounding surface hypoplasticity model for sand. *J Eng Mech* 116:983–1003
- Yoshida F, Uemori T (2002) A model of large-strain cyclic plasticity describing the Bauschinger effect and work hardening stagnation. *Int J Plast* 18:661–686

Fracture of Cortical Bone Tissue

Simin Li, Adel Abdel-Wahab, Emrah Demirci
and Vadim V. Silberschmidt

Abstract In this chapter, mechanical behaviours of a unique type of composite material—cortical bone tissue—are considered for different length scales. Both experimental and computational approaches are discussed in this study to evaluate the effects of mechanical anisotropy and structural heterogeneity on the fracture process of cortical bone. First, variability and anisotropic mechanical behaviour of cortical bone tissue are characterised and analysed experimentally for different loading conditions and orientations. Then, results from the experimental studies are used to develop finite-element models across different length-scales to elucidate mechanical and structural mechanisms underpinning the anisotropic and non-linear fracture processes of cortical bone.

Keywords Cortical bone · Fracture · Variability · Anisotropy · Microstructure · Extended finite-element method (X-FEM)

1 Introduction

Research on the mechanical behaviour of the naturally occurring composite material, cortical bone tissue, has attracted increasing attention over the past few decades, not only because bone plays an important role in structural integrity of a musculoskeletal system, but also due to our growing knowledge of its intrinsic hierarchical structure and heterogeneous mechanical properties. This mineralized biological tissue provides both sufficient stiffness and toughness for the skeleton system to serve as the

S. Li · A. Abdel-Wahab · E. Demirci · V.V. Silberschmidt (✉)
Wolfson School of Mechanical and Manufacturing Engineering,
Loughborough University, Leicestershire, UK
e-mail: V.Silberschmidt@lboro.ac.uk

S. Li
e-mail: S.Li@lboro.ac.uk

A. Abdel-Wahab
e-mail: A.A.Abel-Wahab@lboro.ac.uk

E. Demirci
e-mail: E.Demirci@lboro.ac.uk

© Springer International Publishing Switzerland 2015
H. Altenbach and M. Brünig (eds.), *Inelastic Behavior of Materials
and Structures Under Monotonic and Cyclic Loading*, Advanced
Structured Materials 57, DOI 10.1007/978-3-319-14660-7_8

main load-bearing component. And yet, it is light-weight to allow flexible movements around joints through attachment of muscles. Being a living tissue, cortical bone also has the ability to adapt (both its shape and internal structure) to mechanical environment through processes called *modelling and remodelling* (Martin and Burr 1989; Currey 2013). The excellent mechanical ability of cortical bone is defined by its main building blocks: on the one hand, a ‘soft’ organic matrix (mainly type-I collagen) providing sufficient compliance and collagen framework for various bioactivities; on the other hand, the ‘hard’, carbonated apatite nano-particles (hydroxyapatite) providing strength and rigidity. Together, they form a hierarchically organized composite material, which could be categorised into several hierarchical organizations from nano-scale to macro-scale levels (Weiner and Wagner 1998; Ritchie et al. 2005; Launey et al. 2010; Currey 2012).

At the nano-scale, bone is composed of mineralised collagen fibril bundles and extrafibrillar mineral particles (Weiner and Wagner 1998; Rho et al. 1998; Currey 1999; Fratzl et al. 2004). At the sub-micro-scale, cortical bone is laid down in layers of a lamellar structure (3–7 μm in thickness) that is similar to that of plywood composite parallel within each layer, but having a small angle between adjacent layers (Ascenzi and Benvenuti 1986). Across a bone section, concentric layers of lamellae along with the surrounding central vascular channel form the most prominent structure under microscope—Haversian system (containing an *osteon* and a *Haversian canal*) embedded into the remnants of discrete layers of lamellae bone called *interstitial matrix*. Osteons are, on average, 200 μm in diameter and up to 1 cm long cylindrical structures, typically arranged in parallel to a long bone’s main axis (Ethier and Simmons 2007). In addition, a network of canals and channels formed across the bone’s cortex accommodates blood vessels, a nervous system and bone cells; those large canals, on average 50–90 μm in diameter, parallel to the osteon axis are called *Haversian canals*; those channels, running perpendicular to Haversian canals and interconnecting adjacent osteons and Haversian canals, are called *Volkman canals* (Martin and Burr 1989). As a living tissue, bone also houses living cells such as *osteocytes* that live within an oblong space called *lacunae*, which is connected to the surrounding region by a star-like network of miniature-channels called *canaliculi*. The latter are responsible for exchange of nutrients and waste between osteocytes (Ethier and Simmons 2007). The interface which can often be observed between the secondary osteons and interstitial matrix as a result of remodelling process is called *cement line*; it is a 2–5 μm thick interface layer that plays a key role in the bone’s mechanical behaviour, especially its fracture (Martin and Burr 1989; Currey 2013). However, the opinions in the literature with regard to the mechanical properties of cement line are rather controversial. Different experimental observations reported that the cement line can act either as a toughening mechanism, deflecting a crack from osteons, or as a weakening path that facilitates the crack initiation (Ritchie et al. 2005; Currey 2012). At the meso-scale, the dense and thick outer layer of cortical bone and the porous sponge-like trabecular bone make up the tissue-level bone structure (Peterlik et al. 2006). All these hierarchical levels work together in accord, complementing each other to achieve enhanced macroscopic mechanical properties of the bone tissue at the full-bone scale (Peterlik et al. 2006).

Macroscopically, the deformation mechanisms of bones differ from those of metals, polymers and composites since bones consist of a living tissue with a continuously evolving hierarchical microstructure. Mechanical properties of cortical bone vary not only from bone to bone; they demonstrate a spatial variability even within the same bone due to changes of the underlying microstructure (Abdel-Wahab et al. 2011; Li et al. 2013b). They also depend considerably on a loading mode and orientation. Mechanical properties of cortical bone, such as the Young's modulus, yield strain and ultimate stress in a longitudinal direction, i.e. parallel to osteons, were reported to be significantly higher than those in a transverse direction, i.e. perpendicular to osteons (Reilly and Burstein 1975). Dissimilar mechanical properties measured by nano-indentation across different microstructural constituents provided further evidence on its heterogeneous and anisotropic mechanical behaviour (Rho et al. 1997). Furthermore, it was also reported that cortical bone tissue is able to sustain higher yield and ultimate stresses in compression than that in tension (Reilly and Burstein 1975; Thompson et al. 2001; Yeni and Fyhrie 2003). Mercer et al. (2006) suggested that the material's porous structure could directly affect the deformation mechanism under tension and compression (Mercer et al. 2006), which coincides with the deformation patterns observed elsewhere (Boyce et al. 1998). To further complicate matter, results from several authors (Abdel-Wahab et al. 2011; Li et al. 2013b; Bonney et al. 2011) have all indicated a statistically significant variance of mechanical properties at different anatomical sites of the cortical bone (Abdel-Wahab et al. 2011; Bonney et al. 2011). Considering the wide spectrum of material properties of cortical bone and its intricate deformation processes associated with various loading modes and orientations, a further investigation is needed to elucidate the effect of variations in material properties in relation to the local regions and underpinning microstructural constituents.

Microscopically, the intrinsic micro-architecture of cortical bone has a significant effect on its macroscopic mechanical and fracture properties. Anisotropic deformation and fracture behaviours observed at macroscopic level are largely attributed to the preferential alignments of micro-constituents at subsequent length-scales, such as osteons and Haversian canals at micro-scale, or collagen fibrils and mineral crystals at nano-scale (Peterlik et al. 2006). From a fracture-toughness perspective, intricate structural hierarchy and material heterogeneity observed in cortical bone tissue can often lead to an improved fracture resistance owing to the formation of various fracture toughening mechanisms (Ritchie et al. 2005; Launey et al. 2010). Previous experimental results reported orientation-dependent fracture toughness, which had a higher value for fracture perpendicular to osteons' direction and considerably low value when fracture was parallel to it (Ritchie et al. 2005; Nalla et al. 2005a; Martin and Boardman 1993; Behiri and Bonfield 1989). A ratio between the high and low fracture toughness for crack propagation in different directions ranges from 1.5 to 2.4 (Ritchie et al. 2005; Nalla et al. 2004a, 2005b) depending on

- (a) interaction of a propagating crack with respect to the microstructural features and
- (b) activation of respective toughening mechanisms: formation of microcracks in the vicinity of the main crack due to stress concentrations ahead of crack tip (Ziopoulos and Currey 1994; Ziopoulos et al. 1996; Vashishth et al. 2003), crack deflection and blunting at cement lines that are weak interfaces at the boundaries of secondary osteons (Liu et al. 1999), ligament bridging in the wake zone behind the crack tip (Nalla et al. 2004b, 2005a; Martin and Boardman 1993; Behiri and Bonfield 1989).

Being a dynamic living tissue, cortical bone has the ability to continuously remodel, repair and adapt itself to the surrounding environment. Unlike most engineering composite materials, which are manufactured based on predefined structure and volume fraction of their constituents and, consequently, have a limited variability on their mechanical properties, the distribution and volume fraction of the microstructure constituents in a cortical bone can differ dramatically from its one part to another. As a result, toughness varies from 920 to 2,780 N/m (Ritchie et al. 2005) for the same type of bone tested under the same experimental configuration and material orientation. This variability is significant even for different cortices of a single bone (Bonney et al. 2011). However, there is a rather limited number of studies available to focus on unveiling a potential correlation between the variation of microstructure and variability of the mechanical behaviour of cortical bone.

Understanding of underpinning mechanisms of, and processes associated with, damage and fracture is key for prevention and diagnosis of bone-fracture related traumas. In order to do so, the mechanical properties of cortical bone need to be characterised at different length-scales. This is especially important for subsequent implementation of numerical models, incorporating materials properties that depend fully on the accuracy and understanding of the experimental results.

To the author's knowledge, there is no single-source study available in literature that provides a full comparison of the dissimilar deformation and damage behaviours of bovine cortical bone for both loading conditions and orientations. Nor there is a systematic study on the variability of mechanical properties of cortical bone. Hence, in this chapter, uniaxial tension and compression studies were first conducted for a direct comparison of anisotropy and variability of mechanical properties of bovine cortical bone; then, fracture toughness for three crack-propagation directions was measured to characterise the anisotropic fracture resistance of cortical bone. Additionally, to comprehend our understanding of the correlation between heterogeneity of the microstructural constituents and the variability of the macroscopic mechanical properties, the distribution of microstructural constituents were analysed. These studies allowed a complete set of material properties to be extracted and used to assist the development of accurate finite-element models to evaluate fracture process in microstructured cortical bone tissue.

2 Mechanical Properties of Cortical Bone Tissue at Macro-Scale

2.1 Variability of Anisotropic Mechanical Behaviour in Tension and Compression

Uniaxial tensile and compressive tests were conducted to characterise the deformation behaviours of cortical bone at different loading conditions and orientations.

Specimens used for this entire study were obtained from mid-diaphysis of fresh bovine femoral bones from a local butchery shop soon after slaughter. Specimen preparation and storage procedures followed precisely with generally adopted methods in Abdel-Wahab et al. (2011), Roe et al. (1988), Rho and Pharr (1999), details can be found in Li et al. (2013a, 2014). Dumb-bell shape specimens (15 mm in gauge length \times 5 mm \times 2 mm) oriented along both the longitudinal and transverse directions were prepared and divided into four groups according to the anatomical positions: anterior, medial, posterior and lateral for uniaxial tension tests (Fig. 1). The same categorisation was applies to the cylindrical-shaped specimens (\varnothing 5 mm \times 5 mm) for uniaxial compression test.

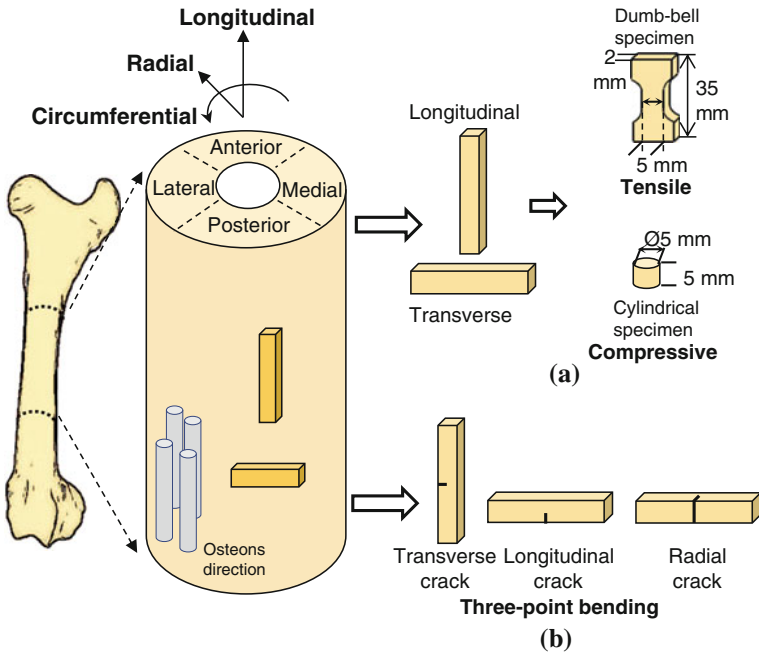


Fig. 1 Schematic illustration of specimen preparation process for: **a** uniaxial tension and compression tests; **b** three-point bending tests

Experiments with specimens from four different quadrants of the bone were performed on an Instron 3366 (Instron, USA) system with a 10 kN load cell under quasi-static loading conditions. Displacements were measured using an extensometer (2630 Series, Instron) and a linear variable differential transducer (LVDT) sensor (2601 Series, Instron) for uniaxial tensile and compressive tests, respectively. The detailed experimental procedure can be found in Li et al. (2013b).

2.1.1 Results and Analysis

The obtained results (detailed in Li et al. 2013b) are well correlated with those reported in literature (Reilly and Burstein 1975) and indicate that the mechanical response of cortical bone diverge dramatically under different loading conditions and orientations. Among the material properties measured for four anatomic quadrants, two orientations and two loading modes, the anterior quadrant has the highest Young’s modulus in longitudinal direction, while the medial quadrant has the highest one in transverse direction (Fig. 2). The lowest values are in lateral and posterior quadrants for longitudinal and transverse directions, respectively. The difference between the highest and lowest values of the Young’s modulus in each orientation is more than 20%. The relations across different quadrants (Factor A) and loading

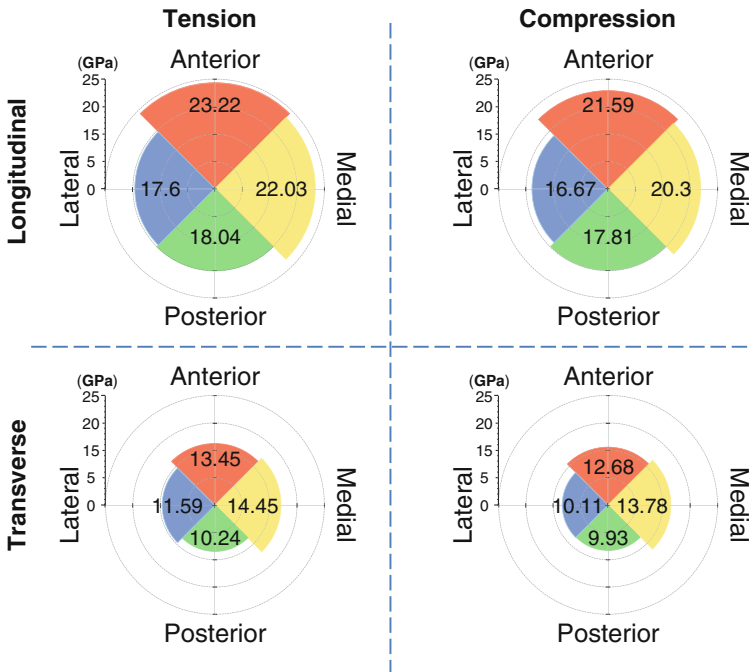


Fig. 2 Variability of Young’s modulus across cortices for longitudinal and transverse directions

modes (Factor B) were compared in terms of significance of variances using the two-way ANOVA analysis ($\alpha = 0.05$) with a Tukey HSD test. Overall, the results show a statistical significance in factor A (between cortices), but there is no uniform significance in factor B (between loading modes). The interaction between the two factors appears to be negative, which means that loading modes do not have effective contribution to the variability across cortices and vice versa. Results of detailed Tukey HSD tests together with pairwise comparisons between factors are summarised in Li et al. (2013b). According to the statistical analysis, no significant variances are found between anterior to medial and posterior to lateral quadrants in all analyses, which suggests a strong linkage between each of the two pairs. On the other hand, the differences between the opposite quadrants are consistently significant ($p < 0.05$ for all the comparisons), which could be attributed to dissimilar microstructures distribution. Less-consistent values are found between anterior to lateral and medial to posterior quadrants, where the transition of the microstructure happens to be the most severe (Li et al. 2013b). The ANOVA analysis for post-yield mechanical properties did not reveal statistical correlation between cortices due to simultaneous effects of strain hardening and progressive damage softening.

2.2 Fracture Toughness of Cortical Bone Tissue

Fracture toughness of cortical bone in different orientations is studied in this section to deepen our understanding on the anisotropy and variability of the fracture resistance of cortical bone tissue.

The specimens extracted from fresh bovine femurs were grouped according to their anatomic positions—anterior, posterior, medial and lateral (Fig. 1). Fifteen specimens cut from each cortex were notched to allow crack growth along three different orientations relative to the bone axis—longitudinal, transverse and radial as shown in Fig. 1. After cutting, specimens were polished and then checked under microscope to insure that their surfaces were free from scratches and damage. Specimens were kept hydrated in a 0.9% physiological saline solution prior to tests. All specimens were prepared with the same dimensions for comparison, according to British Standard: BS 7448-1 (Standard 1999): 25 mm \times 2.72 mm \times 5.43 mm (total length \times width \times thickness). Also, a very fine slit of 2.7 mm was produced using a low-speed diamond blade for all specimens according to Standard (1999). Due to dimensional constraints of the cortical bone tissue, and in order to provide comparability, specimens with the same length ($L = 25$ mm) were used for all cortices and crack directions. Hence, the span (S), width (W), thickness (B) of specimens and crack length (a) were chosen based on the full length of 25 mm and proportions for dimensions defined in Standard (1999). The used dimension proportions are $L = 4.6W$, $S = 4W$, $a/W = 0.5$, and $B = W/2$.

The fracture toughness tests were performed according to British Standard—BS 7448-1 (Standard 1999) on an Instron 3345 single column bench-top machine (Instron, USA) using single-edge-notch specimens for bending. All specimens were

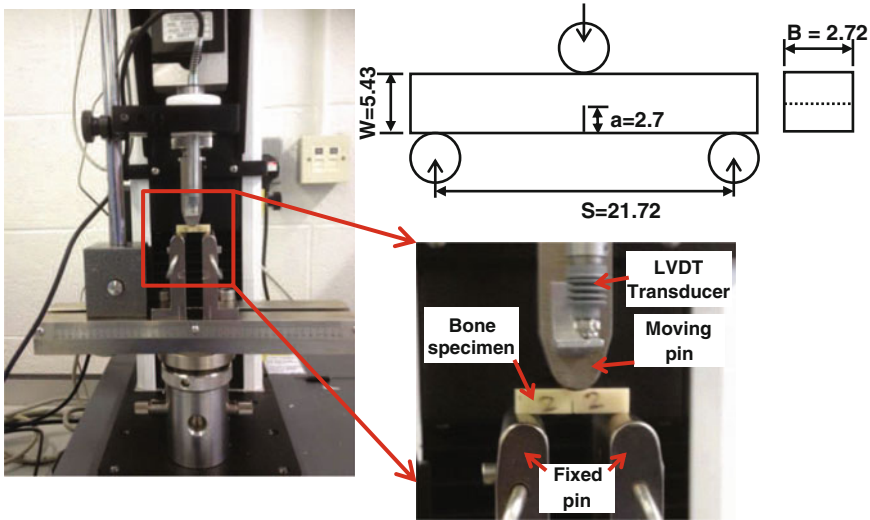


Fig. 3 Three-point bending setup with single-edge-notch cortical bone specimen and LVDT mounted on Instron 3345 machine

loaded quasi-statically up to failure with a displacement-controlled loading rate of 1 mm/min. The load was measured using a 5 kN load cell and the corresponding load-line displacement was measured synchronously using a LVDT sensor (2601 Series, Instron, USA), see Fig. 3. The obtained load-displacement curves were then analysed according to the classification described in Standard (1999). After tests, fracture surfaces of all the specimens were gold-coated and analysed using scanning electron microscopy (SEM).

In this study, the fracture behaviour of all specimens was predominantly non-linear; therefore, an elastic-plastic fracture mechanics parameter, J -integral, was calculated based on British Standard BS 7448-1, using the following equation (Standard 1999):

$$J = \left[\frac{FS}{BW^{1.5}} f\left(\frac{a_0}{W}\right) \right]^2 \frac{(1-\nu^2)}{E} + \frac{2U_p}{B(W-a_0)}, \quad (1)$$

where S is the bending span, F is the applied force, $f\left(\frac{a_0}{W}\right)$ is a function of $\left(\frac{a_0}{W}\right)$, ν is Poisson's ratio, E is elastic modulus, U_p is the plastic part of area under plot of force versus specimen displacement along the load-line, B is the specimen's thickness, W is the effective width of the test specimen and a_0 is the average original crack length.

2.2.1 Results and Analysis

Critical values of fracture toughness J_C of the cortical bone tissue were calculated with respect to three crack-growth directions: longitudinal, radial and transverse; in addition, anisotropy ratios of the fracture toughness values were analysed. The

Table 1 Average and standard deviation for critical J -integral values for all cortex positions and crack growth directions

Units: N/m	Anterior		Medial		Posterior		Lateral	
	Mean	SD	Mean	SD	Mean	SD	Mean	SD
Longitudinal	1033.9 ± 254.5		1768.5 ± 98.8		1165.7 ± 340.1		2034.3 ± 509.9	
Radial	1199.1 ± 153.1		1418.2 ± 97.2		983.0 ± 369.5		2664.2 ± 554.4	
Transverse	4509.1 ± 422.1		5925.5 ± 802.9		3876.7 ± 847.3		5661.6 ± 452.7	

obtained experimental data demonstrates that all specimens exhibits a non-linear fracture process; hence, the J -integral (Table 1) was used to quantify the fracture toughness based on British Standard: BS 7448-1 (Standard 1999).

It can be noticed from these results that the fracture-toughness values for specimens cut from different cortices are significantly different. In general, cortical bone shows higher resistance to fracture when a crack grows perpendicular to the osteon direction and lower resistance for those grow parallel to osteons (i.e. radial and longitudinal directions, respectively). For a crack growing in transverse direction, specimens from the medial quadrant has the highest critical value of J -integral while those from posterior quadrant are the lowest. The Tukey HSD test ($\alpha = 0.05$) demonstrates statistically significant differences between medial to posterior ($p = 0.035$) and posterior to lateral ($p = 0.028$) cortices. On the other hand, specimens with radially extended cracks have the highest fracture toughness in case of the lateral quadrant and the lowest for the posterior one. The calculated critical values of J -integral for the radial cracks, ranging from 983 to 2,664 N/m, are significantly lower compare with specimens having transverse cracks. Significant differences are found between anterior to lateral ($p = 0.027$) and posterior to lateral ($p = 0.015$) quadrants. Finally, for specimens with cracks extending along the direction parallel to osteons (longitudinal cracks), the critical J -integral values are comparable with those for radial cracks, and their highest value is found in the lateral quadrant whereas the lowest is in anterior specimens. Statistically significant differences in this case are found between anterior to medial ($p = 0.043$) and anterior to lateral ($p = 0.02$) quadrants. Generally, comparing data between cortices, higher fracture toughness is usually found in specimens cut from the medial and lateral quadrants. The disparity between these two groups ranges from as low as 18.3 up to 171 %.

This non-uniform fracture resistance across different cortices of the bovine femur implies that the variation of microstructure has a great impact on the local fracture toughness values. Previous research (Abdel-Wahab et al. 2011; Li et al. 2013b) showed that a change in the volume fraction of constituents at microstructure level largely affects the local material properties, such as elastic modulus, yield stress, ultimate strength, which, in turn, influences fracture properties. Preferential alignment of microstructural constituents also has an important effect on anisotropy of fracture toughness values. Higher resistance to fracture are found where the cracks propagate perpendicular to osteons orientation, while lower resistance when cracks extend parallel to osteons direction. The anisotropy ratios (calculated as ratios of respective values of J_C) between transversely-orientated cracks and longitudinally- or

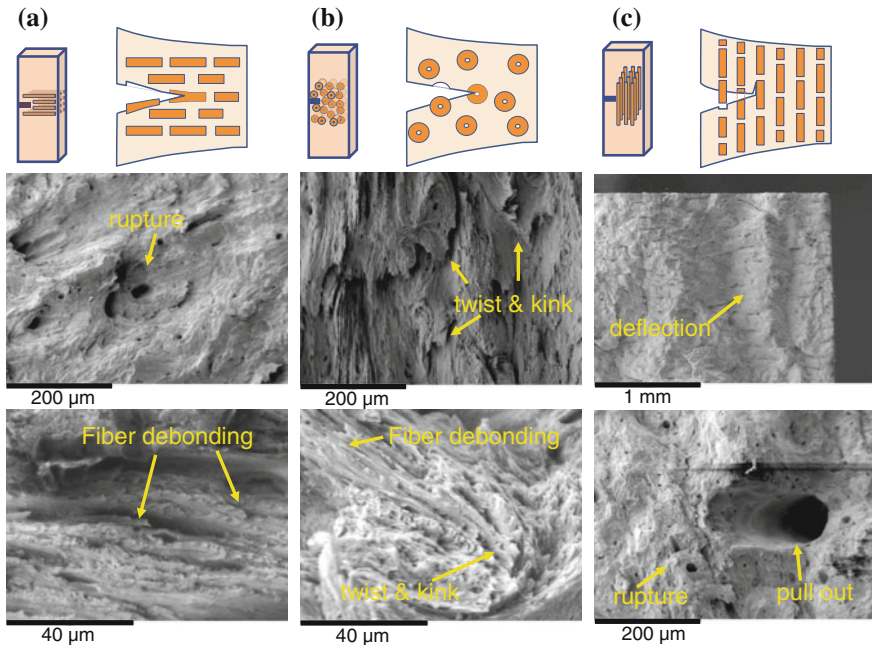
Table 2 Anisotropy ratios of fracture toughness values compared for different crack growth directions for various cortex positions

	Anterior	Medial	Posterior	Lateral
Transverse/Longitudinal	4.36	3.35	3.33	2.78
Transverse/Radial	3.76	4.18	3.94	2.13

radially-orientated cracks are presented in Table 2. Apparently, the anisotropy ratio also varies for different cortices ranging from 2.13 to 4.36, with the lowest ratio found in the lateral quadrant and the highest ratio in the anterior quadrant.

Fracture surfaces were analysed for all the tests using SEM. A dissimilar character of fracture surfaces is evident among different crack-extension directions and cortex positions.

The combination of microstructural changes and different crack-extension directions triggers various toughening mechanisms, which, in turn, are reflected in different fracture-toughness values and levels of surface roughness. Generally, for the longitudinal fracture specimens, with crack fronts propagating along the direction parallel to the axis of osteons, the fracture toughening mechanism is dominated by uncracked-ligament bridging (Ritchie et al. 2005; Launey et al. 2010) during the process of osteons splitting, rupture, interface failure and fibre debonding (Fig. 4a).

**Fig. 4** Schematic illustrations and SEM images of various toughening mechanisms for longitudinal **a**, radial **b** and transverse **c** cracks-growth directions

Similarly, for cracks propagating in the radial direction, this toughening mechanism is still active as a result of osteon splitting or fibre debonding. However, the difference in this case is the influence of interface areas or empty spaces such as cement line or Haversian canals that had a larger contribution towards cracks arresting at these regions (Ural and Vashishth 2006). As a result, twists and kinks of osteons are observed in current analysis (Fig. 4b). In contrast to the previous two cases, cracks growing along the transverse direction require a larger traction force for the crack front to penetrate and cross the osteons as longitudinal strength of osteons is much higher than transverse one. Cracks are therefore more likely to be deflected due to imperfections and heterogeneity of the microstructure as a result of osteons' pull outs (Fig. 4c). Consequently, the overall results are higher fracture toughness and rougher crack surfaces. In the elastic-plastic fracture regime, the tensional field at the back of the crack tip also promotes a multi-scale bridging effect through shear sliding between interface regions at different levels (Fig. 4c).

3 Mechanical Properties of Cortical Bone Tissue at Micro-Scale

3.1 Microstructure Distribution

In this section, a detailed microstructural analysis was introduced to quantify the effect of heterogeneously distributed microstructural constituents, well known from the literature (Abdel-Wahab et al. 2011; Li et al. 2014), on the macroscopic mechanical behaviour of cortical bone. Two cross-sectional rings from the upper and lower mid-diaphysis of one femur were excised, polished and analysed with optical microscopy (Olympus BX60M, Japan). 16 evenly distributed cross-sectional images were taken for each ring section and then analysed using Image-Pro software (Image-Pro 7.0, Media Cybernetics, USA). The images were taken by stitching a series of tilting images across the thickness (from ectosteal to endosteal) of the cross-section area. The microstructural constituents were distinguished into four categories: osteons (including both primary and secondary osteons), plexiform, interstitial matrix and porosity areas. A detailed procedure to analyse and calculate the area fraction of each constituent can be found in Li et al. (2013b), Saha and Hayes (1977). Due to occasional undistinguishable boundaries between constituents, manual adjustment was required to compensate for deficiency of a computer algorithm. As a result, a reproducibility measurement was employed by this study and the result showed standard deviation of $\pm 4\%$.

Based on a modified Voigt-Reuss-Hill (VRH) averaging scheme (Bonfield and Clark 1973; Carter and Hayes 1977), the effective Young's modulus was calculated according to the following equation:

$$E_{\text{total}} = (E_O V_O + E_I V_I + E_P V_P) (1 - V_{P_0})^3 \quad (2)$$

Table 3 Magnitudes of Young's modulus (GPa) used in the calculations based on Eq. 2

	Osteonal	Interstitial	Plexiform
Longitudinal	22.7 ^a	25.1 ^b	26.5 ^a
Transverse	12.85 ^c	14.12 ^d	15.67 ^c

^aReilly and Burstein (1975)

^bRho and Pharr (1999)

^cKatz et al. (1984)

^dBudyn and Hoc (2007)

The subscripts O, I and P denote osteonal, interstitial and plexiform areas, respectively; E and V represent the Young's modulus and volumetric (area in 2D) fractions of respective parts; V_{Po} is the fraction of porosity. The Young's moduli used in the calculation are listed in Table 3.

3.1.1 Results and Analysis

The results from the optical microscopic analysis confirmed regional differences between different quadrants (Table 4). Generally, the anterior quadrant is dominated by plexiform bone (over 50%) and the posterior quadrant is extensively remodelled with a large proportion of osteonal bone (over 50%). The medial and lateral quadrants are transition sections between the two. This transition could also be evidenced by a relatively large standard deviation of porosity for these two quadrants, ± 2.21 and $\pm 3.94\%$, respectively (Table 4). Within each quadrant, plexiform bone is usually located at the ectosteal cortex, and then there is transition from plexiform to a mixture of osteonal and interstitial bone with osteonal structure positioned predominately between ectosteal and endosteal cortices (Fig. 5).

The results in Table 4 demonstrate large standard deviations of each constituent as the microstructure changes considerably within and between cortices. Substantial variations are also observed for upper to lower mid-diaphysis. The average area

Table 4 Microstructure analysis of average and standard deviation of volumetric area fractions for constituents for four cortices

Volumetric fraction (%)	Osteonal		Interstitial		Plexiform		Porosity	
	Value	(\pm SD)	Value	(\pm SD)	Value	(\pm SD)	Value	(\pm SD)
Anterior	13.13	(± 10.16)	17.66	(± 16.01)	65.69	(± 24.79)	3.53	(± 0.73)
Medial	16.4	(± 14.49)	25.51	(± 19.56)	53.4	(± 34.52)	4.69	(± 2.21)
Posterior	54.01	(± 17.58)	30.4	(± 16.96)	7.58	(25.6) (0)	8.02	(± 1.89)
Lateral	44.43	(± 16.41)	35.81	(± 9.51)	10.26	(35.1) (0)	9.51	(± 3.94)

Note the maximum and minimum values instead of standard deviations were used for the volumetric fraction of plexiform for posterior and lateral cortices due to large fluctuations of the data

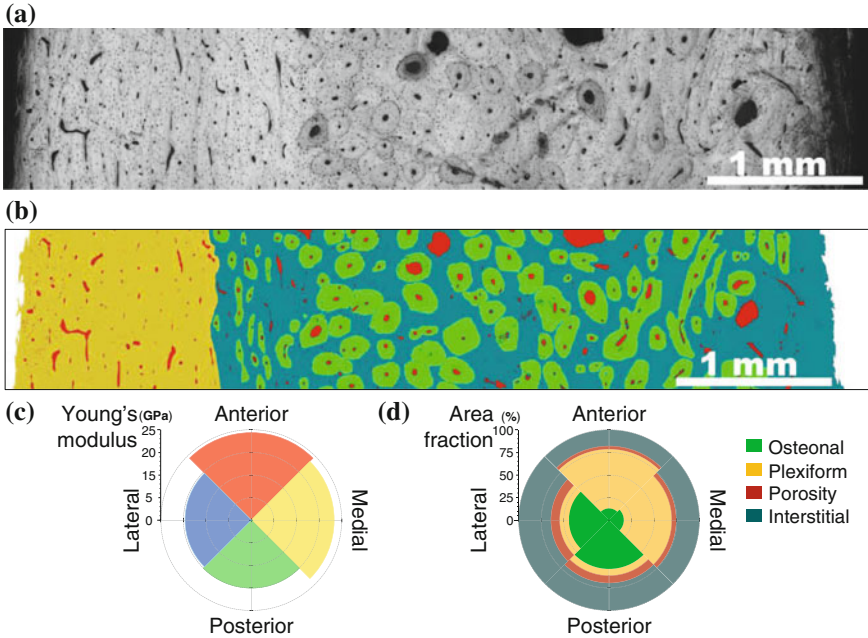


Fig. 5 **a** Microstructure transition across thickness at medial quadrant; **b** colour-coded image after image analysis; **c–d** comparison between Young’s modulus and volumetric fraction for four cortices from different quadrants

fraction of osteonal bone is between 13 and 54 %; interstitial bone ranges from 17 to 35 %; plexiform bone from 10 to 56 % and porosity around 3–9.5 %.

Comparing the Young’s moduli and the area fractions of microstructural constituents for four cortices (see Fig. 5), the correlation between the transition of microstructural constituents and the variation of the Young’s moduli indicates that the overall stiffness of cortical bone tissue depends strongly on the microstructure, i.e. distribution and orientation of constituents (Hamed et al. 2010). For the volume fractions of each individual constituent, porosity (Sevostianov and Kachanov 2000; Currey 1988) and secondary osteons (Saha and Hayes 1977) were reported to be inversely correlated with the Young’s modulus, which corroborates current findings.

The values of the effective Young’s modulus calculated using Eq. (2) are compared with experimental results in Table 5. Apparently, for both the longitudinal and transverse Young’s moduli for four anatomic quadrants, the theoretical estimation closely agrees with the experimental results. A larger error for the transverse direction is due to the fact that the volumetric fractions were measured in the transversal plane of the femur, and may not be the same for the longitudinal or circumferential planes.

Table 5 Comparison between theoretical prediction of effective elastic moduli and experimental data, experimental data are based on average for compression and tension specimens

Young's modulus (GPa)		Theoretical prediction	Experimental data	Error (%)
Anterior	Longitudinal	22.29	22.40	0.52
	Transverse	13.00	13.06	0.52
Medial	Longitudinal	21.02	21.17	0.71
	Transverse	12.19	14.11	13.6
Posterior	Longitudinal	17.04	17.93	4.94
	Transverse	9.67	10.08	4.13
Lateral	Longitudinal	16.15	17.14	5.75
	Transverse	9.17	10.85	15.5

4 Numerical Modelling of Fracture Process of Cortical Bone

Finite-element analysis of crack initiation and growth is a powerful tool, which enables studying of fracture and damage processes of cortical bone in direct vicinity of the fracture interaction zone. This is hard to achieve using approaches such as element de-bonding, cohesive zone method (CZM) or a virtual crack closer technique (VCCT) due to a well-known fact that the crack path has to be pre-defined in these modelling schemes. However, with the Extended Finite-Element Method (XFEM), a crack propagation process can be modelled based on a solution-dependent criterion without introducing such a predefined crack path. Thus, in this section, two XFEM-based finite-element models were developed to evaluate the fracture processes of cortical bone at both macro- and micro-scales. The models were developed for the same three-point bending configuration as in our previous experiments for model-validation purposes.

4.1 Modelling of Three-Point Bending at Macro-Scale

For macro-scale simulations, two groups with a total of eight finite-element models were developed to analyse fracture propagation at four anatomic quadrants: Group A and Group B for longitudinal and transverse cracks, respectively. The geometry and dimensions of specimens followed the same specification as in previous experiment (Fig. 3). A total number of 8,600 linear quadrilateral (CPE4R) elements were used to generate a mesh for the simulated bone specimen. The fixtures of three-point bending were modelled as 2D analytical rigid shells with diameter of 10 mm. The following assumptions were made in the developed numerical models:

1. plain-strain conditions of the specimen;
2. elastic transversally isotropic material properties for the bone specimens (Table 6);
3. a friction coefficient of 0.3 was considered between the pins and specimen.

Table 6 Transverse isotropic material properties used in FE models

	E ₁ (GPa)	E ₂ (GPa)	E ₃ (GPa)	ν_{12}	ν_{13}	ν_{23}	G ₁₂ (GPa)	G ₁₃ (GPa)	G ₂₃ (GPa)
Anterior	23.15	13.20	13.20	0.29	0.29	0.44	3.00	3.00	6.00
Posterior	18.00	10.20	10.20	0.29	0.29	0.44	3.00	3.00	6.00
Medial	21.13	14.67	14.67	0.29	0.29	0.44	3.00	3.00	6.00
Lateral	15.14	11.18	11.18	0.29	0.29	0.44	3.00	3.00	6.00

Subscripts denote axial orientation: 1—longitudinal, 2—transverse and 3—radial

Cracks were modelled using an X-FEM technique implemented within the finite-element software Abaqus 6.11/Explicit. It allows a crack to initiate and propagate through an arbitrary, solution-dependent path, subject to a local material response. Hence, the X-FEM enrichment was applied to the whole model for all the cases. A surface-based cohesive traction-separation criterion was employed to model the non-linear fracture processes through the crack initiation and evolution criteria. Crack initiation in a hard biological tissue (cortical bone) was commonly described as a strain-driven criterion (Nalla et al. 2004a). Therefore, a fracture strain of 0.6% was chosen based on our previous study (Li et al. 2013b). When the fracture strain was reached, damage evolution took place. The evolution criterion was defined in terms of the fracture energy based on the fracture toughness obtained from the experimental part of this study. An initial notch was introduced as a 2.7 mm-long straight line in the model.

4.1.1 Results and Analysis

The simulation part of the study was focused on the crack initiation and propagation processes in the cortical bone specimens under different loading conditions. The simulations were performed for quasi-static loading using the Abaqus/Explicit solver at a constant loading rate until complete specimen's fracture. Results of finite-element simulations are compared with the experimental data in Fig. 6 for different cortices and crack orientations; this comparison shows very good agreement for force and loading-pin displacement curves. The developed finite-element models successfully reproduce the variability of material responses across four cortices for both longitudinal and transverse crack directions. The results indicate that the fracture-toughness values are largely affected by the local anisotropic material properties linked to the variation of microstructure (Li et al. 2013b). The models also predict an early-stage damage initiation (Fig. 6, horizontal dotted lines), followed by a non-linear progressive damage-evolution process. By using a surface-based cohesive traction-separation criterion based on the experimental results, these complex non-linear damage propagation processes are captured reasonably well.

Both initial curvatures of the graphs and the determined peak-force levels are close to the obtained experiment results. It is also observed that damage initiation for transverse-crack specimens from the medial quadrant is lower than for

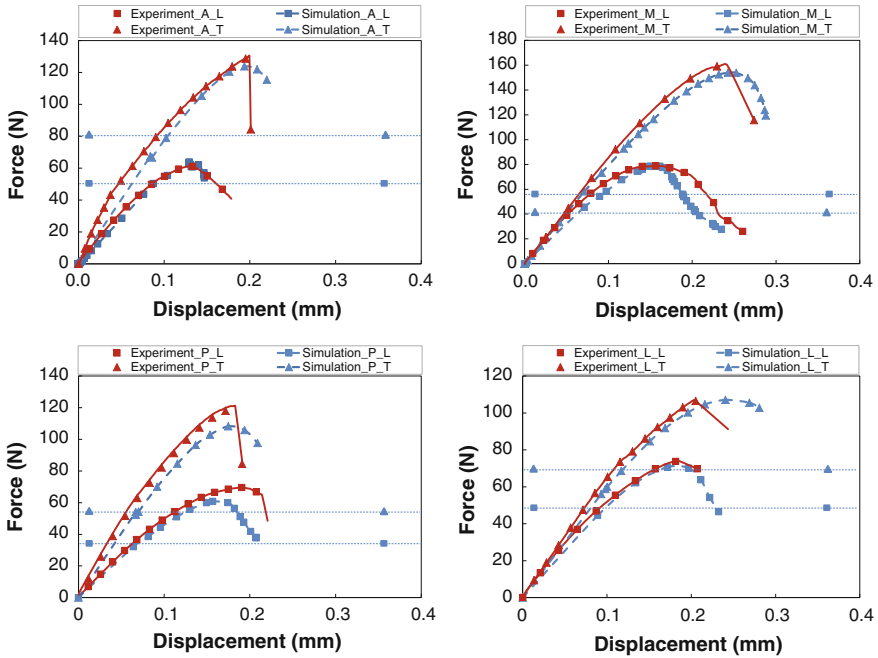


Fig. 6 Comparison of experimental and calculated force-displacement curves: A, M, P and L denote anterior, medial, posterior and lateral specimens; _L and _T denote *longitudinal* and *transverse crack propagation directions*; dotted lines indicate damage initiation

longitudinal-crack specimens. The lower damage initiation combined with a higher ultimate fracture force indicates the existence of a strong toughening mechanism for medial transverse-crack specimens (Fig. 6). On the other hand, a late damage-initiation combined with a low peak force in longitudinal crack specimens from the anterior quadrant is an indication of a weak toughening mechanism.

4.2 Modelling the Fracture Processes at Micro-Scale

Heterogeneous distribution of microstructural constituents significantly affects the mechanical behaviour of cortical bone in both elastic as well as post-yield and damage regimes. However, the macroscopic bone model cannot fully realize the microstructure-induced mechanical variability and complex crack propagation processes. Therefore, three two-dimensional microstructured models of cortical bone were developed in this section to further investigate the effect of randomly distributed microstructure on variability and fracture processes of cortical bone. The models were established based on the same macroscopic three-point-bending model discussed earlier. A submodelling technique was used to focus computational power at

the crack-propagation region while maintaining boundary conditions of the full-scale model. This technique allows development of multiple models based on the same modelling object and extends the level of interest into a pre-defined region (usually with a finer mesh or more local geometric details) to achieve adequate and accurate results. The computational cost of submodelling technique is usually lower when compared with the full-size model having the same level of accuracy. The developed approach employed two different levels of modelling of the bone tissue: a full-size global model for the macroscopic response of the entire specimen under three-point bending and three submodels reflecting heterogeneous responses of different localized microstructures during the crack propagation process. The boundary conditions in the submodel were derived for the correspondent region from the results of the global model using the displacement-control criterion based on the nodal field variables. The global constrains were maintained the same as in previous macroscopic model. Then, the submodel was extruded from the central un-cracked region of the global model with dimension of 2.72 mm \times 2.72 mm (Fig. 7). The pre-crack is mostly outside the submodel with only one element of its bottom middle surface cut by it.

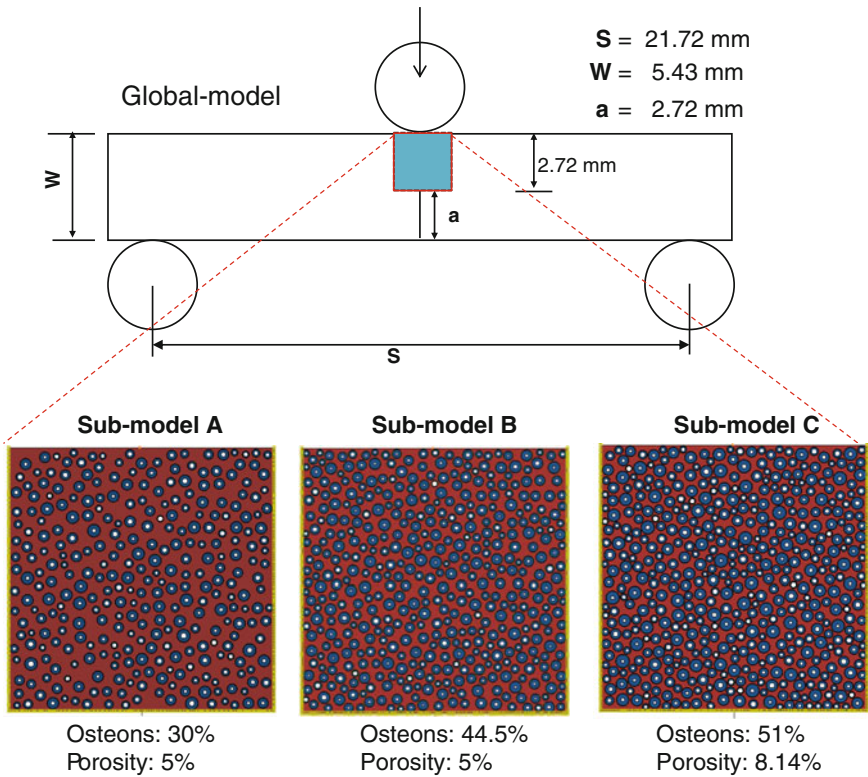


Fig. 7 Schematic illustration of model configurations for three-point-bending setup using *global model* and *microstructured sub-models*

Table 7 Volume fractions of microstructure constituents for Models A, B and C

Constituent	Model A (%)	Model B (%)	Model C (%)
Osteon	30	44.5	51.2
Porosity	5.01	5.02	8.14
Interstitial matrix	58.77	41.25	30.04
Cement line	6.22	9.23	10.62

The submodels were constructed as four-phase composite structures with randomly distributed microstructural features:

- interstitial bones,
- osteons,
- Haversian canals and
- cement line.

All geometrical parameters of each model were defined based on statistical analysis of real microstructures (for details see Abdel-Wahab et al. 2010). The average width of cement line was close to $5\ \mu\text{m}$. The distributions of diameters of osteons and Haversian canals were statistically regularized using best-fit functions described in detail in Abdel-Wahab et al. (2010). The average diameters for osteons and Haversian canals were 99.89 and $23.1\ \mu\text{m}$, respectively.

The algorithm to generate random microstructures in the submodels was first programed in a custom-developed Matlab code according to the statistical data for real bone specimens, and then all the geometrical parameters were encoded into a python script to construct the microstructural model in Abaqus. Three representative microstructured cortical bone models were constructed in this study based on the statistical measurements for each constituent: osteons volume fraction varies from 30 to 51 %, while porosity changes from 5 to around 8 % (Fig. 7). Full data on the volume fractions of microstructure constituents used in the models are listed in Table 7.

In this study, the mechanical behaviour of cortical bone was introduced using an elasto-plastic transverse isotropic material formulation with regard to the radial-transverse section plane. At macroscopic level, the effective homogeneous material was used in the global model. The effective elasto-plastic material properties obtained from our macroscopic experiments (Abdel-Wahab et al. 2011) were applied in the global model. On the other hand, at microscopic level, microstructural constituents play an important role in the localized fracture process and formation of toughening mechanisms. Consequently, the four-phase microstructured models of cortical bone were employed in the submodel, and individual material properties based on nano-indentation results (Abdel-Wahab et al. 2010) were assigned to constituents. The elastic modulus of cement line was initially set to be 25 % lower than that of osteon based on the findings in Budyn and Hoc (2007), Montalbano and Feng (2011), and two other levels—equal to that of osteon and 25 % higher—were also used to investigate the effect of cement line's properties on the fracture process in cortical

Table 8 Material properties used in global model and microstructured submodels (Ritchie et al. 2005; Abdel-Wahab et al. 2011; Budyn and Hoc 2007; Abdel-Wahab et al. 2010)

	Effective homogenised material	osteons	Interstitial matrix	Cement Line
Elastic modulus (GPa)	11.18	12.85	14.12	9.64
Poisson's ratio	0.167	0.17	0.153	0.49
Yield strain (%)	0.6	0.6	0.6	0.6
Fracture initiation strain (%)	0.65	0.65	0.65	0.65
Fracture energy release rate (N/m)	2043	860	238	146

bone. A summary of material properties used in this study is given in Table 8. The post-yield material behaviours in both global and sub-models were based on flow stress-strain curves obtained experimentally (Abdel-Wahab et al. 2010, 2011).

Damage and crack propagation in this study were modelled using the X-FEM technique in Abaqus (Dassault Systèmes 2012). The local crack initiation and evolution criteria were chosen to be the same as those employed in the macro-scale model. It assumes that crack initiates when the maximum principal strain reaches its critical value and the newly defined crack direction is orthogonal to that of the maximum principal strain. Once initiated, crack conforms to the energy-based damage evolution criterion, and the cracked element starts degradation and eventually fails. It describes the rate, at which the cohesive stiffness of the cracked surface degrades once the crack-initiation criterion is fulfilled at particular element. The energy dissipated (fracture energy) as a result of damage progress is equal to the area under the traction-separation curve at the point of complete damage. The fracture energy in our models (Table 8) was defined according to the previous results (Ritchie et al. 2005; Abdel-Wahab et al. 2010, 2011).

4.2.1 Results and Analysis

Three microstructured models of cortical bone were analysed in this study. Their results are compared with the effective homogeneous model as well as experimental data in terms of force and loading-pin-displacement diagram in Fig. 8a. Dissimilar fracture-resistance behaviours are evidenced for three different models as a result of varying microstructural constituents at microscopic level. Among the three models, Model A has the highest overall critical value of J integral—2503 N/m, while Models B and C result in 2,369 and 2,212 N/m, respectively. This decreasing trend in the fracture toughness is apparently linked to the increasing volume fractions of osteons and porosity (Haversian canals in this case). From the histology point of view, the bone remodelling process generates new Haversian systems (each including an osteon, a Haversian canal and a cement line) to replace the old, damaged regions as an adaptation process. The newly formed bone is usually less mineralized than its

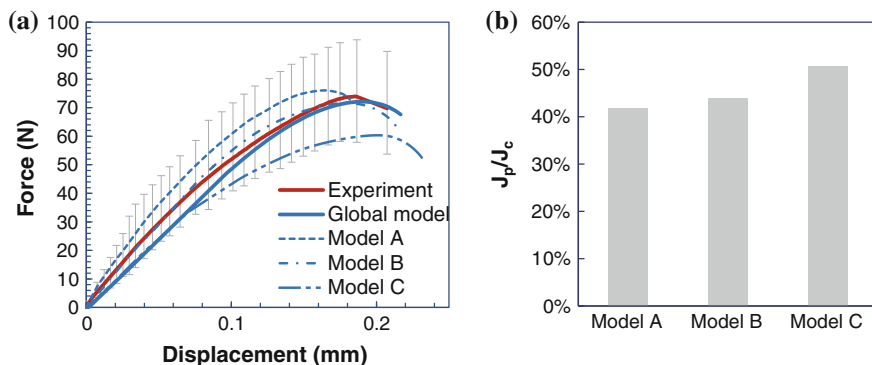


Fig. 8 **a** Comparison of experimental *force—displacement diagram* (Li et al. 2013a) with results for different FE models (*error bars* indicate variations of experimental results); **b** comparison of proportions of energy associated with plastic deformation for different models

surrounding area due to the fact that mineral concentration period lasts longer than the remodelling process (Currey 2012). As a result, a large fraction of less mineralized osteons associated with the bone-mass and stiffness reduction has a negative impact on the overall fracture resistance of cortical bone. Still, benefiting from their low stiffness but high fracture toughness, osteons demonstrate a higher failure strain when compared with interstitial matrix and, in general, offer a positive effect on fracture toughness. On the other hand, the increasing proportion of Haversian system leads to the increase in structural compliance as a result of cavitation, hence, to increased overall fracture strain (Fig. 8a). These mutual effects of microstructural constituents result in the variation of macroscopic fracture toughness. Significant nonlinearity observed at the initial loading stage during the experiment is successfully captured using the microstructured model. Comparing the proportion of the plastic component (J_p) of the critical value of J -integral (J_c) in each model, an increased tendency for the energy associated with plastic deformation is observed for the increase of osteon and porosity volume fractions (Fig. 8b). Based on the above findings, the bone remodelling process related with the increasing fraction of osteons and porosity changes the bone's fracture resistance from a stress-based mode to a more strain-based mode—fracture stress resistance reduces but fracture strain resistance increases.

At the global level, the effective homogeneous material model is able to capture a macroscopic response in terms of force and loading-pin displacement (Fig. 8a). However, the detailed fracture-evolution process, especially the localized damage zone is neglected. On the contrary, the heterogeneous microstructured models, operating within the framework of the global model using direct displacement-controlled boundary conditions, emphasise the effect of the local non-uniform stress-strain field on the crack propagation process at microscopic level. Figure 9 presents contour plots for von Mises stress, maximum principal strain, equivalent plastic strain (PEEQ) and a damage scale factor for X-FEM (STATUS) for Model B when the

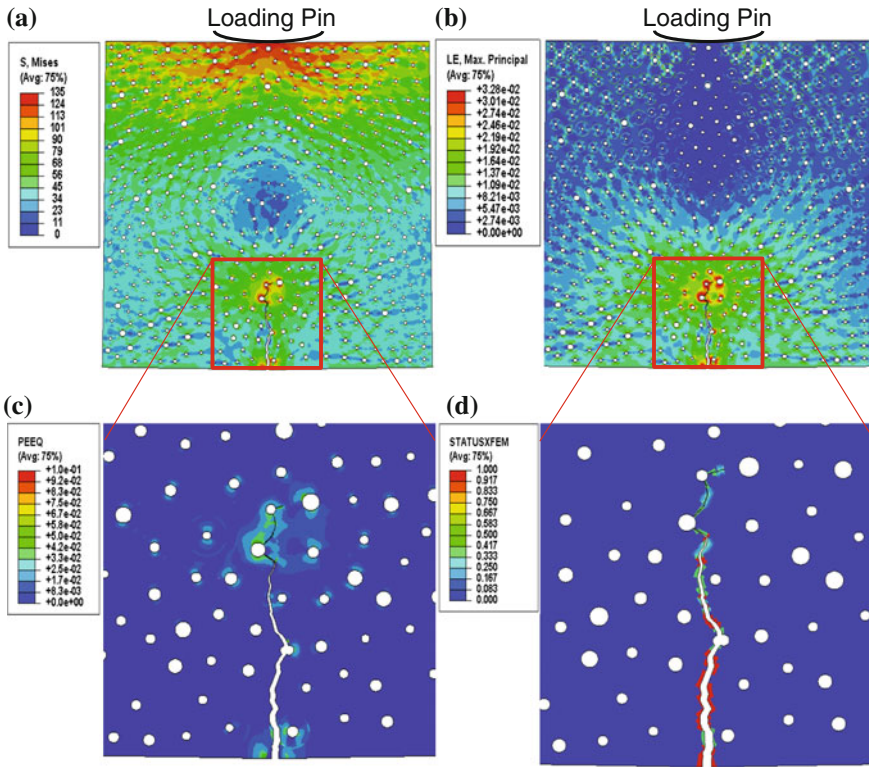


Fig. 9 a Contour plots for von Mises stress, b maximum principal strain, c equivalent plastic strain (PEEQ) and d damage scale factor for XFEM (STATUS) for Model B for crack propagation at maximum reaction force (a and b represent full Model B)

crack is approaching the state of the maximum reaction force. As evidenced from the Fig. 9a, b, a diffused stress pattern is characteristic for the von Mises contour, while a cross-hatched strain pattern for the maximum principal strain contour is located ahead of the crack tip (in the compressive region of the specimen) with a diffused strain pattern near it (in the tensile region). These dissimilar stress and strain patterns around the crack tip coincide with results of the previous experimental studies (Ebacher and Wang 2008; Boyce et al. 1998; Nyman et al. 2009), in which the authors indicated that such distinctive stress and strain fields in tension and compressive regions could lead to realization of different damage fracture mechanisms. Equivalent plastic strain illustrated in Fig. 9c indicates that the area undergoes plastic deformation during the crack propagation process.

The identified plastic zone around the crack tip is within 1–2 osteonal radius i.e. approximately $100\ \mu\text{m}$ in length. The value seems to be higher than $17\ \mu\text{m}$ reported in the experimental work (Robertson et al. 1978). One possible reason for this larger plastic-zone size predicted in our model is the lack of multiple cracks formation in the

current model, while, in reality, micro-cracks and natural imperfections inclusions in front of the crack tip may develop into mini cracks frontal that can release local stress concentration, thus, reducing the plastic-zone size.

The damage scale factor denoted as STATUS in Fig. 9d indicates that one third of the crack surface is still under traction force and acts as toughening mechanisms that contributes to the non-linear fracture process. The toughening mechanisms active in a radial-transverse crack specimen can be divided predominantly into three types (Ritchie et al. 2005):

- interfacial debonding as a result of the material's discontinuity at the interface between osteons and interstitial matrix—the formation of the weak path of cement line;
- crack diversion due to microstructural heterogeneity and material imperfections, at which the crack is redirected towards the most vulnerable part producing a twisted and deflected fracture path;
- uncracked-ligament bridging caused by osteon splitting and rupture acting as a post-crack toughening mechanism behind the crack tip.

In this study, the microstructured models are capable to capture these main features of the toughening mechanisms as shown in Fig. 10.

Figure 10d demonstrates an interface failure predicted by the model as the crack bends away from the osteon due to the discontinuity in the cement-line region. Figure 10e reveals the crack-diversion mechanism as crack deviates from its central

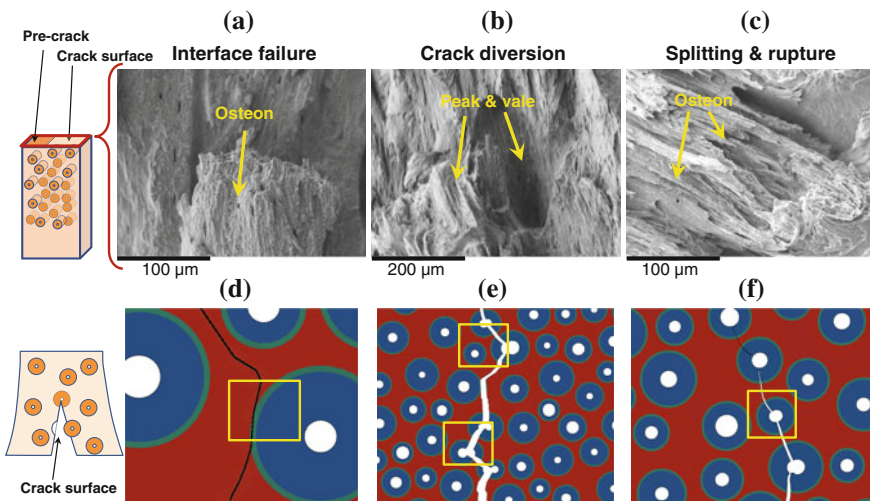


Fig. 10 Comparison of toughening mechanisms in radial-transverse crack plane between experimental results **a**, **b** and **c** and numerical simulations **d**, **e** and **f**: **a** and **d** interface failure between osteon and interstitial matrix; **b** and **e** crack deviation from its central line towards weak part resulting in twisted and deflected crack path; **c** and **f** splitting of osteons and breakage of ligament due to crack opening observed in SEM image **c**

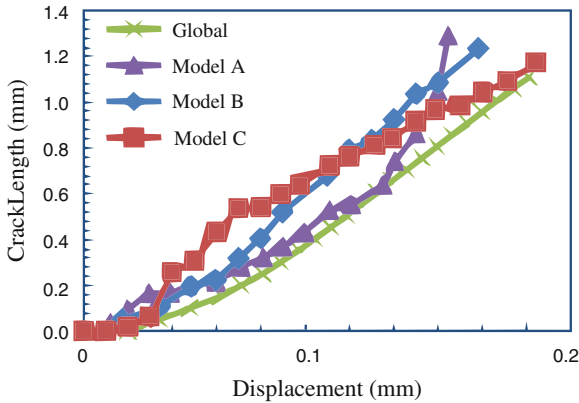


Fig. 11 Crack length and loading-pin displacement diagram for global and microstructured models (total crack length is measured until reaching maximum reaction force)

line towards a weak but twisted and deflected crack path. The uncracked-ligament bridging behind the crack tip is implicitly represented as a cohesive traction force between the damaged elements along the crack path (Fig. 10f).

To investigate the effect of microstructural constituents on the crack propagation process, the crack lengths are plotted in Fig. 11 as a function of displacement of loading-pin for the global model and three different sub-models. Their respective crack propagation paths are demonstrated in Fig. 12, row a. The total crack length was measured until reaching the maximum reaction force. It is clear from Fig. 11 that Model A has the longest overall crack length, while Model C has the shortest one. Comparing the respective crack trajectories, the higher crack length related to Model A is largely defined by significant crack deflections observed in Fig. 12a. As a result of increase in the fractions of osteons and porosity from Model A to Model C, the effect of crack-deflection mechanism gradually reduces (Fig. 12a–c). On the other hand, the crack-propagation rate (with respect to the loading-pin displacement) in Model C is higher at the initial stage, but gradually reduces as the crack propagates through more Haversian systems, whereas Model B shows a moderate linear evolution process and Model A demonstrates an increased crack-propagation rate.

It seems that an increased fraction of Haversian systems has a negative effect on the crack-propagation rate and constrains the crack-diversion magnitude. This finding is consistent with experimental observation in Zimmermann et al. (2011), where the authors concluded that age-related changes in morphology of microstructure as a result of remodelling process may lead to suppression of the crack-deflection mechanism and reduction of the total crack length.

The effect of cement line was studied by changing the magnitude of its elastic modulus within the range 25% below and above that of osteon. The respective results for the crack propagation trajectory are compared in Fig. 12 for three different microstructural models. The result indicates that an increase in the cement line's

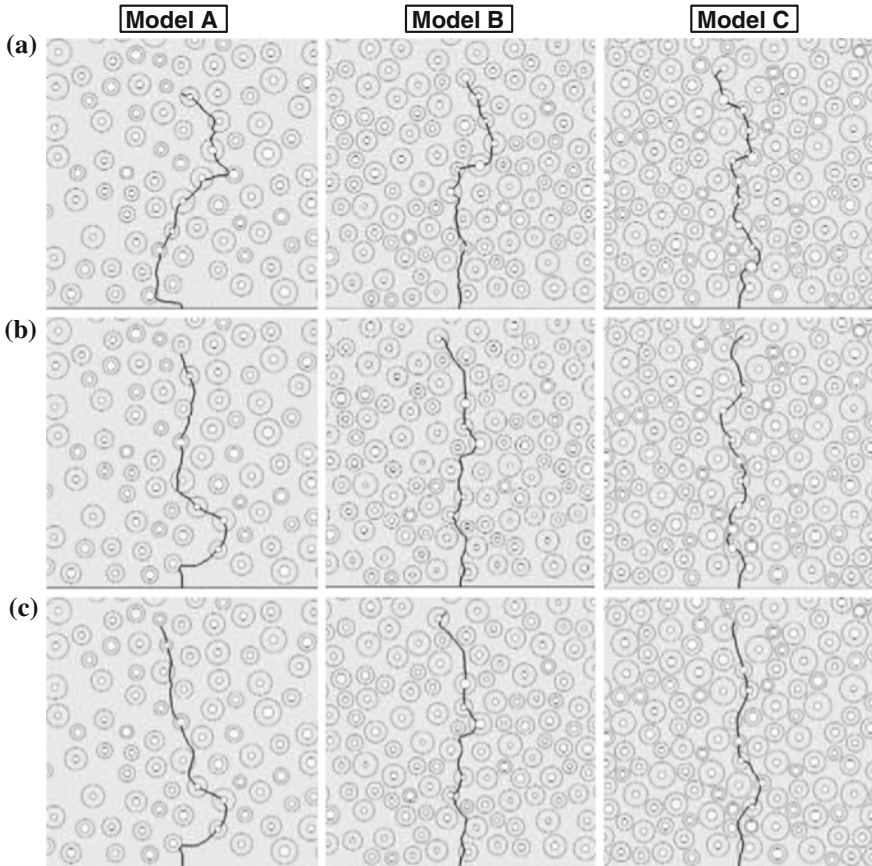


Fig. 12 Crack propagation trajectories for various elastic moduli of *cement line* for three microstructured models: row **a**: 25% lower than that of osteon; row **b**: equal to that of osteon; row **c**: 25% higher than that of osteon

modulus to the levels equal to, or 25% higher than, that of the osteon results in similar crack trajectories, that differ from the initial ones (i.e. for 25% lower modulus) for both Model A and Model B.

This higher stiffness of cement lines leads to some rise of fracture propagation in the regions with low fracture toughness—interstitial areas (Fig. 13). Moreover, higher stiffness also results in a higher rate of interface debonding in Model A and Model B (Fig. 12b, c) where cement lines facilitate crack propagation around osteons. However, no substantial difference is found between the two groups (equal to and 25% higher). On the other hand, the lower modulus increases the chance of osteonal fracture and penetration into Haversian canal in Models A and B, where high fracture toughness and high compliance regions could potentially increase the overall fracture resistance and may lead to more crack deflections and arrests. As the fractions of osteons and porosity increase in Model C, the effect of the local

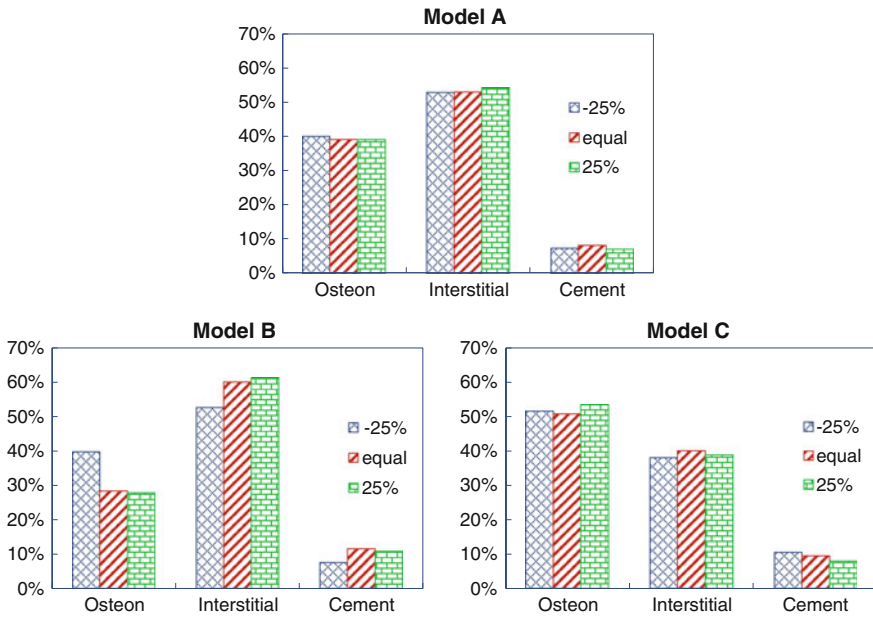


Fig. 13 Fractions of crack path in microstructure constituents for various magnitudes of *cement line’s modulus*

heterogeneity becomes more dominant. Cracks are likely to grow along the most vulnerable path, and the effect of cement lines relents. Therefore, the influence on the crack-propagation trajectory is less pronounced than in two other models. In summary, cement lines play an important role in the crack-propagation process in cortical bone. Variation of its mechanical properties can considerably affect the shape of local crack trajectory. Both scenarios demonstrated in our models have been widely discussed in the previous research (Ritchie et al. 2005; Currey 2012). Considering the fact that bone is a dynamic living tissue, the mechanical properties of cement line are likely to vary with time and locations. It is thus sensible that a 25 % differences in the cement line’s modulus within the local area can cause both toughening and weakening mechanisms as observed in experiment (Chan and Nicolella 2012).

5 Conclusions

In this chapter, the study was focused on the fracture processes of cortical bone at various length scales. In order to do so, characterisation of mechanical behaviour of cortical bone tissue was undertaken for elastic, post-yield and damage regimes. The results from our studies demonstrate specific features of varying anisotropic deformation and fracture behaviours of the cortical bone tissue, which also depend on the applied loading conditions. Combining the results from statistical and microstructural

analyses, a strong correlation of the orientation and distribution of underlying microstructural constituents on the effective macroscopic properties of cortical bone tissue is revealed. Due to a natural loading regime exerted by species' weight and muscle forces, long bones are normally exposed to combined loading conditions that are spatially non-uniform (Martin and Boardman 1993). As it is well known from the literature, bone is a dynamic tissue that reacts to mechanical loading by adapting its shape, internal microstructure and material properties to meet external loading environment (Currey 2012). The differences in the values of the Young's modulus and fracture toughness (critical J -integral) could be the outcome of bone adaptation to its natural non-uniform loading conditions.

Combining the characterised local material properties and crack initiation and evolution techniques based on fracture mechanics, the developed macroscopic model adequately characterizes the non-linear fracture processes of cortical bone. The further implementation of the random distribution of microstructured cortical-bone model enables the numerical realisation of various toughening mechanisms associated with material heterogeneity at micro-scale whereby affecting the macroscopic response of the cortical bone tissue.

Acknowledgments The authors acknowledge the financial support from EPSRC United Kingdom (Grant no. EP/G048886/1).

References

- Abdel-Wahab AA, Maligno AR, Silberschmidt VV (2010) Micro-scale numerical model of bovine cortical bone: analysis of plasticity localization. In: Proceedings of the ASME 2010: 10th Biennial conference on engineering systems design and analysis (ESDA2010), 12–14 July 2010, Istanbul, Turkey, vol. 1, ESDA2010-25329, pp 821–829
- Abdel-Wahab AA, Alam K, Silberschmidt VV (2011) Analysis of anisotropic viscoelastoplastic properties of cortical bone tissues. *J Mech Behav Biomed Mater* 4(5):807–820
- Ascenzi A, Benvenuti A (1986) Orientation of collagen fibers at the boundary between two successive osteonic lamellae and its mechanical interpretation. *J Biomech* 19(6):455–463
- Behiri JC, Bonfield W (1989) Orientation dependence of the fracture mechanics of cortical bone. *J Biomech* 22(8–9):863–872
- Bonfield W, Clark EA (1973) Elastic deformation of compact bone. *J Mater Sci* 8(11):1590–1594
- Bonney H, Colston BJ, Goodman AM (2011) Regional variation in the mechanical properties of cortical bone from the porcine femur. *Med Eng Phys* 33(4):513–520
- Boyce TM, Fyhrie DP, Glotkowski MC, Radin EL, Schaffler MB (1998) Damage type and strain mode associations in human compact bone bending fatigue. *J Orthop Res* 16(3):322–329
- Budyn E, Hoc T (2007) Multiple scale modeling of cortical bone fracture in tension using X-FEM. *Eur J Comput Mech* 16:213–236
- Carter DR, Hayes WC (1977) The compressive behavior of bone as a two-phase porous structure. *J Bone Jt Surg* 59(7):954–962
- Chan KS, Nicoletta DP (2012) Micromechanical modeling of R-curve behaviors in human cortical bone. *J Mech Behav Biomed Mater* 16:136–152
- Currey JD (1988) The effect of porosity and mineral content on the Young's modulus of elasticity of compact bone. *J Biomech* 21(2):131–139

- Currey JD (1999) The design of mineralised hard tissues for their mechanical functions. *J Exp Biol* 202:3285–3294
- Currey JD (2012) The structure and mechanics of bone. *J Mater Sci* 47(1):41–54
- Currey JD (2013) *Bones: structure and mechanics*. Princeton University Press, Princeton
- Ebacher V, Wang R (2008) A unique microcracking process associated with the inelastic deformation of Haversian bone. *Calcif Tissue Int* 19:57–66
- Ethier CR, Simmons CA (2007) *Introductory biomechanics: from cells to organisms*. Cambridge Texts in Biomedical Engineering. Cambridge University Press, Cambridge
- Fratzl P, Gupta HS, Paschalis EP, Roschger P (2004) Structure and mechanical quality of the collagen-mineral nano-composite in bone. *J Mater Chem* 14:2115–2123
- Hamed E, Lee Y, Jasiuk I (2010) Multiscale modeling of elastic properties of cortical bone. *Acta Mech* 213(1–2):131–154
- Katz JL, Yoon HS, Lipson S, Maharidge R, Meunier A, Christel P (1984) The effects of remodeling on the elastic properties of bone. *Calcif Tissue Int* 36:31–36
- Launey ME, Buehler MJ, Ritchie RO (2010) On the mechanistic origins of toughness in bone. *Annu Rev Mater Res* 40:25–53
- Li S, Abdel-Wahab A, Silberschmidt VV (2013a) Analysis of fracture processes in cortical bone tissue. *Eng Fract Mech* 110:448–458
- Li S, Demirci E, Silberschmidt VV (2013b) Variability and anisotropy of mechanical behavior of cortical bone in tension and compression. *J Mech Behav Biomed Mater* 21:109–120
- Li S, Abdel-Wahab A, Demirci E, Silberschmidt VV (2014) Penetration of cutting tool into cortical bone: experimental and numerical investigation of anisotropic mechanical behaviour. *J Biomech* 47(5):1117–1126
- Liu D, Weiner S, Wagner HD (1999) Anisotropic mechanical properties of lamellar bone using miniature cantilever bending specimens. *J Biomech* 32(7):647–654
- Martin RB, Boardman DL (1993) The effects of collagen fiber orientation, porosity, density, and mineralization on bovine cortical bone bending properties. *J Biomech* 26(9):1047–1054
- Martin RB, Burr DB (1989) *Structure, function, and adaptation of compact bone*. Raven Press, New York
- Mercer C, He MY, Wang R, Evans AG (2006) Mechanisms governing the inelastic deformation of cortical bone and application to Trabecular bone. *Acta Biomater* 2(1):59–68
- Montalbano T, Feng G (2011) Nanoindentation characterization of the cement lines in ovine and bovine femurs. *J Mater Res* 26:1036–1041
- Nalla RK, Kinney JH, Ritchie RO (2004a) On the origin of the toughness of mineralized tissue: microcracking or crack. *Bone* 34:790–798
- Nalla RK, Kruzic JJ, Ritchie RO (2004b) On the origin of the toughness of mineralized tissue: microcracking or crack bridging? *Bone* 34(5):790–798
- Nalla RK, Kruzic JJ, Kinney JH, Ritchie RO (2005a) Mechanistic aspects of fracture and R-curve behavior in human cortical bone. *Biomaterials* 26(2):217–231
- Nalla RK, Stolken JS, Kinney JH, Ritchie RO (2005b) Fracture in human cortical bone: local fracture criteria and toughening mechanisms. *J Biomech* 38(7):1517–1525
- Nyman JS, Leng H, Dong XN, Wang X (2009) Differences in the mechanical behavior of cortical bone between compression and tension when subjected to progressive loading. *J Mech Behav Biomed Mater* 2(6):613–619
- Peterlik H, Roschger P, Klaushofer K, Fratzl P (2006) Orientation dependent fracture toughness of lamellar bone. *Int J Fract* 139(3–4):395–405
- Reilly DT, Burstein AH (1975) The elastic and ultimate properties of compact bone tissue. *J Biomech* 8(6):393–405
- Rho JY, Pharr GM (1999) Effects of drying on the mechanical properties of bovine femur measured by nanoindentation. *J Mater Sci: Mater Med* 10(8):485–488
- Rho JY, Tsui TY, Pharr GM (1997) Elastic properties of human cortical and trabecular lamellar bone measured by nanoindentation. *Biomaterials* 18(20):1325–1330

- Rho JY, Kuhn-Spearing L, Zioupos P (1998) Mechanical properties and the hierarchical structure of bone. *Med Eng Phys* 20(2):92–102
- Ritchie RO, Kinney JH, Kruzic JJ, Nalla RK (2005) A fracture mechanics and mechanistic approach to the failure of cortical bone. *Fatigue Fract Eng Mater Struct* 28(4):345–371
- Robertson DM, Robertson D, Barrett CR (1978) Fracture toughness, critical crack length and plastic zone size in bone. *J Biomech* 11(8–9):359–364
- Roe SC, Pijanowski GJ, Johnson AL (1988) Biomechanical properties of canine cortical bone allografts: effects of preparation and storage. *Am J Vet Res* 49:978–986
- Saha S, Hayes WC (1977) Relations between tensile impact properties and microstructure of compact bone. *Calcif Tissue Res* 24(1):65–72
- Sevostianov I, Kachanov M (2000) Impact of the porous microstructure on the overall elastic properties of the osteonal cortical bone. *J Biomech* 33(7):881–888
- Standard (1999) Fracture mechanics toughness tests. method for determination of K_{Ic} , critical CTOD and critical J values of metallic materials. British Standard Institute, BS7448–BS7449
- Systemes D (2012) Abaqus v6.12 documentation-ABAQUS analysis user's manual. Inc 6.12 edn
- Thompson JB, Kindt JH, Drake B, Hansma HG, Morse DE, Hansma PK (2001) Bone indentation recovery time correlates with bond reforming time. *Nature* 414:773–776
- Ural A, Vashishth D (2006) Cohesive finite element modeling of age-related toughness loss in human cortical bone. *J Biomech* 39(16):2974–2982
- Vashishth D, Tanner KE, Bonfield W (2003) Experimental validation of a microcracking-based toughening mechanism for cortical bone. *J Biomech* 36(1):121–124
- Weiner S, Wagner HD (1998) The material bone: structure-mechanical function relations. *Annu Rev Mater Sci* 28:271–298
- Yeni YN, Fyhrie DP (2003) A rate-dependent microcrack-bridging model that can explain the strain rate dependency of cortical bone apparent yield strength. *J Biomech* 36(9):1343–1353
- Zimmermann EA, Schaible E, Bale H, Barth HD, Tang SY, Reichert P (2011) Age-related changes in the plasticity and toughness of human cortical bone at multiple length scales. *Proc Natl Acad Sci* 108:14,416–14,421
- Zioupos P, Currey JD (1994) The extent of microcracking and the morphology of microcracks in damaged bone. *J Mater Sci* 29(4):978–986
- Zioupos P, Wang XT, Currey JD (1996) The accumulation of fatigue microdamage in human cortical bone of two different ages in vitro. *Clin Biomech* 11(7):365–375

A Nonlocal Model of Plasticity and Damage with Different Internal Lengths

Francesco Marotti de Sciarra

Abstract A nonlocal thermodynamically consistent model of plasticity and damage is presented using an integral approach. The theory is developed in the framework of the generalized standard material and the constitutive model is identified by the specification of a nonlocal first law of thermodynamics and of a local second one. The constitutive model is then addressed by defining a suitable expression of the free energy which yields a nonlocal plastic model in the stress space and a nonlocal damage model in the strain space. A variational formulation depending on local and nonlocal state variables is thus provided.

Keywords Nonlocal damage · Nonlocal plastic behavior · Internal energies · Internal variables · Standard materials · Strain-based damage · Variational formulation · Yield function

1 Introduction

Engineering structures may be subjected to loading conditions which can lead the material to undergo plastic flow and damage. Phenomenological local damage models, see e.g. Lemaitre and Chaboche (1990), Chaboche (1988b), Lemaitre (1996), consider the effects associated with a certain damage state through the definition of thermodynamic state variables. In addition the material stiffness is reduced by damage through the effective stress concept introduced by Kachanov (1958). As a consequence several damage theories have been proposed in the framework of thermodynamics of irreversible processes which are either phenomenologically based or micro-mechanically motivated (Chaboche 1988a, b; Lemaitre 1996; Brünig 2003b; Brünig et al. 2011).

F. Marotti de Sciarra (✉)

Department of Structures for Engineering and Architecture,
University of Naples Federico II, via Claudio 21, 80125 Napoli, Italy
e-mail: marotti@unina.it

A model of generalized standard elastoplastic material has been proposed by Halphen and Nguyen (1975) where the flow rule is given in terms of a normality rule to a generalized elastic domain defined in the product space of stresses and thermodynamic forces. Then several local models of plasticity coupled with damage have been proposed and investigated in the framework of continuum mechanics with internal variables (Brüning 2003a; Menzel et al. 2005; Wu et al. 2006; Cicekli et al. 2007).

The necessity for introducing nonlocal theories in a continuum model is due to the fact that the classical rate-independent plasticity or damage theories do not possess an intrinsic length scale.

The evolution of damage causes softening in the continuum theories and it is known that softening leads to pathological localization and strongly mesh dependent results in a finite element procedure. To overcome this difficulty, the continuum model has to be supplied with an internal time scale in the form of a strain rate dependent behavior (see e.g. Perzyna 1963; Glema et al. 2000) or with an internal length scale such as Cosserat and Cosserat (1909), gradient (de Borst and Mühlhaus 1992; Peerlings et al. 1996; Steinmann 1999; Nedjar 2001; Wang et al. 2003; Voyiadjis et al. 2004; Polizzotto 2003a, b, 2007, 2008, 2011; Marotti de Sciarra 2013, 2014) and nonlocal (Pijaudier-Cabot and Bazant 1987; Bazant and Pijaudier-Cabot 1988; Voyiadjis and Dorgan 2001; Bazant and Jirasek 2002; Polizzotto 2003a; Marotti de Sciarra 2009b) models.

Gradient models have been used in recent years for both small-strain and large-strain plasticity with damage (see e.g. Nedjar 2001; Geers et al. 2003) and for modeling nanostructures (Arash and Wang 2012; Barretta and Marotti de Sciarra 2013; Simsek and Reddy 2013; Barretta et al. 2014). Gurtin and Murdoch (1975) proposed a model of surface stresses describing the surface elastic properties of solids. This model has found many applications for materials at the micro- and nano-scales, see e.g. Javili et al. (2012), Eremeyev and Altenbach (2013) and Altenbach and Eremeyev (2011). In particular, the surface effects are used for the description of deviancy of the properties of nanospecimens from the ones of bulk materials.

In this paper a phenomenological model for a class of nonlocal elastoplastic damaging materials is proposed considering a nonlocal model of integral type. A nonlocal elastoplastic model is defined in the generalized stress space and is coupled with nonlocal damage which is formulated in the strain space. The nonlocal elastoplastic formulation and the stress decomposition of the nonlocal strain damage model behavior consistently follows from the thermodynamic analysis in a nonlocal integral context. The nonlocal constitutive equations are derived from a nonlocal form of the first law of thermodynamics, from the classical form of the second law and a suitable expression of the free energy. Accordingly the nonlocal counterpart of the Clausius–Duhem inequality is attained and the maximum dissipation principle for the nonlocal elastoplastic damage problem can be straightforwardly obtained.

The proposed general thermodynamic framework provides the tools to derive a new consistent variational formulation for the nonlocal constitutive problem of elastoplasticity coupled with damage in the strain space. Hence the variational formulation associated with the nonlocal constitutive model is explicitly provided. Finally

it is worth noting that an advantage from a computational point of view of models with strain-based damage is that the stress corresponding to a given strain can be evaluated directly without any need for solving a nonlinear system of equations (see e.g. Marotti de Sciarra 2009a).

2 Nonlocal Constitutive Model

A continuum body occupying a finite regular domain Ω of a three-dimensional Euclidean space is considered. The inelastic model is subjected to a given load history and a quasi-static evolution process in a geometrically linear range is assumed. Further the mechanical behavior of the body is time-independent.

The classical theory of small deformation plasticity is based on the additive decomposition of the total strain $\boldsymbol{\varepsilon}$ into elastic \boldsymbol{e} and plastic parts \boldsymbol{p} , with \boldsymbol{e} being the elastic component and \boldsymbol{p} being the corresponding plastic strain.

A model governing a nonlocal stress-based plasticity with a nonlocal strain-based damage is developed in this paper following the generalized standard material and the constitutive framework presented in Marotti de Sciarra (2012) for local plasticity. The plastic and damage state of the body is phenomenologically described by a set of internal variables and by the related mechanisms for energy exchange. Reversible phenomena modify the stored energy and the irreversible phenomena induce energy dissipation.

The evolution of the hardening phenomena of associated type is described in terms of a set of dual kinematic and static internal variables which account for the changes in the material structure at the microscale level (Halphen and Nguyen 1975). The dual set of internal variables are reported in Table 1. The back-stresses $\boldsymbol{\chi}_1, \boldsymbol{\chi}_2$ are associated with the kinematic hardening and the drag-stresses $\boldsymbol{\chi}_3, \boldsymbol{\chi}_4, \boldsymbol{\chi}_5$ are associated with isotropic hardening/softening.

It is known that classical inelastic theories are unable to describe the softening behavior, small-scale phenomena or effects of the relative size on the mechanical properties of the material since such theories do not possess an intrinsic material

Table 1 The dual set of kinematic and static variables

State variables		Associated conjugates
Observable	Internal	
$\boldsymbol{\varepsilon}$		$\boldsymbol{\sigma}, s, \boldsymbol{\sigma}^e$
	\boldsymbol{p}	$\boldsymbol{\chi}$
	$\boldsymbol{\alpha}_1$	$\boldsymbol{\chi}_1$
	$\boldsymbol{\alpha}_2$	$\boldsymbol{\chi}_2$
	$\boldsymbol{\alpha}_3$	$\boldsymbol{\chi}_3$
	$\boldsymbol{\alpha}_4$	$\boldsymbol{\chi}_4$
	$\boldsymbol{\alpha}_5$	$\boldsymbol{\chi}_5$

length scale. These problems can then be avoided with the use of a nonlocal theory which introduces the length scale in the constitutive equations.

It is shown in Al-Rub and Voyiadjis (2003), Fleck and Hutchinson (2001) that the multiplicity of plastic phenomena at small-scale levels implies the necessity of more than one length parameter in the nonlocal gradient description. Since plasticity and damage correspond to different mechanisms acting on different scales, the two inelastic behaviors are modeled by nonlocal relations with different internal length scales as hereafter shown.

The nonlocal behavior associated with plasticity is governed by the nonlocal field $R\alpha_2$ which can be obtained as a spatial weighted average of the local variable α_2 by the following parametric relation

$$\bar{\alpha}_2(x) = R\alpha_2(x) = \int_{\Omega} W_p(x, y) \alpha_2(y) dy \quad (1)$$

where $W_p(x, y)$ is the plastic weight function. An explicit expression of the weight function is reported in Marotti de Sciarra (2009a). Similar relations hold for the nonlocal counterparts of the kinematic internal variables α_3 and α_5

$$\begin{aligned} \bar{\alpha}_3(x) &= R\alpha_3(x) = \int_{\Omega} W_p(x, y) \alpha_3(y) dy, \\ \bar{\alpha}_5(x) &= R\alpha_5(x) = \int_{\Omega} W_p(x, y) \alpha_5(y) dy. \end{aligned} \quad (2)$$

The long range forces arising in a damaged structure are provided by the nonlocal static internal variable \bar{s} which has the mechanical meaning of the nonlocal relaxation stress s as shown in the sequel. It is expressed in the following form

$$\bar{s}(x) = Ss(x) = \int_{\Omega} W_d(x, y) s(y) dy \quad (3)$$

where W_d is the weight function for damage phenomena. The weight functions will be left unspecified since it is not necessary to give them an explicit expression to the for the development of the constitutive model.

Generally deformation processes in metals enhances the creation, motion, and storage of the dislocations. In particular, the material hardening is caused by the storage of dislocations which can be referred to as statistically-stored dislocations (SSDs) and geometrically-necessary dislocations (GNDs). The SSDs are generated by trapping the dislocations each other in a random way and the GNDs represent the stored dislocations which are required for compatible deformations within the polycrystals. During plastic deformations, the density of SSDs increases due to a wide range of processes that lead to the production of new dislocations. The new

generated dislocations travel on a background of GNDs which causes additional storage of defects and increases the deformation resistance by acting like obstacles to the SSDs (Gao et al. 1999). The SSDs and GNDs are different in nature since experimental evidences show that the SSDs dependent on the effective plastic strain while the GNDs are associated with the gradient of the effective plastic strain (Ashby 1970; Fleck and Hutchinson 1997; Arsenlis and Parks 1999; Gao et al. 1999).

The determination of the evolution of the assumed internal state variables is one of the main challenge of the constitutive modeling. This task can be effectively achieved through the thermodynamic principles for the development of a continuum thermo-elasto-plastic-damage based model where damage is modeled in the strain space.

The first principle of thermodynamics (Edelen and Laws 1971; Lemaitre 1996; Polizzotto 2003a; Marotti de Sciarra 2009c) for a nonlocal model is expressed point-wise in the following form

$$\dot{u} = \boldsymbol{\sigma} * \boldsymbol{\varepsilon} + \dot{Q} + P \quad (4)$$

where the explicit dependence on the point has been dropped for simplicity. The heat supplied to an element of volume is $\dot{Q} = -\text{div } \mathbf{q}$, being \mathbf{q} the heat flux, and $\boldsymbol{\sigma}$ is the actual stress. The internal energy density u depends on the kinematic internal variables $\boldsymbol{\alpha}_1, \boldsymbol{\alpha}_4$, on the kinematic nonlocal internal variables $R\boldsymbol{\alpha}_2, R\boldsymbol{\alpha}_3, R\boldsymbol{\alpha}_5$ and on the nonlocal static internal variable Ss . The nonlocality residual function P takes into account the energy exchanges between neighbor particles, see e.g. Edelen and Laws (1971).

The body is assumed to be a thermodynamically insulated system with reference to energy exchanges due to nonlocality so that the following isolation condition holds (Polizzotto 2011)

$$\int_{\Omega} P(x) dx = 0. \quad (5)$$

The second principle of thermodynamics for a nonlocal behavior, is written in its classical point-wise form

$$\dot{s}T + \text{div } \mathbf{q} - \nabla T * \frac{q}{T} \geq 0 \quad (6)$$

in any point of the body where \dot{s} is the internal entropy production rate per unit volume. Considering isothermal processes, the total dissipation is then given by

$$D = \boldsymbol{\sigma} * \dot{\boldsymbol{\varepsilon}} - \dot{\Phi} + P \geq 0 \quad (7)$$

where Φ denotes the Helmholtz free energy.

The complexity of the constitutive model is directly determined by the form of the free energy so that its definition constitutes a crucial point of the formulation. In this model the constitutive equations are based on the following expression of the free energy

$$\Phi(\boldsymbol{\varepsilon}, \mathbf{p}, \boldsymbol{\alpha}_1, R\boldsymbol{\alpha}_2, R\boldsymbol{\alpha}_3, \boldsymbol{\alpha}_4, R\boldsymbol{\alpha}_5, S\mathbf{s}) = \psi(\boldsymbol{\varepsilon} - \mathbf{p}, \boldsymbol{\alpha}_1, R\boldsymbol{\alpha}_2, R\boldsymbol{\alpha}_3, \boldsymbol{\alpha}_4, R\boldsymbol{\alpha}_5) - S\mathbf{s} * \boldsymbol{\varepsilon} \quad (8)$$

where the elastic energy ψ depends on the difference between the total strain and the plastic strain and on kinematic local and nonlocal internal variables. Moreover, the additive term in the free energy Φ is based on the fact that damage has a distinctive morphology which is different from the plastic deformation mechanisms. Furthermore the expression (8) allows us to derive a yield criterion in the stress space and a damage domain in the strain space as shown in the sequel.

Expanding the inequality (7) and substituting the rate of the expression (8) above of the free energy, one obtains the following thermodynamic constraints

$$D = (\boldsymbol{\sigma} + \bar{\mathbf{s}} - d_{\boldsymbol{\varepsilon}}\Phi) * \dot{\boldsymbol{\varepsilon}} - d_{\mathbf{p}}\Phi * \dot{\mathbf{p}} - d_{\boldsymbol{\alpha}_1}\Phi * \dot{\boldsymbol{\alpha}}_1 - d_{R\boldsymbol{\alpha}_2}\Phi * \dot{R\boldsymbol{\alpha}}_2 - d_{R\boldsymbol{\alpha}_3}\Phi * \dot{R\boldsymbol{\alpha}}_3 - d_{\boldsymbol{\alpha}_4}\Phi * \dot{\boldsymbol{\alpha}}_4 - d_{R\boldsymbol{\alpha}_5}\Phi * \dot{R\boldsymbol{\alpha}}_5 + P \geq 0 \quad (9)$$

Assuming that the axiom of entropy production holds, the inequality (9) results in the thermodynamic state laws reported in Table 2.

The relations in Table 2 describe the relationships between the state variables and their associated thermodynamic conjugate forces. The stress $\boldsymbol{\sigma}$ is a measure of the elastic changes in the internal structure, the elastic stress $\boldsymbol{\sigma}^e$ is related to the elastic strain, the variables $\boldsymbol{\chi}_1, \boldsymbol{\chi}_2, \boldsymbol{\chi}_3, \boldsymbol{\chi}_4, \boldsymbol{\chi}_5$ are the conjugate forces corresponding to the plastic internal state variables $\boldsymbol{\alpha}_1, R\boldsymbol{\alpha}_2, R\boldsymbol{\alpha}_3, \boldsymbol{\alpha}_4, R\boldsymbol{\alpha}_5$. The conjugate forces $\boldsymbol{\chi}_i$ ($i = 1, \dots, 5$) are measures of plastic changes in the internal structure and \mathbf{s} is a measure of the damage changes in the internal structure.

The sum of the actual stress $\boldsymbol{\sigma}$ and of the nonlocal stress $S\mathbf{s}$ provides the elastic stress $\boldsymbol{\sigma}^e$. From a mechanical point of view the nonlocal stress $S\mathbf{s}$ provides the total damage which is accumulated during loading and the elastic stress causes the same state of deformation in a virgin material as in a damaged material. The relationships between the proposed damage model and the classical one are analyzed in Marotti de Sciarra (2012). The nonlocal stress $S\mathbf{s}$ is then associated with the elastic-damage changes in the internal structure resulting from crack and voids during the loading process.

Table 2 The thermodynamic state laws

		$\boldsymbol{\sigma}^e = d_{\boldsymbol{\varepsilon}}\Phi$
		$\boldsymbol{\chi} = d_{\mathbf{p}}\Phi = -\boldsymbol{\sigma}^e$
Plasticity	Kinematic hardening	$\boldsymbol{\chi}_1 = d_{\boldsymbol{\alpha}_1}\Phi$
		$\boldsymbol{\chi}_2 = d_{R\boldsymbol{\alpha}_2}\Phi$
	Isotropic hardening	$\boldsymbol{\chi}_3 = d_{R\boldsymbol{\alpha}_3}\Phi$
		$\boldsymbol{\chi}_4 = d_{\boldsymbol{\alpha}_4}\Phi$
		$-\boldsymbol{\chi}_5 = d_{R\boldsymbol{\alpha}_5}\Phi$
Damage		$\boldsymbol{\sigma} = \boldsymbol{\sigma}^e - \bar{\mathbf{s}}$

At every point where an irreversible mechanism develops, the dissipation can be assumed in a bilinear form and following the procedure reported in Marotti de Sciarra (2008), the nonlocal counterpart of the Clausius–Duhem inequality expresses the fact that the dissipation energy D is necessarily nonnegative as follows

$$D = \sigma^e * \dot{p} - \chi_1 * \dot{\alpha}_1 - R\chi_2 * \dot{\alpha}_2 - R\chi_3 * \dot{\alpha}_3 - \chi_4 * \dot{\alpha}_4 + R\chi_5 * \dot{\alpha}_5 + \dot{s} * S\varepsilon \geq 0. \quad (10)$$

This result requires that the inelastic work is dissipated away as heat, except for that energy which is stored because of the rearrangement of the material internal structure. Although the dissipation D is written in the additive form as shown by Eq. (10), the corresponding physical mechanisms is not decoupled. In fact coupling does occur between plasticity and damage since the conjugate forces and their associated fluxes are related each other so that two damage mechanisms are introduced: one mechanism is coupled with plasticity and the other can occur independent of plastic deformation.

Finally the nonlocality residual function has the following expression

$$P = \chi_2 * R\dot{\alpha}_2 - R\chi_2 * \dot{\alpha}_2 + \chi_3 * R\dot{\alpha}_3 - R\chi_3 * \dot{\alpha}_3 - \chi_5 * R\dot{\alpha}_5 + R\chi_5 * \dot{\alpha}_5 - S\dot{s} * \varepsilon + \dot{s} * S\varepsilon. \quad (11)$$

Note that the presented approach provides a path to incorporate a nonlocal model, based on the concept of nonlocality residual, into an existing thermodynamic framework.

3 Evolution Criteria for Plasticity and Damage

The plastic and damage evolution criteria for the considered nonlocal model can be obtained by assuming that the sublinear function D is lower-semicontinuous (Rockafellar 1970). Hence the dissipation D turns out to be the support function of a closed convex domain C which is given by the local and nonlocal state variables such that the following inequality is fulfilled

$$D \geq \sigma^e * \dot{p} - \chi_1 * \dot{\alpha}_1 - R\chi_2 * \dot{\alpha}_2 - R\chi_3 * \dot{\alpha}_3 - \chi_4 * \dot{\alpha}_4 + R\chi_5 * \dot{\alpha}_5 + \dot{s} * S\varepsilon \quad (12)$$

for any $(\dot{p}, -\dot{\alpha}_1, -\dot{\alpha}_2, -\dot{\alpha}_3, -\dot{\alpha}_4, \dot{\alpha}_5, \dot{s})$.

In mechanical terms, the domain C is the set of admissible elastic stresses, local and nonlocal static internal variables and nonlocal strains and its boundary represents the elasto-plastic-damage surface. As a consequence such a model provides a unique generalized evolutive relation for plasticity and damage.

Since plasticity and damage correspond to different mechanisms acting on different scales, the two inelastic models have to be modeled by different evolution equations. Accordingly the proposed nonlocal elastoplastic-damage model is now specialized to a nonlocal elastoplastic model and to a nonlocal damage model depending on two evolutive relations.

To this end the dissipation D can be splitted into two parts which are associated with plastic and damage mechanisms

$$\begin{cases} D_1 = \boldsymbol{\sigma}^e * \dot{\boldsymbol{p}} - \boldsymbol{\chi}_1 * \dot{\boldsymbol{\alpha}}_1 - R\boldsymbol{\chi}_2 * \dot{\boldsymbol{\alpha}}_2 - R\boldsymbol{\chi}_3 * \dot{\boldsymbol{\alpha}}_3 - \boldsymbol{\chi}_4 * \dot{\boldsymbol{\alpha}}_4 + R\boldsymbol{\chi}_5 * \dot{\boldsymbol{\alpha}}_5 \geq 0 \\ D_2 = \dot{\boldsymbol{s}} * S\boldsymbol{\varepsilon} \geq 0. \end{cases} \quad (13)$$

It is apparent that the inequalities (13) ensure the non-negativeness of D . The two dissipations $D_1(\dot{\boldsymbol{p}}, -\dot{\boldsymbol{\alpha}}_1, -\dot{\boldsymbol{\alpha}}_2, -\dot{\boldsymbol{\alpha}}_3, -\dot{\boldsymbol{\alpha}}_4, \dot{\boldsymbol{\alpha}}_5)$ and $D_2(\dot{\boldsymbol{s}})$ are the support functions of two closed convex domains C_1 and C_2 , respectively. From the physical standpoint, C_1 is the set of admissible elastic stresses $\boldsymbol{\sigma}^e$, local and nonlocal static internal variables $\boldsymbol{\chi}_1, R\boldsymbol{\chi}_2, R\boldsymbol{\chi}_3, \boldsymbol{\chi}_4, R\boldsymbol{\chi}_5$ and its boundary represents the elastic surface. The domain C_2 is the set of admissible nonlocal strains $S\boldsymbol{\varepsilon}$ and its boundary represents the damage surface.

The dissipation processes (13) imply the existence of the complementary laws

$$\begin{cases} \boldsymbol{\sigma}^e \in \partial_{\dot{\boldsymbol{p}}} D_1, & R_i \boldsymbol{\chi}_i \in \partial_{-\dot{\boldsymbol{\alpha}}_i} D_1, & R\boldsymbol{\chi}_5 \in \partial_{\dot{\boldsymbol{\alpha}}_5} D_1 \\ S\boldsymbol{\varepsilon} \in \partial_{\dot{\boldsymbol{s}}} D_2 \end{cases} \quad (14)$$

with $i = 1, \dots, 4$ where $\{R_i\} = \{I, R, R, I\}$ and ∂ denotes the subdifferential operator.

The indicator functions of the domains C_1 and C_2 are denoted by I_{C_1} and I_{C_2} and turn out to be the Fenchel's conjugates of the dissipation functions D_1 and D_2 respectively. Therefore the evolutive relations (14) can be equivalently expressed in terms of the following normality laws

$$\begin{cases} (\dot{\boldsymbol{p}}, -\dot{\boldsymbol{\alpha}}_i, \dot{\boldsymbol{\alpha}}_5) \in \partial I_{C_1}(\boldsymbol{\sigma}^e, R_i \boldsymbol{\chi}_i, R\boldsymbol{\chi}_5) \\ \dot{\boldsymbol{s}} \in \partial I_{C_2}(S\boldsymbol{\varepsilon}) \end{cases} \quad (15)$$

with $i = 1, \dots, 4$. It can be easily proved that the subdifferentials of the indicator functions I_{C_1} and I_{C_2} coincide to the normal cone to the elastoplastic domain C_1 and to the damage domain C_2 , respectively. Consequently the evolution laws of the flux variables can be expressed in terms of the dual local and nonlocal variables in the form

$$\begin{cases} (\dot{\boldsymbol{p}}, -\dot{\boldsymbol{\alpha}}_i, \dot{\boldsymbol{\alpha}}_5) \in N_{C_1}(\boldsymbol{\sigma}^e, R_i \boldsymbol{\chi}_i, R\boldsymbol{\chi}_5) \\ \dot{\boldsymbol{s}} \in N_{C_2}(S\boldsymbol{\varepsilon}) \end{cases} \quad (16)$$

with $i = 1, \dots, 4$, and represent the generalized normality relations.

Properties of Fenchel's conjugates allow one to state that the nonlocal counterpart of the classical maximum dissipation principle holds for this nonlocal elastoplastic-damage model following the reasoning reported in Marotti de Sciarra (2009a). The nonlocal maximum dissipation principle states that the actual state of the thermodynamic forces $(\boldsymbol{\sigma}^e, \boldsymbol{\chi}_1, R\boldsymbol{\chi}_2, R\boldsymbol{\chi}_3, \boldsymbol{\chi}_4, R\boldsymbol{\chi}_5)$ is that which maximizes the inelastic nonlocal dissipation functions over all other possible admissible states.

4 Plastic and Damage Flow Rules for the Nonlocal Model

The associative evolution laws can be obtained in terms of the plastic and damage multipliers by assuming that the admissible elastoplastic and damage domains are defined in terms of the plastic and damage modes

$$\begin{cases} h(\boldsymbol{\sigma}^e, \boldsymbol{\chi}_1, R\boldsymbol{\chi}_2, R\boldsymbol{\chi}_3, \boldsymbol{\chi}_4, R\boldsymbol{\chi}_5) = h_1(\boldsymbol{\sigma}^e, \boldsymbol{\chi}_1, R\boldsymbol{\chi}_2) - h_2(R\boldsymbol{\chi}_3, \boldsymbol{\chi}_4, R\boldsymbol{\chi}_5) - \sigma_y \\ g(S\boldsymbol{\varepsilon}) = g_1(S\boldsymbol{\varepsilon}) - \varepsilon_d \end{cases} \quad (17)$$

where σ_y is the initial size of the yield surface and ε_d is the initial damage threshold.

Substituting relations (17) in (16), the flow rules (16) can be equivalently rewritten in terms of the plastic and damage multipliers (see Marotti de Sciarra 2008) to get

$$\begin{cases} (\dot{\boldsymbol{p}}, -\dot{\boldsymbol{\alpha}}_1, -\dot{\boldsymbol{\alpha}}_2,) = \lambda_p dh_1(\boldsymbol{\sigma}^e, \boldsymbol{\chi}_1, R\boldsymbol{\chi}_2) \\ (\dot{\boldsymbol{\alpha}}_3, \dot{\boldsymbol{\alpha}}_4, -\dot{\boldsymbol{\alpha}}_5) = \lambda_p dh_2(R\boldsymbol{\chi}_3, \boldsymbol{\chi}_4, R\boldsymbol{\chi}_5) \\ \dot{\boldsymbol{s}} = \lambda_d dg(S\boldsymbol{\varepsilon}) \end{cases} \quad (18)$$

under the complementarity conditions

$$\begin{cases} \lambda_p \geq 0, & h(\boldsymbol{\sigma}^e, R_i \boldsymbol{\chi}_i, R\boldsymbol{\chi}_5) \leq 0, & \lambda_p h(\boldsymbol{\sigma}^e, R_i \boldsymbol{\chi}_i, R\boldsymbol{\chi}_5) = 0 \\ \lambda_d \geq 0, & g(S\boldsymbol{\varepsilon}) \leq 0, & \lambda_d g(S\boldsymbol{\varepsilon}) = 0 \end{cases} \quad (19)$$

with $i = 1, \dots, 4$. Here λ_p is the plastic multiplier and λ_d denotes the damage multiplier.

If the yield mode h_1 is such that the norm of its derivative with respect to $\boldsymbol{\sigma}^e$ is equal to one, i.e. $\|d_{\boldsymbol{\sigma}^e} h_1(\boldsymbol{\sigma}^e, \boldsymbol{\chi}_1, R\boldsymbol{\chi}_2)\| = 1$, the plastic flow

$$\dot{\boldsymbol{p}} = \lambda_p d_{\boldsymbol{\sigma}^e} h_1(\boldsymbol{\sigma}^e, \boldsymbol{\chi}_1, R\boldsymbol{\chi}_2) \quad (20)$$

is such that $\|\dot{\boldsymbol{p}}\|$ coincides to the plastic multiplier, i.e. $\|\dot{\boldsymbol{p}}\| = \lambda_p$. Moreover assuming that $d_{R\boldsymbol{\chi}_3} h_2(R\boldsymbol{\chi}_3, \boldsymbol{\chi}_4, R\boldsymbol{\chi}_5) = 1$ it results $\dot{\boldsymbol{\alpha}}_3 = \lambda_p = \|\dot{\boldsymbol{p}}\|$.

Hence the actual value of the kinematic internal variable $\boldsymbol{\alpha}_3$ assumes the mechanical meaning of the effective plastic strain

$$\alpha_3 = \int_0^t \|\dot{\mathbf{p}}(\tau)\| d\tau. \quad (21)$$

Accordingly the internal variable α_3 can be associated to SSDs.

5 Finite-Step Nonlocal Variational Formulation

Let $t_0, t_1, \dots, t_n, t_{n+1} = t_n + \Delta t$ be convenient time instances along the time interval over which the response of the body is sought. Consider the time step $\Delta t = t_{n+1} - t_n$. At the time $t = t_n$ all quantities are known since they are the converged values of the previous step and the solution must be computed at $t = t_{n+1}$ for a given strain increment $\Delta \boldsymbol{\varepsilon}$.

Hence the time discretization is performed according to the Euler backward scheme and the constitutive behavior of the body in the small strain range is governed at the time step $n+1$ by the relations reported in Table 2 and by the flow rules (16). The finite-step counterparts of the flow rules associated with the nonlocal model are enforced at the end of the step according to the relations

$$\begin{cases} (\Delta \mathbf{p}, -\Delta \alpha_1, -\Delta \alpha_2, -\Delta \alpha_3, -\Delta \alpha_4, -\Delta \alpha_5) \in N_{C_1}(\boldsymbol{\sigma}^e, \boldsymbol{\chi}_1, R\boldsymbol{\chi}_2, R\boldsymbol{\chi}_3, \boldsymbol{\chi}_4, R\boldsymbol{\chi}_5) \\ \Delta \mathbf{s} \in N_{C_2}(S\boldsymbol{\varepsilon}), \end{cases} \quad (22)$$

and the time increment Δt has been dropped being N_{C_1} and N_{C_2} normal cones. Note that the finite-step flow rule can be equivalently expressed in terms of the dissipation.

Thus the finite-step nonlocal elastoplastic-damage model is governed by the following relations

$$\begin{cases} \boldsymbol{\sigma}^e = -d_{\mathbf{p}}\psi, & \boldsymbol{\chi}_1 = d_{\alpha_1}\psi, & \boldsymbol{\chi}_2 = d_{\alpha_2}\psi, \\ \boldsymbol{\chi}_3 = d_{\alpha_3}\psi, & \boldsymbol{\chi}_4 = d_{\alpha_4}\psi, & \boldsymbol{\chi}_5 = -d_{\alpha_5}\psi, \\ \boldsymbol{\sigma}^e \in \partial_{\mathbf{p}}D_1, & R_i\boldsymbol{\chi}_i \in \partial_{-\alpha_i}D_1, & R\boldsymbol{\chi}_5 \in \partial_{\alpha_5}D_1 \\ S\boldsymbol{\varepsilon} \in \partial_S D_2 \end{cases} \quad (23)$$

with $i = 1, \dots, 4$. Therefore the nonlocal potential associated with the nonlocal model can then be evaluated following the direct procedure reported in Marotti de Sciarra (2009b) and the following variational formulation holds:

Theorem 1 (Nonlocal variational formulation) *The set $(\boldsymbol{\varepsilon}, \mathbf{p}, R_i\alpha_i, R\alpha_5, \mathbf{s})$ is a solution of the saddle problem*

$$\text{stat}_{\alpha_5} \min_{\boldsymbol{\varepsilon}, \mathbf{p}, \alpha_i, \mathbf{s}} \Pi(\boldsymbol{\varepsilon}, \mathbf{p}, R_i\alpha_i, R\alpha_5, \mathbf{s}) \quad (24)$$

where

$$\begin{aligned}
 \Pi(\boldsymbol{\varepsilon}, \mathbf{p}, \boldsymbol{\alpha}_1, R\boldsymbol{\alpha}_2, R\boldsymbol{\alpha}_3, \boldsymbol{\alpha}_4, R\boldsymbol{\alpha}_5, \mathbf{s}) &= \int_{\Omega} \psi(\boldsymbol{\varepsilon} - \mathbf{p}, R_i \boldsymbol{\alpha}_i, R\boldsymbol{\alpha}_5) dx \\
 &+ \int_{\Omega} D_1(\Delta \mathbf{p}, -\Delta \boldsymbol{\alpha}_i, \Delta \boldsymbol{\alpha}_5) dx \\
 &+ \int_{\Omega} D_2(\Delta \mathbf{s}) dx - \int_{\Omega} \mathbf{s} * S \boldsymbol{\varepsilon} dx \\
 &- \int_{\Omega} \boldsymbol{\sigma} * \boldsymbol{\varepsilon} dx \tag{25}
 \end{aligned}$$

with $i = 1, \dots, 4$, if and only if it is a solution of the finite-step nonlocal elastoplastic model coupled with damage. ■

The stationary conditions of the potential Π enforced at the point

$$\boldsymbol{\varepsilon}, \mathbf{p}, R_i \boldsymbol{\alpha}_i, R\boldsymbol{\alpha}_5, \mathbf{s},$$

with $i = 1, \dots, 4$, provides the finite-step nonlocal elastoplastic-damage model (23). In fact the stationary conditions are:

$$(0, 0, 0, 0, 0, 0, 0, 0) \in \partial \Pi(\boldsymbol{\varepsilon}, \mathbf{p}, \boldsymbol{\alpha}_1, R\boldsymbol{\alpha}_2, R\boldsymbol{\alpha}_3, \boldsymbol{\alpha}_4, R\boldsymbol{\alpha}_5, \mathbf{s}) \tag{26}$$

which are equivalent to the following relations:

$$\begin{aligned}
 0 \in \partial_{\boldsymbol{\varepsilon}} \Pi &\iff S\mathbf{s} + \boldsymbol{\sigma} = d_{\boldsymbol{\varepsilon} - \mathbf{p}} \psi(\boldsymbol{\varepsilon} - \mathbf{p}, R_i \boldsymbol{\alpha}_i, R\boldsymbol{\alpha}_5) = \boldsymbol{\sigma}^e, \\
 (0, 0, 0, 0, 0, 0) \in \partial_{(\mathbf{p}, \boldsymbol{\alpha}_i, \boldsymbol{\alpha}_5)} \Pi &\iff \begin{bmatrix} -d_{\mathbf{p}} \psi \\ d_{\boldsymbol{\alpha}_1} \psi \\ R d_{\bar{\boldsymbol{\alpha}}_2} \psi \\ R d_{\bar{\boldsymbol{\alpha}}_3} \psi \\ d_{\boldsymbol{\alpha}_4} \psi \\ -R d_{\bar{\boldsymbol{\alpha}}_5} \psi \end{bmatrix} \in \partial D_1(\Delta \mathbf{p}, -\Delta \boldsymbol{\alpha}_i, \Delta \boldsymbol{\alpha}_5) \tag{27}
 \end{aligned}$$

with $i = 1, \dots, 4$ where $\boldsymbol{\sigma}^e = -d_{\mathbf{p}} \psi$, $\boldsymbol{\chi}_1 = d_{\boldsymbol{\alpha}_1} \psi$, $\boldsymbol{\chi}_2 = d_{\bar{\boldsymbol{\alpha}}_2} \psi$, $\boldsymbol{\chi}_3 = d_{\bar{\boldsymbol{\alpha}}_3} \psi$, $\boldsymbol{\chi}_4 = d_{\boldsymbol{\alpha}_4} \psi$, $\boldsymbol{\chi}_5 = -d_{\bar{\boldsymbol{\alpha}}_5} \psi$, and further it results:

$$0 \in \partial_{\mathbf{s}} \Pi \iff S\boldsymbol{\varepsilon} \in D_2(\Delta \mathbf{s}). \tag{28}$$

Reverting the steps above a solution of the finite-step nonlocal elastoplastic model with damage in the strain space makes the potential Π stationarity.

6 Conclusions

- An efficient building of a consistent thermodynamic integral nonlocal elastoplastic behavior coupled with damage in the strain space is presented.
- A variational formulation of the nonlocal elastoplastic and damage problem is derived.
- It is also shown that the inelastic internal variables can be related to the effective plastic strain and, then, to the SSDs by a suitable choice of the plastic mode.

Acknowledgments The author gratefully acknowledges the financial support of Project FARO IV Tornata, 2012.

References

- Al-Rub RKA, Voyiadjis GZ (2003) On the coupling of anisotropic damage and plasticity models for ductile materials. *Int J Solids Struct* 40(11):2611–2643
- Altenbach H, Eremeyev VA (2011) On the shell theory on the nanoscale with surface stresses. *Int J Eng Sci* 49(12):1294–1301 (Advances in generalized continuum mechanics a collection of studies in engineering sciences in memory of the late A.C. Eringen (1921–2009))
- Arash B, Wang Q (2012) A review on the application of nonlocal elastic models in modeling of carbon nanotubes and graphenes. *Comput Mater Sci* 51(1):303–313
- Arsenlis A, Parks DM (1999) Crystallographic aspects of geometrically-necessary and statistically-stored dislocation density. *Acta Mater* 47(5):1597–1611
- Ashby F (1970) The deformation of plastically non-homogeneous materials. *Philos Mag* 170(21):399–424
- Barretta R, Marotti de Sciarra F (2013) A nonlocal model for carbon nanotubes under axial loads. *Adv Mater Sci Eng* 2013:1–6
- Barretta R, Marotti de Sciarra F (2014) Small-scale effects in nanorods. *Acta Mech* 225(7):1945–1953
- Bazant Z, Jirasek M (2002) Nonlocal integral formulations of plasticity and damage: Survey of progress. *J Eng Mech* 128(11):1119–1149
- Bazant ZP, Pijaudier-Cabot G (1988) Nonlocal continuum damage, localization instability and convergence. *J Appl Mech* 55(2):1945–1953
- de Borst R, Muhlhaus HB (1992) Gradient-dependent plasticity: formulation and algorithmic aspects. *Int J Numer Meth Eng* 35:521–539
- Brüning M (2003a) An anisotropic ductile damage model based on irreversible thermodynamics. *Int J Plast* 19(10):1679–1713
- Brüning M (2003b) Numerical analysis of anisotropic ductile continuum damage. *Comput Methods Appl Mech Eng* 192(26–27):2949–2976
- Brüning M, Albrecht D, Gerke S (2011) Modelling of ductile damage and fracture behavior based on different micro-mechanisms. *Int J Damage Mech* 20:558–577
- Chaboche JL (1988a) Continuum damage mechanics—part II: damage growth, crack initiation, and crack growth. *Int J Damage Mech* 55(1):65–72
- Chaboche JL (1988b) Continuum damage mechanics theory and application—part I: theory. *Int J Damage Mech* 7(2):250–273
- Cicekli U, Voyiadjis GZ, Al-Rub RKA (2007) A plasticity and anisotropic damage model for plain concrete. *Int J Plast* 23(1011):1874–1900, (in honor of Professor Dusan Krajcinovic)

- Cosserat E, Cosserat F (1909) *Théorie des Corps Déformables*. Librairie Scientifique A. Herman et Fils, Paris, France
- Edeleson DGB, Laws N (1971) On the thermodynamics of systems with nonlocality. *Arch Ration Mech Anal* 43(1):24–35
- Eremeyev VA, Altenbach H (2013) Equilibrium of a second-gradient fluid and an elastic solid with surface stresses. *Meccanica* 1–9. doi:10.1007/s11012-013-9851-3
- Fleck NA, Hutchinson JW (1997) Strain gradient plasticity. *Adv Appl Mech* 295–361
- Fleck NA, Hutchinson JW (2001) A reformulation of strain gradient plasticity. *J Mech Phys Solids* 49:2245–2271
- Gao H, Huang Y, Nix WD, Hutchinson JW (1999) Mechanism-based strain gradient plasticity—i. Theory. *J Mech Phys Solids* 47(6):1239–1263
- Geers MGD, Ubachs RLJM, Engelen RAB (2003) Strongly non-local gradient-enhanced finite strain elastoplasticity. *Int J Numer Methods Eng* 56:2039–2068
- Glema A, Lodygowski T, Perzyna P (2000) Interaction of deformation waves and localization phenomena in inelastic solids. *Comput Methods Appl Mech Eng* 183(12):123–140
- Gurtin ME, Murdoch AI (1975) A continuum theory of elastic material surfaces. *Arch Ration Mech Anal* 57(4):291–323
- Halphen B, Nguyen QS (1975) Sur les matériaux standards généralisés. *Comput Methods Appl Mech Eng* 14:39–63
- Javili A, McBride A, Steinmann P (2012) Thermomechanics of solids with lower-dimensional energetics: on the importance of surface, interface, and curve structures at the nanoscale. a unifying review. *Appl Mech Rev* 65:1–31
- Kachanov LM (1958) On the creep fracture time (in Russian). *Izv Akad, Nauk USSR, Otd Tech* 8:26–31
- Lemaitre J (1996) *A Course on damage mechanics*. Springer
- Lemaitre J, Chaboche JL (1990) *Mechanics of solid materials*. Cambridge University Press, Cambridge
- Marotti de Sciarra F (2008) A general theory for nonlocal softening plasticity of integral-type. *Int J Plast* 24(8):1411–1439
- Marotti de Sciarra F (2009a) A nonlocal model with strain-based damage. *Int J Solids Struct* 46(22–23):4107–4122
- Marotti de Sciarra F (2009b) Novel variational formulations for nonlocal plasticity. *Int J Plast* 25(2):302–331
- Marotti de Sciarra F (2009c) On non-local and non-homogeneous elastic continua. *Int J Solids Struct* 46(34):651–676
- Marotti de Sciarra F (2012) Hardening plasticity with nonlocal strain damage. *Int J Plast* 34:114–138
- Marotti de Sciarra F (2013) A nonlocal finite element approach to nanobeams. *Adv Mech Eng* 2013(Article ID 720406):1–8
- Marotti de Sciarra F (2014) Finite element modelling of nonlocal beams. *Physica E* 59:144–149
- Menzel A, Ekh M, Runesson K, Steinmann P (2005) A framework for multiplicative elastoplasticity with kinematic hardening coupled to anisotropic damage. *Int J Plast* 21(3):397–434
- Nedjar B (2001) Elastoplastic-damage modelling including the gradient of damage: formulation and computational aspects. *Int J Solids Struct* 38(3031):5421–5451
- Peerlings RHJ, de Borst R, Brekelmans WAM, de Vree JHP (1996) Gradient enhanced damage for quasi-brittle materials. *Q Appl Math* 39:3391–3403
- Perzyna P (1963) The constitutive equations for rate-sensitive materials. *Q Appl Math* 20:321–332
- Pijaudier-Cabot TGP, Bazant ZP (1987) The constitutive equations for rate-sensitive materials. *ASCE J Eng Mech* 113:1512–1533
- Polizzotto C (2003a) Gradient elasticity and nonstandard boundary conditions. *Int J Solids Struct* 40(26):7399–7423
- Polizzotto C (2003b) Unified thermodynamic framework for nonlocal/gradient continuum theories. *Eur J Mech A Solids* 22(5):651–668 (General and plenary lectures from the 5th EUROMECH solid mechanics conference)

- Polizzotto C (2007) Strain-gradient elastic–plastic material models and assessment of the higher order boundary conditions. *Eur J Mech A Solids* 26(2):189–211
- Polizzotto C (2008) Shakedown theorems for elastic–plastic solids in the framework of gradient plasticity. *Int J Plast* 24(2):218–241
- Polizzotto C (2011) A unified residual-based thermodynamic framework for strain gradient theories of plasticity. *Int J Plast* 27(3):388–413
- Rockafellar RT (1970) *Convex anal.* Princeton, Princeton University Press
- Simsek M, Reddy JN (2013) Bending and vibration of functionally graded microbeams using a new higher order beam theory and the modified couple stress theory. *Int J Eng Sci* 64:37–53
- Steinmann P (1999) Formulation and computation of geometrically non-linear gradient damage. *Int J Numer Methods Eng* 46:757–779
- Voyiadjis GZ, Dorgan RJ (2001) Gradient formulation in coupled damage-plasticity. *Arch Mech* 53(4–5):565–597
- Voyiadjis GZ, Abu Al-Rub RK, Palazotto AN (2004) Thermodynamic framework for coupling of non-local viscoplasticity and non-local anisotropic viscodamage for dynamic localization problems using gradient theory. *Int J Plast* 20(6):981–1038 (Recent advances in multiscale modeling of plasticity)
- Wang W, Huang Y, Hsia KJ, Hu KX, Chandra A (2003) A study of microbend test by strain gradient plasticity. *Int J Plast* 19(3):365–382
- Wu JY, Li J, Faria R (2006) An energy release rate-based plastic-damage model for concrete. *Int J Solids Struct* 43(34):583–612

Hysteresis Loop Analysis in Cyclically Strained Materials

Jaroslav Polák and Roman Petráš

Abstract The generalized statistical theory of the hysteresis loop is adopted to describe the stress-strain relations, preferably in cyclic straining. The effective stress and the distribution of the internal critical stresses in cyclic straining are evaluated in two materials cycled at room and at elevated temperatures using the analysis of the hysteresis loop shape. The evolution of the shape of the probability density function of the internal critical stresses yields deeper insight into the mechanisms of cyclic plastic straining. It indicates the important role of cyclic plastic strain localization in room temperature fatigue softening. The approximation of the probability density function by Weibull distribution leads to the assessment of the effective and internal stresses and allows the simulation of the relations between the stress and strain in case of different cyclic histories.

Keywords Cyclic plastic straining · Hysteresis loop · Statistical theory · Effective stress · Internal stress

1 Introduction

The stress-strain relations in the materials are requisite for the calculation of the stress and strain distributions in structural members or in entire structures subjected to mechanically or thermally induced forces. Numerous efforts have been devoted to propose appropriate phenomenological relations that can describe the stress-strain

J. Polák (✉) · R. Petráš

Institute of Physics of Materials, Academy of Sciences of the Czech Republic,
Žižkova 22, 616 62 Brno, Czech Republic
e-mail: polak@ipm.cz

R. Petráš

e-mail: petras@ipm.cz

J. Polák

CEITEC, Institute of Physics of Materials Academy of Sciences of the Czech Republic,
Žižkova 22, Brno, Czech Republic

© Springer International Publishing Switzerland 2015

H. Altenbach and M. Brünig (eds.), *Inelastic Behavior of Materials and Structures Under Monotonic and Cyclic Loading*, Advanced Structured Materials 57, DOI 10.1007/978-3-319-14660-7_10

relations under stress and strain histories, namely in cyclic loading (Chaboche 2008; Abdel-Karim and Khan 2010) or to model cyclic hardening/softening behavior of polycrystals derived from the properties of single crystals (Evrard et al. 2010; Lin et al. 2010). Both approaches are based on the assumption of a homogeneous material behavior represented by the Representative Volume Element (RVE). These approaches can model cyclic stress-strain relations in good agreement with the experiment provided the numerous input parameters are previously determined from experimental results.

All approaches based on the phenomenological characterization of the cyclic stress-strain response can achieve reasonable quantitative description of this response provided enough parameters are introduced in the model. It is however difficult to link the input parameters with characteristic internal structural parameters and their evolution in cyclic plastic straining. Cyclic plastic straining of materials has number of specific features which distinguish it from unidirectional straining (Polák 1991). Cyclic straining is characterized by small amplitude of the total strain and elastic and plastic strain components of the same order of magnitude. The prominent feature of cyclic plastic straining is the localization of the cyclic plastic strain into the bands of localized cyclic slip called persistent slip bands (PSBs). In the description of the cyclic stress-strain response it is therefore important to use models that can take into account the inhomogeneous distribution of the cyclic plastic strain in the material.

The basis of such a model represents the approach developed already in the 30ties of the last century by Masing (1923, 1925) who recognized the inhomogeneity of the material and the heterogeneity of the plastic strain. The main sources of the heterogeneity of the plastic strain were believed to be the different orientations of the grains in polycrystalline materials. Masing proposed to model the actual behavior of a polycrystalline material by a number of elements having different critical yield stresses that are arranged in parallel. In a more general approach Afanasjev (1953) proposed the continuous distribution of the critical yield stresses of individual volumes of the material characterized by the probability density function. In both approaches each volume is deformed elastically, either in tension or in compression, until critical yield stress σ_c is achieved and deforms further plastically without hardening. The behavior of an individual volume is thus similar to the behavior of a single crystal oriented for single slip. Total stress is derived as the weighted average provided the individual volumes are arranged in parallel. Parallel arrangement of the deformed volumes is close to the real arrangement especially in low amplitude cyclic straining. The occurrence of the individual volumes is determined by the probability density function of the critical yield stresses $f(\sigma_c)$. Macroscopic stress can be calculated as the weighted average of the stresses of individual microvolumes. Due to both simplifying assumptions the model is suitable for small strains which are generally the case in cyclic plastic loading.

Based on the knowledge of the mechanisms of cyclic plastic straining in which plastic strain is due to the motion of dislocations driven by the effective stress in individual volumes of the crystal general statistical theory has been proposed by Polák and Klesnil (1980, 1982), Polák et al. (1982) and in a different form by Burmeister and Holste (1981). The application of this theory to the cyclic plastic

deformation of both polycrystals and single crystals is supported by the recent findings that cyclic plastic strain is highly localized and the amplitude of the cyclic plastic strain in PSBs varies considerably and can reach up to several percents (Polák 1991; Man et al. 2009; Weidner et al. 2008a, b).

Based on the theory of the thermal activation (Seeger 1956; Caillard and Martin 2003) dislocations in a crystal move with a velocity which depends on the effective shear stress τ_{eff} provided by the applied stress. The effective shear stress component is equal in all microvolumes since the effective stress is determined by the properties of dislocation motion in a particular lattice and is temperature and strain rate dependent. The second component of the critical stress of a particular microvolume stems from the stress field of all other dislocations acting on the dislocation in a direction opposite to the direction of straining. This component, the internal critical shear stress of the microvolume τ_{ic} is nearly temperature and strain rate independent. It depends on the dislocation arrangement in the particular microvolume. The internal critical shear stress component is different in individual microvolumes and the occurrence of a volume with internal critical shear stress is given by the probability density function $f(\tau_{\text{ic}})$.

Since internal critical shear stresses of microvolumes are proportional to the internal tensile stresses of these microvolumes the statistical theory of the hysteresis loop has been formulated in quasi-elastic approximation in terms of the internal critical tensile stresses σ_{ic} , their probability density function $f(\sigma_{\text{ic}})$ and saturated effective stress of the material σ_{es} (Polák 1991; Polák and Klesnil 1982).

The analysis of the loop shape using this generalized statistical theory have been applied to the hysteresis loop of carbon steel (Polák et al. 1982), austenitic and duplex stainless steels (Polák et al. 2001a, b) and recently also to nickel-based superalloy (Petre nec et al. 2014). The statistical theory without considering explicitly the effective stress component has been adopted by Christ (1991), Skelton et al. (1997), Heino and Karlsson (2001) and Sivaprasad et al. (2010). Recently Mayer et al. (2013a, b) attempted to describe temperature and strain-rate dependent plasticity of bainitic steel using the Masing approach, surprisingly without considering the effective stress contribution.

Present study is devoted to the presentation of basic principles of the general statistical theory of the hysteresis loop and to its application to the analysis of the cyclic plastic stress-strain response of two polycrystalline materials. Austenitic steel represents single phase material and nickel based superalloy consists of two phases with markedly different effective stresses. Both materials are intended for the design of components working at high temperatures. Total macroscopic cyclic stress has two components, the effective and internal stress and both contribute to the high fatigue resistance of these materials. Effective stress represents not only an important contribution to the total cyclic stress but on strain reversal leads to transient relaxation phenomena which are reflected on the shape of the hysteresis loop. Internal stress can be calculated using probability density function of the internal critical stresses. Its evolution determines the fatigue hardening/softening behavior in cyclic loading.

2 Analysis of the Hysteresis Loop

Generalized statistical theory of the hysteresis loop (Polák 1991; Polák and Klesnil 1982) has been formulated for a homogeneous polycrystalline material. Since critical shear stresses of individual volumes determine critical tensile and compressive stresses the theory is formulated using critical stresses σ_c , the internal critical stresses σ_{ic} , and saturated effective stress σ_{es} . Internal critical stress is the stress at which the microvolume starts yielding without hardening provided the strain rate is infinitesimally low (i.e. effective stress is zero). The saturated effective stress corresponds to a given plastic strain rate and temperature and is the same in all volumes. It is called saturated since it corresponds to the plastic strain rate of the microvolume equal to the applied strain rate (Polák 1991). The distribution of microvolumes according to their internal critical stresses is characterized by the probability density function $f(\sigma_{ic})$.

The probability density distribution function $f(\sigma_{ic})$ determines the frequency of occurrence of a volume with internal critical stress σ_{ic} . All microvolumes are supposed to be arranged in parallel and therefore the macroscopic internal stress component is given by integration over all elements. The total stress σ as well as the macroscopic internal σ_I and the macroscopic effective stress σ_E components were calculated in quasi-elastic approximation. In quasi-elastic approximation the effective stress increases linearly with strain with the slope of the effective elastic modulus E_{eff} until saturated value of the effective stress σ_{es} is reached and is constant later. In quasi-elastic approximation no stress and strain relaxation is allowed.

The shape of the hysteresis loop is easily described using second integral function $G(x)$ of the probability density function of the internal critical stresses defined as

$$G(x) = \int_0^x \left(\int_0^z f(z) dz \right) dx. \quad (1)$$

The shape of the hysteresis loop in quasi-elastic approximation can be expressed in terms of the relative stress σ_r and relative strain ε_r (Polák 1991)

$$\sigma_r \begin{cases} = \varepsilon_r E_{eff} & \text{for } \varepsilon_r \leq 2\sigma_{es}/E_{eff}, \\ = \varepsilon_r E_{eff} - 2G(\varepsilon_r E_{eff}/2 - \sigma_{es}) & \text{for } 2\sigma_{es}/E_{eff} \leq \varepsilon_r \leq 2\varepsilon_a \end{cases} \quad (2)$$

where E_{eff} is effective elastic modulus. Relative stress and relative strain for tensile and compression hysteresis-half-loops are

$$\begin{aligned} \sigma_r &= \sigma + \sigma_a, \varepsilon_r = \varepsilon + \varepsilon_a & \text{for tensile half-loop,} \\ \sigma_r &= \sigma_a - \sigma, \varepsilon_r = \varepsilon_a - \varepsilon & \text{for compression half-loop,} \end{aligned} \quad (3)$$

where σ_a and ε_a are the stress and strain amplitude, respectively. The relations for macroscopic internal and effective stress components in the four intervals of the strain range can be found elsewhere (Polák 1991; Polák and Klesnil 1982).

By double differentiation of the relation (2) we can obtain the relation for the probability density function of the internal critical stresses

$$f\left(\frac{\varepsilon_r E_{\text{eff}}}{2} - \sigma_{\text{es}}\right) = -\frac{2}{E_{\text{eff}}^2} \frac{\partial^2 \sigma_r}{\partial \varepsilon_r^2} \quad \text{for} \quad 2\sigma_{\text{es}}/E_{\text{eff}} \leq \varepsilon_r \leq 2\varepsilon_a \quad (4)$$

Relation (4) shows that by plotting the second derivative of the hysteresis half-loop (multiplied by $-2/E_{\text{eff}}^2$) versus fictive stress $\varepsilon_r E_{\text{eff}}/2$ we can evaluate the saturated effective stress σ_{es} from the offset of the probability density function relative to the origin. The first and the second derivatives of the relation (2)₁, derived in quasi-elastic approximation, yields zero. In reality, due to plastic strain relaxation during unloading the first derivative for very small fictive stresses ($\varepsilon_r E_{\text{eff}} < \sigma_{\text{es}}$) decreases from $2E_{\text{eff}}$ to E_{eff} . The negative second derivative is thus initially positive, large, decreases to zero and should become zero for ($\sigma_{\text{es}} < \varepsilon_r E_{\text{eff}} < 2\sigma_{\text{es}}$) (Polák 1991). The total shift of the probability density function in fictive stress is thus σ_{es} .

The analysis of the hysteresis loop with the help of the general statistical theory thus allows separating the effect of temperature and strain rate on the effective and internal stress component. The effective stress component is influenced strongly by temperature and strain rate since both parameters directly influence the mobile dislocation density and dislocation mobility. The probability density function is affected only indirectly by the temperature and strain rate dependence of the dislocation arrangement.

In case that two phases participate in the cyclic plastic straining both their saturated effective stresses and the probability density functions could differ. Since the statistical theory of the hysteresis loop is based on the Masing approach (Masing 1923, 1925) in which all microvolumes are deformed in parallel, Eq. (4) can be applied separately to both phases, provided their effective stresses differ substantially. In case the experimental data are precise enough so that the first and the second derivatives could be assessed with good precision the saturated microscopic effective stresses and the probability density functions characterizing the distribution of the critical internal stresses in both phases could be evaluated.

3 Experimental Conditions

3.1 Material

Two materials designed primarily for high temperature applications were studied. Austenitic stainless steel grade UNS S31035, Sanicro 25, was supplied by Sandvik, Sweden in the form of cylindrical rod of 150 mm in diameter. The chemical

composition of the material in wt.% was: 0.1 C, 22.5 Cr, 25.0 Ni, 3.6 W, 1.5 Co, 3.0 Cu, 0.5 Mn, 0.5 Nb, 0.23 N and the rest Fe. After the production of the rough shape of specimens they were annealed at 1,200 °C for 1 h and cooled in the air. Inconel 738LC was provided by PBS Turbo, Velká Bíteš a. s. in the form of conventionally cast polycrystalline rods of a diameter 22 mm in fully heat treated condition. Chemical composition of the superalloy in wt.% was: 16.22 Cr, 8.78 Co, 3.37 Ti, 3.35 Al, 1.77 Ta, 2.63 W, 1.71 Mo, 0.84 Nb, 0.2 Fe, 0.04 Zr, 0.1 C, 0.008 B, rest Ni. Cylindrical specimens with the diameter 8 mm and the gage length 14 mm for room temperature testing and 6 mm in diameter and 15 mm gage length with button ends for elevated temperature testing were produced.

3.2 Testing Procedures

Specimens were cyclically strained in computer controlled electro-hydraulic MTS testing system with constant total strain rate $2 \times 10^{-3} \text{ s}^{-1}$ in symmetric strain cycle using extensometers with 12 mm base. Materials were cycled either at room temperature or at temperature 700 °C using split resistance furnace. High temperature hydraulic grips and high temperature longitudinal extensometer were used in high temperature cyclic loading. Either constant strain amplitude or blocks of stepwise increasing constant strain amplitudes ε_a (multiple step test procedure) were applied to the specimen at each temperature. High data recording rate (up to 3,000 samples s^{-1}) allowed obtaining the highest number of data points on the hysteresis loop. In case the noise of both strain and load channels was low enough and control loop of the hydraulic system was optimized only 500 data points on the hysteresis loop recorded using standard MTS LCF program were enough for performing the analysis of the hysteresis loop shape. The evolution of the loop shape in cyclic straining was thus studied with only 500 data points on the hysteresis loop.

3.3 Evaluation Procedures

Using maximum and minimum strains and stresses in a cycle, the relative strain ε_r and the relative stress σ_r were calculated both for tensile and compression hysteresis half-loops. The first and the second derivatives of the hysteresis half-loops in relative coordinates were evaluated using numerical procedures and plotted versus fictive stress equal to $\varepsilon_r E_{\text{eff}}/2$. Appreciable care was paid to choose appropriately the strain interval on which the first and the second derivatives were numerically evaluated by fitting a linear relation to the data points. The optimum strain interval had to be found large enough for which the derivatives did not fluctuate exceedingly but small enough not to distort the actual shape of the derivatives.

Individual peaks of the second derivative were fitted in some cases to the general Weibull distribution using least squares fitting procedure. In quantitative evaluation of

individual peaks the data around the peak of the second derivative were approximated by the translated Weibull distribution in the form

$$f(x) = \frac{b}{a} \left(\frac{x-d}{a} \right)^{b-1} \exp \left[- \left(\frac{x-d}{a} \right)^b \right] \quad (5)$$

where a is scale parameter, b the shape parameter and d is location or shift parameter equal to the saturated effective stress σ_{es} . All three parameters could be evaluated from the experimental data using least squares fitting procedure. In practical evaluation of a cyclically deformed material the shape parameter b was first evaluated from a number of half-loops and an integer close to the average of the values obtained for the particular material was chosen and fixed in further fitting.

In the evaluation of the changes of the probability density distribution with the number of loading cycles the following notation will be used in denoting the individual segments of the hysteresis loops. The initial quarter-cycle starts always in tension and is denoted as zero segment. The first complete half-loop runs in compression and will be called the first half-loop or segment (shortly sgm). The second complete half-loop runs in tension and is called the second half-loop or segment (shortly sgm). Analogically, all odd segments are compression segments and all even segments are tensile segments.

4 Results

4.1 Sanicro 25 Steel

4.1.1 Saturated Behavior

Low cycle fatigue tests are ordinarily performed with constant strain amplitude and constant strain rate. In digitally controlled testing systems hysteresis loops are recorded but usually only stress amplitude and possibly plastic strain amplitude are evaluated and plotted versus number of loading cycles. In majority of polycrystalline materials the changes of the stress amplitude are eminent in the early stages of cycling and with increasing number of cycles saturated behavior is found. Figure 1 illustrates hardening/softening behavior of Sanicro 25 steel in room temperature cycling and in cycling at temperature 700 °C. High amplitude cyclic straining at room temperature (Fig. 1a) leads to initial cyclic hardening; stress amplitude reaches maximum at the number of cycles lower than 100 and cyclic softening follows until the end of fatigue life. In low amplitude cyclic straining fatigue softening starts from the first cycle. In all cases the softening rate decreases and a tendency to reach saturation is apparent for all strain amplitudes. Substantially different behavior is found in cycling at temperature 700 °C (Fig. 1b). Stress amplitude starts at much lower value than in room temperature cyclic straining however for all strain amplitudes rapid

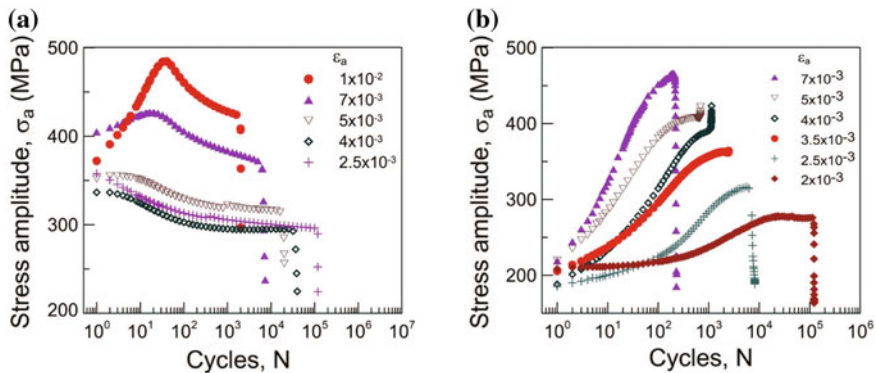


Fig. 1 Cyclic hardening/softening curves in constant total strain amplitude loading: **a** $T = 22^\circ\text{C}$, **b** $T = 700^\circ\text{C}$

cyclic hardening is present. Hardening rate decreases during cyclic loading and at temperature 700°C also the tendency to reach saturation is apparent.

For separation of the internal and effective stress components the analysis of the hysteresis loops in the domain of saturation has been performed. In order to eliminate the effect of different specimens the multiple step test procedure used usually for the determination of the cyclic stress-strain curve has been programmed on the control computer. Figure 2 shows the plot of the stress amplitude versus the number of loading cycles in cycling the specimens with blocks of increasing strain amplitudes. One specimen was cycled at room temperature, the other at temperature 700°C . Similar behavior of the material at both temperatures is found in cycling with constant strain amplitudes up to fracture (see Fig. 1). Cycling at room temperature is characterized by cyclic softening, cycling at temperature 700°C by cyclic hardening. Hysteresis loops at the end of each block were plotted for both temperatures in Fig. 3. They are plotted in relative coordinates corresponding to the tensile half-loop of each hysteresis loop, i.e. the origin of coordinates was put in the minimum of the stress and strain of each loop. This plot allows checking whether material exhibits Masing behavior or non-Masing behavior. The real behavior of the material in cyclic straining is more complicated—see discussion in Sect. 5.

In order to separate the effective and internal stress contribution to the total stress the tensile and compression hysteresis half-loops at the end of each block were analyzed using the second derivatives. Simultaneously the probability density function of the internal critical stresses was assessed using relation (4). Figure 4 shows the negative second derivative of the tensile hysteresis half-loop (multiplied by $-2/(E_{\text{eff}})^2$) recorded at the end of a block run with the strain amplitude 2.5×10^{-3} and 2.7×10^{-3} at two temperatures versus fictive stress equal to $\varepsilon_r E_{\text{eff}}/2$. Initial drop of the second derivative at both temperatures close to zero corresponds to the relaxation of the plastic strain under decreasing effective stress during unloading. Plastic strain relaxation is positive until the effective stress is positive and drops to zero at fictive stress for which the second derivative reaches zero. Due to the finite number

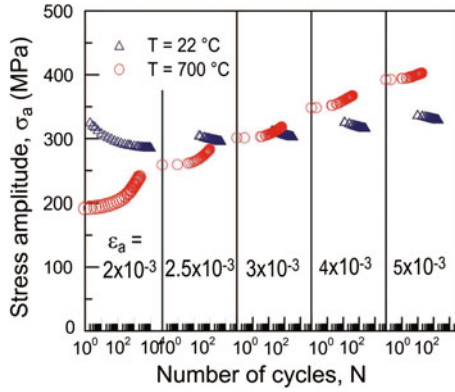


Fig. 2 Stress amplitude versus number of cycles in block loading of Sanicro 25 with increasing strain amplitudes at two temperatures

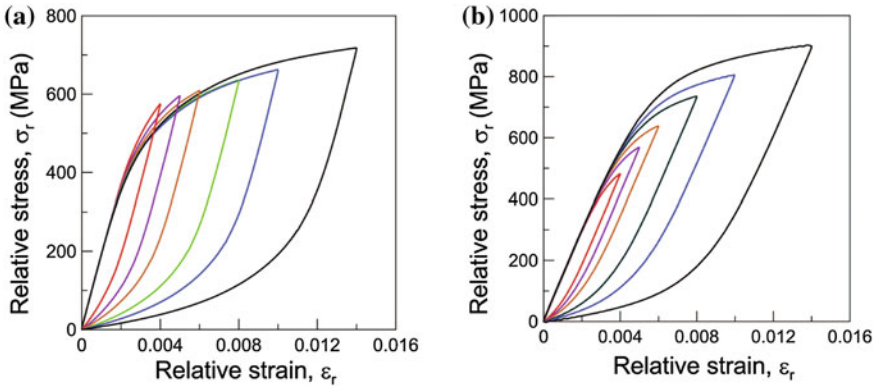


Fig. 3 Hysteresis loops at the end of each block of increasing strain amplitudes: **a** room temperature cycling, **b** cycling at temperature 700 °C

of points used for the evaluation of the first and the second derivative zero of the second derivative is only rarely achieved. Either zero or a minimum close to zero in y coordinate is obtained on the plots corresponding to low strain amplitudes. For fictive stresses above the minimum the second derivative approximates the probability density function of the internal critical stresses $f(\sigma_{ic})$. The shifted probability density function has been approximated by the general Weibull distribution (Eq. 5). By fitting Eq. (5) to the second derivative around the peak corresponding to the probability density distribution of the internal critical stresses we can evaluate effective saturated stress using relation (4) and parameters characterizing the distribution function. The characteristic parameters obtained using least square fitting are shown in Table 1.

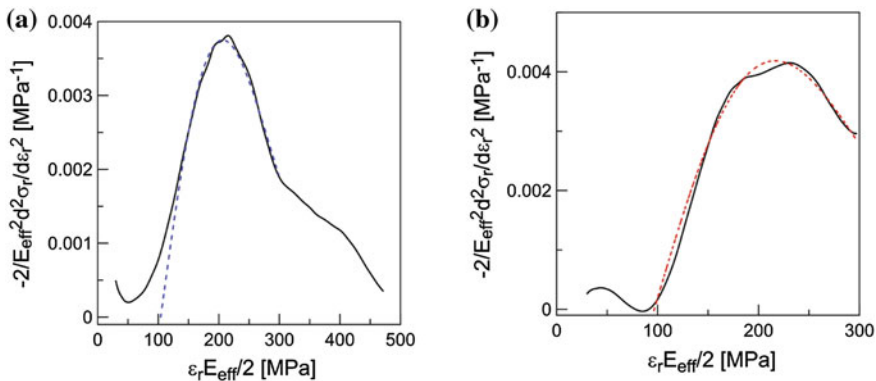


Fig. 4 Second derivative of the tensile hysteresis half-loop in cycling with constant strain amplitude and the Weibull fits (*dashed lines*): **a** $\varepsilon_a = 2.7 \times 10^{-3}$, room temperature cycling, **b** $\varepsilon_a = 2.5 \times 10^{-3}$, cycling at temperature 700 °C

Table 1 Parameters of the Weibull distribution Eq. (2) fitted to hysteresis half-loops of individual materials and their constituents

Material	E_{eff} (GPa)	a (MPa)	b	$d = \sigma_{es}$ (MPa)
Sanicro 25, $T = 22^\circ\text{C}$, $\varepsilon_a = 2.5 \times 10^{-3}$	190	145	2	104
Sanicro 25, $T = 700^\circ\text{C}$, $\varepsilon_a = 2.7 \times 10^{-3}$	151	169	2	97
IN 738LC γ matrix, $T = 800^\circ\text{C}$	137	219	2	205
IN 738LC γ' precipitates, $T = 800^\circ\text{C}$	137	182	2	610

4.1.2 Evolution of the Hysteresis Loop

Evolution of the hysteresis loop is nicely illustrated by evaluating the second derivatives of the hysteresis half-loops during cyclic loading. Figure 5 shows the second derivative of the tensile half-loops produced by cycling at room temperature with two different strain amplitudes during the fatigue life. In low amplitude cycling (Fig. 5a) two pronounced peaks on the second derivative appear. With increasing number of cycles the second peak diminishes until it completely disappears at 10,000 cycles, i.e. 20,000 segments ($0.1N_f$). The first peak increases and its maximum shifts in direction of lower fictive stress. From the position and the shape of the peak we can estimate the saturated effective stress σ_{es} by extrapolating the rising part of the second derivative to zero and using Eq. (4). Initially its value evaluated from the 2nd segment is around 140 MPa and it decreases during cyclic loading to about 100 MPa. In cycling with the highest strain amplitude (Fig. 5b) only one pronounced peak of the second derivative is obtained from the onset of cycling. With increasing number of cycles the height of the peak decreases, its width increases and the position of the peak shifts slightly to lower fictive stress until 63rd segment. These changes correspond to fatigue softening. However, inspecting

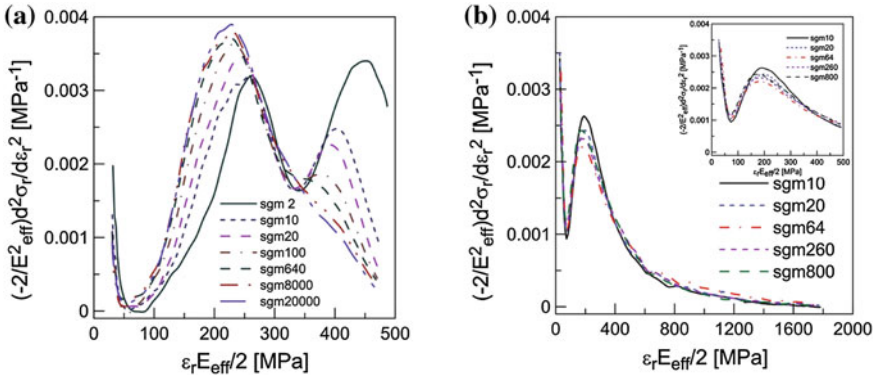


Fig. 5 Evolution of the second derivative of the tensile segments during the fatigue life at room temperature: **a** $\epsilon_a = 2.7 \times 10^{-3}$, **b** $\epsilon_a = 1.0 \times 10^{-2}$

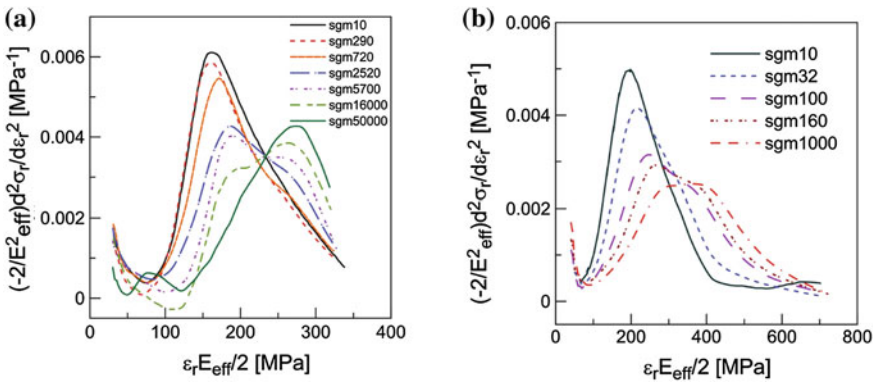


Fig. 6 Evolution of the second derivative of the tensile segments during the fatigue life at temperature: 700 °C: **a** $\epsilon_a = 3.0 \times 10^{-3}$, **b** $\epsilon_a = 7.0 \times 10^{-3}$

the whole spectrum (Fig. 5b) we can see that at higher fictive stresses the second derivative at 64th segment is well above that corresponding to the first segment. This corresponds to fatigue hardening (compare with Fig. 1). Above 64th segment the height of the peak starts increasing again however the drop of the second derivative at higher fictive stresses corresponds to cyclic softening.

Much more pronounced changes in the second derivative were found in cyclic loading at temperature 700 °C. Figure 6 shows the changes of the second derivative of the tensile half-loop with increasing number of cycles. In cycling with small strain amplitude (Fig. 6a) single peak at fictive stress around 160 MPa appears and does not change significantly up to the 10th segment. With further cycling it decreases, widens and is shifted to higher fictive stresses. In the 2,500th segment the new peak at fictive stress around 270 MPa starts to appear and is well developed at 16,000th segment. Still later single peak at the fictive stress 280 MPa characterizes the shape of the

tensile half-loop. Evaluation of the saturated effective stress based on Eq. (4) shows that during cyclic loading it increases from the initial value 90 MPa to about 120 MPa for 50,000th segment. Both these processes led to cyclic hardening (compare with Fig. 1b). Similar behavior is found in cycling with the high strain amplitude (Fig. 6b). High and narrow peak of the second derivative at number of segments smaller than 10 decreases, widens and a tendency to the formation of a new peak at 370 MPa is apparent. Simultaneously the saturated effective stress increases from 90 MPa to around 120 MPa for 1,000th segment.

4.2 Nickel Based Superalloy

Hysteresis loop analysis of 738LC superalloy was performed at three temperatures during multiple step test. Figure 7 shows the record of the stress amplitude versus number of loading cycles during multiple step test at room temperature and at temperature 800 °C. At each level of the strain amplitude the stress amplitude is nearly constant. Fatigue hardening is apparent only during cycling with the highest strain amplitude at room temperature. Data for temperature 500 °C are in between those at room temperature and temperature 800 °C.

The evolution of the second derivative with cycling at three temperatures shows Fig. 8. The drop of the second derivative due to strain relaxation is very steep at room temperature (Fig. 8a) and at temperature 500 °C (Fig. 8b) where the initial part is missing. At temperature 800 °C the initial drop of the second derivative extends to substantially higher fictive stresses than at room temperature. Two peaks can be identified in the plot of the second derivative at all three temperatures. They correspond to the successive cyclic plastic straining of the matrix (γ phase) and coherent γ' precipitates (Petre nec et al. 2014). The first peak is very weak in room

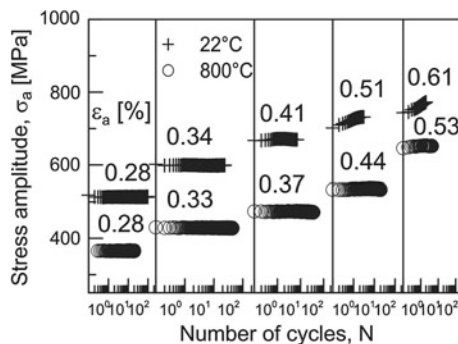


Fig. 7 Stress amplitude versus number of cycles in block loading of 738LC superalloy with increasing strain amplitudes at two temperatures

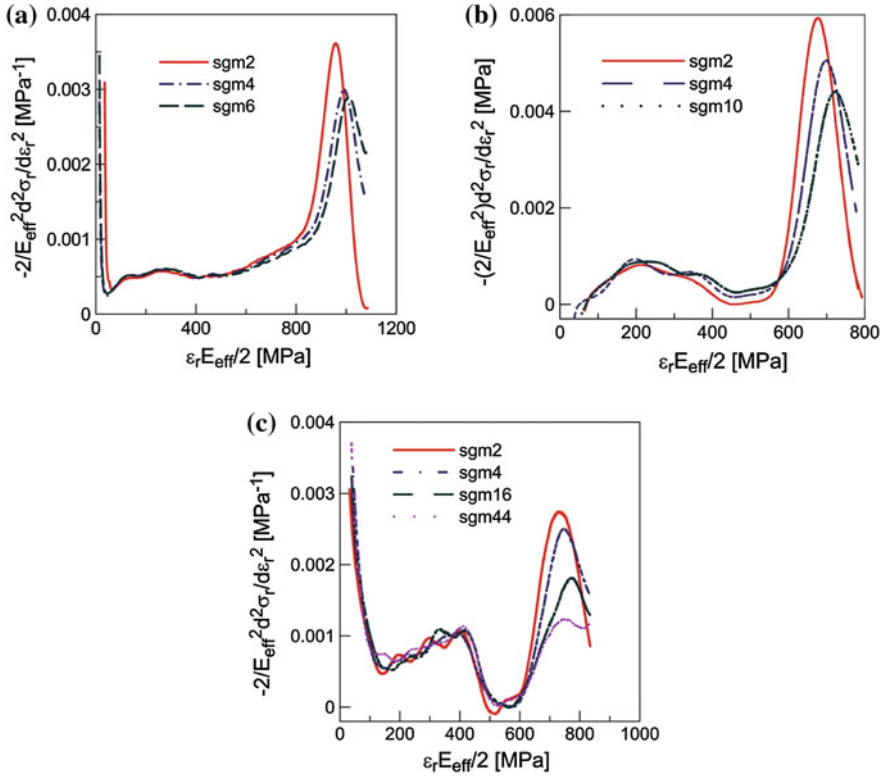


Fig. 8 Evolution of the second derivative of the tensile segments with the number of cycles at three temperatures: **a** $\varepsilon_a = 3.0 \times 10^{-3}$, $T = 22 \text{ }^\circ\text{C}$, **b** $\varepsilon_a = 7.0 \times 10^{-3}$, $T = 500 \text{ }^\circ\text{C}$, **c** $\varepsilon_a = 7.0 \times 10^{-3}$, $T = 800 \text{ }^\circ\text{C}$

temperature cycling. The position of the first peak is shifted to higher fictive stresses with increasing temperature (from 130 MPa to 400 MPa). The shape and the height of the first peak do not depend on the number of loading cycles. The second peak is more pronounced and its position depends on temperature and on the number of loading cycles. At all temperatures with increasing number of cycles the maximum decreases and the position of the peak moves to higher fictive stress.

Quantitative evaluation of the saturated effective stresses and probability density functions of internal critical stresses in both phases was possible only at temperature 800 °C using loops having low noise in strain and stress. Figure 9 shows two pronounced peaks of the 38th segment. Each peak was fitted by the Weibull distribution in such a way that only data above 50% of the maximum value of each peak were used for the fitting. The shape parameter b was always between 2 and 3 provided all parameters were free. In agreement with the results on Sanicro 25 steel we have fixed parameter b to $b = 2$. All other parameters were obtained using least square fitting and are shown in Table 1.

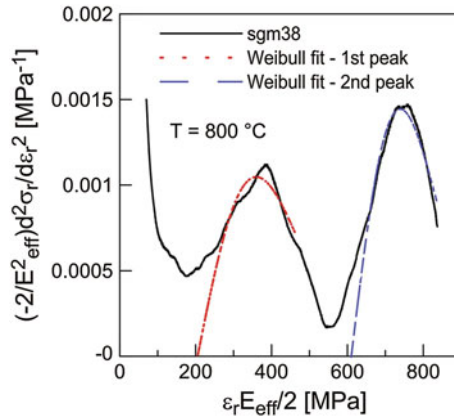


Fig. 9 Second derivative of the tensile segment of 738Ls superalloy cycled with strain amplitude $\varepsilon_a = 7.0 \times 10^{-3}$ at temperature $T = 800^\circ\text{C}$ and Weibull fits to the two peaks

5 Discussion

5.1 Separation of the Effective and Internal Stress

The principal aim of this investigation was to demonstrate the usefulness of the hysteresis loop shape analysis based on the generalized statistical theory (Polák 1991). We have studied two materials, single phase Sanicro 25 steel destined for use at elevated temperatures and 738LC cast superalloy with the main application also in high temperature domain. It was proved that the hysteresis loop analysis is preferentially useful in two areas:

1. for the separation of the contribution of the effective stress and internal stress components,
2. for the study of the probability density distribution of the internal critical stresses and its evolution in cyclic straining which determines the internal stress contribution.

Study of both components contributes to the understanding of the mechanisms of cyclic straining and identification of the sources of cyclic stress.

In order to separate the effective and internal stress component most often the approximate procedures based on the method firstly proposed by Kuhlmann-Wilsdorf and Laird (1979) (the KWL method) were used. The method is based on a simplified Cottrell's analysis (Cottrell 1953) of the dislocation motion in reversed straining. Subsequently it was modified (Dickson et al. 1984) and is used until now (Vogt and Magnin 1993; Feaugas et al. 2008; Chang and Zhang 2012; Vucko et al. 2014). It was shown by Polák et al. (1996) that the use of the second derivative in the analysis of the shape of the hysteresis loop could yield more exact separation of the two components of the cyclic stress. Present investigation demonstrates that even

in case of a low number of data points on the hysteresis loop the effective stress could be estimated reasonably well provided the strain amplitude is low. However, the processes of smoothing and evaluation of the first and second derivatives are very critical, especially in the evaluation of the saturated effective stress. Only the data with low noise can be used for numerical differentiation using a small basic interval.

In case of cycling with high strain amplitude several slip systems become activated and probability density function becomes wider. While during unloading the majority of microvolumes still continue to flow plastically under decreasing effective stress other microvolumes with low critical internal stress start deforming in the opposite direction. As a result zero value of second derivative is never reached and only the position of the minimum of the second derivative could be determined. The extrapolation to zero second derivative can thus result in erroneous saturated effective stress. This situation is apparent in Fig. 5b during cyclic loading with strain amplitude 1×10^{-2} . Therefore the reliable values of the effective stress are obtained from the analysis of the loop shape run only with low strain amplitudes.

The effective stress in a particular phase of the material depends on the mobile dislocation density and their mobility. According to the Orowan equation (Caillard and Martin 2003) the plastic strain rate is

$$\dot{\epsilon}_p = M\rho_m b v \quad (6)$$

where M is Taylor or Sachs factor, ρ_m mobile dislocation density, v dislocation velocity and b the modulus of Burgers vector. Neglecting back fluctuations the dependence of the dislocation velocity on the effective stress σ_e is

$$v = v_0 \exp \left\{ - \left[\Delta G_0 - b \int_0^{\sigma_e/M} A(\tau) d\tau \right] / kT \right\} \quad (7)$$

where v_0 is the frequency of atomic oscillations ΔG_0 the activation energy of an obstacle that can be overcome by thermal fluctuations, A is the activation area of an obstacle and T is the absolute temperature.

Provided the activation area is constant or is replaced by an effective activation area the plastic strain rate is

$$\dot{\epsilon}_p = M\rho_m b K_s \exp \left(\frac{\sigma_e}{M\alpha_s} \right) \quad (8)$$

where parameter K_s depends on temperature and activation enthalpy of an obstacle

$$K_s = v_0 \exp \left(\frac{-\Delta G_0}{kT} \right)$$

and α_s is function of the activation area of an obstacle. Thus

$$\sigma_e = M\alpha_s \ln \left(\frac{\dot{\epsilon}_p}{M\rho_m b K_s} \right) \quad (9)$$

and replacing plastic strain rate $\dot{\epsilon}_p$ by strain rate $\dot{\epsilon}$ saturated effective stress is

$$\sigma_{es} = M\alpha_s \ln \left(\frac{\dot{\epsilon}}{M\rho_m b K_s} \right) \quad (10)$$

In constant strain rate loading the effective stress thus depends strongly on temperature and on mobile dislocation density. If mobile dislocation density were constant effective stress should decrease with temperature. In Sanicro 25 steel the saturated effective stress at temperature 700°C is approximately the same as that at room temperature. It implies that the decrease of the mobile dislocation density with temperature is compensated by the increase of the dislocation mobility.

The identifications of the sources of the cyclic stress, preferentially in materials designated for high temperature applications, is important in improving their properties or in the design of new materials for a specific application. Though considerable attention has been paid to the separation of the cyclic stress in a number of materials (Kuhlmann-Wilsdorf and Laird 1979; Cottrell 1953; Dickson et al. 1984; Vogt and Magnin 1993; Feugas et al. 2008; Chang and Zhang 2012), a number of studies (Christ 1991; Skelton et al. 1997; Heino and Karlsson 2001; Sivaprasad et al. 2010; Mayer et al. 2013a, b) have neglected the contribution of the effective stress in the analysis of the hysteresis loop shape. In some cases the effective stress was not considered even in case when studying the temperature and strain rate sensitivity in cyclic loading (Mayer et al. 2013a, b). Neglecting the contribution of the effective stress can result in modification of the real situation and in hiding the actual sources of the cyclic stress. Cyclic loading results in the evolution of the internal structure of the material which is reflected in the evolution of the probability density distribution of the internal critical stresses. This evolution at elevated temperatures could be more important than at room temperature. The changes in the effective stress due to variations in temperature and strain rate should be, however, distinguished from the changes of the probability density function.

5.2 Sanicro 25 Steel

The probability density function of Sanicro 25 steel undergoes important changes during cyclic plastic straining. These changes are much more pronounced in straining with low strain amplitudes (Fig. 5a) than with high strain amplitude (Fig. 5b). The presence of two peaks witnesses two types of cyclic plastic straining. The explanation of two peaks and subsequent gradual disappearance of the second peak can be explained in relation to the observation of the surface relief and dislocation

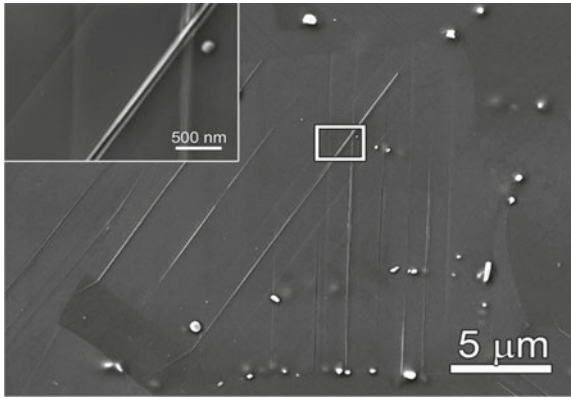


Fig. 10 Surface of the Sanicro 25 cycled at room temperature with strain amplitude $\varepsilon_a = 3.0 \times 10^{-3}$ for 74 cycles ($0.002N_f$)

arrangement after cyclic straining of Sanicro 25 (Polák et al. 2014). Due to the high nitrogen content in Sanicro 25 the stacking fault energy is very low. Cyclic plastic strain starts to be localized to the persistent slip bands from the onset of cycling. Figure 10 shows the surface of the steel cycled with low plastic strain amplitude 3×10^{-3} only for 74 cycles. Fine persistent slip markings (PSMs) develop very early on the surface of the grains. They consist of extrusions and intrusions (see the inset in Fig. 10) while the majority of the grain surface has no signs of slip. This indicates that the yield stress in the majority of the grain volume is high and only in small volumes corresponding to slip bands and later to PSBs plastic deformation is effective. Therefore the second peak in Fig. 5a corresponds to the deformation of the matrix and the first peak to developing deformation of PSBs. With increasing number of cycles the cyclic plastic strain is completely localized to PSBs and the second peak disappears. The disappearance of the second peak and the shift of the first peak to the lower fictive stress correspond to fatigue softening observed in low amplitude cycling (Fig. 1a).

In cycling with high strain amplitude already in the first cycle enough slip bands and later PSBs not only in primary system but also in secondary slip systems are formed in the material. Cyclic plastic straining concentrates in the system of intersecting PSBs which leads originally to fatigue hardening but very early PSBs start to transform in the low energy dislocation structures (Laird et al. 1986; Obrtlík et al. 1994; Polák 2003) which results in long-term cyclic softening, similarly to cycling with low strain amplitudes (Fig. 1a).

Cycling at temperature 700°C results in single peak of the second derivative (Fig. 6). For all amplitudes with increasing number of cycles the peak is shifted to higher fictive stresses which corresponds to cyclic hardening. Due to elevated temperature and high thermal activation the cross slip is more frequent and therefore the localization of the cyclic plastic strain is much smaller in comparison with room

temperature cycling (Polák et al. 2014). The shift of the peak to higher fictive stress and also the widening of the peak corresponds to cyclic hardening of the material.

Different evolution of the probability density function of the internal critical stresses is reflected in the shape of the hysteresis loops recorded at the end of each loading block (Fig. 3). Both in room temperature cycling and in cycling at 700 °C non-Masing behavior was found. However in room temperature cycling the relative stress of the larger loop for the same relative strain is lower than that of the smaller loop. In cycling at temperature 700 °C it is the other way round. Principal role here plays cyclic softening at room temperature and cyclic hardening at high temperature and respective shifts of the probability density functions (Figs. 5 and 6).

5.3 738LC Superalloy

The advantage of the hysteresis loop analysis is most evident in the case of materials containing two deformable phases like duplex steels (Polák et al. 2001b) or nickel base superalloys. Two peaks in the second derivative of IN738LC superalloy (Fig. 8) at all three temperatures correspond to the subsequent plastic deformation of the γ matrix and γ' precipitates that are coherent with the matrix. The peaks are well separated since effective stresses of both phases differ substantially. Figure 8 shows that the fraction of plastic strain accommodated by the matrix increases with increasing temperature. Nearly saturated behavior of the superalloy was observed in multiple test at all three temperatures (Fig. 7). Only high strain amplitude cyclic loading at room temperature and at temperature 500 °C resulted in fatigue hardening.

Effective stresses and probability density distributions of the internal critical stresses evaluated in cyclic straining at temperature 800 °C (Table 1) show very different saturated effective stresses of both phases. High saturated effective stress of the ordered γ' phase (around 600 MPa) is due to the difficult movement of superdislocations in ordered lattice. The width of the probability density distribution of the internal critical stresses in the γ matrix (proportional to the parameter a) is larger than that in γ' precipitates. This is connected with high plastic strain imposed to the γ matrix which must be accommodated by the activation of multiple slip systems.

5.3.1 Loop Shape Simulation

Basic parameters determining the shape of the hysteresis loop are thus the effective stress and the probability density function of the internal critical stresses. Both parameters are related to physical parameters of the material. Effective stress is determined by the density and mobility of mobile dislocations and probability density function is determined by the arrangement of dislocations in the fatigued material. Knowing both these quantities and the effective Young modulus we can simulate the hysteresis loop of the material. Provided the probability density function $f(\sigma_{ic})$ can be approximated by the Weibull distribution

$$f(x) = \frac{b}{a} \left(\frac{x}{a}\right)^{b-1} \exp\left[-\left(\frac{x}{a}\right)^b\right] \quad (11)$$

Equation (2) can be simplified to

$$\sigma_r = \begin{cases} \varepsilon_r E_{\text{eff}} & \text{for } \varepsilon_r \leq 2\sigma_{\text{es}}/E_{\text{eff}} \\ a\sqrt{\pi} E_b \left(\frac{\varepsilon_r E_{\text{eff}} - 2\sigma_{\text{es}}}{2a}\right) & \text{for } 2\sigma_{\text{es}}/E_{\text{eff}} \leq \varepsilon_r \leq 2\varepsilon_a \end{cases} \quad (12)$$

where $E_b(x)$ is the generalized error function

$$E_b(x) = \frac{2}{\sqrt{\pi}} \int_0^x \exp(-z^b) dz \quad (13)$$

The relation between the stress and strain in cyclic straining can be thus expressed using only a small number of characteristic parameters, namely E_{eff} , a , b (see Table 1). Expression (12) predicts the shape of the hysteresis loop in quasi-elastic approximation, i.e. no stress and strain relaxation is possible. Moreover, the use of single probability density function for all strain amplitudes would produce saturated hysteresis loops which satisfy completely the Masing behavior. This is not in good agreement with the behavior of real material see Fig. 3. Therefore the simulation which matches closely the real cyclic stress-strain behavior of the material in saturation region would require for each temperature and each strain amplitude the different set of parameters E_{eff} , a and b .

6 Conclusions

Experimental study of the hysteresis loops recorded in cyclic loading of two materials at different temperatures and their analysis using general statistical theory of the hysteresis loop led to the following conclusions:

1. Analysis of the hysteresis loop yields important additional information on the sources of cyclic strength of materials.
2. Loop shape analysis allows separating the contributions of the effective and the internal stresses.
3. Evolution of the hysteresis loop shape contributes to the understanding of the of the room temperature fatigue softening of Sanicro 25 steel.
4. The determination of the effective stresses and probability density distributions of the internal critical stresses in single phase and in two phase materials helps in optimization of their composition and thermal treatment.
5. The approach using general statistical theory allows simulating the stress-strain response of materials in cyclic loading based on physical parameters related to properties of dislocations and their internal structure.

Acknowledgments This work was realized in CEITEC - Central European Institute of Technology with research infrastructure supported by the project CZ.1.05/1.1.00/02.0068 financed from European Regional Development Fund. The support by the project RVO: 68081723 and grant no. 13-23652S of GACR is gratefully acknowledged.

References

- Abdel-Karim M, Khan A (2010) Cyclic multiaxial and shear finite deformation responses of OFHC Cu. Part II: An extension to the KHL model and simulations. *Int J Plasticity* 26:758–773
- Afanasjev NN (1953) Statistical theory of fatigue strength of metals (in Russ.: Statisticheskaja teorija ustalostnoj prochnosti metallov). Izd. Akad. Nauk USSR, Kiev
- Burmeister HJ, Holste C (1981) Change of activation area during cyclic deformation II. Quantitative interpretation with a model of heterogeneous plastic deformation. *Phys Stat Sol* 64:611–624
- Caillard D, Martin JL (2003) Thermally activated mechanisms in crystal plasticity. Elsevier, Oxford
- Chaboche JL (2008) A review of some plasticity and viscoplasticity constitutive theories. *Int J Plasticity* 24(10):1642–1693
- Chang B, Zhang Z (2012) Low cycle fatigue behavior of a high nitrogen austenitic stainless steel under uniaxial and non-proportional loadings based on the partition of hysteresis loops. *Mater Sci Eng A* 547:72–79
- Christ HJ (1991) Wechselverformung von Metallen-Zyklisches Spannungs-Dehnungs-Verhalten und Mikrostruktur. In: Ilschner B (ed) *Werkstoff-Forschung und - Technik*, vol 9. Springer, Berlin, pp 457–460
- Cottrell AH (1953) Dislocations and plastic flow in crystals. Clarendon Press, Oxford
- Dickson JI, Boutin J, Handfield L (1984) A comparison of two simple methods for measuring cyclic internal and effective stresses. *Mater Sci Eng* 64(1):L7–L11
- Evrard P, Alvarez-Armas I, Aubin V, Degallaix S (2010) Polycrystalline modeling of the cyclic hardening/softening behavior of an austenitic-ferritic stainless steel. *Mech Mater* 42:395–404
- Feaugas X, Catalao S, Pilvin P, Cabrillat MT (2008) On the evolution of cyclic deformation microstructure during relaxation test in austenitic stainless steel at 823 K. *Mater Sci Eng A* 483–484:422–425
- Heino S, Karlsson B (2001) Cyclic deformation and fatigue behaviour of 7Mo-0.5N superaustenitic stainless steel—stress-strain relations and fatigue life. *Acta Mater* 49:339–351
- Kuhlmann-Wilsdorf D, Laird C (1979) Dislocation behavior in fatigue. II. Friction stress and back stress as inferred from an analysis of hysteresis loops. *Mater Sci Eng* 37(2):111–120
- Laird C, Charsley P, Mughrabi H (1986) Low energy dislocation structures produced by cyclic deformation. *Mater Sci Eng* 81:433–450
- Lin B, Zhao LG, Tong J, Christ HJ (2010) Crystal plasticity modeling of cyclic deformation for a polycrystalline nickel-based superalloy at high temperature. *Mater Sci Eng A* 527:3581–3587
- Man J, Obrtlík K, Polák J (2009) Extrusions and intrusions in fatigued metals. Part 1. State of the art and history. *Phil Mag* 89:1295–1336
- Masing G (1923) Zur Heyn'schen Theorie der Verfestigung der Metalle durch verborgene elastische Spannungen. *Wissenschaftliche Veröffentlichung aus dem Siemens-Konzern* 3:231–239
- Masing G (1925) Eigenspannungen in kaltgereckten Metallen. *Z Tech Phys* 6:569–573
- Mayer T, Mazza E, Holdsworth SR (2013a) A continuous Masing approach for a physically motivated formulation of temperature and strain-rate dependent plasticity. *Mater Sci Eng A* 102–103:1–12
- Mayer T, Mazza E, Holdsworth SR (2013b) Parameter evolution in a continuous Masing approach for cyclic plasticity and its physical interpretation. *Mech Mater* 57:86–96
- Obrtlík K, Kruml T (1994) Low energy dislocation structures produced by cyclic deformation. *Mater Sci Eng A* 187:1–9

- Petrenec M, Polák J, Tobiáš J, Šmíd M, Chlupová A, Petráš R (2014) Analysis of cyclic plastic response of nickel based IN738LC superalloy. *Int J Fatigue* 65:44–50
- Polák J (1991) Cyclic plasticity and low cycle fatigue life of metals. *Mater Sci Monogr*, vol 63. Academia-Elsevier, Praha-Amsterdam
- Polák J (2003) Cyclic deformation, crack initiation and low cycle fatigue. In: Milne I, Ritchie RO, Karimhaloo B (eds) *Comprehensive structural integrity*, vol 4. Elsevier, Amsterdam, pp 1–39
- Polák J, Klesnil M (1980) Statistická teorie hysterézní smyčky (in Czech.). *Kovové Mater* 18: 319–344
- Polák J, Klesnil M (1982) The hysteresis loop 1. A statistical theory. *Fatigue Eng Mater Struct* 5:19–32
- Polák J, Klesnil M, Helešic J (1982) The hysteresis loop 2. An analysis of the loop shape. *Fatigue Eng Mater Struct* 5:33–44
- Polák J, Fardoun F, Degallaix S (1996) Effective and internal stresses in cyclic straining of 316 stainless steel. *Mater Sci Eng A* 215:104–112
- Polák J, Fardoun F, Degallaix S (2001a) Analysis of the hysteresis loop in stainless steel. I. Austenitic and ferritic steels. *Mater Sci Eng A* 297:144–153
- Polák J, Fardoun F, Degallaix S (2001b) Analysis of the hysteresis loop in stainless steel. II. Austenitic-ferritic duplex steel and the effect of nitrogen. *Mater Sci Eng A* 297:154–161
- Polák J, Petráš R, Heczko M, Kuběna I, Kruml T, Chai G (2014) Low cycle fatigue behavior of Sanicro25 steel at room and at elevated temperature. *Mater Sci Eng: A* 615:175–182
- Seeger A (1956) On the theory of the low-temperature internal friction peak observed in metals. *Phil Mag* 1:651–662
- Sivaprasad S, Das A, Narasaiah N, Tarafder S (2010) Cyclic plastic behaviour of primary heat transport piping materials: Influence of loading schemes on hysteresis loop. *Mater Sci Eng A* 527:6858–6869
- Skelton RP, Maier HJ, Christ H (1997) The Bauschinger effect, Masing model and the Ramberg-Osgood relation for cyclic deformation in metals. *Mater Sci Eng A* 238:377–390
- Vogt JB, Magnin TJ (1993) Effective stresses and microstructure in cyclically deformed 316L austenitic stainless steel-effect of temperature and nitrogen content. *Fatigue Fracture Eng Mater Struct* 16:555–564
- Vucko F, Bosch C, Delafosse D (2014) Low cycle fatigue behavior of a high nitrogen austenitic stainless steel under uniaxial and non-proportional loadings based on the partition of hysteresis loops. *Mater Sci Eng A* 597:381–386
- Weidner A, Blochwitz C, Skrotzki W, Tirschler W, Strunk W Jr (2008a) Formation of slip steps and growth of extrusions within persistent slip bands in cyclically deformed polycrystals. *Mater Sci Eng A* 479:181–190
- Weidner A, Man J, Tirschler W, Klapetek P, Blochwitz C, Polák J, Skrotzki W (2008b) Half-cycle slip activity of persistent slip bands at different stages of fatigue life of polycrystalline nickel. *Mater Sci Eng A* 492:118–127

Creep, Plasticity and Fatigue of Single Crystal Superalloys: Physics-Based Life Prediction for Turbine Components in Severe Operating Environments

Alexander Staroselsky and Thomas J. Martin

Abstract The chapter reports the process and computer methodology for a physics-based prediction of overall deformation and local failure modes in cooled turbine airfoils, blade outer air seals, and other turbomachinery parts operating in severe high temperature and high stress environments. The computational analysis incorporated coupled aero-thermal CFD with non-linear deformation finite element calculations with a crystallographic slip-based constitutive model. The methodology utilized a fully-coupled elastic-viscoplastic model that was based on crystal viscoplasticity, and a semi-empirical lifing model introduced the use of dissipated energy to estimate the remaining part life in terms of cycles to failure. The viscoplastic model used an incremental large strain formulation additively that decomposed the inelastic strain rate into components along the octahedral and cubic slip planes of single crystal nickel-based superalloys. This crystallographic-based viscoplastic constitutive model based on Orowan's law was developed to represent sigmoidal creep behavior. Inelastic shear rate along each slip system was expressed as a sum of a time dependent creep component and a rate independent plastic component. A new robust and computationally efficient rate-independent crystal plasticity formulation was developed and combined with the creep flow model. The transient variation of each of the inelastic components included a back stress for kinematic hardening and latent hardening parameters to account for the stress evolution with inelastic strain as well as the evolution for dislocation densities. The model was evaluated at real engine characteristic mission times and flight points for part life prediction. The method was effective for use with three-dimensional finite element models of realistic turbine airfoils using commercial finite element applications. The computationally predicted part life was calibrated and verified against test data for deformation and crack growth.

Keywords Gas turbine · Thermal transient · Coupled conjugate heat transfer · Crystal plasticity · Creep · Thermo-mechanical fatigue · Life prediction

A. Staroselsky (✉) · T.J. Martin
United Technologies Research Center, East Hartford, USA
e-mail: starosav@utrc.utc.com

T.J. Martin
e-mail: martintj@utrc.utc.com

1 Introduction

In modern turbomachines, which comprise turbofans, turbojets, gas turbine engines, and the like, the purpose of the turbine component is to extract work from the high pressure and high temperature core flow. The two most important parameters that determine the turbine's power output and fuel efficiency are the rotor speed and turbine inlet temperature. Increases in the rotor speed and turbine inlet temperature offer the greatest improvements to the fuel efficiency and power output of the engine. It is well understood that the turbine rotor speed determines the maximum pressure ratios that can be obtained by the turbine, and increasing the speed, temperature and cross-sectional area of the core flow increases the amount of energy that can be extracted as work to drive the fan and compressor (Lakshminarayana 1996). As a consequence, turbine airfoils are subjected to the highest possible temperatures and centrifugal loads, which result in increased risk of structural failure, and accelerated material deterioration and degradation due to creep, oxidation, corrosion and thermo-mechanical fatigue at high temperature. These damage mechanisms ultimately set the limit of the entire engine. In addition, the accumulation of structural damage due to high temperatures and stresses constrains the time allowed between engine overhauls leading to greater cost of operation. In particular, the amount of time an engine can spend in continuous service depends on the life of the worst turbine airfoil, which is limited by the service-life capability, often referred to as the turbine durability. The goal of a turbine durability engineer is to provide a design for those turbine airfoils that will maintain a specified (service) life against all forms of damage, and in order to maintain their required service life, one must generate a turbine airfoil shape, select a high-temperature resistant material, develop an internal cooling configuration, an external film cooling scheme, and a thermal barrier and oxidation resistant coating on the (hot section) components exposed to those high stresses and temperatures. Hence, it is important to be able to predict the ultimate life, which requires an accurate prediction of the onset and accumulation of damage due to oxidation, corrosion, coating spallation, thermo-mechanical fatigue, low cycle fatigue, high cycle fatigue, and tertiary creep.

In modern turbomachines, high turbine efficiency requires the ability of turbine airfoils and outer air seals to withstand gas temperatures of the order of 2000 °C, yet most modern turbine components, especially the airfoils, are constructed from nickel-based super alloys that cannot withstand metal temperatures in excess of 1200 °C. Superalloys are widely used in the aerospace and power industries, as they were specifically designed for hot sections components of jet engines. They exhibit high mechanical strength, resistance to deformation at high stress and temperature (creep), fatigue life, and corrosion and oxidation resistance. In polycrystalline materials these increased temperatures would cause creep strains that would be unacceptable. Directionally solidified and single crystal materials were developed to mitigate the effects of creep at high temperatures. A typical modern single crystal superalloy has the ordered $L1_2$ structure, with a matrix based on a face-centered cubic structure and regular cubes of γ' phase which occupy from 65 to 70 % of the volume.

This two-phase structure of a superalloy provides improved creep strength at high temperatures because the hard phase and the phase boundaries provide obstacles to dislocation motion. Even single crystal materials must be pushed to their creep limits to ensure that engine performance is maximized.

Internal cooling passages, cold-side impingement, film (external) cooling and thermal barrier coatings are used on turbine airfoils and air seals in order to allow these components to withstand greater heat loads, resulting in increases in allowable turbine inlet gas temperatures. For a given cooling effectiveness, the turbine durability engineer can increase the amount of cooling air to produce a greater benefit, but high pressure cooling air must be extracted from the engine's compressor, thereby draining energy from the work-producing cycle. In addition, aerodynamic losses will also occur because of larger airfoil cross-sectional requirements, larger leading and trailing edge diameters, and the ejection of the cooling air through film cooling holes and slots reduces the boundary layer (Crawford and Kayes 1976) momentum leading to lower turbine aerodynamic efficiency (film mixing losses). About 400 °C of the increase in temperature capability can be attributed to internal convective cooling alone (Goldstein 1971). Internal cooling works by passing cooling air through internal passages inside the turbine airfoil, or impingement air inside the airfoil or on the backside of the air seals, and transferring heat by conduction through the blade walls to the air, and by convection, transferring back into the hot gas stream (Le Grives 1986). A large internal surface area is desirable for this purpose, so the cooling paths tend to be serpentine and full of small heat exchangers such as impingement holes, pin fins (pedestal banks), and turbulators, and the technology is moving towards smaller and smaller cooling features. Film cooling can be targeted upon specific areas of the turbine airfoil that absorb the most heat, for example, shower head cooling at the leading edges of the airfoils (Bunker 2005). Thin ceramic top coatings, called thermal barrier coatings (TBC), shield the turbine airfoils from the high temperature external gases, providing another 400 °C protection, which allows the turbine components to be fully operable and durable at higher temperatures, providing greater power and fuel efficiency. However, TBCs are prone to delaminate and spall during operation, especially at the edges of the parts, and the loss of the thermal barrier must be compensated by increasing the internal cooling at the leading and trailing edges using impingement cooling features.

2 Turbine Airfoil Failure Modes

At the high temperatures experienced in a turbine, corrosion and oxidation damage affects the life of the airfoil. In regions where surface temperatures are extremely high, surface atoms react with oxygen and oxidation occurs, and this reaction rate increases with increasing temperature. When the metal alloy is exposed to cyclic thermal operation, oxide is formed by consuming the alloy, creating and extending defects in the alloy. This process continues over time and operation, and results in the erosion of the alloy wall, as well as depletion of the γ' material; reducing its strength and resistance to creep. Thermal protection is provided by a low thermal

conductivity ceramic top coat that decreases the heat flux into the part, called a thermal barrier coating (TBC). In order to protect the superalloy against oxidation and corrosion, environmental barrier coatings (EBC), usually metallic aluminide or platinum aluminide, are added as an interlayer as well as to improve bonding of the TBC to the alloy substrate. The addition of TBCs, EBCs and age-hardening materials such as chromium and cobalt to the nickel-based alloys make the part resistant to oxidation and corrosion, but these materials are expensive. TBCs are prone to rapid degeneration in service (spallation) caused by cyclic thermal and structural loading. After repeated thermal cycling, the ceramic coating spalls or delaminates, exposing the alloy to the harsh temperature and the oxidative/corrosive gases of the combustion chamber. Sulfidation is a corrosion phenomenon that results primarily from the condensation of sodium sulfate on the surface of the blade. With increasing surface temperature, the corrosion rate first increases and then decreases because the temperatures are nearer to the vapor pressure of the sodium sulfate and less condensation occurs. Therefore, metal durability is at a maximum at a specific high temperature, so turbine airfoils and attached components are designed such that the maximum temperature in the metal and coating do not exceed some material limit, and so that the material temperature is maintained within a certain range of metal temperatures to achieve peak life expectancy.

Thermo-mechanical fatigue (TMF) is the weakening of material as it is subjected to cyclic thermal loading experienced when the engine is throttled through its operating cycle. The predominant factor in TMF endurance is the thermal strain; relatively small changes in the strain range have a significant effect on the TMF endurance of a part, which is measured as the number of cycles until failure. TMF can result in thermal-strain induced cracking, weakening of the materials' resistance to creep, and TBC spallation. Advanced cooling features inside modern turbine airfoil designs increase the concerns of TMF, because the external airfoil wall is hotter and the internal walls are cooler. For example, when designers add small cooling channels inside the coolant wall very close to the surface exposed to the hot gases, they effectively separate the wall into two thermal regions, resulting in extremely high thermal gradients around these features. Such configurations can produce three times higher strains than allowed by conventional cooling standards. Failure usually occurs under thermal mechanical fatigue loading, where the creep damage accumulates during the compressive high temperature deformation and the cracks emanate from the cooling hole or other micro-feature during the tensile low temperature cooling cycle.

Turbine components of aircraft engines are subject to strain controlled cyclic elastic-plastic deformations during airplane maneuvers which are combined with dwell times resulting in viscoplastic effects such as creep and/or stress relaxation. This combination of creep and plasticity leads to damage nucleation and growth and a significant reduction of the expected service life. It is a well-known fact that, at peak (e.g. take-off and climb) operating conditions, the service life and mission analysis of components operating in modern high pressure turbines of aircraft engines can reduce by half if the blade metal temperature prediction is increased by 30°C.

In recent years considerable attention has been given to the analysis of the structures and components operating under these extreme thermal and mechanical

loads and the prediction of these failure modes. Special interest has arisen in high temperature rotating turbine blades which are subject to long term viscoplastic deformation as well as time independent inelasticity caused by high levels of mechanical stress (see, for example, Stouffer and Dame 1996). It is also observed that creep accumulation typically show greater creep strain rates and/or reduced strain or time to creep rupture for thinner specimens than predicted by current, size-independent theories (Gullickson et al. 2008). Accurate predictions of material response for combined creep and plastic deformations are complex and greatly compounded during cyclic loading which is directly related to creep-fatigue interaction phenomena. Hence the development of a unified creep-plasticity model capable of predicting cyclic non-isothermal loading conditions and implementation of it in the engineering design practice is of extreme importance. An advanced creep-LCF/TMF lifing system would increase part life and engine usage, and allow for an expansion of maintenance limits.

We assert that high fidelity computational thermal and plastic deformation analysis will provide accurate predictions of hot section part life, allow for more durable hot section components at elevated engine conditions, reduce the number of design iterations, increase the time interval between service and overhaul, and result in a significant increase of product reliability and decreased warranty costs. As a rule of thumb, the quality of the different models used in such a system should be comparable; otherwise, one loses the advantages of the precise tool components. The accuracy and detail of the transient thermal analysis of the cooled turbine airfoils is critical to predict local transient strains, creep deformation and thermo-mechanical failure, and to use these to evaluate the effects of transient heating and cooling rates on the deformation and resulting life, and then to compare these predictions against damage criteria. This transient thermal prediction required the 3D modeling of four distinct heat transfer phenomenon, external convective heat transfer, external film cooling and mixing with the hot gases, internal cooling convective heat transfer, and transient heat conduction in the solid, all of which are coupled together in a transient conjugate heat transfer process. Heat radiation was neglected.

The time-dependent evolution of the operating conditions were coupled with the energy, momentum and mass flow conservation in all four domains using conjugate heat transfer interface conditions at different time scales. The predictions are physics-based, using empirical models only where the computational methods were inefficient, or unable to reliably predict the physical phenomenon. Using constitutive creep and lifing models, the material capability was calculated using the engine performance at key flight points. Through the use of sensitivity studies, the most damaging parameters were deduced and used to determine the directions for design improvement and optimization. The predictions were compared against experimental results for the specific failure design criteria, best practice were documented, and the methodology implemented in Pratt and Whitney engineering standard work.

3 Cooled Turbine Airfoil Design

The external shapes of the turbine airfoils are designed primarily from an aerodynamic perspective, optimized for turbine airfoil efficiency, minimum pressure loss, and a specified work extraction (loading). However, the external airfoil shape must be able to accept internal and external cooling features, as well as hold manufacturing tolerances and provide enough rigidity and solidity against creep, fatigue, high cycle fatigue (vibration modes) and to maintain structural integrity. For example, the cross-sectional areas of the internal cooling passages must be large enough to pass the needed cooling air, the walls and ribs must be thick enough to handle the centrifugal loads and to resist creep, the trailing edges must be designed large enough for the placement of slots required to eject the cooling air at the trailing edge, and the leading edge must be large enough to accommodate impingement and showerhead cooling schemes, as well as to withstand impacts from foreign particles. As in all engineering problems, turbine airfoils operation reaches the limits of inherently conflicting conditions, for example, the airfoil shapes are made thinner to improve aerodynamic performance until the limits of structural integrity, durability and manufacturing are reached.

A typical high turbine cross section and turbine blade design are illustrated in Fig. 1. This figure shows the external aerodynamic turbine airfoil shape, platform, attachment and internal convective cooling scheme. The image on the left is the cross section of the high turbine flowpath. The schematic on the right illustrates the external airfoil, platform, film cooling holes and ejection slots. A fully parametric proprietary CAD program is used to generate two- and three-dimensional models of turbine blades and vanes. Features captured by the parametric model are shown on Fig. 2.

For rotating turbine blades, inverse shape design was used for the global requirements of meeting the maximum section-averaged creep-rate, allowable vibratory stress (Goodman diagram), and the centrifugal stress limit at the blade root. Since creep rate is severely temperature-dependent, the radial variation of the average metal temperature of the blade must be estimated in order to set the nominal wall thickness to maintain an allowable average creep rate (Menon 1992). That is, the average creep life of the blade is set first by a Larson-Miller based function (Larson and Miller 1952), then after computing the radial variation of the centrifugal stress limit from this requirement, the thickness of the coolant wall is determined in order to not to exceed the centrifugal and vibratory stress limitations. Since the hottest gases in the turbine tend to migrate to the mid-span radius, and the centrifugal stresses in the blade are the highest at the root of the blade and decrease radially, the combined three-dimensional temperature and stress environment predicts that the worst creep is experienced at some critical span location between the root and the tip. A radially varying (circumferentially-averaged) gas temperature profile, $T_g(r)$, from a CFD calculation was used to approximate a radial variation of the blade's cross-section averaged metal temperature, $T_m(r)$. With this approximate average blade temperature variation, cross-sectional area of the load-bearing metal, and a given average

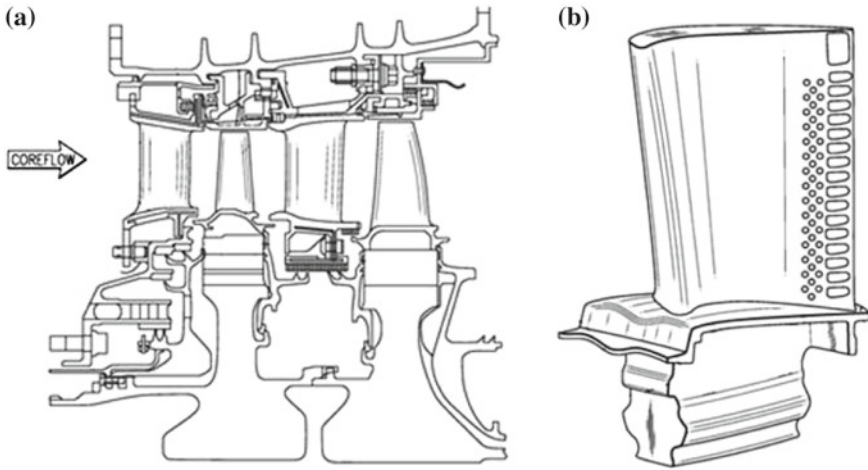


Fig. 1 a Engine cross-section of high turbine showing first and second turbine vanes and blades, b Drawing of turbine blade showing airfoil, platform, attachment, tip, film cooling holes, and trailing edge slots (US Patent #US 8356975 B2)

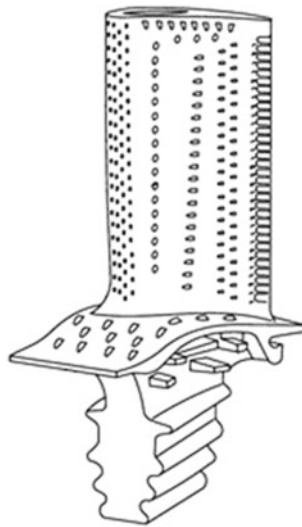


Fig. 2 Film cooled turbine blade, showing airfoil, tip and platform film cooling holes

creep life of the blade, we estimated the radial variation of the allowable average centrifugal stress in the blade metal usually using the Larson-Miller relation. In the design of this turbine blade, a ± 5 to 10 % margin of error in coolant flow rate was accounted for with a 5 % margin of error in metal temperature.

A parametric CAD routine was used to generate rows of film cooling holes and the airfoil (see Fig. 2). The parametric definition for round and shaped film holes, such

as hole position, in-plane angle, surface angle, diameter, shape, number of holes and pitch of the holes of the film cooling, completely defined the rows of film holes that break out of the pressure and suction sides of the cavities, and those that break out of the leading edge cavity as showerhead film, trailing edge slots, and tip surfaces (Martin and Dulikravich 2002). Leading edge (showerhead) film holes were defined by internal (ligament) distances, external position, diameter, shape, number of holes, and pitch of the holes. This information was sufficient to get empirical estimates for film coverage, heat transfer augmentation, cooling air discharge coefficients (Gritsch et al. 1997) and manufacturability. For example, film hole coverage was calculated by finding the footprint that each hole makes on the external airfoil surface, and factoring the angle that the hot gas flow streaklines make with the vector through the centerline of the hole. This film hole information was used to generate elements in the internal cooling flow model in order to provide boundary conditions to the thermal model of the solid, as well as for the generation of heat sink terms in the thermal model to account for the convection cooling on the internal surfaces of the film holes.

4 Loosely Coupled Conjugate Heat Transfer

We used computational fluid dynamics (CFD) and heat conduction/convection finite element model (FEM) within a loosely-coupled, conjugate heat transfer (LC-CHT) framework, where the external aero-thermodynamics of the turbine cascade, external film cooling, internal cooling thermal-fluid flow, and heat conduction phenomena were solved separately and coupled using compatibility relations at their interfaces. The conjugate approach was needed because studies show that, when compared to a decoupled solution of a convectively cooled airfoil, the material temperature can change by up to 8% of the difference in the mainstream and coolant temperature (Martin 2001). This is even more important when the turbine airfoil is film cooled because the film effectiveness is a strong function of the time-varying internal cooling flow rate, blowing ratio and coolant temperature, coupled to the static pressures at the film exits, lagged coolant supply pressure and temperature, and mission-varying engine rotor speed. Multiple steady state CFD simulations were run at specific time points of the mission to provide realistic estimates of hot gas temperature while minimizing the computational costs of a fully transient CFD simulation. We justified this by the fact that the time scales of the external flow physics are much shorter than the response time of the heat conduction in the metal, therefore not requiring time-accurate CFD simulation of the mission. Many simulations have shown that the loosely-coupled process converges efficiently and provides temperature and heat flux results that are just as accurate as the full conjugate procedure (Kassab and Li 1994). The latter involves the prediction for the heat conduction and convection in the main gas path, solid and internal coolant flow passages simultaneously within one multi-domain solver. Note that the loosely coupled approach is different from a

fully coupled conjugate heat transfer (CHT) approach in only its “black-box” style implementation of the component solvers, but the goals are the same.

LC-CHT procedure starts with a CFD prediction of the hot gas (combustion products) flow through the entire multistage high and low turbine. We used a steady-state, non-reacting, compressible Reynolds-Averaged Navier-Stokes (RANS) flow solver (White 1994) supplemented with a realizable $k-\omega$ turbulence model (Wilcox 1988). Each row of airfoils in the turbine were modeled as a single airfoil (vane or blade), where each stator vane and rotor blade was coupled with circumferential symmetry and averaging at the interfacial mixing planes. Hence, our CFD analyses neglected unsteady interactions (rotor-stator interaction due to shocks, loadings and wakes) between any two airfoil rows. In the initial RANS CFD run, we assumed all walls were adiabatic ($Q_g = 0$) and we neglected film cooling and leakage flows at the endwalls and air seal matesfaces and gaps. This initial RANS-CFD run did not consider the local effects of film and leakage, however, the global effect of the mixing of coolant air with the main hot gas path was considered by injecting cooling air uniformly distributed at various axial stations. The purpose of the initial RANS-CFD run was to predict adiabatic temperature distributions, T_G on the external walls of the airfoils, endwalls and air seals.

Figure 3 illustrates the LC-CHT problem that we considered important to the cooling design of a turbine blade. In order to balance the heat transfer between the hot gas, solid airfoil and internal cooling flow, we ran a series of coupled thermal analyses, where the RANS-CFD analyses of the hot gas path flow was coupled to heat conduction analyses in the solid, and the internal coolant flow inside the airfoil. The RANS-CFD runs were supplied with an external (airfoil, endwalls, tip, shroud, etc.) wall temperature, T_w , as a boundary conditions (instead of $Q_g = 0$) in order

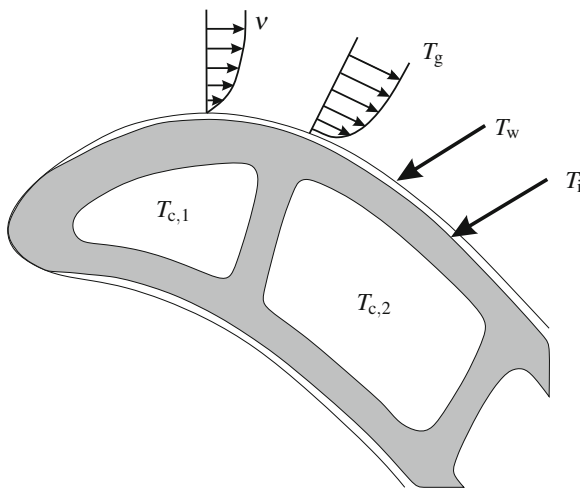


Fig. 3 Illustration of conjugate heat transfer problem of a turbine airfoil, including the velocity boundary layer, thermal boundary layer, and heat transfer

to develop a thermal boundary layer on the external surfaces. Since T_w was initially unknown, we used an initial guess as a fraction of the adiabatic wall temperature (e.g. $T_w = 0.85T_g$). These RANS-CFD runs calculated a distribution of heat flux, Q_g , or heat transfer coefficient, $h_g = Q_{gs}/(T_g - T_w)$, on the external surfaces. To account for the presence of the film cooling, the external gas temperature, T_g , was converted to a film temperature, T_f , via film cooling effectiveness distribution. The new heat transfer and film temperature coefficient distributions, h_g and T_f , were provided as an external boundary condition to a heat conduction analysis of the solid. This heat conduction analysis also required internal coolant temperatures, T_c , and heat transfer coefficient, h_c , boundary conditions, which are also temperature dependent, since the solid provides heating to the internal and film cooling air. The heat conduction analyses, in turn, produced a new wall temperature distribution, T_w , which were used as boundary conditions to subsequent RANS-CFD runs. The external-solid-internal loosely-coupled conjugate aero-thermal process was solved in succession until the wall temperature converged to within less than 0.5°C .

5 Film Cooling

Film cooling involves the injection of higher density, lower temperature cooling air into the external (hot gas) free stream through the film holes on the external surface of the airfoil, tip and endwalls. The film air was assumed to be injected into the thermal boundary layer in order to provide a layer of film on the airfoil surface that protects it from the hot gases. It might appear to be straight-forward and desirable to include film cooling air in the RANS-CFD simulation. The approach most often implemented is called film injection modeling, but unfortunately, most attempts at doing so have not met the accuracy requirements for the prediction of film effectiveness and external heat transfer on turbine airfoils. In our analysis procedure, the film cooling air was not modeled in the external RANS-CFD simulation but instead, the external gas temperature was augmented using experimentally derived adiabatic film effectiveness correlations.

The temperature of the external hot gas, T_g , was augmented by the presence of the film using the adiabatic film cooling effectiveness, η_t , and the film cooling air temperature, T_{fc} , in order to produce a film temperature, $T_f = T_g - h_f(T_g - T_{fc})$. Here, T_g is the adiabatic wall temperature predicted by the RANS-CFD solution. The adiabatic film effectiveness was derived empirically in a proprietary code by correlating heat transfer measurements in the vicinity and downstream of rows of inclined film cooling holes. Empirical convection correlations were used for the heat transfer coefficients inside the hole (circular channel with an entrance effect). The film effectiveness and heat transfer factor are taken from empirical data. The film effectiveness varies along the streamwise and lateral (hole-to-hole) directions, and it is known to be a functions of a number of parameters, $\eta_f(M_B, D, s/D, L/D, \alpha, dp/dx, Tu)$, specifically, the blowing ratio, M_B , film hole diameter, D , relative film hole spacing, s/D , relative distance downstream of the film hole, relative length of the film hole, L/D ,

film injection angle, α , pressure gradient, dp/dx , and turbulence intensity, Tu . The film cooling effectiveness was attenuated along CFD-predicted streaklines emanating from the film cooling holes, and included the coverage of the film due to the footprints of the holes on the surface (the local area made by the round or shaped and diffused film cooling holes projected onto the surface and lateral to the streamwise direction). Three-dimensional streaklines were generated from the CFD solution along the airfoil, tip, platform and endwall surfaces. The streaklines on the airfoil surface were divided into several groups; those that originate at the leading edge and travel to the trailing edge, those that originate at the leading edge and travel down to the airfoil root and run along the platform, and those that originate at the leading edge and travel up to the airfoil tip. These streaklines were used to capture the physics of hot gas migration in the turbine cascade, as well as the flow direction of the film cooling air. In order to do this, the streaklines were grouped into regions on the airfoil pressure side, suction side, tip, root and endwalls. The injection of the film disrupts the external thermal boundary layer. Therefore, the distribution of external heat transfer coefficient, h_g , was also modified by an empirical factor, $h_f = h_g \cdot \text{factor}$, which was correlated to experimental film cooling measurements of rows of shaped and inclined holes. The result was the balance of local RANS-CFD predicted heat flux, Q_g , into the external turbine airfoil surface, so that it matched the heat flux into the solid at the LC-CHT converged wall temperature, T_w , such that, $Q_g = h_f(T_f T_w)$.

6 Internal Cooling

The internal cooling air systems within modern turbine airfoil are extremely complex and three-dimensional, having many branches of low to moderate Mach number, recirculating flows caused by the existence of miniature heat exchangers, skewed trip strips, sudden expansions or contractions, bifurcations of the flow stream, entrance-effect flows, 180° bends, pedestal cooling schemes, impingement holes producing jet flows, diffusing cooling air ejection slots for film holes, etc. An example of three-pass serpentine cooling scheme (Brillert et al. 1999) with leading edge and trailing edge impingement cooling, showerhead film, and coolant air ejection out of the trailing edge is shown in Fig. 4. The heat transfer characteristics in a rotating serpentine coolant flow passage are very complex and three-dimensional, being affected by Coriolis forces and centrifugal forces combined with thermal buoyancy (Webb 1998). Thermal buoyancy within the boundary layer is an important effect caused by the rotation, because Coriolis forces affect each portion of the serpentine coolant passages differently depending upon whether the coolant stream is traveling radially-outward or radially-inward. Secondary flows are induced by the Coriolis force, making the heat transfer coefficients in the radially outward passages diminish on the leading surfaces and increase on the trailing surfaces, with an increase in rotational speed. The trend is reversed in the radially inward passage. Hot zones have a distinct effect on the heat transfer rate because higher temperatures produce

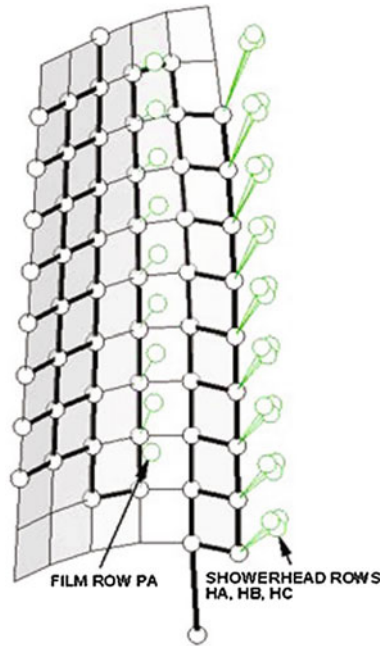


Fig. 4 Schematic of internal coolant flow network in a turbine blade

greater buoyancy forces and enhanced heat transfer, therefore, the ratio of rotating to non-rotating heat transfer coefficients, Nu_r/Nu , were a function of the local wall temperature.

At present, the computational requirements needed for this type of CFD analysis are beyond the scope of this work. Instead, the application of thermal boundary conditions on the internal coolant flow passage surfaces was greatly simplified by a steady-state semi-empirical approach using a network of quasi-one-dimensional thermal fluid elements, in conjunction with an equation of state to solve for the coolant air flow rate, coolant static pressure, and coolant static temperature. The friction, heat transfer, and cooling (head) loss coefficients were derived from empirical correlations given the known geometry of the cooling passages within geometric limits and operating ranges (Dipprey and Sabersky 1963; Han and Park 1988). The coolant supply pressure and wall temperature at the source (supply) nodes, and static pressures at the sink (dump) nodes (film holes and ejection slots), which might vary in time, were applied at specific time points in multiple steady-state analyses of this thermal fluid network (Kawaike et al. 1992). Wall temperatures on each element were taken from the transient heat conduction solution from the FEM at selected mission points.

7 Heat Conduction

ANSYS was used for the prediction of the transient heat conduction response in the solid, which consisted of two material domains in FEM; the metal superalloy and the multi-component thermal barrier coating (TBC). The transient heat conduction model consisted of two material domains in a finite element model (FEM); the nickel metal alloy and the thermal barrier coating (TBC). The transient heat conduction in the metal alloy assumed that the specific heat, $C(T)$, and thermal conductivity, $k(T)$, of the metal alloy were functions of temperature within each domain.

$$\rho C(T) \frac{\partial T}{\partial t} = \nabla \cdot [k(T) \nabla T] \quad (1)$$

The thermal barrier coating was modeled by a layer of thin elements on the surface of the finite element model, which included the bond coat and diffusion layer into the metal using a thermal resistance weighting methodology, where k_{eff} is the effective coefficient of thermal conductivity of the coating, $k_{\text{tbc}}(T)$, $k_{\text{b}}(T)$, and $k_{\text{d}}(T)$ are the thermal conductivities of the TBC, bond and diffusion layers, respectively, and t_{tbc} , t_{b} and t_{d} are the thicknesses of those layers.

$$\frac{t_{\text{tbc}} + t_{\text{b}} + t_{\text{d}}}{k_{\text{eff}}} = \frac{t_{\text{tbc}}}{k_{\text{tbc}}} + \frac{t_{\text{b}}}{k_{\text{b}}} + \frac{t_{\text{d}}}{k_{\text{d}}} \quad (2)$$

The transient LC-CHT process continued by iteratively solving the external (hot gas) CFD model and internal cooling flow model aerothermodynamics by applying wall temperature boundary conditions predicted by the transient heat conduction model of the solid airfoil at the interface surfaces (external hot gas/TBC & internal metal alloy/cooling air)

$$T_{\text{w,gas}} = T_{\text{w,solid}}, \quad Q_{\text{w,gas}} = Q_{\text{w,solid}}$$

These interface conditions are required to couple the heat conduction in the metal alloy and the thermal barrier coating.

8 Transient Aero-Thermal Analysis

For the transient LC-CHT procedure, we supplied a mission profile, that is, the engine operating conditions as a function of time in order to generate time-varying boundary conditions for the thermo-fluid analysis solvers (coupled CFD and FEM), which consisted of the time-varying engine performance variables such as high or low pressure turbine rotor speed, core engine airflow into the turbine row (FLOW), relative total temperature at the inlet to the turbine airfoil row (T4IREL), relative total pressure at the inlet to the turbine airfoil row (P4IREL), internal coolant supply pressure (PSUPPLY), and internal coolant supply temperature (TSUPPLY), versus

time as shown in Fig. 5. The coolant supply pressure and temperature may alternately be supplied as functions of, or scaled by, the time-varying compressor discharge total pressure (PT3) and total temperature (TT3). For our analysis, the time-varying mission parameters were supplied as radially and circumferentially averaged values. A radially varying profile factor was applied to the inlet relative total temperature and this factor was held constant in the transient thermal analysis, with only the average (scaling) value varying in time. In addition, all other required boundary conditions were scaled to the time varying condition. For the analysis and lifing of the part, mission profiles were generated to provide actual or representative time varying conditions, leading to the evaluation of the temperature, stress and strain fields for that particular class of missions. The coolant supply pressure and temperature, which vary in time, were applied to the source nodes (supply) of internal cooling air flow model. Dump (static) pressures were specified at the sink nodes (film holes and ejection slots). A constant initial guess for the wall temperatures along each element of the coolant network was required to start the LC-CHT. This provided the necessary boundary conditions to solve the internal cooling flow model for the internal cooling air pressures, temperatures, flow rates and internal heat transfer coefficients.

The transient loosely-coupled conjugate heat transfer (LC-CHT) process was solved iteratively by sequentially running the external aero-thermodynamic RANS-CFD, transient heat conduction, and steady-state compressible internal cooling flow analysis tools, coupled by the transference of wall temperature and heat flux interface conditions predicted by them. About 4–8 LC-CHT iterations were required to converge the wall temperature, T_w , to under 1 °F. The LC-CHT procedure was compared

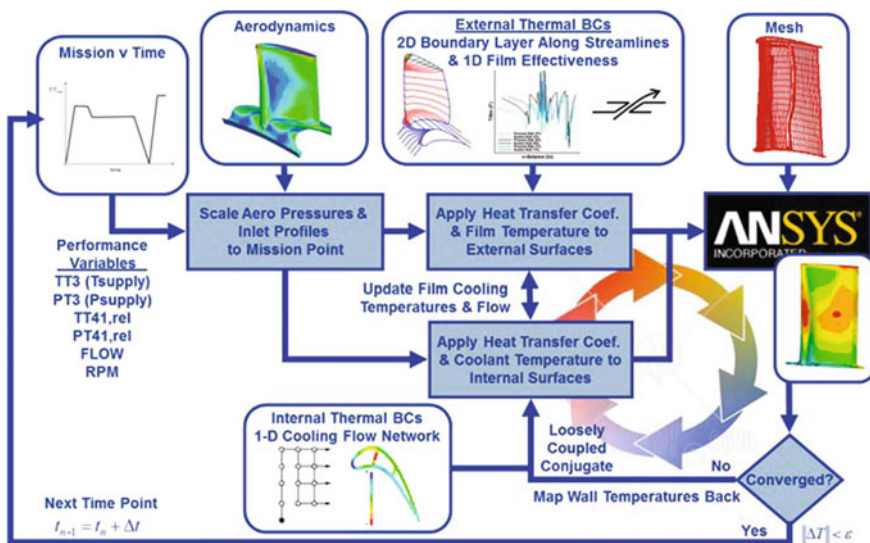


Fig. 5 Flow chart of the loosely-coupled conjugate transient thermal analysis process for an internally and film cooled turbine airfoil

to actual thermal measurements of a second stage turbine blade, where thermocouple measurements were taken at several locations around the turbine blade, and where pyrometry was available on the suction side. The loosely-coupled conjugate RANS-CFD and heat conduction solution shown as a solid line compares very well with the data. A non-conjugate (decoupled), two-dimensional thermal prediction is also shown (dashed line).

9 Structural Non-linear Analysis for the Life Prediction

In order to reach our goal of physics-based life prediction, the thermal analysis was followed by rigorous, time-integrated, visco-plastic structural prediction for the permanent deformation and accumulated damage. In this work, we focus on the micromechanics of the high temperature creep, plasticity, and damage accumulation in single crystal nickel base superalloy and their interaction with the failure processes, for applications in advanced commercial and military gas turbines. We have developed a unified crystal-plasticity based materials constitutive model including thermally-dependent creep activation mechanisms for different crystallographic orientations. The model extends existing approaches to increase the accuracy of elastic-visco-plastic material deformation response predictions for cyclic and thermal-cyclic loading.

During a typical flight mission the transient temperature changes cause non-homogeneous thermal mechanical loading of single crystal components leading to inhomogeneous local creep and damage evolution accompanied with extensive stress redistribution and relaxation. The higher the value of applied stress and working temperature, the faster the accumulation of deformation takes place, which can be understood as energy dissipation in the microstructure. Energy dissipation in a loaded structure could take place either by inelastic (plastic) deformation or by microcracking. The single crystal (SX) Ni-based superalloy (for example PWA1484) exhibits nonlinear characteristics, where inelastic deformation is the primary damage-inducing mechanism; therefore life prediction is based on a fully coupled cyclic visco-plastic damage accumulation model. Study of phenomena such as strain hardening and saturation requires the analysis of the stability of inelastic deformation under cyclic loading. Cyclic relaxation, like cyclic creep, also depends on the mean stress/strain. During load and non-homogeneous temperature cyclic variations a residual stress-strain state arises, which in turn leads to cracks or voids nucleation and growth.

Creep in single crystal superalloys is highly anisotropic. Single crystal crystallography indicates orientation-dependent creep behavior and, hence, it is extremely important to be able to predict the creep rates in different crystallographic orientations, especially due to non-homogeneous temperature distributions in the material. This anisotropic behavior dictates the choice of the modeling technique (i.e., a crystal plasticity based model). The proposed state variables approach for deformation

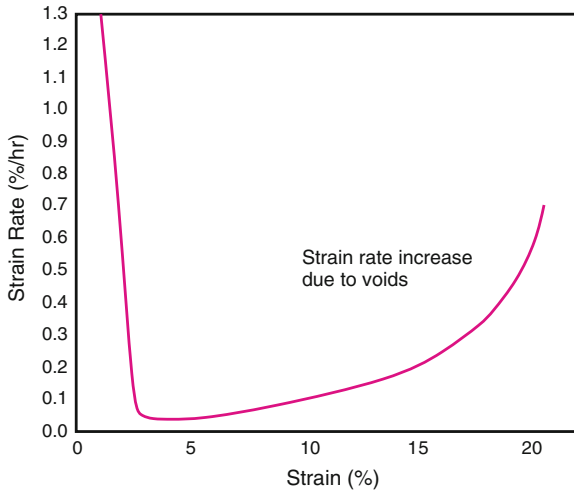


Fig. 6 Strain rate versus creep strain for $\langle 001 \rangle$ creep of single crystal PWA 1484 at 850°C and an engineering stress of 550 MPa

simulations of $L1_2$ single crystals gives us a tool to deduce the physics-based behavior of the structure and relate it to the microstructure evolution and orientation.

Creep deformation mechanisms dominate at high temperature, while time-independent plasticity mechanisms become very important at relatively low temperature (in our case in the range $750\text{--}850^\circ\text{C}$). It is typical for Ni-based super-alloys at operational temperatures to creep without steady state regime. This response is referred to as sigmoidal creep (Levitin 2006). During the primary creep regime the strain rate decreases with increasing strain until it reaches a minimal value. After this point, the creep strain rate increases without a long constant strain-rate interval. At high temperatures and moderate values of the applied load it is observed that creep can occur without any noticeable primary stage. Figure 6 illustrates the sigmoidal character of PWA1484 creep deformation along $\langle 001 \rangle$ crystallographic direction. The latter tertiary creep interval has a much steeper slope and is associated with active creep cavitations and deformation localization near the fracture surfaces. Predicting tertiary creep implies that damage mechanisms must be modeled. A combination of these two mechanisms provides a description of the complete thermal-deformation cycle when extensive deformation takes place at high peak temperatures, and the residual strain/stress generated on cooling or even at engine shut down, which can eventually lead to the failure initiation.

10 Visco-Plastic Constitutive Model

The general form of the incremental governing relation for the visco-plastic shearing, γ , may be written as a function of a number of physical effects:

$$\Delta\gamma^\alpha = \dot{\gamma}^\alpha(\tau^\alpha, s^\alpha, \omega^\alpha, \rho^\alpha, T)\Delta t = \dot{\gamma}_{\text{creep}}^\alpha \Delta t + \Delta\gamma_{\text{plast}}^\alpha, \quad (3)$$

where α is the index of the slip system, τ^α is resolved shear stress, s^α is the deformation resistance, ω^α is a kinematic hardening; ρ^α is the dislocation density, T is the temperature, and Δt is the time step.

Our finite deformation model (Kalidindi et al. 1992; Staroselsky 1997) is a standard visco-plastic models that can be used to represent the macroscopic mechanical response of the single crystal material. In this formulation creep will be included to the total inelastic strain rate as will be shown in this section. The deformation of a crystal is taken as the sum of contributions from overall elastic distortion and generalized plastic deformation. The overall plastic response is a sum of responses from small regions of a single crystal playing the role of representative volume elements (RVE).

For metallic materials the constitutive equation for the second Piola-Kirchhoff stress tensor is given by a linear relation

$$\begin{aligned} \mathbf{T}^* &= \mathbf{C}[\mathbf{E}^* - \mathbf{A}(T - T_0)], \\ \mathbf{E}^* &= \frac{1}{2} \left[\mathbf{F}^{\text{eT}} \mathbf{F}^{\text{e}} - \mathbf{1} \right] \end{aligned} \quad (4)$$

The governing variables in this constitutive model are the Cauchy stress, \mathbf{T} , the deformation gradient, \mathbf{F} , the plastic deformation gradient, \mathbf{F}^{p} , where $\det[\mathbf{F}^{\text{p}}] = 1$, \mathbf{A} is the second order thermal extension tensor, \mathbf{C} is temperature dependent anisotropic elasticity tensor, T is the temperature, and T_0 is a reference temperature. Each crystal slip system is specified by a unit normal, \mathbf{n}_0^α , to the slip plane, and a unit vector, \mathbf{m}_0^α , denotes the slip direction along slip system α .

The elastic deformation gradient is defined by decomposition of the total deformation gradient.

$$\mathbf{F} = \mathbf{F}^{\text{e}} \mathbf{F}^{\text{in}} \quad (5)$$

Here, \mathbf{F}^{e} describes the elastic distortion of the lattice, where $\det[\mathbf{F}^{\text{e}}] > 0$, which gives rise to the stress \mathbf{T} . The Cauchy Stress tensor is calculated as follows

$$\mathbf{T} = \frac{1}{\det(\mathbf{F}^{\text{e}})} \mathbf{F}^{\text{e}} \mathbf{T}^* \mathbf{F}^{\text{in}} \quad (6)$$

The evolution equation for the visco-plastic deformation gradient is

$$\begin{aligned}\dot{\mathbf{F}}^{\text{in}} &= \mathbf{L}^{\text{in}} \mathbf{F}^{\text{in}}, \\ \mathbf{L}^{\text{in}} &= \sum_{\text{slip systems}} \dot{\gamma}^{\alpha} \mathbf{S}^{\alpha}, \\ \mathbf{S}^{\alpha} &= \mathbf{m}^{\alpha} \otimes \mathbf{n}^{\alpha}\end{aligned}\quad (7)$$

The shear rate along each slip system $\dot{\gamma}^{\alpha}$ is given in terms of the slip systems resistances, equilibrium stress (or back stress), and the resolved shear stress (RSS)

$$\tau = \mathbf{T}^* \cdot \mathbf{S}^{\alpha} \quad (8)$$

Evolution of crystallographic texture is explicitly defined by the elastic part of the deformation gradient

$$\begin{aligned}\mathbf{m}_t^{\alpha} &= \mathbf{F}^{\text{e}} \mathbf{m}_0^{\alpha}, \\ \mathbf{n}_t^{\alpha} &= \mathbf{F}^{\text{e}-\text{T}} \mathbf{n}_0^{\alpha}\end{aligned}\quad (9)$$

We use the twelve octahedral slip systems $\langle 110 \rangle (111)$. At high temperatures, the cube slip systems $\langle 110 \rangle (001)$ may also contribute to maintaining the plastic flow of superalloys, and the material model parameters are different for the octahedral and cube slip systems. We use Orowan's assumption that the creep strain rate is proportional to the density of the mobile dislocations, ρ_m . If we denote an arbitrary reference dislocation density throughout as ρ_0 , then the non-dimensional parameter, ρ_m / ρ_0 , serves as a measure of the mobile dislocation density, and can be used to predict tertiary creep.

11 Creep Constitutive Model

The constitutive law for the secondary-tertiary creep strain rate along α th slip system was written as follows (Staroselsky and Cassenti 2008)

$$\dot{\gamma}^{\alpha} = \dot{\gamma}_0 \left(\frac{\rho_m^{\alpha}}{\rho_0} \right) \left| \frac{\tau^{\alpha} - \omega^{\alpha}}{s^{\alpha}} \right|^n \text{sign}(\tau^{\alpha} - \omega^{\alpha}) \exp\left(-\frac{Q}{k_B T}\right) \quad (10)$$

where $\dot{\gamma}_0$ is a temperature dependent time parameter, and k_B is Boltzmann's constant. The Arrhenius term with the activation energy, Q , accounts for the temperature changes and reflects the accumulated damage along the particular slip system. The power n is the creep exponent, which was assumed $n = 3$ in this work. We have chosen latent hardening evolution to be described by the following,

$$s^{\alpha} = h_0 \left(1 - \frac{s^{\alpha}}{s^*} \right)^p \sum_{\beta} h^{\alpha\beta} |\dot{\gamma}^{\beta}| \quad (11)$$

with hardening matrix

$$h^{\alpha\beta} = q + (1 - q)\delta^{\alpha\beta} \quad (12)$$

for temperature dependent h_0 and s^* , and $q = 1.4$. The exponent $p = 2$ in this work. The back stress (or kinematic hardening) has a limiting saturation value, $\omega_\infty = C_1/C_2$, corresponding to the end of the primary creep stage which evolves according to the following relationship (Stouffer and Dame 1996).

$$\dot{\omega}^\alpha = C_1\dot{\gamma}^\alpha - C_2|\dot{\gamma}^\alpha|\omega^\alpha = \lambda(\dot{\gamma}^\alpha\omega_\infty - |\dot{\gamma}^\alpha|\omega^\alpha) \quad (13)$$

The back stress requires two additional experimentally measured coefficients C_1 and C_2 that are explicit functions of temperature. It is important to note that hardening terms indirectly account for the microstructure evolution during the creep. Dislocation generation and motion represents a non-recoverable state for the material. We postulated that dislocation generation rate is proportional to the rate of entropy production which can be expressed by

$$\dot{S} \sim \sum_{\alpha=1}^{n_{\text{slip}}} \left(\frac{\tau^\alpha - \omega^\alpha}{s^\alpha} \right) \dot{\gamma}^\alpha \geq 0, \quad (14)$$

where n_{slip} is the number of active slip systems, which is 18 (12 octahedral and 6 cube) for a Ni-base superalloy.

We consider two types of the dislocations: mobile and pinned. Using concepts from chemical kinetics we have chosen to represent the dislocation density evolution as two body interactions. We assume that dislocation immobilization takes place when two corresponding dislocation loops interact with each other. Note that since $\dot{\gamma}^\alpha$ is already a linear function of the mobile dislocation density, then for two body interactions the dislocation densities growth rates can be taken as the product of $\dot{\gamma}^\alpha$ and linear functions of the current dislocation densities. Assuming the existence of dislocation densities saturation values, ρ_m^{ss} for mobile dislocations and ρ_p^{ss} for pinned, we obtain relations for mobile and pinned dislocations along each slip system as following (Staroselsky and Cassenti 2008, 2010).

$$\begin{aligned} \dot{\rho}_m^\alpha &= M \left(\frac{\tau^\alpha - \omega^\alpha}{s^\alpha} \right) \dot{\gamma}_{\text{in}}^\alpha \left(\frac{\varepsilon^2 \rho_m^{\text{ss}} + \rho_p^{\text{ss}} - \rho_p^\alpha - \varepsilon^2 \rho_m^\alpha}{\rho_0} \right), \\ \dot{\rho}_p^\alpha &= \Pi \left(\frac{\tau^\alpha - \omega^\alpha}{s^\alpha} \right) \dot{\gamma}_{\text{in}}^\alpha \left(\frac{\rho_p^{\text{ss}} - \rho_p^\alpha}{\rho_0} \right) \end{aligned} \quad (15)$$

Here, M and Π represent specific time constants, different for octahedral and cube slip systems, ε^2 is a positive constant. These equations include the annihilation of mobile dislocations and also include their conversion to pinned dislocations. The pinned dislocations grow at a rate that is proportional to the mobile dislocation density because of the presence of the plastic strain rate term. Dislocation densities evolutions

have strong temperature dependence because inelastic strain rates expression for $\dot{\gamma}^\alpha$ contains Arrhenius term.

In order to predict primary creep in Ni-based superalloys, we have developed rate-dependent crystal plasticity formalism with a threshold stress on each slip system.

$$\dot{\gamma}_{\text{primary}}^\alpha = \dot{\gamma}_0 \left\langle \frac{(\tau^\alpha - \omega_p^\alpha) - \kappa \sqrt{\rho_p^\alpha}}{s^\alpha} \right\rangle^n \text{sign} \left(\frac{\tau^\alpha - \omega_p^\alpha}{s^\alpha} \right) \exp \left(-\frac{Q}{k_B T} \right) \quad (16)$$

Here,

$$\langle a \rangle = \begin{cases} a & \text{if } a > 0 \\ 0 & \text{if } a \leq 0 \end{cases}$$

and κ is temperature dependent fitting parameter. In the formula for the back stress, parameter λ is a characteristic time parameter describing how fast the back stress converges to its saturation value, ω_∞ . Thus, dislocations cross-slip causes strain hardening which in turn decreases the rate of creep deformation. Increases in the dislocation density and in the number of dislocation pile-ups makes further deformation more and more difficult, resulting in the transition of creep from the primary stage to a secondary one. The rate of the primary creep gradually decreases with deformation or with the development of slip resistance. Since dislocation strengthening is proportional to the square root of the dislocation density (for example, Mughrabi 1975), we introduced the threshold value to also be proportional to the square root of the total dislocation density. The threshold stress reflects the resistance to plastic flow arising from hardening associated with an increase of dislocation density and cross-slip. All threshold parameters as well as hardening parameters depend on temperature.

With an increase in primary creep deformations, dislocation density increases reducing the applied effective stresses to very small values. Thus, the primary creep slip rate gradually decreases from a significant value to zero. The back stress during the primary creep stage has the same functional form as (16) but due to the fact that primary creep is much faster process than secondary and tertiary ones, a value of γ_0^α for primary creep is smaller than the value of γ_0 while the saturation value ω_∞ , is the same for all creep stages.

The total creep deformation rate for each slip system is the direct sum of tertiary creep Orowan's type expression and the primary one.

$$\dot{\gamma}_{\text{creep}}^\alpha = \dot{\gamma}_{\text{primary}}^\alpha + \dot{\gamma}^\alpha \quad (17)$$

Primary creep has been mainly observed in Ni-based superalloy at relatively low temperatures and high applied nominal stresses. Typical creep curves obtained at 760°C and the model predictions are shown in Fig. 7 (Staroselsky and Cassenti 2011). Figure 8 illustrates the creep model predictions curves against test data for single crystal superalloy at 982°C. The same model applied to the dwell fatigue isothermal process and to the thermal mechanical fatigue (TMF) gives predictions very close to the experimental observations as shown on graphs in Fig. 9.

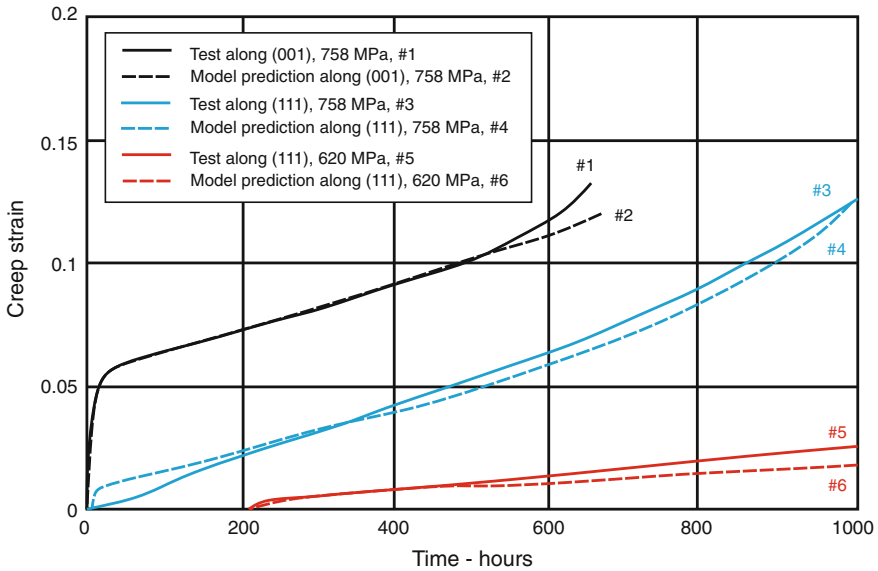


Fig. 7 Model predictions and creep test results at temperature 760°C. Lines #1 and #2 are tests and simulation results correspondingly of creep along (001) crystallographic direction with nominal (initial) stress of 758 MPa. Lines #3 and #5 are creep test results along (111) direction conducted at nominal stress levels of 758 and 620MPa correspondingly. Lines #4 is the simulation results for the test #3 and line #6 is the results of simulations for the test curve #5

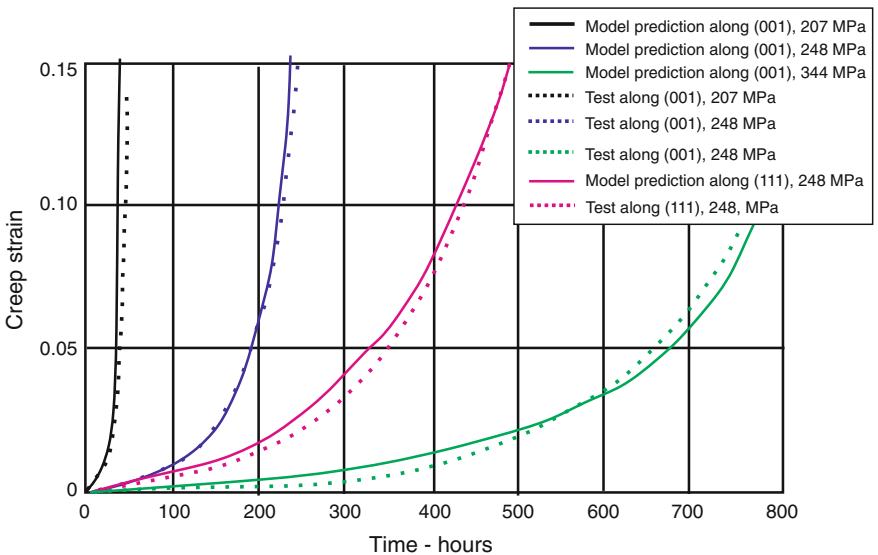


Fig. 8 Creep prediction versus experimental data for 982°C corresponding to three different nominal stress levels of 207, 248, and 344 MPa applied along (001) crystallographic direction and of 248 MPa applied along (111) direction

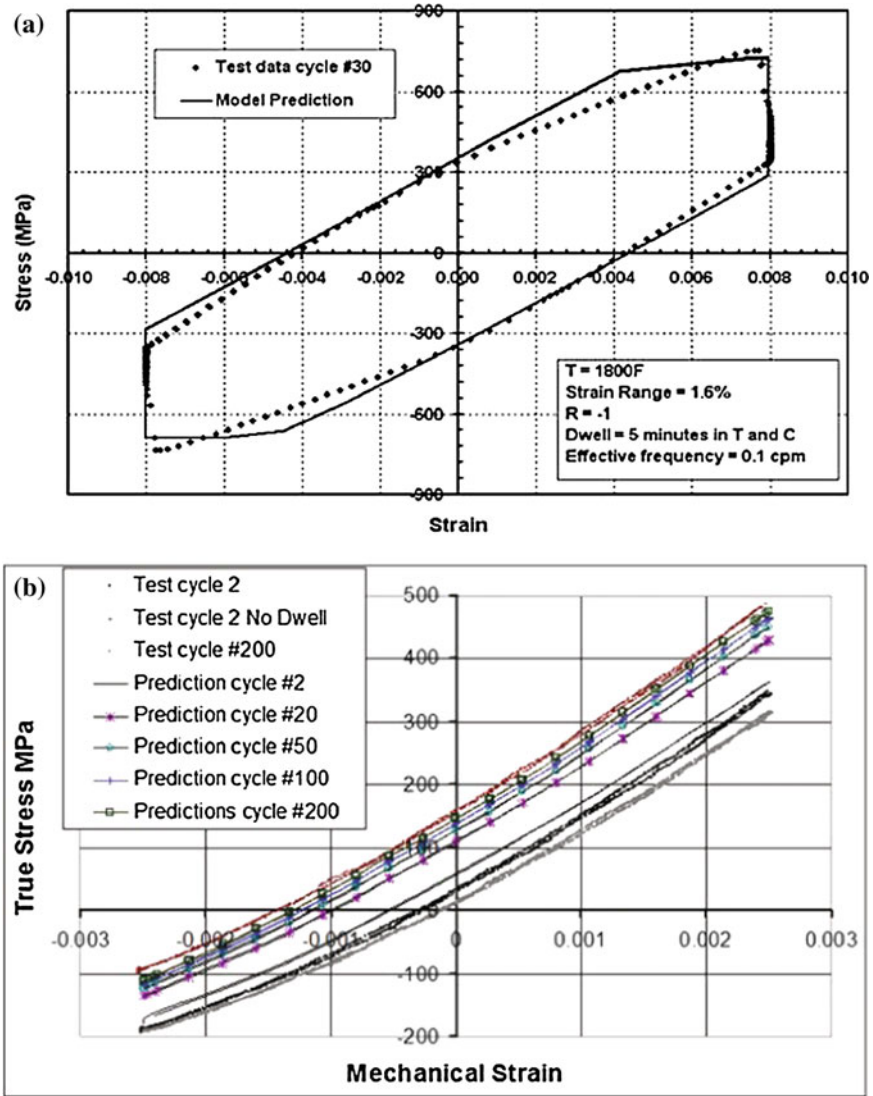


Fig. 9 Test data and model predictions of **a** creep-fatigue interaction with 5 min dwell time for strain-controlled cyclic test up to 0.8 % strain range along (001) crystallographic direction at 982 °C; and **b** OP TMF test up to 0.25 % strain range along (001) crystallographic direction at the temperature range from 427 °C to 1038 °C with hot dwell of 30 min

Due to the creep, stress in the part redistributes and some, mostly non-creeping, sub-volumes of the parts experience very high stresses leading to plastic deformation. Plasticity causes severe damage significantly reducing service life. The details of the presented rate-independent formulation can be found in Staroselsky and Cassenti (2010). Here we briefly summarize the idea how to combine the computational

benefits of rate independent plastic formulation with the advantages of a power method affirming the uniqueness of active slip increments calculations.

12 Plasticity Constitutive Model

We postulate that a plastic strain rate is proportional to the rate of plastic work,

$$\dot{\gamma}^\alpha = \frac{\tau^\alpha - \omega^\alpha}{(s^\alpha)^2} \left| \frac{\tau^\alpha - \omega^\alpha}{s^\alpha} \right|^m \langle \dot{W}^P \rangle \tag{18}$$

By dividing both parts on \dot{W}^P and integrating, we get an explicit function of plastic work, W^P and subsequently the model can be labeled as rate independent. We use the ramp function to satisfy Kuhn-Tucker condition or in other words, there is no plasticity under unloading. It means that when the energy is removed from the material, $W^P < 0$, and no plastic deformation occur. We use the advantage of the power model to limit activities of the slip systems with small resolved shear stresses and to assure the unique choice of active slip systems. Values of the exponent, $m < 30$, provide good selection of slip activities and do not cause computational problems specific for stiff rate-dependent power models with very high values of the exponent values. We generalize the formulation above by substituting the plastic work rate with a weighted sum of the total and elastic work rates, and replace the plastic work rate in the following way

$$\dot{\gamma}^\alpha = \frac{\tau^\alpha - \omega^\alpha}{(s^\alpha)^2} \left| \frac{\tau^\alpha - \omega^\alpha}{s^\alpha} \right|^m \langle \dot{W} - k(\dot{W} - \dot{W}^P) \rangle \tag{19}$$

Here, k is a temperature dependent material parameter. The total work rate is given by

$$\dot{W} = \sum_{i,j} \sigma_{ij} \dot{\epsilon}_{ij} \tag{20}$$

and the plastic work rate is

$$\dot{W}^P = \sum_{\alpha} (\tau^\alpha - \omega^\alpha) \dot{\gamma}^\alpha \tag{21}$$

After algebraic manipulation, we get the final form of the rate independent plastic strain increment.

$$\Delta\gamma^\alpha = \frac{(1-k) \left\langle \frac{\sum_{i,j=1,3} \sigma_{ij} \Delta\varepsilon_{ij}^{\text{total}}}{s^\alpha} \right\rangle \left| \frac{\tau^\alpha - \omega^\alpha}{s^\alpha} \right|^m \left(\frac{\tau^\alpha - \omega^\alpha}{s^\alpha} \right)}{1 - k \sum_{\alpha} \left| \frac{\tau^\alpha - \omega^\alpha}{s^\alpha} \right|^{m+2}} \quad (22)$$

Thus, we have formulated a rate-independent flow rule which automatically guarantees a unique selection of active slip systems at each time increment without any additional criteria and constraints. We also introduced one more model weight parameter, $0 \leq k < 1$. If the value of this parameter is close to zero, yield values change gradually as it usually observed during hardening. In the limiting case of $k \rightarrow 1$, there will be a sudden change in the plastic strain rate when $\tau^\alpha - \omega^\alpha = s^\alpha$, and, hence, s^α can be interpreted as a yield stress. The described model gives good predictions for different crystallographic orientations.

13 Thermo-Mechanical Fatigue Model

Hot section components in advanced aircraft engines experience severe cyclic temperature gradients and mechanical loads, particularly during takeoff and landing operations. As a consequence, TMF is a major life-limiting factor air cooled turbine airfoils (Amaro et al. 2010; Kersey et al. 2013) because they are subject to the combined influences of thermally driven strain transients and creep damage during operation. The phasing between thermal and mechanical loads defines the TMF response of the airfoil. The extremes of load-temperature phasing are in-phase (IP) and out-of-phase (OP). In-phase cycles occur when an unconstrained local area of the blade is mechanically loaded at the same time the temperature increases. Out-of-phase cycling occurs when a locally constrained area of the blade tries to expand as temperature increases, which usually causes the local compression with the rise of temperature. OP cycling is generally the most harmful because stress relaxation at the maximum temperature develops high mean stresses. In addition, TMF cracking occurs at varying locations on turbine airfoils, including pressure and suction sides, leading and trailing edges, and both parallel and normal to the casting growth direction. TMF cracks are often nucleated at the airfoil film cooling holes due to a combination of high mechanical and thermal cyclic stresses and strains.

We have conducted several sets of TMF tests to study the underlying mechanisms of damage evolution. The first series of OP-tests was performed on single crystals flat dog bone specimens (Getsov et al. 2008). The loading direction was close to (001) crystallographic direction. EBSD mapping (measurement of crystal orientation) was performed in an area of $9 \times 12 \mu\text{m}^2$ in different spots along the specimens. Because the measurements were performed on the side plane (perpendicular to the loading direction) the EBSD results shown as inverse pole figures in Fig. 10 are close to (011). All orientation results measured in 10 points far from the failure site

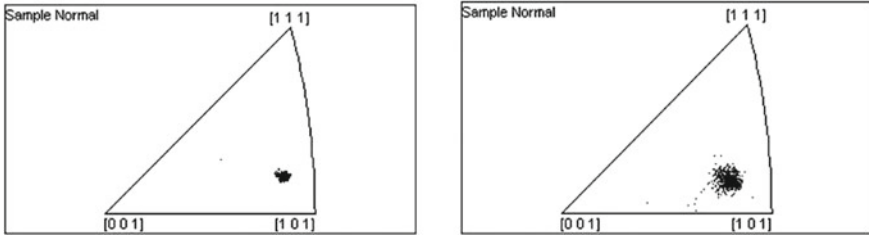


Fig. 10 Creep prediction versus experimental data for 982°C corresponding to three different nominal stress levels of 207 MPa, 248 MPa, and 344 MPa applied along (001) crystallographic direction and of 248 MPa applied along (111) direction

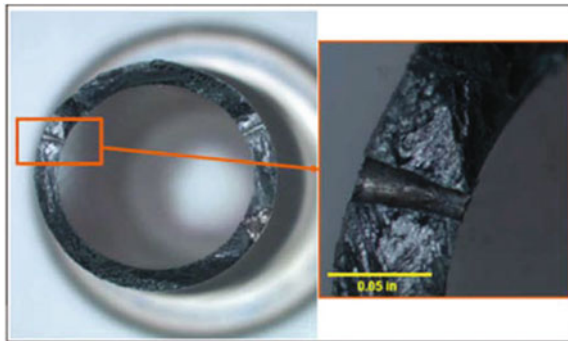


Fig. 11 TMF crack fracture surface after testing up to $\Delta\varepsilon = 0.8\%$ at 426–1038°C temperature range

(further than 4 mm) are almost identical with minimal scattering indicating that the tested material is the single crystal. There are some minor scattering due to not perfectly prepared surface. The results in the spots located within 1 mm from the TMF fracture edge demonstrate significant scatter, indicating noticeable plastic deformation accompanies TMF process. It suggests that the primary driver for TMF failure would be amount of creep and plasticity energy dissipated during each cycle.

The second set of TMF tests (Kersey et al. 2013) was performed on cylindrical specimens MT41 loaded along $\langle 100 \rangle$ crystallographic direction and having drilled two holes with dimer of 0.6 mm and located 135 degrees apart (for example, along $\langle 010 \rangle$ and $\langle 011 \rangle$ crystallographic directions). As one can see in Fig. 11, the crack initiated at $\langle 110 \rangle$ oriented hole is the dominant one. Initially two cracks emanate from both holes. Crack nucleation is a relatively slow process and for most of the life time the acquisition system does not register any crack growth. Once crack initiation has occurred the crack growth rate increases very rapidly. With the increase of the maximum temperature of the TMF cycle, the number of cycles to failure drops as can be seen from graphs in Fig. 12a, b.

Based on the fatigue crack growth (FCG) test data we compare the crack propagation rate under TMF loading conditions against corresponding isothermal LCF

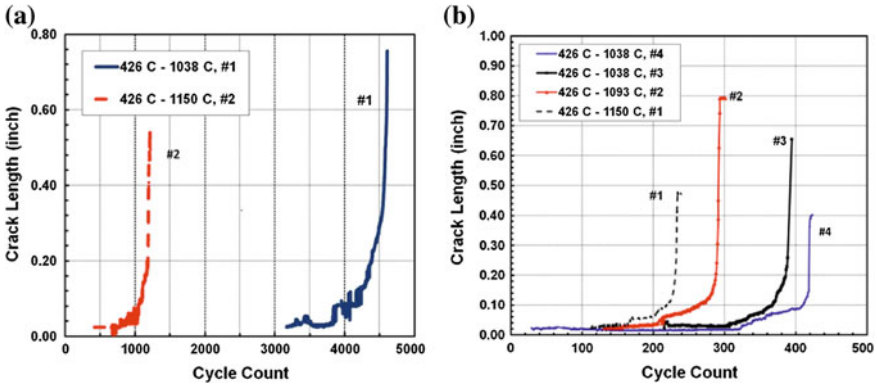


Fig. 12 Dominant crack growth at a 0.5% mechanical strain range for two different temperature ranges and b at 0.8% mechanical strain range for three different temperature ranges of OP TMF test

crack growth at the low TMF cycle temperature. As one can see from the Fig. 13, the TMF crack propagates considerably faster than corresponding crack growth rates of the isothermal low cycle fatigue tests. The difference is at least of a half of an order of magnitude. From these results one can conclude that at the high temperature portion of the TMF cycle, the compressive visco-plastic deformations generate the damage, which in turn reduces material crack resistance. The difference in the crack

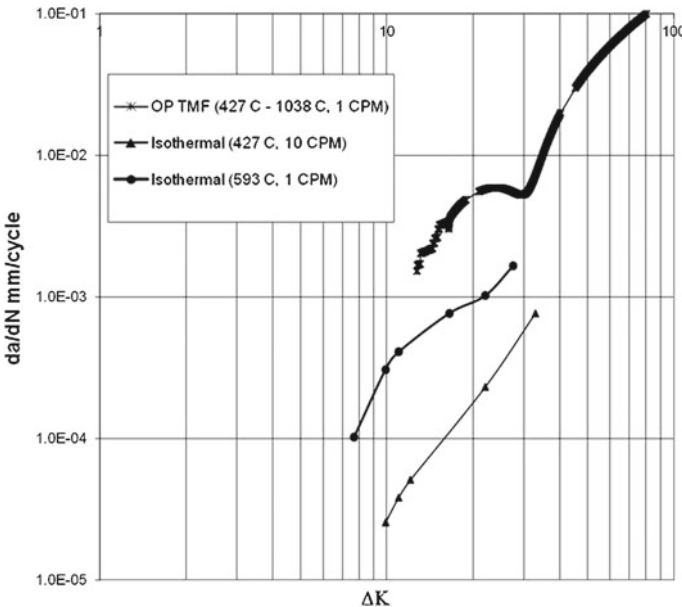


Fig. 13 Comparison of crack growth rate during TMF tests against corresponding isothermal data

growth rate is noticeable, so the damage tolerant design for TMF-limited parts should account for TMF accelerating damage effects.

At low homologous temperatures, fatigue cracks in PWA1484 propagate predominantly along $\{111\}$ octahedral crystallographic planes and failure is driven by the shear mode. Micrographs of the test specimens demonstrate initial crystallographic crack propagations, which later changed to a non-crystallographic crack growth mode. The typical fracture surface is rather flat mode I failure with numerous small crystallographic facets. Hard γ' precipitates in a superalloy behave as barriers to dislocations motion and hence strengthen the material microstructure.

FCG in single crystals is complex phenomenon with two major manifestations:

1. crack propagation in the matrix usually along precipitate interface (so-called precipitate avoidance) or
2. crystallographic precipitate cutting along multiple (111) planes or sometimes as 001 cleavage along cubic planes

It is widely accepted (Henderson and Martin 1996) that the specific crystallographic or non-crystallographic fracture mode is a strong function of temperature. Low temperatures favor crystallographic fracture. At higher temperatures, (above 982°C), propagation is almost entirely non-crystallographic (Lerch and Antolovich 1990; Staroselsky 2004; Kersey et al. 2013). Mixture of the precipitate avoidance and matrix tearing along crystallographic steps indicate the damage progression at all temperature regimes: the crystallographic step formation at low temperature and high temperature creep and plastic deformation at high temperature. As one can see the SEM analysis in Fig. 14 (Kersey et al. 2013) suggests that crack propagation is the mix of crystallographic shear and Mode I separation processes.

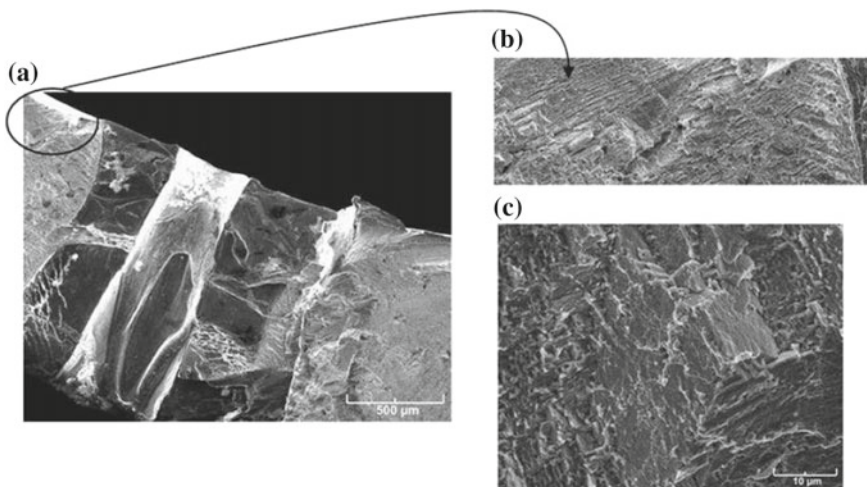


Fig. 14 SEM images of TMF fracture surface: **a** Next to the initial hole, **b** the details of transition region with deformation in two crystallographic orientation, **c** the high magnification showing the cracking on multiple crystallographic planes

The rate of the dissipated energy is the sum of the products of effective resolved shear stress $\tau^\alpha - \omega^\alpha$ acting along each of the slip system by the shear rate along the same slip system, $\dot{\gamma}^\alpha$. The amount of the energy dissipated during each cycle is the integral of the dissipated energy rate over one cycle.

$$\Delta W = \int_{\text{cycle}} \left[\sum_{\substack{\text{slipsystems} \\ \alpha=1,18}} (\tau^\alpha - \omega^\alpha) \dot{\gamma}^\alpha \right] dt \quad (23)$$

The test data analysis shows that the value of dissipated energy ΔW controls the life of the specimens. It is worth noting that the damage evaluated based on ΔW effectively accounts for the combined effect of fatigue and creep/plasticity through the width of the hysteresis loop and cannot be readily decomposed into a direct summation of the damages caused by fatigue and inelastic dissipation as widely used in engineering practice (i.e., Miner's rule).

14 Damage Model

Thermally induced damage rate is defined by the energy (or entropy) generation rate. Using kinetic form of the damage rate (Zhurkov 1965) and assuming that the energy barrier for damage generation, D , depends on the value of dissipated energy per each cycle, we have the following integral

$$D_0^T = A \int_0^{T_{\text{period}}} \exp\left(-\frac{Q - \Delta W}{k_B T(t)}\right) dt \quad (24)$$

where $T(t)$ is the local metal temperature. Typical values of $\Delta W/k_B T \ll 1$ and, subsequently, using the Taylor expansion, we obtain the damage due to thermo-mechanical fatigue

$$D^T = A \int_0^{T_{\text{period}}} \exp\left(-\frac{Q}{k_B T(t)}\right) dt \quad (25)$$

If the dissipated energy per cycle is significant, which corresponds to creep rupture and to cycles to large strain (>1% strain magnitude), then the second term should be also taken into account. Analysis of the D^T term suggests that it represents the oxidation diffusion and corresponding damage effect in a part process zone. A regression analysis of the test data yields for the following semi-empirical formula to predict number of cycles to failure.

$$\frac{1}{N_f} = e^{\frac{q \Delta W}{T_{\max}}} \left[\frac{1}{C_1 / \sigma_{\max}^m} + \frac{1}{C_2 / (\Delta W \cdot D^T)^k} \right] \tag{26}$$

Here, σ_{\max} is the maximum principal stress, and C_1, C_2, ν, q and m are empirical constants. Thus, the number of cycles to failure due to inelastic rupture can be expressed as follows

$$N_R = \frac{C_2}{(\Delta W \cdot D^T)^\nu} \tag{27}$$

Note also that the specimen life is controlled by the energy dissipation, or in other words, damage initiation life varies with the product $(\Delta W \cdot D^T)^\nu$, where the power, $\nu < 1$ reflects the part of the dissipated energy dissipated in the failure process. Assuming now that fatigue crack propagation is controlled by a Paris law it is easy to show that the crack growth life is inversely proportional to the maximum principal stress to some power, $N_F \propto C_1 / \sigma_{\max}$. Using this reduced order approach we neglect the difference in crystallographic and non-crystallographic crack growth mechanisms. Field experience demonstrates that the majority of the airfoil failures follow in average Mode I crack growth trend, which justifies the chosen method. Combining expressions for expected life prediction due to different mechanisms, we obtain the final result.

$$\frac{1}{N_f} = \frac{1}{N_F} + \frac{1}{N_R} \tag{28}$$

Equation (28) agrees with the work of Neu and Sehitoglu (1989), and indicates that failure due to elastic and fracture of inelastic rupture are independent quantities. Finally, we use multi-linear regression to fit the coefficients C_1 and C_2 , in the empirical life prediction formula. The quality of different coupon tests life calculations are shown in Fig. 15.

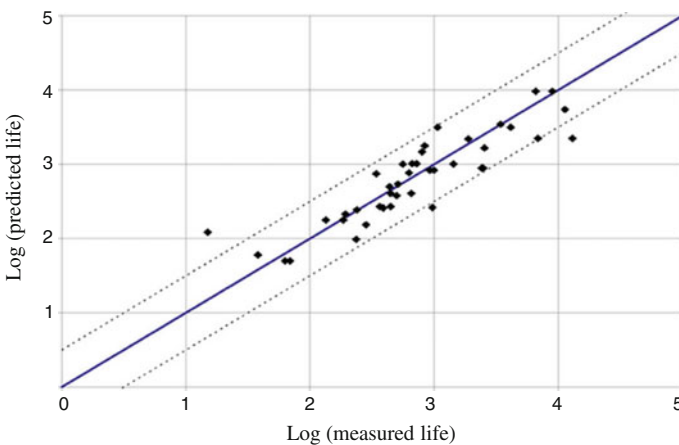


Fig. 15 Life Prediction is within 2X interval against measured data for both OP TMF and isothermal LCF tests

15 Simulations of Transient Thermal Mission

The developed formula has been implemented into USERMAT ANSYS in the form of damage rate evolution and the life predictions. The variation in damage can be used to identify locations where airfoil cracking will occur and to allow a redesign of the airfoil before production starts. It helps to eliminate expensive iterations of blade production and testing to assess durability. In the following examples we demonstrate our physics-based life prediction model on a second turbine blade of a commercial aircraft engine. This turbine airfoil consists of a conventionally-cast single crystal (SX) Ni-based superalloy and a thermal barrier coating.

An ANSYS turbine blade model with 200,000 finite elements was used for both the thermal and structural analysis. The model used the geometry of the air-foil, internal channels, heat transfer enhancement features, and impingement cooling holes, but not the internal turbulators (boundary layer trip strips) and film cooling holes. Rate-dependent viscoplastic deformation commenced near cooling holes on the concave surfaces of the blade, propagated across the thickness of the blade, in turn, put extra tension on the leading-edge region, which then necked, and a crack formed at the trailing edge at about the midspan region. We considered the airfoil deformation and damage accumulation during a typical combined mission consisting of several combined cycles, which represented a simplified turbine block test profile. Our damage summation law provided estimates for the damage accumulation for each cycle, resulting in the part life from the analysis of the combined mission.

During each cycle, the engine began from the idle stage to the maximum takeoff regime (MTO), which was then stabilized at a slightly lower level at the maximum continuous thrust (MCT) regime, and finally shut down to the idle condition. The maximum gas temperature T_{\max} for the turbine blade inlet temperature, $T_{4,1}$, was at takeoff. The maximum continuous thrust regime had a maximum gas temperature about 10% cooler. Each simulated cycle had long MTO and MCT legs of a representative mission. The transient heat transfer procedure described in the first section of the chapter was used to calculate a time-varying airfoil metal temperature distribution at each nodal point of the finite element model (FEM) of the solid. The simulation included a thermal barrier coating for the reduced convective heat transfer and weight contribution to the overall stress distribution, however, the structural and load bearing characteristics of this material were ignored.

A contour plot of the instantaneous metal temperature at the end of the climb point is shown in Fig. 16a. The distribution of von Mises stress is shown in Fig. 16b, and we show it here only to illustrate an equivalent stress measure for an isotropic material. We are using this measure to reflect the intensity of the residual stresses because plasticity is driven by shear stress rather than hydrostatic stresses. Stress concentrations were seen on the internal cooling surfaces and around cooling holes. These were found to die out rapidly away from the concentrations; therefore, this effect on the life prediction was limited and could be ignored. The thermal analyses showed that the leading edges and blade tip had the highest metal temperature. The internal airfoil ribs adjacent to the cooling passages were much cooler than the metal

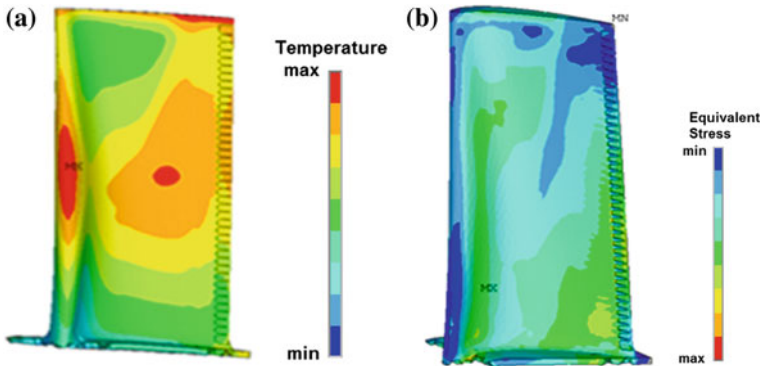


Fig. 16 Instantaneous contour of **a** wall temperature on the coating/metal interface of the blade at the end of climb and **b** equivalent stress on the external surface of the blade at maximum continuous thrust

surface at the airfoil leading edge. Thus, the metal temperature varied over a wide range, high enough to cause creep deformations and, subsequently, significant stress redistribution.

16 Simulations Using Viscoplastic Model

Since we are focusing on creep-plasticity deformation, we are interested in characterizing its contribution to the residual stress field and the susceptibility of the material to yielding. The thermally induced stresses caused noticeable creep deformation within the range of temperature distribution. Our analysis showed that localized creep strain might exceed 10%, so the large deformation options in the damage accumulation model were, and should be, included in the analysis. It is also important to emphasize that airfoil cross-section average deformation were small (less than a couple percent), however, the local deformation was significant, and led to the permanent damage and cracking.

A slice of the FEM solution is plotted in Fig. 17a to show that stress redistributes from creeping areas to the cold ribs. As a result, after completion of the mission cycle (creep inducing heating followed by non-homogeneous part cooling down), the residual stress builds in the crept areas due to deformation constraints during the blade cooling. Figure 17b shows that the equivalent stress is highest at the trailing edge, which is also where the creep deformation was the most pronounced. The tensile residual stress is built in and ratchets with cycles until it reaches the stable value.

Experience shows that many high temperature components suffer from high stresses at low (even room) temperature during the mission cooling leg and shut-down. Materials creep to a new equilibrium state at high temperature and the creep

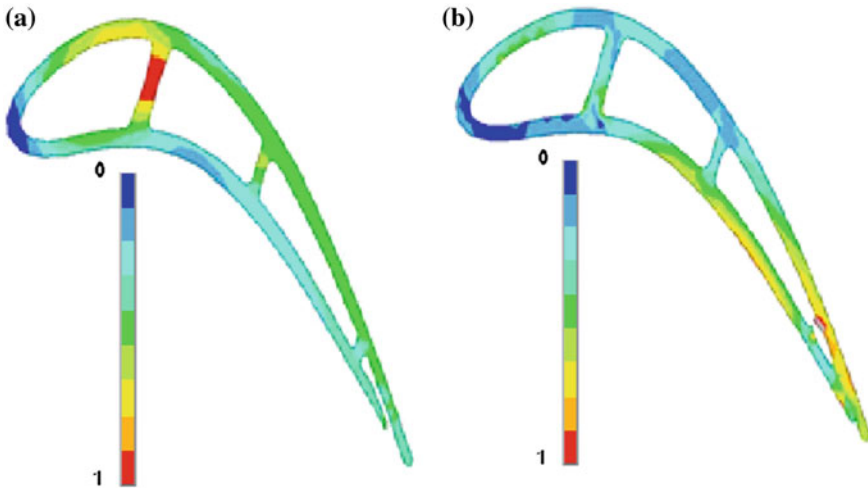


Fig. 17 Slice of the stress distribution in the blade showing normalized stress concentration (a), and residual stress distribution (b)

stress relaxes. During mission cooling and shut-down the non-uniform temperature fields and the internal mechanical constraints in the component cause high local residual stresses at low temperatures. In the analyzed example, the maximum residual tensile stress increases from basically zero up to a very high value in several cycles. This residual stress is one of the driving forces for TMF cracking. Generally speaking, the compression creep under the high temperature regime leads to the stress relaxation, which in turns leads to the increase of the tensile stress at the low temperature mission leg. This process stabilizes when the compressive stresses become small enough to cause significant creep. Thus, initially high compressive stresses relax faster than initially moderate compressive stresses, but both stabilize at approximately the same temperature dependent level.

Our damage measure accounts for the combined effect of fatigue, creep and plasticity through the width of the hysteresis loop. Figure 18 illustrates the predicted damage distribution in the analyzed blade after the combined mission cycles consistent with a real blade run through block tests under similar loading conditions and over a simplified associated mission. The relative variation in damage can be used to identify locations where actual airfoil cracking occurred. The largest damage calculations are predicted to be on the pressure side of the airfoil, with the peaks also at the trailing edge and at the blade tip. Due to Pratt & Whitney Co. proprietary concerns, we do not show a figure of the actual tested blade. In the actual test, a crack initiated at approximately midspan on the pressure side at the trailing edge, which was in the same location where damage was predicted to accumulate.

As can be seen in Fig. 18, the highest amounts of creep occurred at the thin-walled areas of the pressure side surface between the trailing edge slots and the impingement holes. In addition, our plasticity model predicted radial growth of the blade that

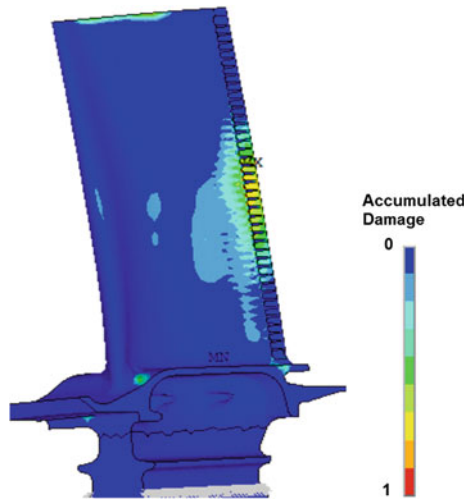


Fig. 18 Calculated damage distribution in the blade after the block test which lead to cracking in the actual test

matched the mean measured blade growth, and local creep strains and stress relaxations were evident at expected points in the mission. Specifically, creep accrued primarily in the maximum take-off stage, while little accrued during maximum continuous thrust. The majority of plastic strain and stress redistribution occurred upon initial loading, with the highest plastic strains in areas highlighted in the figure. The estimated life of the airfoil in this particular calculation was about 350 actual cycles, which is very close to tests observations. Also the observed damage resembles oxidation damage, which is effectively predicted by the use of the term in Eq. 25. Thus, the conceptual process for damage evaluation is established, tested and validated.

17 Concluding Remarks

The chapter outlines the methodological approach for gas turbine airfoil durability life prediction and reliability analysis. Our methodology utilizes a fully-coupled elastic-viscoplastic model that was based on crystal morphology and combined with an accurate transient conjugate thermal analysis. Our semi-empirical lifing model introduced the use of dissipated energy to estimate the remaining part life in terms of cycles to failure. The method was effective for use with three-dimensional finite element models of turbine airfoils using commercial finite element applications.

The equations governing the mechanical response have been calibrated against experimental data to accurately predict deformation, stress, and damage evolution especially during creep, LCF and TMF cycles. The analysis shows that the value of dissipated energy over the cycle controls the life of the specimens, and that the

combined creep and TMF plastic damage is not simply the direct sum of both forms of damage. Our constitutive model was also demonstrated and validated on a turbine blade of a commercial airfoil engine. Results showed that the major damage and TMF cracking took place at low temperature while tensile stresses emerged at the crept areas of the airfoil. The computational results are in extremely good accord with the results of the engine block test in that the model accurately predicts the location of the damage and time to failure.

Our methodology was specifically designed to predict the effects of non-homogeneous transient temperature variation on airfoil component deformations and life prediction, which are necessary for the TMF failure prediction, especially for military fighter missions. Civil aviation mission analysis is not so sensitive to the very short transient effects, however take off and shut down regimes are still needed to be analyzed using transient methodology. With this approach, turbine durability engineers are able to predict damage and design to account for crucial creep-fatigue interaction the local deformation effects, and make a major step to-wards a damage tolerant design.

References

- Amaro RL, Antolovich SD, Neu RW, Staroselsky A (2010) On thermo-mechanical fatigue in single crystal Ni-base superalloys. *Procedia Eng* 2(1):815–824
- Brillert D, Reichert AW, Simon H (1999) Calculation of flow losses in rotating passages of gas turbine cooling systems. In: *International gas turbine & aeroengine congress & exhibition*. ASME, Indianapolis, pp Paper 99-GT-251
- Bunker RS (2005) A review of shaped hole turbine film cooling technology. *ASME J Heat Transf* 127(4):441–453
- Crawford ME, Kayes WM (1976) STAN5—program for numerica-computation of two-dimensional internal and external boundary layer flows. Technical Report NASA-CR-2742, Stanford University
- Dipprey DF, Sabersky RH (1963) Heat and momentum transfer in smooth and rough tubes at various prandtl number. *Int J Heat Mass Transf* 6:329–353
- Getsov L, Semenov A, Staroselsky A (2008) A failure criterion for single-crystal superalloys during thermocyclic loading. *Mater Technol* 42:3–12
- Goldstein RJ (1971) Film cooling. *Adv Heat Transf* 7:321–379
- Gritsch M, Schulz A, Wittig S (1997) Discharge coefficient measurements of film-cooling holes with expanded jets. In: *International gas turbine & aeroengine congress & exhibition*. ASME, Orlando, pp Paper 97-GT-165
- Gullickson J, Needleman A, Staroselsky A, Cassenti B (2008) Boundary damage effects on the evolution of creep strain. *Model Simul Mater Sci Eng* 16(7):075.009 (14pp)
- Han JC, Park JS (1988) Developing heat transfer in rectangular channels with Rib turbulators. *Int J Heat Mass Transf* 31(1):183–195
- Henderson MB, Martin JW (1996) The influence of crystal orientation on the high temperature fatigue crack growth of a Ni-based single crystal superalloy. *Acta Mater* 44(1):111–126
- Kalidindi SR, Bronkhorst CA, Anand L (1992) Crystallographic texture evolution in bulk deformation processing of FCC metals. *J Mech Phys Solids* 40(3):537–569
- Kassab AJ, Li H (1994) A coupled FVM/BEM approach to conjugate heat transfer in turbine blades. In: *6th joint thermophysics and heat transfer conference*, AIAA and ASME, Colorado Springs

- Kawaike K, Shunichi A, Sasada T (1992) Integrated CAE system for cooled turbine blade design and verification tests of analytical codes. In: Goldstein RJ, Metzger DE, Leontiev AI (eds) Proceedings of the international symposium on heat transfer in turbomachinery, Greece
- Kersey RK, Staroselsky A, Dudzinskia DC, Genest M (2013) Thermomechanical fatigue crack growth from laser drilled holes in single crystal nickel based superalloy. *Int J Fatigue* 55:183–193
- Lakshminarayana B (1996) Fluid dynamics and heat transfer of turbomachinery. Wiley, New York
- Larson FR, Miller J (1952) A time-temperature relationship for rupture and creep stresses. *Transf ASME* 74:765–775
- Le Grives E (1986) Cooling techniques for modern gas turbines. In: Japiske D (ed) Chapter 4 in advanced topics in turbomachinery technology. Concepts ETI Inc, no 2 in Principal Lectures Series
- Lerch B, Antolovich SD (1990) Fatigue crack propagation behavior of a single crystalline superalloy. *Metall Mater Trans A* 21(8):2169–2177
- Levitin V (2006) High temperature strain of metals and alloys. Wiley-VCH, Weinheim
- Martin TJ (2001) Computer-automated multi-disciplinary analysis and design optimization of internally cooled turbine blades. PhD thesis, Department of Aerospace Engineering, The Pennsylvania State University, University Park
- Martin TJ, Dulikravich GS (2002) Analysis and multi-disciplinary optimization of internal coolant networks in turbine blades. *AIAA J Propuls Power* 18(4):896–906
- Menon MN (1992) A model for primary, secondary and tertiary creep rates. In: Proceedings of the 5th International conference on creep of materials. Lake Buena Vista, pp 163–169
- Mughrabi H (1975) Description of the dislocation structure after unidirectional deformation at low temperatures. In: Argon A (ed) Constitutive equations in plasticity. MIT Press, Cambridge, pp 199–251
- Neu RW, Sehitoglu H (1989) Thermomechanical fatigue, oxidation, and creep: part II. Life predict *Metall Trans A* 20(9):1769–1783
- Staroselsky A (1997) Crystal plasticity due to slip and twinning. PhD thesis, MIT, Cambridge
- Staroselsky A (2004) Damage and cracking morphology. In: Varvani-Farahani A, Brebbia CA (eds) Advances in fracture and damage assessment of materials. WIT Press
- Staroselsky A, Cassenti B (2008) Mechanisms for tertiary creep of single crystal superalloy. *Mech Time-Depend Mater* 12(4):275–289
- Staroselsky A, Cassenti BN (2010) Combined rate-independent plasticity and creep model for single crystal. *Mech Mater* 42(10):945–959
- Staroselsky A, Cassenti BN (2011) Creep, plasticity, and fatigue of single crystal superalloy. *Int J Solids Struct* 48(13):2060–2075
- Stouffer D, Dame L (1996) Inelastic deformation of metals. Wiley, New York
- Webb RL (1998) Principles of enhanced heat transfer. Wiley, New York
- White FM (1994) Fluid mechanics. McGraw-Hill Book Co, New York
- Wilcox D (1988) Re-assessment of the scale-determining equation for advanced turbulence models. *AIAA J* 26(11):1299–1310
- Zhurkov SN (1965) Kinetic concept of the strength of solids. *Int J Fract* 1(4):311–322

Ratchetting of Snake Skin: Experiments and Viscoelastic-Plastic Constitutive Model

Yilin Zhu and Guozheng Kang

Abstract In this paper, the cyclic deformation of snake skin is experimentally observed by the in vitro tests under uniaxial cyclic loading conditions and at room temperature for the first time. The effect of loading level on the cyclic deformation and the anisotropic deformation of snake skin are investigated, respectively. The results show that ratchetting (i.e., a cyclic accumulation of strain) occurs during the cyclic tension-tension tests of snake skin, and depends greatly on the loading orientations and levels. Based on the experimental results of uniaxial ratchetting, a simplified version of the finite viscoelastic-plastic model (Zhu et al. in *J Biomech* 47:996–1003, 2014) for soft biological tissues is obtained. The comparison shows that the simulated results are in qualitative agreement with the experimental ones.

Keywords Snake skin · Ratchetting · Viscoelastic-plastic model · Finite deformation

1 Introduction

It is important to understand the biomechanical performances of skin soft tissues, because they are playing a crucial role in the mechanical integrity analysis of living bodies, and are widely involved in many applications such as surgical treatment, orthopedic operation, and cosmetic development and so on. In the last few decades, the biomechanical behaviours of skin soft tissues were studied experimentally and theoretically by many researchers and many great achievements have been made.

Fung (1993), skin soft tissues are typical highly functional composite materials mainly made of collagen and elastin proteins, and possess some specific proper-

Y. Zhu (✉) · G. Kang
School of Mechanics and Engineering, Southwest Jiaotong University,
Chengdu 610031, People's Republic of China
e-mail: lin5210feng@163.com

G. Kang
e-mail: guozhengkang@home.swjtu.edu.cn

ties, such as viscosity, non-linear anisotropic biomechanical responses and preconditioning. Some basic biomechanical properties of skin soft tissues including elastic modulus, ultimate tensile strength and the anisotropic properties were obtained by monotonic uniaxial and biaxial tests (Fung 1993; Cua et al. 1990; Daly 1982; Greven et al. 1995; Silver et al. 2001, 2003; Iatridis et al. 2003; Xie et al. 2005; Gambarotta et al. 2005). Besides, since the cyclic biomechanical response is very important in assessing the fatigue life and wear property of skin soft tissues, some researchers were also devoted to investigate the cyclic deformation of skin soft tissues experimentally (Munoz et al. 2008; Giles et al. 2007; Kang and Wu 2011). Also, plenty of phenomenological constitutive models have developed to simulate the experimental phenomena of soft tissues, and of course the presented models can be used for modeling the tests of skin soft tissues (Zhu et al. 2014; Roan and Vemaganti 2011; Maher et al. 2012; Humphrey and Yin 1987a, b; Peña et al. 2010, 2011a, b; Peña and Doblaré 2009).

At present, snake skin has attracted much attention because it can be used to make elegant crafts for its unique and beautiful pattern. Some basic biomechanical behaviors of snake skin, such as the elastic and friction properties, had been studied by monotonic uniaxial tensile tests and friction tests (Jayne 1988; Bruckner et al. 2011; Klein et al. 2010; Klein and Gorb 2012; Marvi and Hu 2012; Baum et al. 2014). However, very few studies were focused on the cyclic deformation of snake skin. Under the stress-controlled cyclic loading conditions with non-zero mean stresses, it is well-known that ratchetting, a cyclic accumulation of inelastic deformation, shall occur in many engineering materials (Ohno 1990, 1997; Kang and Liu 2008; Chaboche 2008). The occurrence of ratchetting is detrimental to the fatigue behavior, and shortens the low-cycled fatigue life of the materials (Kang and Liu 2008; Kang et al. 2006). Therefore, it is necessary to reveal the ratchetting behavior of snake skin by performing corresponding cyclic loading tests in order to assess its fatigue life and wear property.

Therefore, in this paper, the cyclic biomechanical deformation of snake skin is investigated firstly by uniaxial cyclic tests, especially for the cyclic accumulation of peak strain, i.e., the ratchetting behaviors. The dependencies of ratchetting of snake skin on the loading levels and orientations are discussed. And then, based on the experimental results, a simplified version of the finite viscoelastic-plastic constitutive model developed by Zhu et al. (2014) is proposed. The capability of the simplified model to predict the ratchetting of snake skin is verified by comparing the predicted results with the corresponding experimental ones.

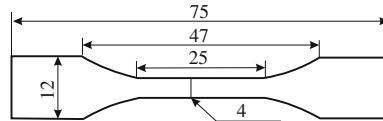


Fig. 1 Shape and size of the testing samples (units: mm)

2 Experimental Observations

2.1 Material and Procedure

The snake skin used in the tests was obtained from the dorsal area of the *orthriophis taeniurus* with a weight of about 450 g and 6 h after death. Tested skin samples were manufactured by CP-25-typed punching machine, with gauge length of 30 mm and gauged section of 4×0.3 mm (i.e., the width and thickness of samples are 4 and 0.3 mm, respectively, as shown in Fig. 1). It should be noted that all the samples were immersed in 0.9 % sodium chloride solution and all the tests were accomplished within two hours to keep the freshness of skin tissue and the samples for each loading mode were obtained from the same snake to keep the repeatability of experimental data.

All the tests were performed with an Instron-5567 (30 kN) machine and at room temperature, and the axial tensile strain was measured by the Instron 2603-080 Long Travel Extensometer (full scale travel is 250 mm) designed for the measurement of large strain. As commented by Kang and Wu (2011), a significant variation of deformation rate occurs in the whole process of deformation in a force-controlled mode, because the stress-strain response of skin tissue is highly nonlinear and small stress increment will cause a large strain response at initial stage of deformation. Therefore, all the tests in this work were performed under a nominal force-controlled mode which was controlled in a displacement-controlled mode with upper and lower force thresholds as is often done in such tests. In order to ensure the obtained mechanical responses steadily, all the samples are firstly preconditioned before testing by one loading-unloading cycle with a prescribed peak force of 2 N and loading rate of 20 mm/min. During the tests, applied displacement rate is prescribed to be 20 mm/min.

2.2 Monotonic Tensile Behavior

Before the ratchetting of snake skin was studied, some basic biomechanical properties were first investigated by monotonic tension, which are very useful to determine the loading levels of ratchetting tests and understand the ratchetting more deeply. The experimental results obtained in the monotonic tensile tests in different loading

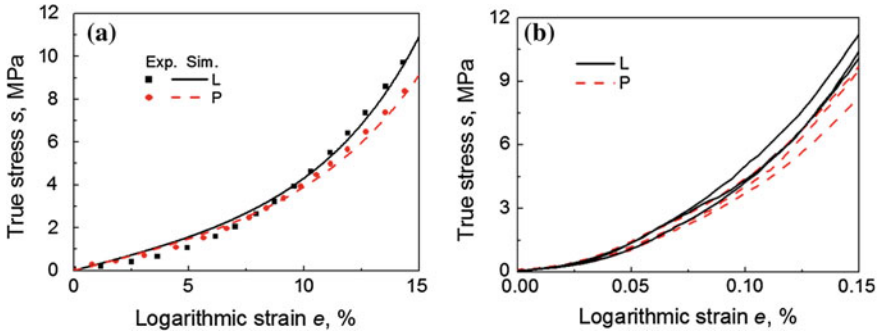


Fig. 2 Tensile stress-strain curves of snake skin: **a** experimental and simulated curves in different loading directions; **b** raw data in *L* and *P* directions

orientations are shown in Fig. 2. The orientations denoted as *L* and *P* in the figures represent the loading directions along and perpendicular to the Langer's lines of snake skin, respectively. As shown in Fig. 2a the stress-strain response of snake skin is highly nonlinear, and tensile stress-strain curve can be divided into two parts, i.e., the first part with an increasing tangent modulus, and the second one with a constant tangent modulus. It is also seen that the biomechanical response of snake skin is anisotropic with regard to the Langer's lines, and the snake skin presents a higher stress-strain response in the direction along the Langer's lines than in the perpendicular ones as shown in Fig. 2a. Hereafter, the values of true stress s and logarithmic strain e shown in the figures are calculated from the nominal stress σ and strain ε (originally from the measured forces, areas and lengths) according to the definitions of $s = \sigma(1 + \varepsilon)$ and $e = \ln(1 + \varepsilon)$.

The anisotropic deformation of snake skin is similar to the existed results of monotonic tension for other skin tissues (Fung 1993; Kang and Wu 2011). It should be noted that each curve shown in Fig. 2a was obtained from averaging the results of three samples with the same loading condition in order to diminish the dispersion of experimental data. The raw data of three averaging curves in different loading orientations shown in Fig. 2a are shown in Fig. 2b. It is seen from Fig. 2b that there is fairly apparent dispersion in raw data.

3 Uniaxial Ratchetting Behavior

Both the effects of loading orientation and level on the ratchetting behavior of snake skin were investigated in this section. Firstly, the nominal force-controlled cyclic tension-tension tests were performed in the directions along and perpendicular to Langer's lines, respectively, and the results are shown in Fig. 3. The applied peak and valley forces are 6 and 2 N, respectively, and the number of cycles is set to be 40.

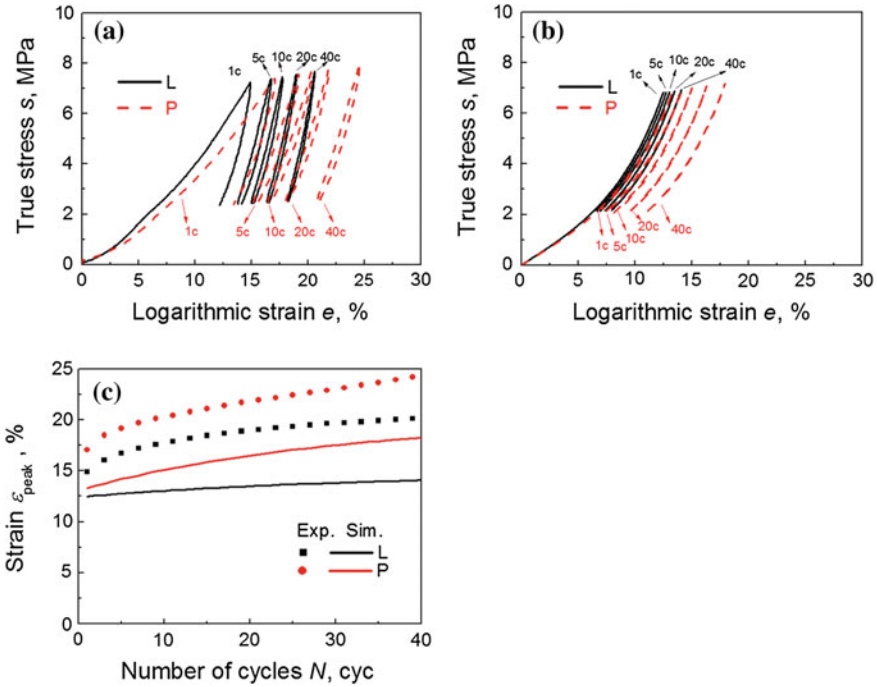


Fig. 3 Ratchetting of snake skin in the cyclic tension-tension tests and in different loading directions: **a** experimental cyclic stress-strain curves; **b** simulated cyclic stress-strain curves; **c** curves of peak strain ϵ_{peak} versus number of cycles N

To illustrate the ratchetting of snake skin more clearly, the peak strain ϵ_{peak} during each loading cycle is used in the figures.

It is seen from Fig. 3 that the cyclic accumulation of the peak strain occurs in the snake skin during the cyclic tension-tensile tests, especially in the direction perpendicular to the Langer’s lines. It means that the peak strain increases progressively with the increasing number of cycles, which is similar to that of ordinary metals subjected to a stress-controlled cyclic loading with non-zero mean stress (Ohno 1990, 1997; Kang and Liu 2008; Chaboche 2008). Thus, the cyclic accumulation of the peak strain presented in the snake skin is also called the ratchetting terminologically. Similar to that of metal materials, the ratchetting strain of snake skin increases with the increasing number of cycles, but the ratchetting strain rate (defined as the increment of ratchetting strain after each cycle) decreases very quickly at the first stage of cyclic loading and then reaches a nearly constant strain rate after certain cycles, as shown in Fig. 3c. Moreover, the ratchetting deformation of snake skin is anisotropic, and the ratchetting in the direction perpendicular to the Langer’s lines is more significant than that in the direction along the Langer’s lines, due to its weaker resistance to the deformation, as shown in Fig. 3.

Table 1 Load cases used in the cyclic tension-tension tests

Load case	Mean force (N)	Force amplitude (N)	Displacement rate (mm/min)
i	8	1	20
		4	
ii	7.5	2.5	20
	12.5		

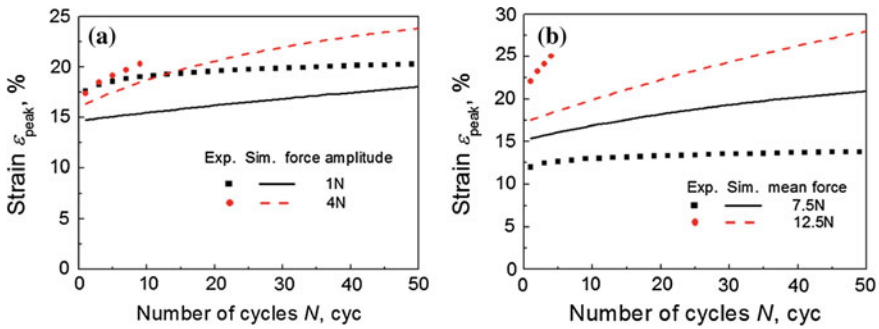


Fig. 4 Experimental and simulated ratchetting of snake skin in the cyclic tension-tension tests with different loading levels: **a** curves of peak strain ϵ_{peak} versus number of cycles N with varied force amplitude; **b** curves of peak strain ϵ_{peak} versus number of cycles N with varied mean force

The effect of loading level on the ratchetting of snake skin is also investigated by the cyclic tension-tension tests with different loading levels (i.e., different force amplitudes and mean forces, as listed in Table 1) in the direction along the Langer’s lines. The load cases shown in the figures, for example, 8 ± 4 N implies that the applied mean force is 8N and force amplitude is 4 N during the cyclic loading (or, in other words, the applied peak force is 12N and valley force is 4 N). It is seen that the ratchetting greatly depends on the loading level, and the ratchetting strain increases with the increasing mean force and force amplitude, as shown in Fig. 4a, b. When the loading level is too high, such as in the case of 8 ± 4 N in Fig. 4a and 12.5 ± 2.5 N in Fig. 4b, the ratchetting strain rate is relatively large and then results in a large ratchetting strain after certain cycles, which causes the failure of snake skin, e.g., 10 cycles in the case of 8 ± 4 N and 4 cycles in the case of 12.5 ± 2.5 N.

4 Simplified Constitutive Model

The finite viscoelastic-plastic constitutive model proposed by Zhu et al. (2014) can describe both the load level-dependence and time-dependence of the ratchetting for soft tissues. However, the experimental observations to the cyclic deformation of snake skin stated in Sect. 3 do not provide any information about the time-dependent ratchetting. Thus, a simplified form of the finite viscoelastic-plastic constitutive

model proposed by Zhu et al. (2014) is adopted in this section, which emphasizes the prediction to the uniaxial ratchetting of snake skin and its load level-dependence.

4.1 Main Equations

The main equations adopted in the simplified finite viscoelastic-plastic constitutive model are as follows:

$$\mathbf{F} = \mathbf{F}^e \mathbf{F}^{pl} \mathbf{F}^{pa} \mathbf{F}^{pv}, \quad (1)$$

$$\mathbf{B}^e = \mathbf{F}^e \mathbf{F}^{eT} \quad (2)$$

$$\mathbf{D} = \mathbf{D}^e + \mathbf{D}^{epl} + \mathbf{D}^{epa} + \mathbf{D}^{epv}, \quad (3)$$

$$\boldsymbol{\tau} = \underbrace{\frac{1}{2} \mu \exp(\alpha (I_1 - 1)) \mathbf{B}^e \mathbf{S}}_{\boldsymbol{\tau}_l} + \underbrace{\left(-\frac{1}{2} \mu \exp(\beta (I_2 - 1)) \mathbf{B}^{e-1} \mathbf{S} \right)}_{\boldsymbol{\tau}_a} + \underbrace{\frac{1}{3} q \mathbf{I}}_{\boldsymbol{\tau}_v}, \quad (4)$$

where \mathbf{F} is the deformation gradient tensor; \mathbf{F}^e is the elastic deformation gradient tensor representing the subsequent stretching and rotation caused by the elastic mechanism; \mathbf{F}^{pv} , \mathbf{F}^{pa} and \mathbf{F}^{pl} represent the local inelastic distortions caused by the plastic mechanisms associated with the deformations of volume, surface and line elements, respectively; \mathbf{B}^e is the left Cauchy-Green tensor; the expression \mathbf{A}^T denotes the transposition of the tensor \mathbf{A} ; \mathbf{D} is the stretching tensor; \mathbf{D}^e represents the elastic stretching tensor; \mathbf{D}^{epl} , \mathbf{D}^{epa} and \mathbf{D}^{epv} are the coupled elastic-plastic stretching tensors related to the line, surface and volume elements of the deformed body, respectively; $\boldsymbol{\tau}$ is the Kirchhoff stress, consisting of three parts, i.e., $\boldsymbol{\tau}_l$, $\boldsymbol{\tau}_a$ and $\boldsymbol{\tau}_v$, which represent the stresses related to the deformations of the line, surface and volume elements, respectively; μ is a material parameter with the dimension of stress; α and β are dimensionless material parameters; q is a Lagrange multiplier associated with the hydrostatic pressure; and \mathbf{S} is the structure tensor which is defined as

$$\mathbf{S} = \nu \mathbf{m} \otimes \mathbf{m} + (1 - \nu) \frac{1}{3} \mathbf{I}, \quad (5)$$

In Eq. (5), \mathbf{I} is the second-order identity tensor; ν denote scalar weight factors; and the unit vector \mathbf{m} represents the orientation of the alignment of the fiber family of soft tissues.

4.2 Evolution Equations of Coupled Elastic-Plasticity

According to the work of Zhu et al. (2014), \mathbf{D}^{epv} is a zero tensor, and the evolution equations of the coupled elastic-plastic stretching tensors \mathbf{D}^{epl} and \mathbf{D}^{epa} are set as follows

$$\begin{cases} \mathbf{D}^{\text{ep}l} = \gamma_l f(I_1) \|\mathbf{D}\| \boldsymbol{\tau}'_l, \\ \mathbf{D}^{\text{ep}a} = \gamma_a g(I_2) \|\mathbf{D}\| \boldsymbol{\tau}'_a, \end{cases} \quad (6)$$

where the expression \mathbf{A}' denotes the deviator of the tensor \mathbf{A} , i.e., $\mathbf{A}' = \mathbf{A} - \frac{1}{3}\text{trace}(\mathbf{A})\mathbf{I}$; the non-negative coupled elastic-plastic parameters γ_l, γ_a are formulated as

$$\begin{cases} \gamma_l = \gamma_l^0 + (\gamma_l^{\text{sat}} - \gamma_l^0) (1 - \exp(-b_l e)), \\ \gamma_a = \gamma_a^0 + (\gamma_a^{\text{sat}} - \gamma_a^0) (1 - \exp(-b_a e)), \end{cases} \quad (7)$$

where γ_i^0 ($i = l, a$) are the non-negative initial values; γ_i^{sta} ($i = l, a$) are the non-negative saturation value; b_i ($i = l, a$) controls the evolution rate of γ_i ($i = l, a$) and then controls the evolution of the ratchetting; e denotes the accumulated strain, and its rate is,

$$\dot{e} = \|\mathbf{D}\|. \quad (8)$$

5 Simulation and Discussion

5.1 Determination of Material Parameters

The elastic parameters μ, α, β and weight factors $v_i, i = 0, 1, \dots, n$, (here n is set as 1, and $v_0 = 1 - v_1$) can be simply determined by fitting the experimental tensile stress-strain curves of the snake skin obtained in different loading directions. Then the coupled elastic-plastic parameters γ_i^0 ($i = l, a$) and γ_i^{sta} ($i = l, a$) can be obtained from one experimental evolution curve of uniaxial ratchetting by a trial-and-error method. The obtained material constants are listed in Table 2.

5.2 Simulation and Discussion

Using the material constants listed in Table 2, the monotonic tensile stress-strain curves and ratchetting curves of snake skin were simulated numerically by the simplified constitutive model in different loading directions and with different loading levels. The simulated results are shown in Figs. 1a, 2, 3 and 4 for different loading

Table 2 Material parameters for snake skin

μ (MPa)	α	β	v_1	γ_1^0	γ_2^0	γ_1^{sat}	γ_2^{sat}	b_1	b_2
27.34	41.40	33.12	0.015	0.02	0.005	0.6	0.03	1.1	3.5

conditions, respectively. From Fig. 2, it is seen that, the anisotropic responses of snake skin during the monotonic tension in different loading orientations are reasonably described, and the simulated results agree with the experimental ones well. From Figs. 3 and 4 it is concluded that the uniaxial ratchetting of snake skin in different loading orientations and with different loading levels can also be simulated, in spite of the discrepancy on value; the simulated results are in qualitative agreement with the experimental ones.

It is noted that the simulated hysteresis loops look narrower than the experimental ones, see Figs. 3a and 4b. It is found that the loading elastic modulus is smaller than the unloading one due to a visco-elastic hysteresis effect, which results in a big hysteresis loop. In the present model, much attention was focused on the prediction of ratchetting strain, rather than the shape of the hysteresis loop. Surely, a future work will be developed to improve the prediction of the hysteresis loops by capturing the difference between loading modulus and unloading modulus. Besides, only a time-independent uniaxial ratchetting of snake skin is experimentally and theoretically investigated in this work. As discussed by Kang and Wu (2011), apparent time-dependent ratchetting of soft skin tissues occurs in the cyclic loading, and then the ratchetting of snake skin should be investigated in the future work by addressing its time-dependence. Furthermore, similar to the previous work (Zhu et al. 2014; Kang and Wu 2011), only the uniaxial ratchetting of soften skin tissues is discussed here, much effort should be paid to the bi-axial or multiaxial ratchetting of skin tissues in the future work.

6 Conclusions

1. The biomechanical responses of snake skin are anisotropic in the monotonic tensions, and the snake skin presents a higher stress-strain response in the direction along the Langer's lines than in the direction perpendicular to the Langer's lines.
2. Ratchetting, a cyclic accumulation of viscoelastic-plastic deformation occurs in the snake skin during the cyclic tension-tension tests. The ratchetting of snake skin also depends greatly on the loading orientations and levels.
3. Based on a simplified constitutive model, the time-independent uniaxial ratchetting of snake skin are reasonably simulated, and the simulated results are in qualitative agreement with the corresponding experimental ones.

Acknowledgments Financial supports by the National Natural Science Foundation of China (11025210), the project for Sichuan Provincial Youth Science and Technology Innovation Team, placecountry-regionChina (2013TD0004), the 2013 Doctoral Innovation Funds of Southwest Jiaotong University and the Fundamental Research Funds for the Central Universities are gratefully acknowledged.

References

- Baum MJ, Kovalev AE, Michels J, Gorb SN (2014) Anisotropic friction of the ventral scales in the snake *Lampropeltis getula californica*. *Tribol Lett* 54(2):139–150
- Bruckner D, Hellmich C, Schmiedmayer HB, Stachelberger H, Gebeshuber IC (2011) *Biomimetics-materials, structures and processes*. Springer, New York
- Chaboche JL (2008) A review of some plasticity and viscoplasticity constitutive theories. *Int J Plast* 24(10):1642–1693 (Issue in Honor of Jean-Louis Chaboche)
- Cua AB, Wilhelm KP, Maibach HI (1990) Elastic properties of human skin: relation to age, sex, and anatomical region. *Arch Dermatol Res* 282(5):283–288
- Daly CH (1982) Biomechanical properties of dermis. *J Invest Dermatol* 79:17–20
- Fung YC (1993) *Biomechanics: mechanical properties of living tissues*. Springer, New York
- Gambarotta L, Massabo R, Morbiducci R, Rapisio E, Santi P (2005) In vivo experimental testing and model identification of human scalp skin. *J Biomech* 38(11):2237–2247
- Giles JM, Black AE, Bischoff JE (2007) Anomalous rate dependence of the preconditioned response of soft tissue during load controlled deformation. *J Biomech* 40(4):777–785
- Greven H, Zanger K, Schwinger G (1995) Mechanical properties of the skin of *Xenopus laevis* (Anura, Amphibia). *J Morphol* 224:15–22
- Humphrey JD, Yin FC (1987a) A new constitutive formulation for characterizing the mechanical behavior of soft tissues. *J Biomech Eng* 52(4):563–570
- Humphrey JD, Yin FC (1987b) On constitutive relations and finite deformations of passive cardiac tissue: I. A pseudostrain-energy function. *J Biomech Eng* 109(4):298–304
- Iatridis JC, Wu J, Yandow JA, Langevin HM (2003) Mechanobiology of force transduction in dermal tissue. *Skin Res Technol* 4(5):208–225
- Jayne BC (1988) Mechanical behaviour of snake skin. *J Zool* 214(1):125–140
- Kang GZ, Liu YJ (2008) Uniaxial ratchetting and low-cycle fatigue failure of the steels with cyclic stabilizing or softening feature. *Mater Sci Country-Regionplace Eng* 472:258–268
- Kang G, Wu X (2011) Ratchetting of porcine skin under uniaxial. *J Mech Behav Biomed Mater* 4(3):498–506
- Kang GZ, Liu YJ, Li Z (2006) Experimental study on ratchetting—fatigue interaction of ss304 stainless steel in uniaxial cyclic stressing. *Mater Sci Eng A* 472(435–436):396–404
- Klein MCG, Gorb SN (2012) Epidermis architecture and material properties of the skin of four snake species. *J R Soc Interface* 9:3140–3155
- Klein MCG, Deuschle JK, Gorb SN (2010) Material properties of the skin of the Kenyan sand boa *Gongylophis colubrinus* (Squamata, Boidae). *J Comp Physiol A* 196:659–668
- Maher E, Creane A, Lally C, Kelly DJ (2012) An anisotropic inelastic constitutive model to describe stress softening and permanent deformation in arterial tissue. *J Mech Behav Biomed Mater* 12:9–19
- Marvi H, Hu DL (2012) Friction enhancement in concertina locomotion of snakes. *J R Soc Interface* 9:3067–3080
- Munoz MJ, Bea JA, Rodriguez JF, Ochoa I, Grasa J, Zaragoza P, Osta R, Doblare M (2008) An experimental study of the mouse skin behaviour: damage and inelastic aspects. *J Biomech* 41(1):93–99
- Ohno N (1990) Recent topics in constitutive modeling of cyclic plasticity and viscoplasticity. *Appl Mech Rev* 43:283–295
- Ohno N (1997) Recent progress in constitutive modeling for ratchetting. *Mater Sci Res Int* 3:1–9
- Peña E, Doblare M (2009) An anisotropic pseudo-elastic approach for modelling Mullins effect in fibrous biological materials. *Mech Res Commun* 36(7):784–790
- Peña E, Alastrue V, Laborda A, Martinez MA, Doblare M (2010) A constitutive formulation of vascular tissue mechanics including viscoelasticity and softening behaviour. *J Biomech* 43(5):984–989

- Peña E, Martins P, Mascarenhas T, Natal J, Ferreira A, Doblaré M, Calvo B (2011a) Mechanical characterization of the softening behavior of human vaginal tissue. *J Mech Behav Biomed Mater* 4(3):275–283
- Peña JA, Martínez MA, Peña E (2011b) A formulation to model the nonlinear viscoelastic properties of the vascular tissue. *Acta Mechanica* 217(1–2):63–74
- Roan E, Vemaganti K (2011) Strain rate-dependent viscohyperelastic constitutive modeling of bovine liver tissue. *Med Biol Eng Comput* 49(4):497–506
- Silver FH, Freeman JW, DeVore D (2001) Viscoelastic properties of human skin and processed dermis. *Skin Res Technol* 7(1):18–23
- Silver FH, Siperko LM, Seehra GP (2003) Mechanobiology of force transduction in dermal tissue. *Skin Res Technol* 9(1):3–23
- Xie C, Liu N, Gao Z, Lin D, Guo Z (2005) Investigating testing elasticity of equivalent material for human skin. In: 27th Annual International Conference of the Engineering in Medicine and Biology Society, 2005. IEEE-EMBS 2005, pp 5862–5864
- Zhu Y, Kang G, Kan Q, Yu C (2014) A finite viscoelastic-plastic model for describing the uniaxial ratchetting of soft biological tissues. *J Biomech* 47(5):996–1003